Vniversitat de València
Departamento de física atómica, molecular y nuclear
INSTITUTO DE FÍSICA CORPUSCULAR

Doctoral Programme in Physics

High resolution ^{80}Se(n,γ) cross section measurement at CERN n_TOF and development of the novel i-TED detection system

Valencia, Enero 2022

Doctoral thesis by:
Víctor Babiano Suárez

Supervisors:
César Domingo Pardo
Javier Balibrea Correa
Jorge Lerendegui Marco

A mi ansiedad

El **Dr. César Domingo Pardo**, investigador del Consejo Superior de Investigaciones Científicas (CSIC), el **Dr. Javier Balibrea Correa**, investigador del Consejo Superior de Investigaciones Científicas (CSIC), el **Dr. Jorge Lerendegui Marco**, investigador del Consejo Superior de Investigaciones Científicas (CSIC), y el **Dr. Juan de Dios Zornoza Gómez** profesor titular de la Universitat de València

CERTIFICAN:

Que la presente memoria titulada **High resolution ^{80}Se(n,γ) cross section measurement at CERN n_TOF and development of the novel i-TED detection system**, ha sido realizada bajo nuestra dirección en el Instituto de Física Corpuscular (Centro Mixto Universitat de València - CSIC) por **Víctor Babiano Suárez** y constituye su Tesis para optar al título de Doctor por la Universitat de València una vez cursados los estudios en el Doctorado en Física.

Y para que así conste, en cumplimiento con la legislación vigente, presenta ante el Departamento de Física Atómica, Molecular y Nuclear la referida memoria, firmando el presente certificado en Paterna (Valencia) a fecha de 31 de Enero de 2022.

Fdo. Dr. César Domingo Pardo

Fdo. Dr. Javier Balibrea Correa

Fdo. Dr. Jorge Lerendegui Marco

Dr. Juan de Dios Zornoza Gómez

This Thesis work has been funded by the European Research Council under Grant Agreement Nr. 681740 - Project HYMNS -

erc

European Research Council

Established by the European Commission

Table of Contents

List of Figures

List of Tables

Abstract

The slow neutron capture (s-) process is responsible for the formation of half of the elements heavier than iron in the universe. Despite the long time scale of this process, the long half-life of some unstable isotopes throughout the s-process reaction flow creates branching points that lead to a split of the nucleosynthesis path. ^{79}Se ($t_{1/2} = 3.27 \times 10^5$ y) represents one of the most relevant and debated s-branching nuclei for two main reasons. On the one hand, the existence of low-energy excited states in ^{79}Se, whose population can vary with the temperature of the stellar medium, makes the local abundance pattern around this branching especially sensitive to the thermal conditions. On the other hand, the observed abundances of the s-only krypton isotopes (^{80,82}Kr) are very well-known from meteoric data. Thus, by comparing these abundances with those predicted by stellar models, information about the thermal conditions of the stellar media in which the s-process occurs can be obtained. To this aim, state-of-the-art hydrodynamic stellar models need experimental input data on the neutron capture cross section of the isotopes involved in the branching over a broad thermal energy range. The latter statement is certainly true for the unstable ^{79}Se and its closest neighbouring nuclei, ^{78,80}Se. However, neutron capture measurements on radioactive nuclei are very challenging and indeed, thus far, there is no experimental data on the ^{79}Se(n, γ) reaction. Also, previous experimental data on ^{80}Se was rather limited in terms of resolution and completeness.

In this context, the present work has contributed in two different fronts with the aim of shedding light on to the ^{79}Se s-process branching.

The first part of this work describes the neutron capture cross section measurement of ^{80}Se at CERN n_TOF, with very high energy resolution and covering the full stellar energy range of interest for the first time. The previous measurement on ^{80}Se(n,γ) suffers from a very limited energy resolution and a short neutron-energy range. These drawbacks have been remarkably improved in this work by means of a high-resolution time of flight (ToF) measurement employing a high purity ^{80}Se sample of 3.8 g of mass. The use of C_6D_6 total energy detectors in combination with the Pulse-Height Weighting Technique (PHWT), have allowed us to obtain a capture yield with high accuracy and covering the entire energy range

of astrophysical interest between 1 eV and 100 keV. One hundred and thirteen resonances have been analyzed by means of the R-matrix formalism, ninety-eight of them for the first time. The impact is sizable, being the MACS at kT = 8 keV 36% smaller than the value recommended in KADoNiS. The statistical uncertainty affecting this new MACS has been reduced from 10% down to 1%. The achieved systematic accuracy between 3.2% and 5.7% is comparable to the uncertainties of the isotopic abundances of the s-only Kr-isotopes, which is the requirement of hydrodynamic stellar models to deliver accurate results.

The second main contribution of this work to the study of the ^{79}Se branching consisted of the first developments towards a novel detection system, called i-TED, for measuring (n,γ) cross sections with enhanced signal-to-background ratio. This new detection system will be applied for the first time in the measurement of the $^{79}\mathrm{Se}(n,\gamma)$ cross-section at CERN n_TOF in 2022. The i-TED imaging capable Total Energy Detector exploits the Compton imaging technique to select mainly the γ-rays generated in the sample by neutrons captured therein, while rejecting contaminant γ-rays coming from stray neutrons captured in the surroundings. In order to technically implement this concept, i-TED consists of two detection planes operating in time coincidence, in which the position, energy and time of the γ-ray interactions are registered. A first demonstrator called i-TED5.3, with three position sensitive detectors (PSDs), has been developed and characterized in this thesis work and the first experimental proof of concept has been carried out. In i-TED5.3, one PSD is placed in the *scatter* plane while the remaining two are arranged in a vertical configuration within the *absorber* layer. Each PSD consists of a monolithic $LaCl_3$(Ce) scintillation crystal optically coupled to a silicon photomultiplier, which is connected to an ASIC-based readout system manufactured by PETsys Electronics. A complete characterization of this prototype yielded position resolutions ranging between 1 mm and 2 mm FWHM, and energy resolutions of 6% and 7% FWHM at 661 keV for the singles and coincidence deposited energy spectra, respectively. Finally, a first experimental proof of concept experiment carried out at CERN n_TOF with i-TED5.3 allowed us to technically validate the system for ToF experiments, and demonstrate the background rejection capabilities. A background reduction by up to a factor of 3.8 was achieved after comparing the ^{56}Fe(n,γ) neutron energy spectra measured with the i-TED5.3 demonstrator and state-of-the-art C_6D_6 detectors. Further improvements undertaken outside of the scope of this thesis work comprise the assembly and characterization of an array of 4 i-TED detectors, each one comprising 5 PSDs, and the use of artificial intelligence and machine-learning techniques for enhancing further the background rejection capability and overall system performance.

Chapter 0

Introduction

Understanding which elements form the universe and how they were formed is an open question that scientists have tried to solve for a long time. Since Frank Wigglesworth Clarke wrote in 1889 about his observations of the Earth's crust composition in the work entitled "The Relative Abundance of the Chemical Elements" [1], there have been many new advances in this field. Some of the latter have focused on obtaining a curve with which to represent the abundances of chemical elements in the universe.

From Clarke's Earth observations arose Harkins' work in 1917 [2]. Harkins is considered as the first to attempt a systematic classification of the stable nuclear species based on their atomic number. However, authors of the time were already beginning to assume that meteoric matter, since the time it formed from solar material, has undergone less chemical fractionation than any material found on the surface of the earth. For that reason, later works looked for these complementary sources of observation [3]. In fact, in subsequent improvements of the abundance curve such as the one made by Suess and Urey in 1956 [4], solar observations were included in addition to terrestrial and meteorite data.

Together with the improvements in the abundance curve, the authors [2, 4] made big efforts to obtain patterns or empirical rules to describe how these elements were formed. The challenge was to find a theory that successfully explains in quantitative detail all the characteristics of the abundance curve. Early theories of the 1940s and 1950s [5, 6], proposed that all elements were formed during the first stages of the universe's development. According to these theories, the material should be spatially distributed uniformly and independent of time (once primordial phases end). However, differences in composition were observed between stars located in very distant regions of space or at different stages of evolution. In addition, Merrill discovered traces of Technetium (Tc) in *s*-type stars in 1952 [7]. Tc is the lightest radioactive element whose longest-lived isotope decays within a few million of years, several order of magnitude lower than the estimated age of the universe [8]. This discovery thus suggested that the stars play an important role in the nucleosynthesis of elements.

Finally, Burbidge, Burbidge, Fowler and Hoyle took a big step in 1957 with their work entitled "Synthesis of the Elements in Stars" [9], whereas a similar analysis was carried out independently by Cameron [10]. These contributions laid the foundations for the modern understanding of nucleosynthesis with a classification of eight processes required to satisfy the abundance curve. Although these works did not focus on figuring out where the elements are created, they assumed that the conditions necessary for these processes to occur are satisfied inside stars during the different stages of their evolution. This led the authors to conclude that nuclear transformations have to be continually occurring in stars, or as they literally wrote *"stars are the seat of origin of the elements"* [9].

0.1 Stellar Nucleosynthesis

The density and temperature conditions necessary for the formation of elements are reached inside stars during different stages of their evolution. Due to the great variety of stars according to their initial mass and composition, those conditions are varied enough to allow all species to be formed.

Elements lighter than iron can be produced inside stars by fusion reactions. According to observations and the stellar models that will be presented in Sec. 0.1.1, most of the stars begin to *burn* H producing He and energy. That energy prevents the star from collapsing due to gravity, keeping an hydrostatic equilibrium. As the H-burning phase continues, the core of the star is compressed due to the effect of gravity on the newly created He nuclei, causing an increase in temperature and density. When the latter are high enough, the He-burning begins. In this new evolutionary stage, the star is able to produce heavier elements such as ^{16}O, ^{20}Ne and ^{24}Mg. Depending on the initial mass of the star, other processes can appear after the He-burning that form heavier elements up to iron and nickel. Since these nuclei have the highest binding energy per nucleon, further massive elements cannot be produced by means of fusion processes.

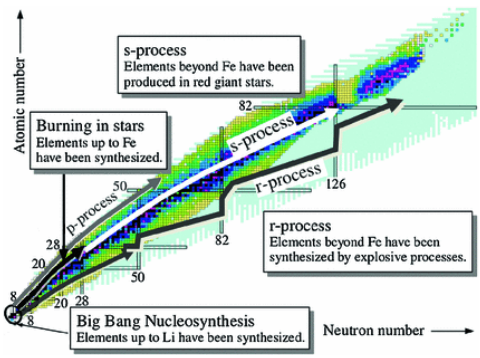

Figure 1: Nuclear chart with the main nucleosynthesis processes displayed. Adapted from [11].

The mechanisms needed to explain the formation of elements heavier than iron were compiled for the first time in [9]. The authors proposed three different processes depending on the stellar conditions: a *slow neutron capture* (s-process), a *rapid neutron capture* (r-process) and a *proton capture* (p-process). Fig. 1 shows the nuclear chart of elements with the highlighted regions in which these processes act respectively. The different locations of these regions with respect to the stability valley shows the different nature of these processes.

- ***s*-process**: is responsible for the formation of half of the elements beyond iron by means of *slow* radiative capture of neutrons (n,γ). This process is called slow since it requires long time scales of hundred or thousands of years between neutron captures. Typically, this time interval is much longer time than β-decay rates of the unstable isotopes formed, which locates this process always close to the stability valley of the nuclear chart. Regarding the *s*-process sites, it mainly occurs in low mass stars during the He-burning of their Asymptotic Giant Branch (AGB) evolutionary stage. In a first approach [12], the almost constant temperature ($\sim 10^8$ K) and neutron density ($\sim 10^7 - 10^8$ cm^{-3}) conditions during this stellar phase allowed one to analytically model this process, thereby deriving relevant information on the stellar medium. Nowadays, hydrodynamic stellar models [13, 14] allow to constrain more precisely the physical conditions and the evolutionary time-scales. For that, the neutron capture cross sections and β-decay rates of the isotopes involved are chosen as the main experimental inputs.

- ***r*-process**: corresponds to the *rapid* radiative capture of neutrons which is responsible of producing the other half of elements heavier than iron. However, unlike the *s*-process, this process is characterized by short time-scales ($\sim 0.01 - 10$ s) and very high neutron densities ($\sim 10^{20} - 10^{23}$ cm^{-3}). Under these conditions, neutron rich isotopes very far away from the stability valley are generated. In order to model this process, data on masses, neutron capture cross sections and β-decay rates are needed. For most nuclei this information is almost inaccessible experimentally since *r*-only isotopes are very unstable and difficult to study in the laboratory. For that reason, the sites in which this process takes place are not yet well identified. Nevertheless, a big step was taken in this sense with the observation of Strontium in the *kilonova* explosion AT2017gfo that occurred after the merger of two neutron stars GW170817 [15]. Since a high neutron flux is available in a kilonova event, this scenario can be a good candidate for the *r*-process. A detailed description of this process is given in [16].

- ***p*-process**: through this process of radiative capture of protons (p,γ), proton-rich isotopes that cannot be built by either *s*- or *r*-process are formed. There are less than 35 *p*-only isotopes, which gives an idea of the low efficiency of this mechanism. This is mainly due to the conditions of high temperature and densities needed for the protons to overcome the Coulomb barrier. Owing to the low number of elements involved in the *p*-process, there are few studies about the astrophysical sites where it can take place. However, such temperature and density conditions indicate that a probable scenario can be the *supernova* explosions. A complete review of this process is given in [17].

0.1.1 The s-process

Almost all elements heavier than iron are created by neutron captures, half by the s-process and the other half by the r-process. The latter is very difficult to study due to the very unstable isotopes involved. On the contrary, a classical approach of the s-process, based on analytical calculations, was already given in [9]. In this section, this approach is introduced as well as its main drawbacks that led to the development of new stellar models.

Classical approach

As mentioned in the introduction of this chapter, the authors in [9] were not concerned about the sites where the s-process takes place. However, they assumed that the necessary conditions for them to occur can be found in the stellar media. In that environment, neutrons are rapidly thermalized following the Maxwell distribution, in which a particle with temperature T has a velocity

$$v_T = \sqrt{\frac{2kT}{\mu}}, \tag{1}$$

where k is the Boltzmann constant and μ the reduced mass of the system.

Therefore, a suitable parameter to describe the probability that a nucleus will capture a neutron in these stellar environments is the Maxwellian Averaged Cross Section (MACS). This quantity, σ^{MACS}, is defined in Eq. 2, in which $\sigma(E_n)$ denotes the neutron capture cross section of the nucleus depending on the neutron energy E_n.

$$\sigma^{MACS} = \frac{\langle \sigma v \rangle}{v_T} = \frac{2}{\pi} \frac{\int_0^\infty \sigma(E_n) E_n e^{-E_n/kT} dE_n}{\int_0^\infty E_n e^{-E_n/kT} dE_n} \tag{2}$$

The most general expression of the classical approach to estimate the rate of change of the abundance N_A of a nucleus with mass number A, is given by Eq. 3,

$$\frac{dN_A}{dt} = \lambda_{n,A-1} N_{A-1} - \lambda_{n,A} N_A - \lambda_{\beta,A} N_A, \tag{3}$$

where $\lambda_{i,X}$ parameters are the reaction rates: $i = n$ corresponds to the neutron capture while $i = \beta$ to the β-decay rate. Suffix $X = A, A-1$ are used to denote the corresponding isotope A or the lighter one $A-1$. The $\lambda_{i,X}$ parameters are defined in Eq. 4, where n_n is the density of neutrons with a velocity v_T, and $t_{1/2}$ the half-life of the unstable isotopes formed.

$$\begin{aligned} \lambda_n &= n_n v_T \sigma^{MACS} \\ \lambda_\beta &= \frac{ln(2)}{t_{1/2}} \end{aligned} \tag{4}$$

Since the s-process flow runs close to the stability valley, the isotopes involved will be stable most of the time, thus cancelling the β-decay parameter ($\lambda_\beta = 0$). In the opposite case of unstable isotopes, the long time-scale of this process ensures that in most of the cases $\lambda_\beta << \lambda_n$. In both situations, the last term in Eq. 3 can be neglected,

$$\frac{dN_A}{dt} = n_n \sigma_{A-1}^{MACS} v_T N_{A-1} - n_n \sigma_A^{MACS} v_T N_A. \tag{5}$$

On the other hand, one can define the neutron exposure as the integrated flux per unit of surface:

$$d\tau = n_n v_T dt. \tag{6}$$

By rewriting Eq. 5 with this neutron exposure:

$$\frac{dN_A}{d\tau} = \sigma_{A-1}^{MACS} N_{A-1} - \sigma_A^{MACS} N_A. \tag{7}$$

If there are sufficient neutrons in the stellar medium available to be captured by all nuclei in the s-process chain, a stable state called the *local equilibrium approximation* is reached. In this situation, the abundance does not vary with the neutron exposure, which leads to the product between MACS and abundance being constant,

$$\frac{dN_A}{d\tau} \approx 0 \rightarrow \sigma_A^{MACS} N_A \approx const. \tag{8}$$

This classical model was first improved by Seeger in 1961 [18], who was able to reproduce the solar abundances of the s-only nuclei with the exponential distribution of exposures given by Eq. 9.

$$\rho(T) = \frac{f N_{56}}{\tau_0} e^{-\tau/\tau_0} \tag{9}$$

Here, f and τ_0 are free parameters to fit the model to the experimental data, and N_{56} the abundance of the ^{56}Fe seed.

By using this distribution of exposures, Clayton and Ward in 1974 [19] found the analytical solution to the Eq. 7:

$$\sigma_A^{MACS} N_A = f N_{56} \tau_0 \prod_{A'=56}^{A} [1 + (\sigma_{A'}^{MACS} \tau_0)^{-1}]^{-1}. \tag{10}$$

With this analytical expression of Eq. 10, the classical model attempts to reproduce the abundance curve with only two experimental inputs:

- the MACS of the involved isotopes, $A' = 56, ..., A$,
- and the observed abundances of the s-only isotopes that are used to adjust the parameters f and τ_0.

The classical approximation is quite successful in describing the solar s-process abundances for nuclei with A $>$ 90, which corresponds to the so-called *main* component of the s-process. Fig. 2 shows the abundances obtained with this classical approach. Despite the good general agreement between this result and the experimental abundances observed for the s-only isotopes, several inconsistencies are found:

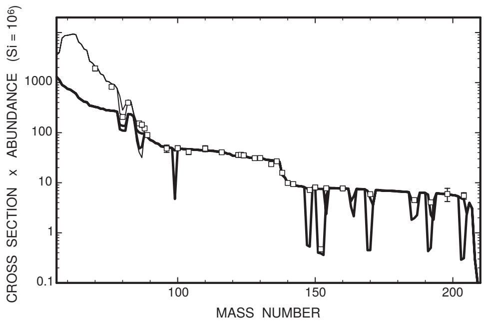

Figure 2: Product between MACS and abundances as a function of the atomic number. Thick line represents the *main* component of the s-process obtained with the classical approach. Thin line shows the *weak* component, whereas open squares are the experimental abundances of the s-only isotopes used to fit the model. Extracted from [12].

- As can be seen in the figure, the classical approach cannot reproduce the experimental abundances of elements with A $<$ 90. It is needed to add another contribution called *weak* component to produce them. This additional component is assumed to occur in massive stars, and its modeling cannot be tackled with the classical model since the local equilibrium approximation is not fulfilled [20].

- Along the s-process flow, there are some points in which the unstable isotope involved has similar rates of neutron capture and β-decay, $\lambda_n \sim \lambda_\beta$. In those *branching points*, temperature and neutron flux play an important role in the final path followed by the s-process, and they must be treated as free parameters in the model. Fig. 2 shows the inconsistencies of the abundance curve due to these branching points in the mass region up to A $=$ 210.

- Finally, a disagreement in the abundance predicted by the classical approach was found for the ^{142}Nd s-only isotope [21]. More precisely, an overproduction of this isotope was obtained after introducing more precise MACS data into the model. This new data came from neutron capture measurements of various elements in the region of the nuclear chart around ^{142}Nd.

Despite of these difficulties, the classical approach still works in the mass region between magic numbers, where the local equilibrium approximation is valid. In fact, in the areas of this region absent of branching points, this model has a deviation of 3% RMS with respect to the observed abundances of s-only isotopes [12].

Nevertheless, in order to overcome the difficulties mentioned above, different stellar models were proposed. The latter allow also for a better insight of the physical structure and dynamics of the stars.

Stellar models

Stellar models are based on the combination of stellar evolutionary codes [13, 14] and post-processing ones [22, 23]. Evolutionary codes try to reproduce the entire life of the stars giving their thermodynamic conditions as a function of the time. By using these data, post-processing codes can obtain the numerical abundances of elements formed in the star. Other approach is used for the FRUITY database, in which calculations are already integrated into the stellar evolution code [24].

The *s*-process is not a unique process, but its beginning and end will depend on several initial conditions of the star such as its mass, metallicity, etc. For that reason, there are many adaptations of stellar models to study the different processes that occur in different types of stars.

AGB stars

As it was introduced at the beginning of this chapter, once H is almost exhausted inside the star, the He-burning phase begins. At this point, the low mass stars (M $< 3M_{\odot}$) leave the *main sequence* region in the Hertzsprung–Russell diagram, to initiate the AGB stage. In the latter, the star becomes a Red Giant composed by an inert C-O core surrounded by a thin He intershell and an extend H-He envelope. Fig. 3 shows the evolution of the structure of an AGB star with the aforementioned layers.

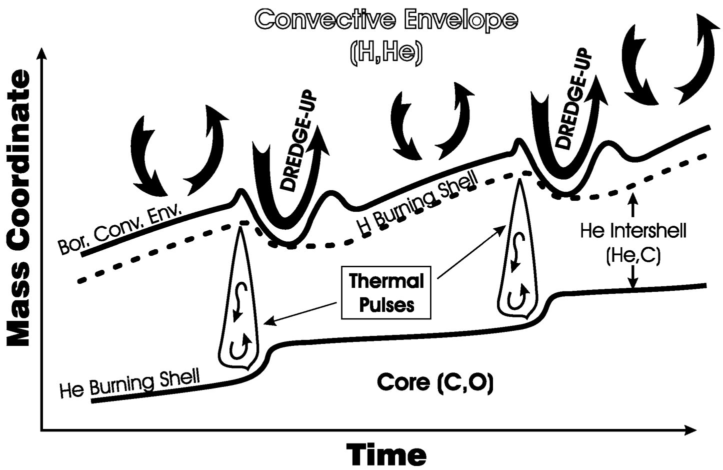

Figure 3: Schematic representation of the evolution of an AGB star. The structure of the star is shown in this typical representation of the radius, in terms of mass fraction, against the time. Extracted from [25].

As can be seen in the figure, during the first part of the AGB phase the He-burning shell progressively widens. Outcoming energy from nuclear reactions expands this shell which reaches the boundary of the convective envelope. The expansion of this layer cools it down and stops the fusion of He.

Owing to the temporary stop of the He burning, this layer rapidly contracts increasing its density and temperature. Changes in the latter conditions lead to a reignition of He, which produces a fast release of nuclear energy. Due to the sudden increase in temperature and luminosity, this episode is known as *He-flash*.

In addition, during the thermal pulse, carbon is produced from 3α reactions that take place at the boundary between the convective H-He envelope and the He-burning shell. The latter accumulates C in a region known as ^{13}C-pocket.

Finally, neutrons are released by the reactions ^{22}Ne(α,n)^{25}Mg and ^{13}C(α,n)^{16}O corresponding to the He-flash and ^{13}C-pocket stages. As it is displayed in Tab. 1, these reactions do not produce very high neutron fluxes which, together with the large inter-pulse period of thousand of years, allow the *s*-process to occur in AGB stars.

Evolutionary phase	He-flash	^{13}C-pocket
Reaction	^{22}Ne(α,n)^{25}Mg	^{13}C(α,n)^{16}O
Neutron density (cm^{-3})	10^9 - 10^{11}	10^7
Temperature (MK)	250	90
kT (keV)	23	8
Duration (y)	10^2	2.5×10^4

Table 1: Some quantities that describe the two phases of the AGB stars in which the main *s*-process component takes place.

Detailed reviews of the *s*-process in AGB stars and the stellar models are given in [25, 26].

Massive stars

AGB stellar models, as well as classical analysis, fail to reproduce cosmic abundances of the *s*-process for isotopes with $A < 90$. The weak component previously mentioned is still needed to explain the abundances of these isotopes. This component takes places in massive stars ($M > 8M_\odot$) in similar way than in AGB stars. The main contributor to the presence of neutrons in massive stars is the ^{22}Ne(α,n)^{25}Mg reaction, which occurs in the He shell during the He-burning phase. In addition, due to the higher mass of these stars compared with AGB, there exists a carbon shell in which the C-burning reaction ^{12}C(^{12}C,n)^{23}Mg occurs. Tab. 2 shows the temperature and neutron density conditions available in these two evolutionary stages of the massive stars in which the *s*-process takes place.

On the other hand, in contrast to the main *s*-process component, the neutron flux in the weak component is too low for achieving reaction flow equilibrium. As a consequence, a particular MACS not only determines the abundance of the respective isotope but also affects the abundances of all heavier isotopes as well [20]. The accumulated uncertainties of the propagation effect are significant even for the heavier isotopes of this weak component up to Kr and Sr. The corresponding uncertainties will be improved once the neutron capture cross sections of the isotopes between Fe and Sr are measured with an accuracy of about 5% [12]. This introduces the first motivation to obtain new experimental data from neutron capture cross sections of isotopes in that mass range such as ^{80}Se, whose measurement will be presented in Part I.

Evolutionary phase	He-burning	C-burning
Reaction	^{22}Ne(α,n)^{25}Mg	^{12}C(^{12}C,n)^{23}Mg [12] ^{22}Ne(α,n)^{25}Mg [20]
Neutron density (cm^{-3})	$< 10^6$	10^{11}
Temperature (MK)	300	1000
kT (keV)	26	90

Table 2: Some quantities to describe the two phases in the evolution of massive stars in which where the weak *s*-process component takes place.

0.1.2 The puzzle around the ^{79}Se *s*-process branching

The ^{79}Se branching is of special relevance since it is located near to the transition region (A $\sim$ 90) between the weak and main *s*-process components. Therefore, experimental data on the neutron capture cross section of this isotope will be useful for the study of both components of the *s*-process.

As it is shown in Fig. 4, the ^{79}Se branching determines the abundances of the ^{80}Kr and ^{82}Kr *s*-only isotopes, which are shielded from the *r*-process by the stable (or almost stable) isotopes ^{80}Se and ^{82}Se ($t_{1/2} = 10^{20}$ y). In addition, the abundance ratio of the *s*-only isotopes of Kr is very well known from meteorites [27, 28, 29], which can be used as tight constraints of the stellar models in this branching point.

The special peculiarity of the ^{79}Se nucleus is the presence of quantum states whose population varies with the thermal conditions of the stellar environment. Since the strength of the β-decay depends on the levels involved in the transition, the ^{79}Se branching becomes sensitive to the temperature of the star. Fig. 4 shows the dependence of the ^{79}Se β-decay with temperature. A variation in the latter from 100 MK to 500 MK, leads to a reduction in the ^{79}Se half-life from thousands of years to less than one. This property would allow one to use this branching as a thermometer of the stellar media, by comparing the abundances of the *s*-only Kr isotopes predicted by stellar models on the basis of the ^{79}Se(n,γ) cross section, with the observed abundance ratio. For that reason, ^{79}Se represents one of the most relevant and debated *s*-branching nuclei [30, 31].

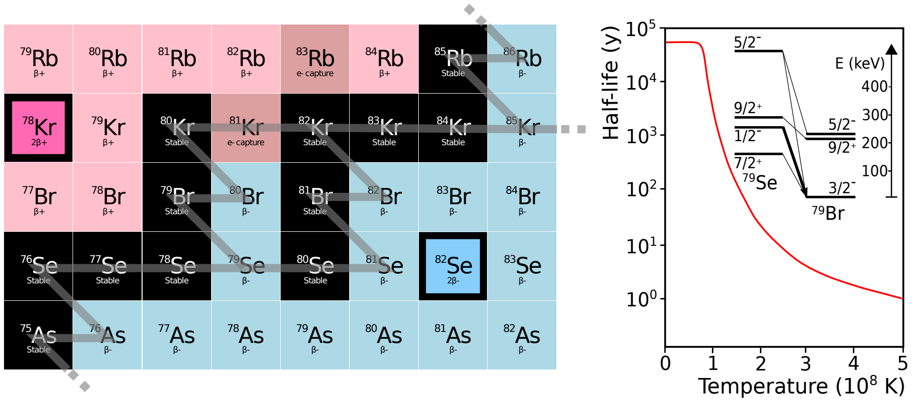

Figure 4: (Left panel) The *s*-process flow through the mass region 75 < A < 86. (Right panel) Dependence of the β-decay rate with the temperature of the stellar media. Within the graph, the energy levels of the ^{79}Se and ^{79}Br nuclei, and the possible β-decays between them are shown.

During the last decade, other motivations have been added to the measurement of this branching:

- In 2011, this nucleus was already considered one of the key branch-point isotopes of the *s*-process in the review by Kaeppeler et al. [12], due to its relevance to constrain the temperature of the stellar environment in massive stars.

- Seven years later, the Monte Carlo studies carried out by Cescutti et al. in [32] revealed ^{79}Se as a key reaction in several investigated *s*-process nucleosynthesis models.

- Finally, in 2020 Prantzos et al. found an underproduction of ^{80}Kr when comparing their Galactic Chemical Evolution model with the abundances observed in the Sun [33]. The authors assigned these discrepancies to the limited precision of the experimental input data.

In order to correctly characterize the ^{79}Se branching and obtain reliable data on the thermal conditions, the experimental neutron capture cross sections and β-decay rates of all isotopes involved in the *s*-process flow around this branching must be known. In the last fifteen years, the neutron capture cross section of several of these isotopes has been measured:

- The stable isotopes ^{77,78}Se were recently measured at CERN n_TOF by Lederer et al. [34] using the time of flight (ToF) technique.

- The ^{79,81}Br isotopes were measured by Heil and coworkers at FZK in Karlsruhe with the activation technique [35].

- A series of ToF measurements of the Krypton isotopes was performed by Mutti et al. in GELINA [36].

The details about the measuring techniques employed in these capture experiments will be given in Part I Sec. 2.1.

In addition, there exists a ToF measurement of the ^{80}Se(n,γ) cross section made by Walter et al. in 1986 [31]. However, their final result on the MACS at $kT = 30$ keV has an uncertainty of 10% (see Part I Sec. 5.2), which is twice the uncertainty required by astrophysicists to study the weak *s*-process in massive stars (see Sec. 0.1.1). With the goal of improving this situation, a ToF measurement of the ^{80}Se neutron capture cross section was carried out at CERN n_TOF during the 2018 campaign [37]. The entire Part I of this manuscript is dedicated to the analysis of these data with the goal of obtaining the MACS at different temperatures with an improved uncertainty and completeness.

Regarding ^{79}Se, there is no previous direct neutron capture measurement on this unstable isotope. This is mainly related to the difficulty of preparing samples that contain sufficient mass of this unstable isotope and with a sufficient level of enrichment for a ToF experiment. The activation technique is also not applicable in this case because ^{80}Se is stable. In the framework of the ERC-funded project HYMNS [38], a sample of ^{79}Se was produced in a collaboration with PSI-Switzerland and ILL-Grenoble by means of neutron activation of a lead-selenide alloy, which was highly enriched in ^{208}Pb and ^{78}Se (see Part II Sec. 1.1). The alloy was a necessary step due to the low melting point of selenium (217 °C) and the safety conditions of the reactor where it was activated, ILL-Grenoble. The main advantage of using lead in a sample designed for a neutron capture experiment is the absence of neutron capture resonances up to several tens of keV of neutron energy. However, the main drawback of lead in the final (^{79}Se)^{78}Se^{208}Pb sample is the enhanced contribution of neutron scattering events. Scattered neutrons can be captured in the detector itself, in structural materials and in the surrounding walls of the experimental set-up, thus increasing the background conditions and limiting the sensitivity of the measurement. With the aim of overcoming some of these background sources, a new detection system called *i-TED* is being developed at Instituto de Física Corpuscular IFIC (Universitat de València - CSIC) under the framework of the aforementioned HYMNS project. Part II describes the development of the first i-TED prototype and the proof-of-concept measurements carried out with i-TED at CERN n_TOF in order to technically validate its components for ToF experiments and to demonstrate experimentally the enhancement in signal-to-background for (n,γ) experiments. Finally, the neutron capture cross section measurement of ^{79}Se is planned with a full array of four i-TED modules at CERN n_TOF in 2022 [39].

Both, the ^{80}Se(n,γ) cross section measurement and the development of i-TED, are expected to contribute to shed light on the puzzle around the ^{79}Se branching. The final characterization and the better understanding of this *s*-process branching will be possible in the near future with the results of the ^{79}Se(n,γ) cross section measurement.

Beyond the astrophysical motivation, the neutron capture cross section of ^{79}Se is also interesting for nuclear transmutation studies [40, 41, 42]. This is because this isotope is one of the main contributors to the long term radiotoxicitiy of spent fuel, due to its long terrestrial half-life (3.27(8) $\times$ 10^5 y [43]).

Part I

Neutron capture cross section measurement of ^{80}Se

Chapter 1

Introduction

In order to employ the ^{79}Se branching as a thermometer of the stellar media, the neutron capture cross section of the ^{79}Se isotope and the neighboring nuclei must be known. The present part of this manuscript is dedicated to the study of one of those neighboring nuclei, the ^{80}Se isotope. This study focuses on measuring the neutron capture cross section of this isotope by means of the time of flight (ToF) method, and obtaining the MACS at several energies (kT) by means of a resonance analysis of the ^{80}Se(n,γ) yield.

Sec. 1.1 of this first chapter introduces the need of new experimental data on the neutron capture cross section of the ^{80}Se isotope by reviewing the available data from the previous measurement. Once the ^{80}Se case is introduced, Sec. 1.2 tackles the theoretical framework required to perform the neutron capture resonance analysis made later in this work. In the same direction, the following chapters 2 and 3 will introduce the measuring technique and the experimental setup, respectively. The steps to determine the energy distribution of the radiative neutron capture yield will be explained in Chapter 4. Finally, a full study of the resolved resonance region and a new value for the MACS of the ^{80}Se(n,γ) reaction will be determined in Chapter 5 and compared with the available values in the literature.

1.1 The case of ^{80}Se: motivations and previous measurements.

As it was introduced in Sec. 0.1.2, there exists only one previous measurement on the ^{80}Se neutron capture cross section performed by Walter et al. in 1986 [31]. This measurement was carried out at the Karlsruhe 3.75 MV Van der Graaff accelerator, where neutrons were produced via ^{7}Li(p,n) reaction by using a pulsed proton beam. The neutron energies were determined using the ToF technique.

In the ToF technique, the time t_{ToF} spent by neutrons travelling a distance L from their production site to the sample location is measured with high precision. The energy E_n of a neutron with mass m_n is then calculated by using the non-relativistic kinetic energy equation Eq. 2.8, which will be given in Sec. 2.3.

As it will be explained there, the relative error on the calculation of the neutron energy can be reduced by employing a long flight path L for which long t_{ToF} are measured with a very low relative uncertainty. Therefore, a simple way to improve this uncertainty consists of using a long flight path L. This is precisely one of the two main limitations of the previous measurement [31], which used a short flight path of only 0.6 m. Taking into account the t_{ToF} precision of 1 ns reported by the authors at 30 keV of neutron energy, a limited resolution of $\Delta E_n \approx 240$ eV was obtained. This resolution is comparable to the width of resonances in this energy region, thus preventing a resonance analysis (more details about resonance analysis will be given in Sec. 5.1.2). The other major limitation of this measurement arises from the low energy cut-off at 3.5 keV.

The two limitations discussed above are clearly displayed in Fig. 1.1. The latter compares the experimental data from Walter's measurement [31] to the neutron capture cross section obtained from the resonance parameters available in the JEFF-3.3 [44] and ENDF/B-VIII evaluated libraries [45]. As it can be seen, the limited energy resolution of the experimental data [31] prevents the authors from resolving any neutron capture resonance of the ^{80}Se(n,γ) reaction. Moreover, owing to the 3.5 keV low energy cut-off, they could not measure the two first resonances, one of them an s-wave resonance at 1.97 keV of neutron energy which could have a big impact in the MACS even at 30 keV. In fact, according to a simple calculation using the R-matrix SAMMY code [46], the resonances below 3 keV may amount to 30% and 7% of the MACS at 8 keV and 30 keV, respectively.

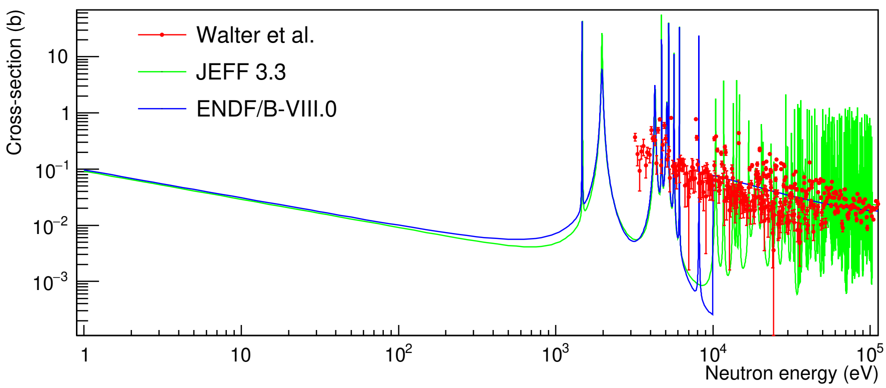

Figure 1.1: Neutron capture cross section of the ^{80}Se(n,γ) reaction. Data from JEFF-3.3 evaluation are compared with data from ENDF/B-VII database and with data from time of flight measurement performed by Walter et al. [31].

The final MACS reported by Walter et al. in [31] has an uncertainty of ±10% at 30 keV. By varying the MACS within this uncertainty, the Monte Carlo sensitivity study performed in [32] shows an asymmetric abundance variation of +29/-6% for the ^{80}Se itself. However, a more realistic error of 50% was assumed on the MACS of the ^{80}Se(n,γ) reaction in a different sensitivity study performed with the NETZ tool [47]. This uncertainty takes into account not only the absence of experimental data below 3 keV, but also the increment in the uncertainty of the MACS at 90 keV corresponding to the C-burning phase of massive stars (see Sec. 0.1.1). In that sensitive study, the abundances of the isotopes heavier than selenium were calculated after a variation in the ^{80}Se(n,γ) MACS by a factor of 0.5. Fig. 1.2 shows the graphical result of this study. For completeness, the ^{80}Se results are compared in the same figure with the results from a similar study performed for ^{79}Se, in which the same 50% variation in cross section was used for the sake of clarity. As can be appreciated, the ^{79}Se affects mainly ^{79}Br and ^{80}Kr, whereas ^{80}Se induces a smaller amplitude but far-reaching propagation effect over nine heavier isotopes of Se, Br and Kr, thus impacting the reference s-only ^{82}Kr and beyond.

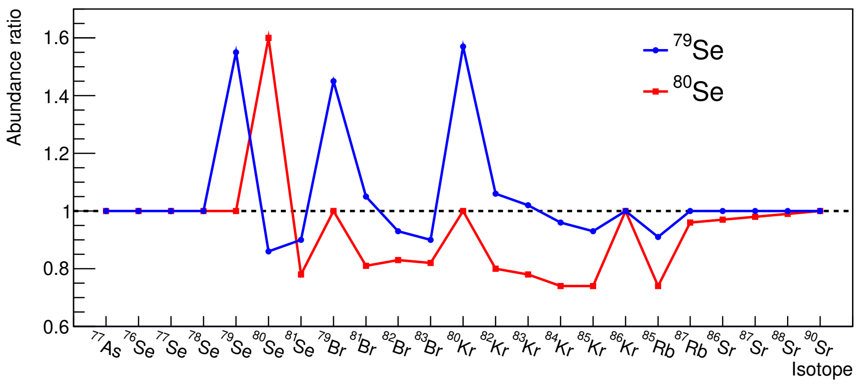

Figure 1.2: Abundance ratios of isotopes in the mass range $77 < A < 90$ calculated with NETZ [47], after a variation of 50% on the MACS of ^{79}Se and ^{80}Se.

The expected variations in the s-process abundance patterns due to the uncertainty in the MACS of the ^{80}Se(n,γ) reaction emphasize the importance of new experimental data with improved resolution and reduced uncertainty. For that reason, a new neutron capture cross-section measurement of the ^{80}Se isotope was carried out at CERN n_TOF [48] during the 2018 experimental campaign [37]. The main advantages of this facility, which will be described in detail in Sec. 3.1, are the high instantaneous flux of up to $\sim 6{\times}10^5$ neutrons per pulse, and the long available flight path of $L \simeq 185$ m. These characteristics allow performing (n,γ) cross-section measurements in a reasonable time with high resolution using the ToF technique. Thanks to the white neutron spectrum of the n_TOF facility and the low duty cycle delivered by the CERN Proton Synchrotron (PS) (1.2 s minimum), the thermal neutron energy range can be also measured. These two improvements can be clearly seen in Fig. 1.3, in which the registered count rate of the ^{80}Se(n,γ) reaction (presented later in Chapter 4) is directly compared with the cross-section data from [31]. Although these two data sets do not show the same quantity, this comparison is displayed with the aim of illustrating the achieved energy resolution and completeness of the new measurement.

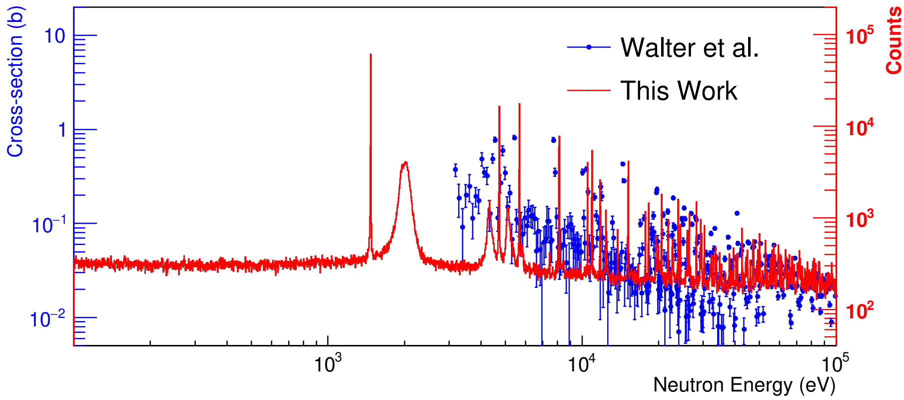

Figure 1.3: Experimental count rate of the ^{80}Se(n,γ) reaction registered in this work (red line) compared to the neutron capture cross-section data from Walter et al. [31] (blue points). Scales are displayed in the same color.

The high energy resolution of the data shown in Fig. 1.3, allows us to perform a resonance analysis with the SAMMY code [46] up to 100 keV. This code applies the R-matrix theory taking into account some experimental effects such as the Doppler broadening or the neutron multiple scattering. In the R-matrix theory, the capture resonances of the ^{80}Se(n,γ) cross section are characterized by a set of parameters that are related to nuclear properties, as it will be explained in Sec. 1.2. Once this method is implemented, the final resonance parameters resulting from different experiments can be compared. Furthermore, SAMMY can make use of the R-matrix theory to reconstruct the neutron capture cross section by using the resonance parameters and some experimental information such as the temperature or the sample thickness. Precisely, this analysis was carried out to obtain the (n,γ) cross-section data shown in Fig. 1.1. Owing to the lack of high quality (n,γ) cross-section data available, the evaluations were made either based on models (JEFF-3.3) or in the data available from transmission measurements[1]

[1] In transmission measurements, the sample under study is interposed between the neutron source and the detection system. The total neutron cross section is calculated by employing the ratio between the number of counts registered in the system with the sample in place and removing it.

(ENDF/B-VIII). The last available transmission measurement of the ^{80}Se isotope was performed by Novoselov et al. in 1995 [49]. Also Mughabghab compiles other similar results [50]. The resonance data from these measurements have a limited range of neutron energy extending up to 40 keV. The range studied in this work extends from 1 eV up to 100 keV of neutron energy. Therefore, it is expected to find new resonances in the R-matrix analysis of these experimental data beyond 40 keV.

1.2 Theory of the radiative neutron capture process

In nuclear physics, the probability that a neutron will interact with a certain nucleus is expressed by the neutron cross section in surface units (barns). For a particular target nucleus, there are several neutron-induced reactions allowed such as the elastic scattering or the neutron radiative capture. Thus, the total cross section $\sigma_T(E_n)$ is the sum of the partial cross sections of all the reaction channels:

$$\sigma_T(E_n) = \sigma_{el}(E_n) + \sigma_\gamma(E_n) + ... \tag{1.1}$$

In this work, we are interested in obtaining the neutron capture cross section σ_γ, which is the probability that a neutron capture reaction will occur followed by the emission of γ-rays, (n,γ). This magnitude cannot be measured directly. Instead, the observable to be measured is the neutron capture yield $Y(E_n)$, which is defined as the fraction of neutrons impinging on the target that are captured by it. This yield strongly depends on the kinetic energy of the incident neutron E_n, exhibiting a resonance structure. These resonances are the signature of the nuclear levels of the *compound nucleus*, formed by the incident neutron and the target nucleus, as it will be explained below. The capture yield is related to the neutron capture cross section by means of Eq. 1.2, where n is the thickness of the target expressed in atoms/barn.

$$Y(E_n) = \frac{\sigma_\gamma(E_n)}{\sigma_T(E_n)} \left(1 - e^{-n\sigma_T(E_n)}\right) \tag{1.2}$$

Therefore, the resonance behaviour of the capture yield is translated to the neutron capture cross section. The neutron energy region in which these resonances can be resolved[2] is known as *Resolved Resonance Region*, RRR. In this region, the *R-matrix* formalism is the most accurate way of describing the existing physics not only for radiative neutron capture, but in a more general way, for any binary reaction. This theory was firstly introduced by Wigner and Eisenbud in 1947 [51], while a more extensive and detailed overview was given by Lane and Thomas in

[2]Two resonances can be resolved when their intrinsic widths are smaller than the distance between them.

1958 [52]. In this section, a brief outline of this formalism is given in order to understand the principles without giving details. The full derivation of the theory can be found in the mentioned Lane's review, or in the more recent contribution by Fröhner [53].

In the R-matrix theory, a collision is described by two wave functions: an incoming wave function that describes two incident particles, and an outgoing wave function for the emerging reaction products. In this theory, the reaction space is divided into two regions:

- External region: nuclear forces are negligible in this region. Here, the wave functions can be calculated by solving the Schrödinger equation of the nuclear system, for which the nuclear potential must be known. This can be considered absent for neutral particles or to be the Coulomb interaction for charged particles.

- Internal region: nuclear forces predominate in this region where the wave functions are so close that they form an intermediate state known as a *compound nucleus*. The wave function that describes this compound nucleus is very complicated and cannot be solved. In contrast, it can be expanded as a linear combination of its eigenstates without solving explicitly the Schrödinger equation of the system.

Matching external and internal wave functions at the boundary between these two regions provides a way of describing the cross section of the reaction in terms of the properties of the nuclear levels of the compound nucleus. These properties are the energy E_0, spin and parity J^P, and partial widths Γ_c related to each decay channel c of the compound nucleus. Therefore, this method does not deal with the nuclear forces involved in the reaction, but describes the resonance behaviour of its cross section using only the properties mentioned above.

The existence of the intermediate state called the compound nucleus was first proposed by Bohr [54], without the mathematical framework of quantum mechanics provided by the R-matrix formalism. Following this theory, once the nucleus ${}^{A}X$ captures a neutron n, the compound nucleus forms in an excited state of energy ${}^{A+1}X^{*}$, from which it decays by emitting γ-rays sequentially down to the lowest bound state,

$$ {}^{A}X + n \rightarrow^{A+1} X^{*} \rightarrow^{A+1} X + \gamma. \tag{1.3}$$

Fig. 1.4 sketches this reaction. As can be appreciated in the figure, the nuclear levels above the neutron separation energy S_n of the ${}^{A+1}X$ nucleus correspond to the excited levels of the compound nucleus. Radiative decay from these and subsequent levels is responsible for the resonance behavior exhibited by the capture yield and translated to the neutron capture cross section, which is also shown in the figure. Neglecting the recoil energy of nucleus, the energy E^{*} of each one of these excited levels is given by the total energy of the emitted de-excitation radiation. Furthermore, if the emission of conversion electrons is not considered, these energies are equivalent to the sum of the energy of all the γ-rays emitted in each prompt cascade,

$$E^* = S_n + \frac{A}{A+1} E_n \approx \sum_j E_j^\gamma = E^C. \tag{1.4}$$

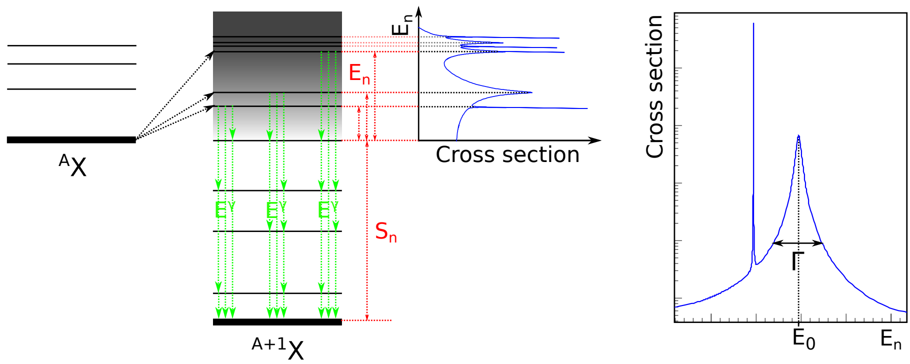

Figure 1.4: Scheme of a neutron capture event according to the compound nucleus theory. The random nature of the emitted radiation from the excited energetic levels of the compound nucleus is shown by means of three different decay possibilities from three different levels. The resonances shape of the energy distribution of the cross section is also presented. A zoom containing two resonances is displayed on the right panel, indicating the energy E_0 and total width Γ for one of them.

Fig. 1.4 also shows a zoom of a cross-section resonance with two properties highlighted, energy E_0 and total width Γ. The latter is related to the half-life τ of the corresponding excited state by the Heisenberg uncertainty principle,

$$\tau \approx \frac{\hbar}{\Gamma}. \tag{1.5}$$

Following the case of the radiative neutron capture, Γ is obtained from the sum of partial widths corresponding to the two available reaction channels: scattering and capture of neutrons, $\Gamma = \Gamma_n + \Gamma_\gamma$. However, other reaction channels such as fission have to be considered for the most general case of any neutron reaction,

$$\Gamma = \Gamma_n + \Gamma_\gamma + \Gamma_f + \ldots\ . \tag{1.6}$$

As mentioned before, Γ_n and Γ_γ are part of the properties required to describe each nuclear excitation level of the compound nucleus together with J^P and E_0.

The R-matrix formalism links these properties to the cross section by means of a collision matrix **U**. In the most general form of this theory, this matrix is related to the partial cross section from the entrance channel c to any other exit channel c' by Eq. 1.7. The latter was obtained by Blatt and Biedenharn in 1952 [55], by applying the boundary condition of a stationary incoming plane wave with a stationary outgoing spherical wave.

$$\sigma_{cc'} = \pi \lambda\!\!\!^{-}{}_c^2 g |\delta_{cc'} - U_{cc'}|^2 \tag{1.7}$$

In this equation:

- $U_{cc'}$ are the elements of the collision matrix **U**, whereas $|U_{cc'}|^2$ corresponds to the probability that the reaction from channel c to c' occurs.
- Kronecker symbol $\delta_{cc'}$ arises since incoming and outgoing particles cannot be distinguished.
- The de Broglie wave length $\lambda\!\!\!^{-}{}_c$ takes into account the relative motion of the collision partners with reduced mass μ_c and relative speed v_{rel},

$$\lambda\!\!\!^{-}{}_c = \frac{\hbar}{2\pi} \frac{1}{\mu_c v_{rel}}. \tag{1.8}$$

- The spin factor g describes the probability of getting the angular momentum J from the combination of spins of the collision partners I and s,

$$g = \frac{(2J+1)}{(2I+1)(2s+1)}. \tag{1.9}$$

The matrix **U** is usually expressed in terms of a matrix **R** called the *channel matrix*. The latter must be inverted in order to determine the elements $U_{cc'}$ necessary to obtain the cross section. However, this is a very complicated task since **R** usually has a very high rank. For that reason some assumptions must be taken.

Experience with experimental data has shown that with the approximation given by Reich and Moore in 1958 [56], all resonance cross-sections data within the RRR can be described in detail [53]. In this approximation, all photon channels contributions to the off-diagonal matrix elements are neglected since their amplitudes are assumed to have similar magnitudes but random signs, thus cancelling between them. Once this assumption is implemented in the channel matrix, it can be inverted allowing to solve analytically Eq. 1.7. In the case of isolated resonances, one arrives to the formula obtained by Breit and Wigner in 1936 [57] and shown in Eq. 1.10, which fits to the resonance shape using the aforementioned properties of the nuclear levels of the compound nucleus.

$$\sigma_{cc'} = \pi \lambda\!\!\!^{-}{}_c^2 g \frac{\Gamma_c \Gamma_{c'}}{(E-E_0)^2 + (\Gamma/2)^2} \tag{1.10}$$

As previously mentioned, in a neutron capture experiment such as the one presented in this work, the total resonance width Γ corresponds to the sum of the partial widths Γ_n and Γ_γ. In this case, Eq. 1.10 is transformed into

$$\sigma_{n\gamma} = \pi \lambda\!\!\!^{-}{}_n^2 g \frac{\Gamma_n \Gamma_\gamma}{(E - E_0)^2 + (\Gamma/2)^2}, \tag{1.11}$$

where now the de Broglie wave length $\lambda\!\!\!^{-}{}_n$ can be expressed as

$$\lambda\!\!\!^{-}{}_n = \frac{\hbar}{2\pi} \frac{A+1}{A} \frac{1}{\sqrt{E}}. \tag{1.12}$$

The area of the resonance A_0 is given by the integral of Eq. 1.11

$$A_0 = \int \pi \lambda\!\!\!^{-}{}_n^2 g \frac{\Gamma_n \Gamma_\gamma}{(E - E_0)^2 + (\Gamma/2)^2} dE = 2\pi^2 \lambda\!\!\!^{-}{}_n^2 R_K, \tag{1.13}$$

where

$$R_K = g \frac{\Gamma_n \Gamma_\gamma}{\Gamma} \tag{1.14}$$

is called the *radiative kernel* of the resonance.

In this work the R-matrix SAMMY code is used to fit the resonances of the capture yield with the expression of Eq. 1.11 obtained under the Reich-Moore approximation. As mentioned above, SAMMY takes into account experimental effects such as the Doppler broadening for that. After this adjustment, the properties E_0, Γ_n, Γ_γ and J^P are found for each nuclear state of the compound nucleus. The procedure followed for that will be explained in Sec. 5.1.

Chapter 2

Measuring technique

A neutron capture experiment was carried out with the objective of measuring the cross section of the ^{80}Se(n,γ) reaction. This chapter explains the measurement technique employed for this experiment. Sec. 2.1 introduces the main techniques available for neutron capture cross-section measurements. That section includes the Total Energy Detection (TED) technique used in this work. The application of this technique requires manipulation of the detector response to obtain the behaviour of a TED. This treatment is explained in Sec. 2.2. Lastly, Sec. 2.3 focuses on the time of flight technique, covering the different aspects in detail.

2.1 Capture reaction detection technique

Measuring the neutron capture cross section involves counting the number of captures produced from a known number of neutrons in the sample of interest. Different strategies can be followed to count A(n,γ)B reactions.

- One approach could be to count the reaction products generated B by measuring the difference in mass of the sample before and after being irradiated with neutrons. However, the complexity of mass measurements at such a level of precision makes this option not feasible.
- On the contrary, if the produced B nuclei are unstable, they can be counted by measuring the radioactivity induced in the sample after its irradiation. This approach is called activation technique.

The result for the two mentioned strategies is the capture cross section integrated in the energy range of the incoming neutrons. Therefore, an energy differential cross section cannot be obtained using either technique. Owing to this limitation, the neutron flux used in the activation is selected according with the goal. For instance, for cross section measurements of relevance to astrophysics, a neutron energy flux that resembles a Maxwellian stellar spectrum can be generated to directly obtain the MACS. As it was introduced in Sec. 0.1.1, the MACS is a suitable magnitude to characterize the neutron capture cross section in the stellar environments where the s-process takes place. However, an activation measurement allows to obtain the MACS only at a certain temperature (kT), which depends on the irradiating neutron flux. For that reason, it is only possible to obtain the MACS for a limited number of temperatures with this technique [58]. Since s-process occurs at different temperatures depending on the stellar evolutionary phase, this technique is insufficient to study this process completely and ideally it should be complemented with differential neutron cross-section measurements.

The most widely used techniques to measure neutron energy differential capture cross sections are based on counting the prompt cascades of γ-rays generated after a capture event. This is also a complicated task due to the random nature of the radiation generated. As it was introduced in the previous Sec. 1.2, a random number of γ-rays compose each cascade with the only restriction being the conservation of the total energy emitted $E_C \approx S_n + E_n$. To quantify the efficiency of detecting a capture event, there are several strategies available depending on the number of γ-rays that are detected per capture event. These strategies are described in the following sections.

2.1.1 Total Absorption Calorimeter (TAC)

One of these techniques is the total absorption calorimetry, which consists in measuring all the γ-rays produced after a capture event. The high efficiency needed for this task is achieved with the use of a Total Absorber Calorimeter (TAC). The TAC detector available at n_TOF is composed by forty BaF_2 scintillator detectors forming a 4π array that covers a 95% of solid angle [59]. By using this configuration, this device achieves a detection efficiency close to 80%. However, the large amount of material surrounding the sample can pose a problem for the use of this device in some specific measurements. Incoming neutrons scattered in the sample can be captured elsewhere, even in the detector volume, increasing the background level. In order to reduce this undesired background, a neutron absorbing material is placed between the sample position and the TAC, as it is shown in Fig. 2.1. Nevertheless, the use of this kind of material is insufficient to measure samples with high ratio between elastic and capture cross sections, which is the case of the ^{80}Se sample. Furthermore, in the

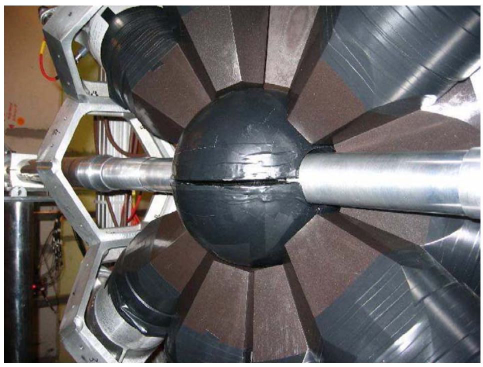

Figure 2.1: TAC detector at n_TOF. The polygonal BaF_2 detectors are surrounding the neutron absorber material within which the sample under study is located. Extracted from [59].

measurement of some nuclei, the data from the TAC beyond a few keV of neutron energy require large dead time corrections. In some cases, this represents also a limitation to study the capture cross section in the energy range of astrophysical interest between 1 eV and 100 keV.

2.1.2 Total Energy Detector (TED)

The approach used in this work derives from the TED technique [60, 61], which is based on two requirements.

First, the use of a low efficiency detection system such that at most one γ-ray per capture event is registered,

$$\varepsilon^{\gamma} << 1. \tag{2.1}$$

Moreover, the efficiency to detect a γ-ray has to be proportional to its energy, as shown shown in Eq. 2.2.

$$\varepsilon^{\gamma} = \alpha E^{\gamma} \tag{2.2}$$

If the two aforementioned conditions are fulfilled, the detection efficiency for a cascade ε^C does not depend on the energy of the particular γ-rays that compose it. Mathematically, ε^C is represented in Eq. 2.3 as the complementary of not detecting any γ-ray from the cascade.

$$\varepsilon^C = 1 - \prod_{j=1}^{N}(1 - \varepsilon_j^{\gamma}) \tag{2.3}$$

By applying the condition of low efficiency shown in Eq. 2.1, ε^C can be approximated by

$$\varepsilon^C \approx \sum_{j=1}^{N} \varepsilon_j^{\gamma}. \tag{2.4}$$

Whereas applying the proportionality condition of Eq. 2.2 the efficiency is then

$$\varepsilon^C \approx \alpha \sum_{j=1}^{N} E_j^{\gamma} = \alpha E^C, \tag{2.5}$$

where $E^C \approx S_n + E_n$ is the energy of the entire cascade. Finally, the efficiency of detecting a capture event, i.e. ε^C, becomes independent from the energy of the individual γ-rays of the cascade after applying conditions 2.1 and 2.2.

The low efficiency condition of Eq. 2.1 is achieved without major problem by using detectors with low detection volumes that are constructed of low-Z materials. The main difficulty of the TED technique arises from achieving the proportionality condition of Eq. 2.2 since, for any detection system the efficiency depends on the energy of the incoming particle. As a result, the probability of counting a cascade will depend on each de-excitation path, which would give an incorrect measurement of the cross section.

Several solutions have been developed over the last decades to attain the desired proportionality between efficiency and γ-ray energy. Moxon and Rae pioneered the implementation of the proportionality condition Eq. 2.2 in the early sixties [60], becoming the first to successfully apply the TED technique. For that, they took advantage of the fact that a Geiger tube with a thick wall of low Z material has a γ-ray detecting efficiency which increases nearly linearly with γ-ray energy. Just the condition required to correctly measure the capture cross section using the TED technique. However, the limited energy range between 500 keV and 2.8 MeV was the main drawback of this approach.

An improved strategy to satisfy condition 2.2 consists in weighting the response function of the detector for each registered γ-ray [61]. This technique is referred to as the Pulse Height Weighting Technique (PHWT) and it will be explained in Sec. 2.2.

A fundamental advantage of the PHWT is that it enables almost any detector type to be used for neutron-capture TOF measurements, in as much as its efficiency is small, and its time response sufficiently fast as to preserve the ToF resolution of the facility used. This flexibility has allowed one to develop a new type of TED with imaging capability (i-TED) [62]. The main objective of this new detector concept is to reduce the contribution of spatially localized background sources by means of its capability to obtain information on the incoming radiation direction. Part II of this manuscript will focus on the development of this new detection technique and further details can be found there.

2.2 Pulse Height Weighting Technique (PHWT)

In the PHWT, a mathematical treatment of the detector response is performed in order to achieve the proportionality condition between efficiency and γ-ray energy required to apply the TED technique. The PHWT was firstly applied by Macklin and Gibbons also in the sixties [61]. A brief mathematical formalism follows to explain this technique.

Let R_i^γ be the response function of a detector to a γ-ray with energy E^γ, discretized in a histogram with $i = 1, ..., N$ bins and normalized to the efficiency of detecting this γ-ray

$$\varepsilon^\gamma = \sum_{i=1}^{N} R_i^\gamma. \tag{2.6}$$

The condition 2.2 is achieved by using a Weighting Function (WF) in such a way that

$$\varepsilon_w^\gamma = \sum_{i=1}^{N} W_i R_i^\gamma = \alpha E^\gamma. \tag{2.7}$$

Monte Carlo (MC) simulations have demonstrated to be the only accurate method to calculate the WF [63]. Thousands of mono-energetic γ-rays can be easily simulated and an averaged response function of every detector can be obtained for each individual energy. After normalization of the resulting response function to the number of simulated γ-rays, a WF is calculated to match the integral value of the weighted response with the energy of the simulated γ-rays. The proportionality constant of Eq. 2.7 can be chosen equal to the unit, $\alpha = 1$.

The simulations dedicated to the calculation of the WF require a detailed implementation of the experimental setup to obtain a realistic averaged response of the detectors. This implementation of the setup must include each measured sample with a great level of detail. The sample itself plays an important role in the simulation of the radiation emitted, with important effects to take into account such as the *self-shielding* effect. Thus, an independent set of MC simulations and corresponding WFs have to be obtained for each specific sample used in the capture experiment.

All details about the implementation of the MC simulations and the application of the PHWT and its associated uncertainties will be given in Sec. 4.3. The procedure followed in that section to obtain these uncertainties consists of simulating the response of the detectors to realistic de-excitation cascades. The resulting deposited energy spectra are convoluted with the experimental energy resolution of detectors that will be shown in Sec. 4.2, and weighted with the WF. The integral of each of these spectra must correspond to the number of simulated cascades. Otherwise, the deviations between these numbers can be considered as the uncertainties from the weighting procedure that are associated to each detector.

2.3 Time of Flight (ToF) technique

The kinetic energy of the incoming neutrons that irradiate the sample must be determined in order to find the energy distribution of the capture cross section. For that, the ToF technique is applied. In this technique, the time t_{ToF} that neutrons spend traveling a well known distance L, from their production site to the experimental area, is measured to calculate their kinetic energy using the classical equation

$$E_n = \frac{1}{2} m_n v_n^2 = \frac{1}{2} m_n \left(\frac{L}{t_{ToF}} \right)^2 . \tag{2.8}$$

This expression is valid for neutrons with energies below $\sim$ 100 MeV. This upper limit is not a real limitation in this analysis. Actually, this value is several orders of magnitude higher than the energy range of astrophysical interest to study the s-process, which extends from 1 eV up to 100 keV.

The energy precision achieved with this method will largely depend on the distance traveled by the neutrons. For a long distance L, a long time t_{ToF} will be measured thus decreasing the relative error made in the measurement of both quantities. Therefore, a better neutron energy resolution will be found. This can be calculated by using Eq. 2.9 corresponding to the error propagation followed from Eq. 2.8.

$$\frac{\Delta E_n}{E_n} = 2\sqrt{\left(\frac{\Delta L}{L}\right)^2 + \left(\frac{\Delta t_{ToF}}{t_{ToF}}\right)^2} \tag{2.9}$$

Fig. 2.2 illustrates the basic principles of the ToF technique in a simple diagram. The neutron pulses are produced in the "black box" on the left. A pulsed beam is needed in order to apply the ToF technique, otherwise the origin of the time cannot be known. As it can be seen, these neutron pulses are shown with multi-colored boxes that represent the different kinetic energies with which neutrons are generated. The neutrons with different energies will reach the experimental area at different ToF producing neutron reactions. This ToF can be used to calculate the kinetic energy of the incident neutron.

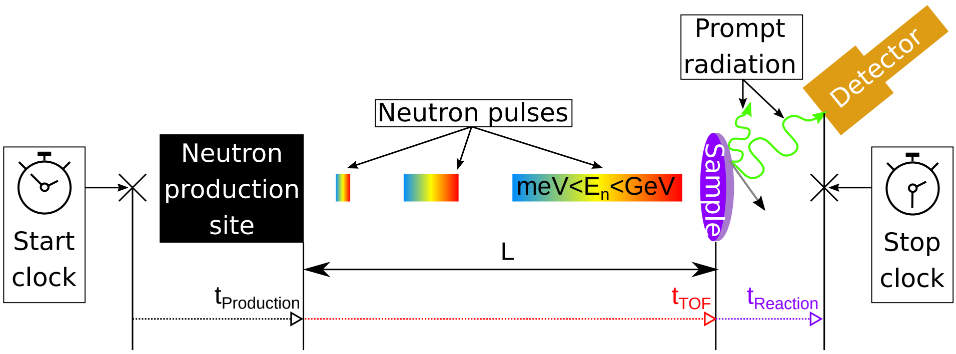

Figure 2.2: Simple diagram to explain the ToF technique.

As it happens in most ToF facilities, Fig. 2.2 shows that the clock starts counting just before neutron production. Normally, an electrical trigger signal indicates the origin of the time. On the other hand, as it was explained in Sec. 2.1, what one detects in a neutron capture cross section measurement are the reaction products. Therefore, the clock stops when γ-rays coming from capture reactions are detected. Thus being the total measured time a sum of several contributions as it is shown in Eq. 2.10, where $t_{Production}$ is the neutron production time and $t_{Reaction}$ the capture reaction time. Since the latter is in the order of 10^{-15} s, it can be neglected without great mistake:

$$t = t_{Production} + t_{ToF} + t_{Reaction} \approx t_{Production} + t_{ToF}. \tag{2.10}$$

Details on the determination of the neutron energy from the measured ToF will be given in Sec. 4.4 for the experiment at CERN n_TOF.

Chapter 3

Experimental setup

The neutron capture cross section of the ^{80}Se isotope was measured with high resolution using the time of flight (ToF) technique at CERN n_TOF during the 2018 campaign. This chapter contains the details of the experimental setup employed in this measurement. Firstly, Sec. 3.1 introduces the n_TOF facility. In that section, the characteristics of the neutron beam and the beam monitors are described. Sec. 3.2 focuses on the ^{80}Se(n,γ) experiment itself. In that section, both the C_6D_6 detectors and all the samples used are explained. Lastly, Sec. 3.3 introduces the processing chain used to convert the raw signals from the C_6D_6 detectors into counting rate histograms for the subsequent analysis of the neutron capture cross-section measurement.

3.1 The n_TOF facility

n_TOF is a neutron ToF facility built at the European Organization for Nuclear Research (CERN) accelerator complex [64]. In this facility, neutrons are generated by means of spallation reactions in a lead block. These reactions are induced by protons previously accelerated in the Proton Synchrotron (PS). The PS provides a 7 ns RMS wide, 20 GeV/c pulsed proton beam spaced by a multiple of 1.2 s. Fig. 3.1 shows an scheme of the CERN acceleration complex in which both the n_TOF experiment and the PS are represented. As it can be seen, the PS supplies protons to other experiments in addition to n_TOF. For that reason, the intensity of the proton beam is not the same in all pulses, rather a distinction is made between *dedicated* or *parasitic* pulses. Pulses which are dedicated to n_TOF have a high intensity of 7×10^{12} protons per pulse. On the contrary, when those dedicated pulses are sent to another experiment, remaining parasitic pulses of 3×10^{12} protons reach the spallation target of n_TOF. Regardless of pulse type, each proton impinges on the massive lead block producing $\sim$ 400 neutrons in the energy range from MeV to GeV [65]. Thanks to this prolific mechanism, a very high instantaneous neutron flux is generated.

Focusing on the horizontal beam line towards the first experimental area, the shower of particles originating from spallation reactions passes through a 4 cm

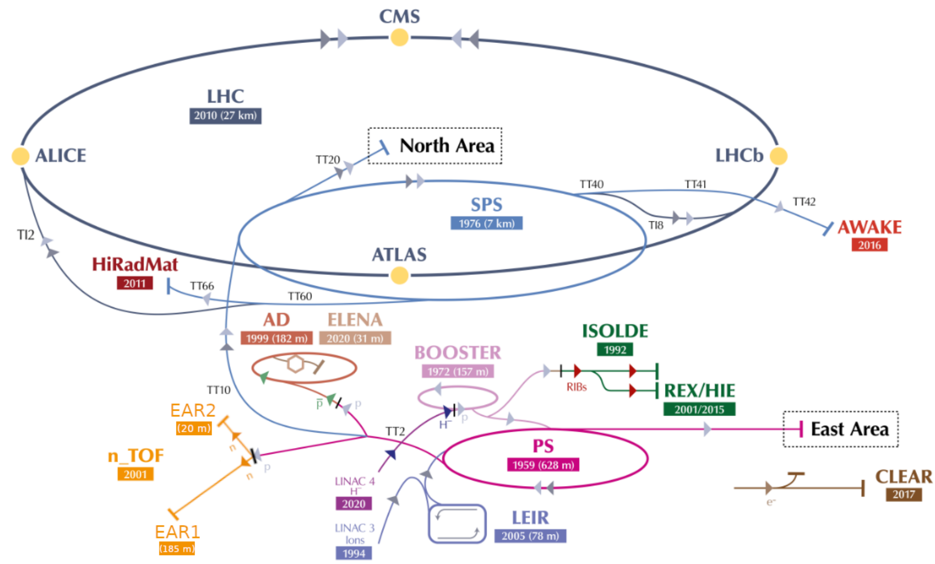

Figure 3.1: CERN accelerator complex scheme layout. The two experimental areas of n_TOF are represented in the bottom-left corner of the image.

thick layer of borated water, which acts as a moderator at the exit of the spallation target. The change from water to borated water moderator reduces the thermal neutron flux through ^{10}B(n,α) reactions, and consequently decreases also the 2.2 MeV γ-rays from thermal capture on water produced via ^{1}H(n,γ) reaction. This became the main component of the γ-ray background that limited some of the measurements in the previous Phase-1 of the n_TOF facility.

Fast neutrons are partially moderated in the aforementioned layer and, as a consequence, the out-coming neutron spectrum covers a large energy range between meV and GeV. In addition, the low repetition rate of the PS allows to measure low energy neutrons down to thermal energies without overlapping with the following PS cycle.

Outgoing particles are collimated in a beam that is guided through a nearly horizontal vacuum tube. The latter passes through a very intense magnetic field that removes all undesired charged particles from the beam. A second cylindrical collimator is placed after the magnets and just before the experimental area. The aperture of this collimator depends on the experiment to be performed, 18 mm diameter for neutron capture experiments and 80 mm diameter for fission experiments. At the end, the neutron beam reaches the experimental area which is known as EAR1. The 185 m of total flight path allows to perform ToF measurements with very high neutron energy resolution at EAR1. More technical information about the facility is available in [48, 66].

The horizontal beam line and the EAR1 experimental area introduced before are in use from the beginning of the n_TOF facility (2001). During the first long shut down (LS1), started in early 2013, a new 20 m vertical beam line was built together with a new experimental area EAR2 [67]. The reduction of the flight path leads to a factor of 25 increase in the available neutron flux compared with EAR1. In return, the relative error associated with the measurement of the ToF becomes greater, which translates into a reduction in the energy resolution.

A third experimental area called NEAR Station was proposed during the LS2 (2019-21). As it can be seen in Fig. 3.2, this new experimental hall would be located next to the spallation target just after a concrete shielding wall. Hence, the sample would be placed at ~ 3 m from the neutron production site, thus enhancing the flux in a factor 10 with respect to EAR2. The NEAR Station will be focused on activation measurements, being a complementary method to measure neutron capture cross sections. As it was explained in Sec. 2.1, in this technique, the sample can be irradiated with a Maxwellian neutron flux to directly obtain the Maxwellian Averaged Cross Section (MACS). As it was demonstrated by simulations [68], samples could be irradiated at the NEAR Station area with a quasi-Maxwellian neutron flux by shaping the neutron flux coming out from the spallation target with filters made of different materials. The combination of the the high flux and the flux shape in this facility will allow to measure MACS at n_TOF using extremely small mass samples and radioactive isotopes by means the activation technique.

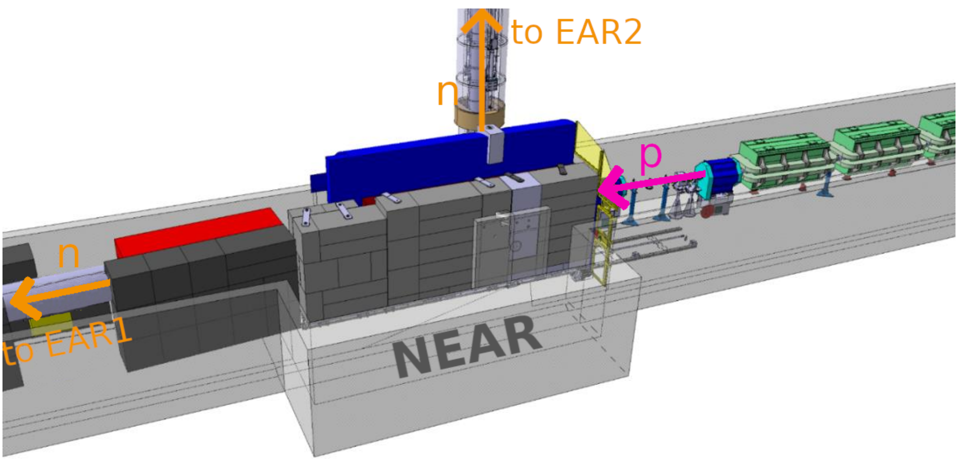

Figure 3.2: CAD diagram of the NEAR Station at CERN n_TOF. The direction of the proton beam is highlighted with a pink arrow, and the directions of neutrons towards the experimental areas with orange arrows. Adapted from [68].

3.1.1 Neutron beam

The characterization of the neutron beam is a key aspect to perform a neutron capture cross section measurement. One important feature of the beam is flux, which is defined here as the energy distribution of the neutrons produced by a bunch of protons. A set of measurements was carried out at n_TOF to measure the flux with high accuracy [69]. The main result of this work was an evaluated version of the flux which is used in this analysis, as it will described in Sec. 4.6. However, this section focuses on other important features of the beam, such as its spatial profile and the properties of its γ-ray components.

The spatial profile of the beam was measured at n_TOF by using MicroMegas detectors [70]. Fig. 3.3 shows the bidimensional profile of the beam at the position of the capture sample. This spatial profile is a Gaussian of 18 mm FWHM. The knowledge of the beam shape at the sample position is crucial to estimate the fraction of the beam intersected by the sample. The latter is the so-called Beam Intersection Factor (BIF). In order to compare capture yields measured with samples of different shapes, a correction is needed due to this BIF. This correction could be relevant in neutron capture measurements where the capture yield is compared to the measured one from a reference sample (see Sec. 4.7.1), and with the yield of some ancillary samples (see Sec. 4.5). However, since all samples employed in this work have the same shape (see Sec. 3.2.2), no correction has to be applied in this sense.

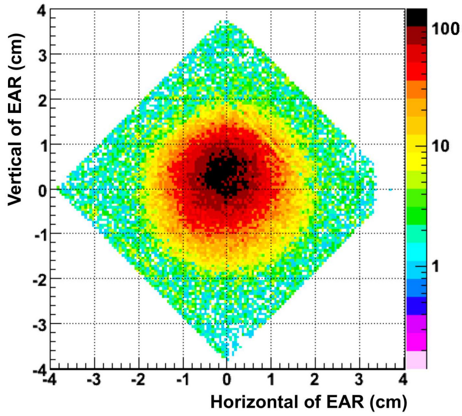

Figure 3.3: Profile of the neutron beam at sample position of n_TOF EAR1. Extracted from [70].

On the other hand, there are not only neutrons in the beam. As it was mentioned before, charged particles are removed from the beam by means of magnetic fields. Nevertheless, some neutral particles as γ-rays remain unaltered in the beam. Most of these photons are directly generated by the spallation reactions in the lead block, or by neutron captures in the moderator. These reactions were studied with Monte Carlo simulations in [71], and a result from this study can be seen in Fig. 3.4. That figure shows the ToF distribution of γ-rays that reach EAR1 after each proton pulse. The resulting distribution can be clearly divided into two different components:

- The *prompt* component corresponds to those γ-rays with a ToF below ~ 700 ns. The distribution shows a very strong narrow peak. This huge amount of γ-rays produces a very intense signal which saturates all detectors in the experimental hall for few μs. This signal is called *γ-flash* and it determines the origin of the time in the ToF analysis, as it will be explained in Sec. 4.4.

- The *delayed* component is composed by γ-rays with a ToF longer than 700 ns. The smooth distribution has its end point at 2×10^3 μs, which means that γ-rays are present in the beam at energies beyond $\sim$ 100 eV. Therefore, this component can interfere with the capture measurement by increasing the background level. The measurement of ancillary samples is needed to subtract this background contribution, as it will be explained in Sec. 4.5.

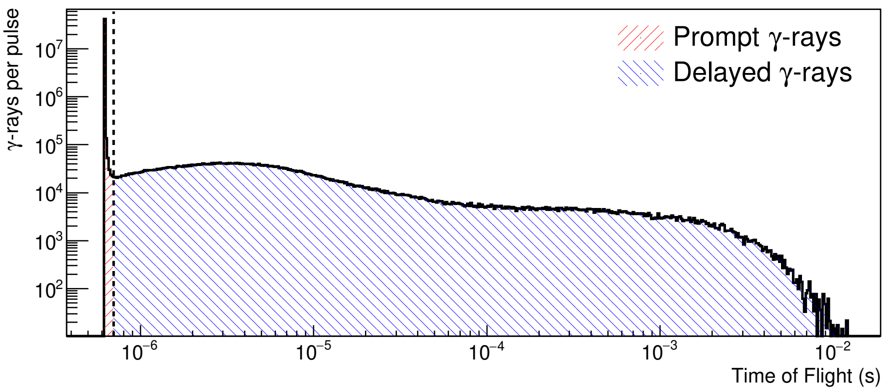

Figure 3.4: Simulated ToF distribution of the γ-rays produced by a bunch of protons in the spallation target and transported to EAR1. Two different components are distinguished depending on the ToF: *prompt* and *delayed* (see text). Extracted from [72].

3.1.2 Beam monitors

Owing to chemical reactions, the boron concentration in the moderator can change from one experimental campaign to another. Thus, it is important to perform a continuous monitoring of the beam in order to identify deviations between the experimental and the evaluated version of the flux below 10 eV. At n_TOF, the monitoring system used for this purpose is composed by two proton current monitors and four Silicon Monitors (SiMon) for neutrons, which are introduced in the following sections.

Proton monitors

Protons monitors are placed in the vacuum pipe that joins the PS and the n_TOF spallation target. There are two different detectors and they both determine the number of protons in the beam by measuring voltage differences:

- **Beam Current Transformer (BCT)**. It is placed ~ 6 m before the target. It measures the voltage induced by the proton beam in a electrical circuit. The signal of this detector is used to trigger the n_TOF digital acquisition system. In this work, this detector is also used to check the performance of the SiMon detectors (see Sec. 4.1).

- **Wall Current Monitor** or **PKUP** [73]. It is installed just after the BCT monitor. It measures the voltage induced in the walls of the vacuum pipe that guides the proton bunch.

Neutron monitors

Since neutrons are non-charged particles, the neutron flux cannot be directly measured by current monitors. Instead, a neutron-converting reaction can be used. For that, the beam passes through a thin foil of converter material and some neutrons interact with it producing charged particles that can be easily detected. By knowing the cross section of the reaction employed one can compute the neutron flux using Eq. 3.1.

$$\phi(E_n) = \frac{C(E_n) - B(E_n)}{\varepsilon(E_n)\left(1 - e^{-n\sigma_t(E_n)}\right)\frac{\sigma_r(E_n)}{\sigma_t(E_n)}} \tag{3.1}$$

In this expression, C is the number of counts and B the background contribution measured with a detector of efficiency ε. The reactions take place in a material of areal density n, with very well-known reaction (σ_r) and total (σ_t) cross sections.

A neutron monitor based on this principle is typically used in n_TOF to measure the flux:

- **Silicon Monitor (SiMon)** [74]. This monitor is placed at the entrance of the experimental area. It is based on the neutron-converting reaction ^{6}Li(n,α)^{3}He. Thus, it has a very thin Mylar foil with a deposit of ^{6}Li which is inserted in the beam. The reaction products are detected by four silicon detectors placed at 45° after the converter foil. Since the cross-sections of this reaction are well known, the flux can be obtained by using Eq. 3.1. In this work, the response of this monitor will be used in Sec. 4.1 to check the stability of the counting rates in the radiation detectors employed in the capture measurement, as well as in the comparison between the energy distribution of the actual and the evaluated flux that will be discussed in Sec. 4.6.

3.2 ^{80}Se(n,γ) experimental setup

In this section, the main features of the experimental setup employed in the ^{80}Se(n,γ) cross-section measurement are detailed. All components described bellow were placed at EAR1 where the experiment was carried out. It is important to note the big efforts of the n_TOF collaboration to minimize the amount of γ-rays coming from neutrons captured in the structural material of the experimental setup, an effect known as *neutron sensitivity*. This contribution increases the background measured during the neutron capture cross-section measurement, thus it is important to keep it as low as possible [75].

Fig. 3.5 shows a photograph of the experimental setup used in this measurement. The different components will be explained in the following sections.

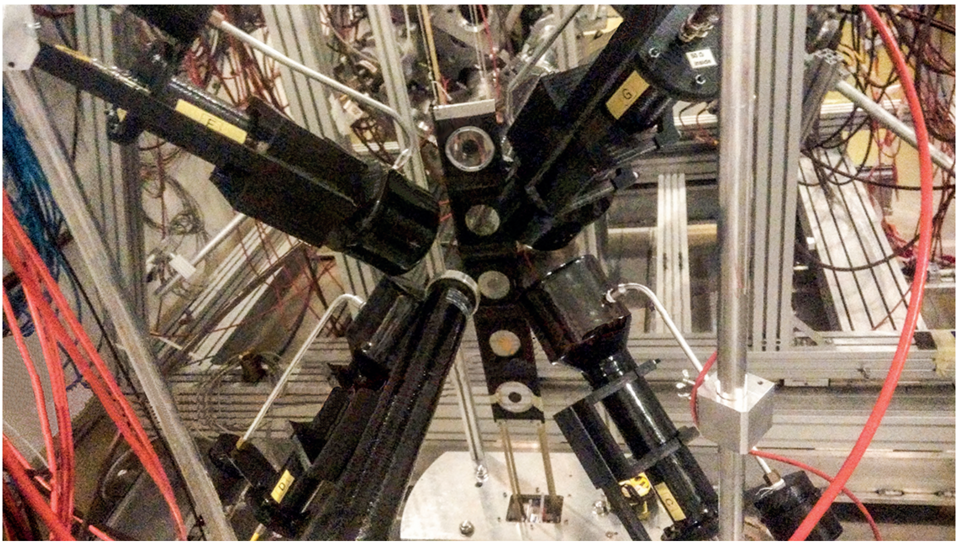

Figure 3.5: General view of the experimental setup at EAR1 used for the ^{80}Se(n,γ) measurement. Four C_6D_6 detectors are set up surrounding the capture sample, which is selected from all the available ones using the sample exchanger.

3.2.1 C_6D_6 detectors

Four C_6D_6 detectors were employed in this experiment to measure the radiative neutron cross section of the ^{80}Se isotope. These detectors are based on an organic liquid scintillator optically coupled to a photo-multiplier tube (PMT) by means of a quartz window.

The C_6D_6 detectors used in this work correspond to an evolution of a previous detector developed at Forschungszentrum Karlsruhe [76]. The new C_6D_6 detectors [77] are built in carbon fiber, which allows to reduce the neutron sensitivity. The high ratio between elastic and capture neutron cross section of C favors the scattering of neutrons whereas minimizing their captures. In addition, the PMT and the quartz window of these detectors were optimized. Since these components are the main source of undesired neutron captures, reducing their volume and boron content also contributes to a decrease in neutron sensitivity. Moreover, a further improvement in terms of neutron sensitivity is expected from a recent development achieved by replacing the full PMT by a lightweight silicon photomultiplier (SiPM) [78].

The low γ-ray detection efficiency of C_6D_6 becomes essential to apply the PHWT, as it was explained in Sec. 2.2. For that reason these detectors have an small amount of scintillation liquid ($\sim$ 1 l) with a very low Z, which minimize the probability to detect more than one γ-ray per capture event.

Furthermore, the rapid response of these detectors and the fast recovery after the γ-flash makes them ideal for ToF measurements in the keV neutron energy range, such as the one presented in this work. The output signal for a γ-ray from a typical capture event has a risetime of a few ns, which is a fast enough response to carry out this type of experiment with high ToF resolution.

As it can be seen in Fig. 3.5, the four C_6D_6 detectors were positioned at a distance of 10 cm pointing to the sample, against the beam direction, and with an inclination of $\sim 125°$ with respect to the beam line. Such orientation aims at minimizing the impact of anisotropic emission of the primary γ-rays for capture events with $l > 0$ [79]. In addition, it reduces the background related to in-beam γ-rays , due to the angular distribution of the Compton effect, which obeys the Klein-Nishina formula [80]. The detectors were fixed by means of four carbon fiber holders to two thin aluminum bars. Both structural materials were selected because of their low neutron sensitivity.

3.2.2 Samples and experimental configurations

The quality of the resulting data will strongly depend on the good characterization of the samples employed in the measurement. Composition, homogeneity and shape are some of the most important parameters to keep under control. Along the ^{80}Se(n,γ) experiment, the following configurations were measured:

- **^{80}Se sample**. It is a 20 mm diameter solid disk of 3.5 mm thickness and 2.965(5) g of mass. The isotopic composition shown in Tab. 3.1 displays that this is a sample of 99.87(10)% pure ^{80}Se with a slight contamination of other selenium isotopes. The disk-shaped sample was produced in the Paul Scherrer Institut (PSI) in Switzerland. Owing to the brittleness of the conformed pellet, it was introduced into a mylar pocket which was attached to a carbon fiber frame.

Isotope	^{74}Se	^{76}Se	^{77}Se	^{78}Se	^{80}Se	^{82}Se
Percentage (%)	0.04(1)	0.01(1)	<0.005	0.01(1)	99.9(1)	0.07(2)

Table 3.1: Isotopic composition of the ^{80}Se sample.

- **Dummy sample**. It is a replica of the ^{80}Se sample without the sample itself. Just an empty mylar pocket attached to a frame built from carbon fiber. The measurement of this configuration gives a direct estimation of the background component unrelated to the sample that is induced by those neutrons captured in the surrounding of the experimental setup (see Sec. 4.5).
- ^{197}**Au sample**. This is a 20 mm diameter and 100 μm thickness disk of 600 mg of ultra-pure ^{197}Au. It is attached to an empty frame similar to the one mentioned above. The ^{197}Au(n,γ) yield is used as a reference to normalize the ^{80}Se(n,γ) yield, as it will be explained in Sec. 4.7.1.
- ^{nat}**Pb sample**. This 20 mm diameter disk of 2.1 mm thickness is formed by 7.3 g of natural lead. It is also attached to the aforementioned empty frame. The measurement of this configuration is intended to determine the background components related to the presence of the sample (see Sec. 4.5).

All these samples were fixed to the carbon fiber belt that is shown in the Fig. 3.5. This ladder was driven by a sample exchanger system that was operated remotely from the n_TOF control room. This remote control allows the operator to change the sample being measured for another one without entering in the experimental area. Reducing the number of accesses to the experimental area is important to maximize beam time. As the rest of setup, this sample exchanger is built from aluminum and carbon fiber to reduce the neutron sensitivity.

On the other hand, a set of five neutron absorbing filters were interposed in the beam path during some measurement runs with the ^{80}Se and dummy samples. The set is composed by filters made of ^{27}Al, ^{59}Co, ^{184}W, ^{nat}Ag and ^{nat}Mo with thicknesses of 50.00 mm, 0.25 mm, 0.80 mm, 0.50 mm and 1.00 mm respectively. The diameter of these disk-shaped filters is large enough to intercept the entire beam section. Once the filters are placed in the beam path, they remove all neutrons whose energy corresponds to the energy of the strongest neutron capture resonances of the materials used. Filter measurements will be employed in Sec. 4.5 to scale the background contribution related to the in-beam γ-rays that are scattered by the sample. This method is known as *the black filter method* [81].

Tab. 3.2 shows the number of protons used in the measurement of all configurations with and without filters. The latter were not used in the measurement of the ^{197}Au and ^{nat}Pb samples. In total, 2.66×10^{18} protons were used in this experiment, of which almost 65% were employed to measure the ^{80}Se sample. Taking into account the daily proton delivery rate of 1.1×10^{17} at n_TOF, that total amount of protons corresponds to 24 days of beam time.

Sample	Number of protons	
	Filters out	*Filters in*
^{80}Se	1.71×10^{18}	1.11×10^{17}
Dummy	1.51×10^{17}	3.58×10^{17}
^{197}Au	2.14×10^{17}	–
^{nat}Pb	1.16×10^{17}	–
Total	$\mathbf{2.66 \times 10^{18}}$	

Table 3.2: Number of protons dedicated to the measurement of each sample during the ^{80}Se(n,γ) campaign.

3.3 Processing chain

The electronic chain that powers the detectors and digitizes their output signals is described in Sec. 3.3.1. The subsequent characterization of raw digital signals is introduced in Sec. 3.3.2.

3.3.1 Data Acquisition System (DACQ) and power electronics

The n_TOF DACQ system is based on flash analog-to-digital (FADC) units that perform digital acquisition of detector output signals [82, 83]. This system is capable of recognizing and storing the electrical pulses generated by the detectors, which have an amplitude proportional to the energy deposited by the detected particle and a rise/falling time characteristic of the detector type. A wide range of detectors is available at the n_TOF facility due to the diversity of measurements performed there [84]. Hence, a versatile DACQ capable of working with different detectors is needed.

The DACQ is composed of 33 Data Acquisition Cards (DACs) installed in six units distributed between the two experimental areas. The DACs are SPDevices ADQ14DC with four channels of 14-bits resolution, 1 GS/s sample rate, 256 MS buffer memory and 400 MHz of bandwidth. The acquisition procedure is performed with two separate threads: *the Acquisition* and *the Writer*. The former is triggered by the signal of the BCT detector from the PS (see Sec. 3.1.2). During 100 ms, in parallel to the arrival of the neutron bunch to the experimental area, this thread is storing raw data into the memory buffer. After the acquisition is finished, the Writer compresses the data by means of a zero-suppression algorithm. The latter removes those signals with an amplitude lower than a certain threshold that is configured by the user. The application of this algorithm optimizes the raw data thus reducing the size of the output file. This file is preliminarily stored in a disk pool by the Writer thread. When the file is closed it is automatically transferred to the Cern's Advanced STORage manager (CASTOR) [85] from which it is accessible to any n_TOF user.

The final output file contains information about the configuration of the high voltage supply, the detectors and the DACQ, in addition to the data recorded by the detectors used in the capture measurement and beam monitoring (see Sec. 3.1.2).

A Graphical User Interface (GUI) allows the user to manage the DACQ system from the n_TOF control room. Detector configurations can be carried out remotely as well as the initialization of the acquisition. Furthermore, some useful information like the measured sample, presence or absence of filters, or the distance between sample and detectors can be introduced to be stored in the online runbook together with the experimental data.

In order to power the C_6D_6 detectors, a Caen SY4527 Universal Multichannel Power Supply System is employed. This power supply contains several cards, each with up to sixteen 3 keV/3 mA high voltage channels. The latter can be individually controlled by the user from the n_TOF control room by means of an Ethernet connection.

3.3.2 Pulse Shape Analysis (PSA)

A generic routine written in C++ programming language was developed at n_TOF [86] to get reliable information from the digitized data. This routine performs a Pulse Shape Analysis (PSA) to process signals measured with different detector types. The characteristics of the detectors used and their configurations are included in an auxiliary parameter file.

The analysis of the signals starts with the adjustment of a baseline. This baseline can be reproduced in a simplest way by a constant line. A weighted moving average is implemented to fit a baseline with slow oscillations, whereas a moving maximum implementation is chosen if the baseline is severely affected by the γ-flash.

Once the baseline is subtracted, PSA analysis is carried out to identify and characterize the pulses corresponding to the γ-rays detected by the C_6D_6 detectors. The PSA routine works with negative signals, the positive ones are multiplied by -1. In order to identify a pulse, the routine calculates the derivative of the signal whose step size is optimized by the user depending on the detector employed. Fig. 3.6 shows a $\sim 2\ \mu$s fragment of real signals obtained with a C_6D_6 detector. As it can be seen, a pulse is recognized when the derivative signal crosses two user-selected thresholds in the lower-lower-upper-upper order.

The amplitude of the identified pulses can be computed with three different methods: the maximum of the signal, a parabolic fit around this maximum or the adjustment of a predefined pulse shape. This pattern can be obtained as the average of a large number of real signals. The use of this method could allow to partially correct the saturation effects from the pulses.

After the PSA analysis, information about the area, amplitude and time of the pulses is obtained. Among all the pulses analyzed, special attention is required for the γ-flash pulse. As it was mentioned in Sec. 3.1.1, a good determination of the γ-flash time is crucial since this time is considered as the origin of time in ToF analysis. For all pulses, thresholds based on their width, amplitude and area are applied to reduce the probability that the electrical noise can be considered as a real signal.

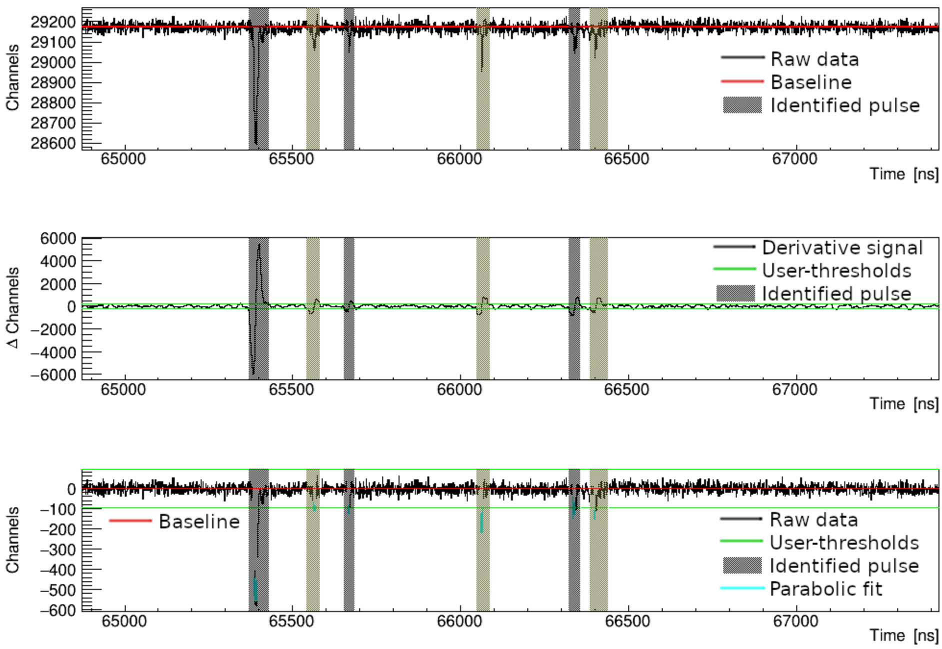

Figure 3.6: Screenshot of the pulse recognition procedure using the PSA routine. (Top panel) Raw signals are shown together with an adjusted baseline (red line). (Middle panel) The derivative signal is displayed together with the signal identification thresholds (green lines). (Bottom panel) The parabolic adjustments performed on top of each raw signal are shown (blue lines) with an amplitude threshold.

In this work, the baseline is fitted with a constant line. The moving average option was tested without remarkable differences. The options for the γ-flash recognition and the thresholds described before remained unchanged with respect to other measurements with C_6D_6 detectors [87]. The amplitude of the signals are obtained by using the parabolic fit. An average pulse was tested to try to remove a kind of electrical rebound signal that appears after some C_6D_6 pulses (see Sec. 4.2.1). However, since they appear at different times after the main pulse, they cannot be modeled by an average pulse and this solution was discarded.

Chapter 4

Determination of the capture yield

One of the goals of this work is to obtain the neutron capture cross section of the ^{80}Se isotope as a function of the neutron energy. To this aim, a capture yield must be determined to later carry out a resonance analysis. In this chapter we describe the steps to obtain the capture yield from the experimental data. Firstly, in Sec. 4.1, data processed by the PSA routine is validated by means of consistency checks. After calibrating the C_6D_6 detectors in deposited energy (Sec. 4.2), the PHWT is applied in Sec. 4.3 to ensure the proportionality between γ-ray energy and efficiency required for the TED technique. The relation between time of flight (ToF) and neutron energy, explained in Sec. 4.4, is needed to relate the yield with the energy of the incoming neutrons. Once we obtain the calibrated and weighted neutron energy spectra for the ^{80}Se(n,γ) and ^{197}Au(n,γ) measurements, their background components are subtracted in Sec. 4.5. Data from the ^{197}Au(n,γ) reaction is needed for normalization purposes by applying the saturated resonance method, as detailed in Sec. 4.7.1. Finally, after determining in Sec. 4.6 the neutron flux for this experiment, the capture yield is obtained in Sec. 4.7. The latter also discusses the corrections that must be applied to the yield to take into account different experimental effects such as the emission of conversion electrons or the summing of multiple capture γ-rays .

All these tasks were performed by developing several C++ scripts based on the ROOT object-oriented data analysis toolkit [88]. This framework provides useful tools to perform operations with histograms such as selections, subtractions and weighing, and other related statistical analysis.

4.1 Consistency checks between detectors

In order to discard data affected by systematic errors, the performance of the C_6D_6 detectors is evaluated in terms of count rate and gain stability. For this purpose, different cross-checks are carried out by comparing the response of the SiMon and C_6D_6 detectors.

4.1.1 Count rate stability

The count rate of the C_6D_6 detectors for a given sample has to be proportional to the neutron flux. Deviations in the count rate of a C_6D_6 detector may artificially modify the calculated yield. These deviations could be due to several factors such as a baseline drift in the analysis with the PSA routine, an accidental geometrical change in the setup or an electronic failure. The comparison between the C_6D_6 count rate and that obtained from the four installed SiMon detectors, proportional to the number of neutrons, allows us to identify these changes.

As introduced in Sec. 3.1.2, SiMon detectors measure the products of the ^{6}Li(n,α)^{3}He reaction to determine the neutron flux. Owing to the low yield of charged particles, detecting all of them may be a complicated task for the precise measurement of the flux in some particular neutron energy regions [74]. For that reason, only the signals belonging to the tritium peak are used in this study. These signals are selected by means of the cuts in amplitude and ToF shown in Fig. 4.1. The accepted ToF range extends from thermal up to 10 keV of neutron energy, where the ^{6}Li(n,α)^{3}He reaction measured with the SiMon has no efficiency and kinematical boost corrections [69]. In this range, signals coming from alpha and tritium particles, and the γ-ray background, are clearly separated as it can be seen in the same figure. The conservative amplitude selection between 3×10^4 channels and 4.5×10^4 channels allows to register only tritium particles.

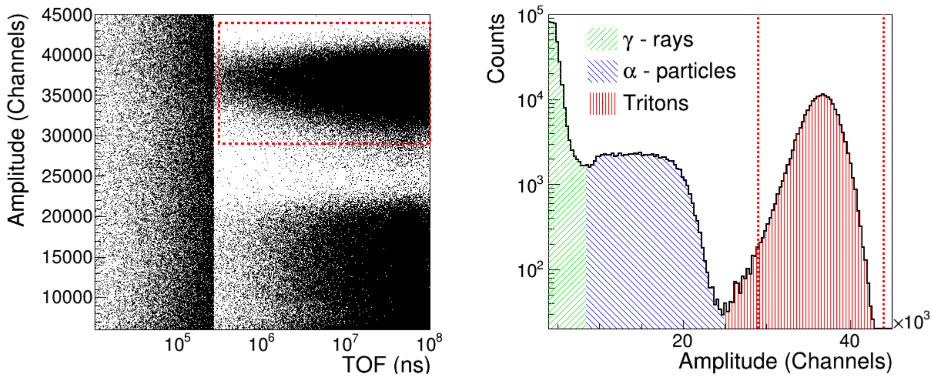

Figure 4.1: SiMon detectors response for all ^{197}Au(n,γ) data. (Left panel) Count rate distribution as a function of ToF and amplitude of the signals with corresponding selections highlighted (red box). (Right panel) Amplitude projection along with the applied amplitude selections (red dashed lines). The contributions of the different detected particles are differentiated by color.

Regarding the C_6D_6 detectors, the ToF range corresponding to the resolved resonance region is selected to minimize the impact of the ambient background in the count rate, which is independent of the neutron flux. For the same reason, only signals with amplitudes greater than 1500 channels ($\sim$ 250 keV) are accepted.

Fig. 4.2 compares the count rate of the SiMon and the C_6D_6 detectors for several measurement runs. Here the count rate is expressed as the number of valid signals accumulated per a thousand of bunches. As it can be observed, both the C_6D_6 and the SiMon detectors follow the same trend within the statistical uncertainty. This is clearly reflected in the bottom panels of the same figure. The ratios between the sum of the four SiMon and every C_6D_6 detector are displayed with points, and their averages by coloured lines. To quantify the dispersion, histograms filled with the projections of these points over the Y axis are fitted with Gaussian distributions.

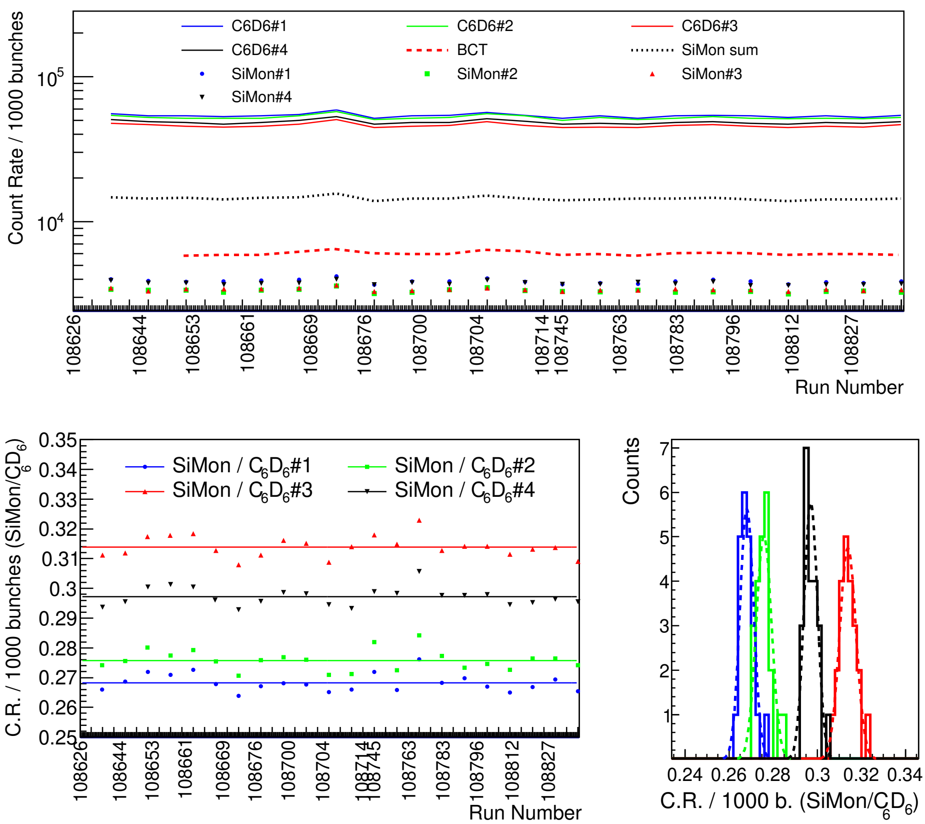

Figure 4.2: (Top) Count rate per 1000 bunches of all C_6D_6 detectors and all SiMon detectors. (Bottom left) Ratio between the count rate per 1000 bunches of all C_6D_6 detectors over all SiMon detectors added, and their projections (bottom right).

Finally, from this study we can conclude that within 1% RMS no systematic deviations are observed between the detector's counting rates and the SiMon neutron flux monitors.

4.1.2 Gain stability

The gain stability of the C_6D_6 detectors is key in order to correctly apply the PHWT. Drifts in the gain along the experiment lead to changes in the weighted count rate and thus, on the measured yield. These drifts can be due to a extremely high count rates as reported in [89], and their impact in the yield can be dramatic because of the non-linear form of the weighting function. Monitoring the gain along the experiment allows us to identify this problem.

Three radioactive sources (^{137}Cs, ^{88}Y and AmBe) were employed to calibrate the C_6D_6 detectors in deposited energy (see Sec. 4.2). Since these sources were repeatedly measured along the experiment, they are a good monitor for the gain. A systematic study is carried out comparing the deposited energy spectra of these calibration sources. Fig. 4.3 shows the deposited energy spectra from two different measurement runs of AmBe, normalized to the measurement time, and compared by a χ^2 test. A multiplicative factor is varied to produce a gain drift that matches the different spectra. Values for the χ^2 parameter are calculated depending on the applied factor. The minimum of the resulting parabola corresponds to the change in the gain.

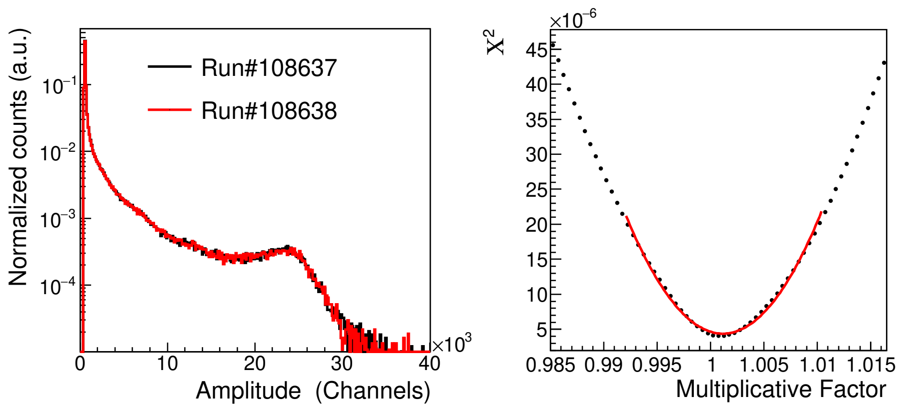

Figure 4.3: (Left panel) AmBe amplitude spectra measured with C_6D_6#2 detector in two different measurement runs. (Right panel) Result of the χ^2 test for the two spectra compared in the left panel.

Fig. 4.4 displays the multiplicative factors required to match the gain of all the C_6D_6 detectors along all measured runs with the AmBe source using as a reference the first measurement (run 108637). Almost all the observed gain shifts are within a 1%, which has been assumed as the associated systematic uncertainty due to the gain stability of C_6D_6 detectors within the ^{80}Se(n,γ) measurement.

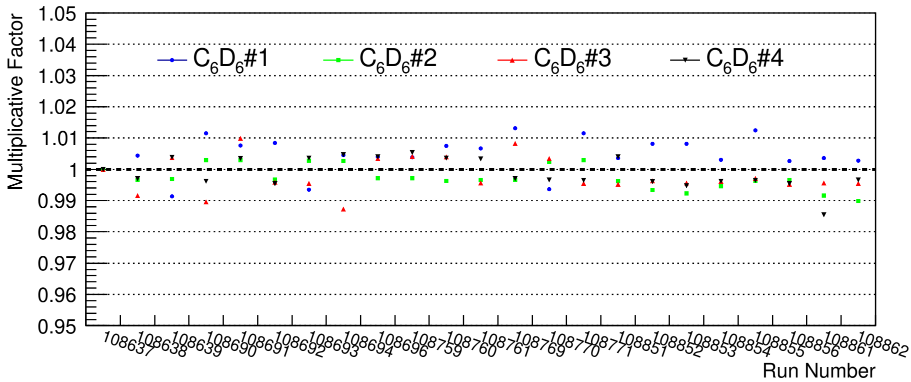

Figure 4.4: Multiplicative factors found in the χ^2 comparison of all measurement runs of AmBe.

4.2 Deposited energy and resolution calibration

As introduced in Sec. 4.1.2, the mathematical manipulation of the detector response by means of the PHWT requires an accurate energy calibration. In addition, a calibration in energy resolution is needed to find the realistic instrumental broadening, which is applied to the ideal detector response from Monte Carlo simulations in the calculation of the weighting function.

For the calibration, we use the three radioactive sources measured periodically during the experiment, ^{137}Cs, ^{88}Y and AmBe, which emit γ-rays with energies of 662 keV (^{137}Cs), 898 keV and 1836 keV (^{88}Y), and 4.438 MeV (AmBe). We also employ the deposited energy spectra from the ^{197}Au(n,γ) measurement in the calibration procedure. For the latter, a selection in ToF is applied to extract the data only from the 4.9 eV resonance of ^{197}Au(n,γ) , thus reducing the contribution of the background to a negligible level. The endpoint of the resulting deposited energy spectrum corresponds approximately to the total energy of the de-excitation cascade of 6.512 MeV [90].

Dedicated Monte Carlo simulations of the experimental setup are implemented for each calibration source (see Sec. 4.3.1 for the details). Matching the simulated and measured spectra gives us the energy calibration of the detectors. For that, the simulated spectra must be broadened by using the form

$$\sigma^2 = a_0 E + a_1 E^2 \tag{4.1}$$

The comparison between measured and simulated spectra is shown in Fig. 4.5. In the latter, the green regions designate the ranges of the energy calibration fit. As it can be seen, a very good agreement is found between measured and simulated detector responses for each source after the fitting procedure.

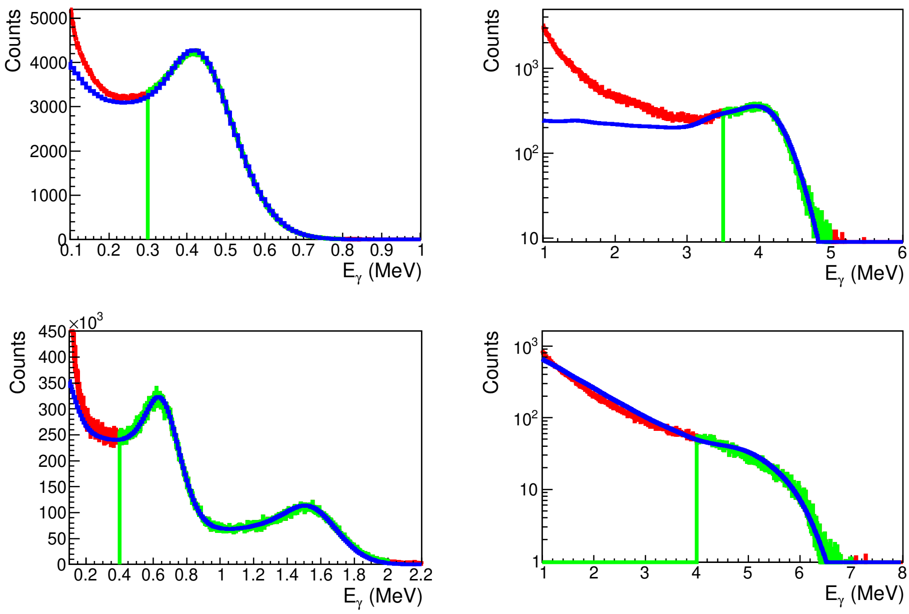

Figure 4.5: Experimental (red) and simulated (blue) deposited energy spectra for the calibration of C_6D_6#2. Sources from top to bottom and from left to right are: ^{137}Cs, ^{88}Y, AmBe and the ^{197}Au capture cascade.

Finally, each individual C_6D_6 detector is calibrated in deposited energy using linear transformations. For that, we divide the energy range into two different regions, in each of which one linear regression is fitted. Fig. 4.6 displays the calibration functions of all C_6D_6 detectors, each one composed of the two mentioned linear regressions. The experimental energy resolution obtained in this study for the C_6D_6 detectors is also included in the figure.

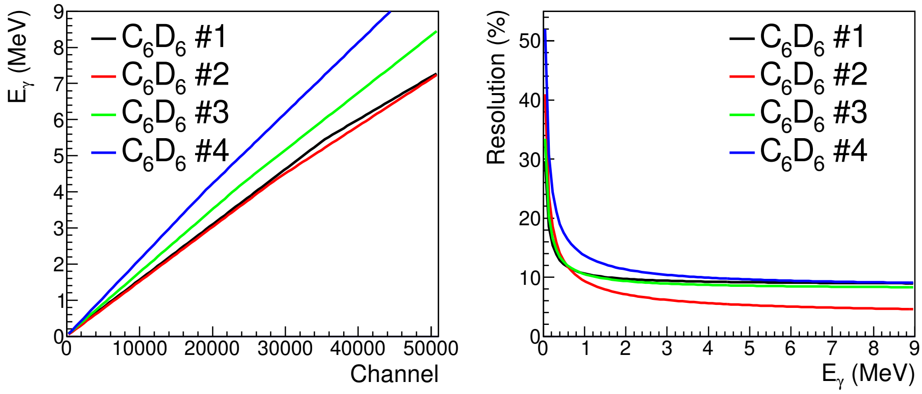

Figure 4.6: Calibration functions (left panel) and instrumental resolutions (right panel) of all C_6D_6 detectors.

4.2.1 Deposited energy thresholds

The use of a deposited energy threshold during the data analysis is mandatory to reduce the background and get rid of artifacts from the PSA routine. Part of this background comes from the ambient activity or from neutron capture events in the surrounding of the experimental setup. Nevertheless, an important part of the low-amplitude events registered by the detection system are due to the electronic noise and the low digital threshold in the digitizers.

In addition, there exist electronic rebounds that occur after some physical primary signals. To study this experimental perturbation, the differences in ToF between two consecutive signals are represented in a histogram. Fig. 4.7 shows the resulting time-difference distribution from events corresponding to the measurement of the ^{197}Au(n,γ) reaction. Two different components can be clearly distinguished: a narrow peak below 100 ns composed of so-called *prompt*-rebounds, and a wide distribution between 500 ns and 1000 ns in which *delayed*-rebounds are represented. The very different shapes of these distributions reflect the different nature of their origin. Prompt-rebounds can be explained by an impedance mismatch between the detectors and the electronic readout chain. According to the manufacturer [91], this mismatch produces a ringing in the output waveform of the photo-multiplier tubes that extends few ns after a real pulse. Since the entire electronic chain remained unaltered along the experiment, the possible mismatch have to be conserved ensuring that all rebounds appear with the same temporal difference. This is consistent with the narrow peak observed in Fig. 4.7 for the prompt component. However, this effect cannot explain the wide distribution of delayed rebounds that occurs hundreds of ns after the pulse. This issue was studied in [92] where the authors attributed it to ionization of the gas impurities by the electrons inside the photo-multiplier tube. This induces a discharge signal whose timing depends on the main pulse charge. The different timings explain the wide distribution of this delayed component shown in Fig. 4.7. The random nature of the delayed rebounds makes it not possible for the PSA to account for them.

Fig. 4.7 also displays the equivalent deposited energy distributions of the prompt and delayed rebounds. As it can be seen, both are narrow peaks that rapidly fall with the γ-ray energy. The shape of these distributions allows us to remove all the rebounds from the two components just by applying a low energy threshold in deposited energy. In the case of the example shown in the figure, a 250 keV threshold would be enough to completely remove them. After performing this study for all C_6D_6 detectors used in this experiment, the final low energy thresholds applied in the analysis are listed in Tab. 4.1.

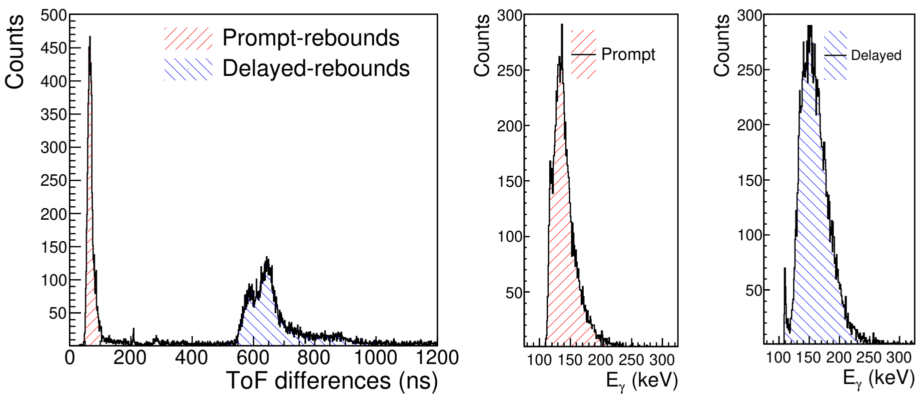

Figure 4.7: (Left panel) Distribution of the ToF differences between two consecutive signals measured using the C_6D_6#2. (Right panel) Deposited energy distributions of the prompt and delayed rebounds, respectively.

Detector	C_6D_6#1	C_6D_6#2	C_6D_6#3	C_6D_6#4
Threshold (keV)	250	250	300	350

Table 4.1: Low deposited energy thresholds in keV applied in this analysis for each single C_6D_6 detector.

The total elimination of the rebound signals is crucial to obtain an accurate ^{80}Se capture yield. Otherwise, some events can be counted twice artificially increasing the yield. This effect is observed in the neutron energy spectra of ^{80}Se(n,γ) that are shown in Fig. 4.8, where we compare the distributions obtained with low energy (zero-suppression) thresholds of $\sim$ 120 keV and high energy (analysis) thresholds of 250 - 350 keV. For the sake of clarity, both distributions are normalized to the top of the 1.47 keV resonance. As it can be seen, all the narrow resonances with the low threshold, exhibit a secondary peak attached to them. This reflects the duplication in the event counting due to the effect of rebounds. By applying the low energy thresholds listed in Tab. 4.1 this effect is completely suppressed, as it is displayed by the blue spectra. Furthermore, low energy events coming from neutrons captured in the surrounding of the experimental hall are also removed using these thresholds. This increases the resulting signal-to-background ratio, which in the case of the first resonance located at 1.47 keV corresponds to a factor of 10.

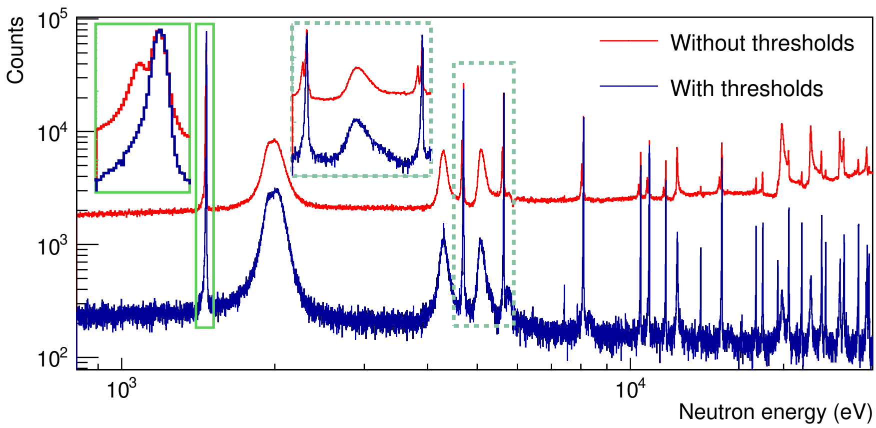

Figure 4.8: ^{80}Se(n,γ) neutron energy spectrum with low energy thresholds applied (blue line) compared to that obtained without thresholds (red line). Spectra are normalized to the top of the 1.47 keV resonance. The two zoom boxes contain details of the rebound effects (see text).

4.3 Application of the PHWT

A weighing of the C_6D_6 calibrated signals is needed to transform the C_6D_6 detector into a Total Energy Detector (see Sec. 2.2). This is achieved by using a weighting function (WF) that makes the experimental efficiency proportional to the γ-ray energy. In this section, we describe the calculation of the WF by means of Monte Carlo simulations.

Since the WF depends on the detector, experimental setup (distance to the sample and surrounding material) and sample properties, different functions are calculated for each C_6D_6 detector and for both samples ^{80}Se and ^{197}Au.

4.3.1 Monte Carlo simulations

Monte Carlo simulations are an appropriate solution to calculate the weighting function in an accurate way. They allow to simulate mono-energetic γ-rays with which to calculate the WF.

In this work, a C++ application based on the Geant4 simulation toolkit [93, 94] was developed for this purpose. The detailed implementation of the entire n_TOF bunker geometry, shown in Fig. 4.9, was taken from previous simulation works of the entire setup, which were carried out to understand the nature of different background components [75, 95]. Besides a detailed implementation of the C_6D_6 detectors geometry [96] and the sample, our code includes details on the sample exchanger used during the experiment, the BaF_2 mock TAC detector present in the experimental hall and the concrete walls that originate most of the unwanted captures of scattered neutrons. Furthermore, both the geometric details and the isotopic composition of the ^{80}Se and ^{197}Au samples are introduced in a realistic way into the model.

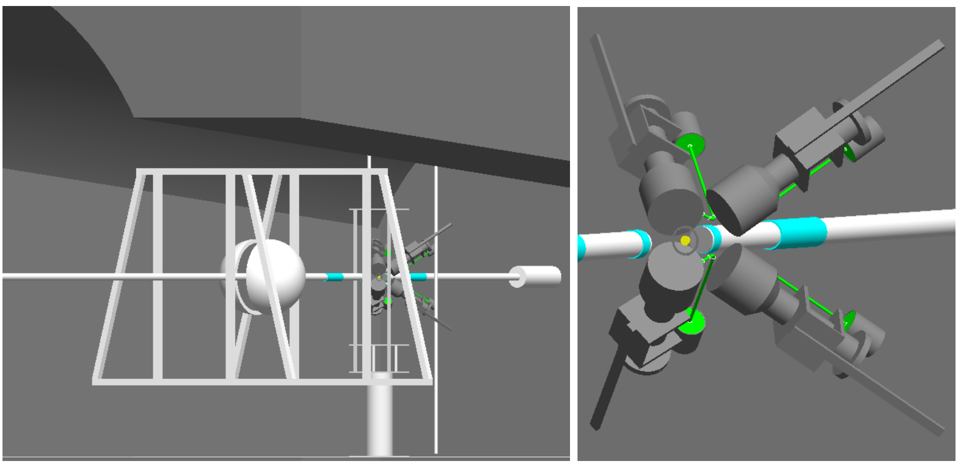

Figure 4.9: Experimental setup implemented in our C++ application based on Geant4. (Left panel) General view of the experimental hall. (Right panel) Detailed geometry of the C_6D_6 detectors and the ^{80}Se sample.

For the MC simulations, mono-energetic γ-rays with 50 different energies from 100 keV to 9 MeV were generated. This energy range is large enough to calculate the WF taking into account the 6.701 MeV neutron separation energy of ^{80}Se. Since the maximum energy with which γ-rays are simulated is 9 MeV, this upper limit establishes a high threshold beyond which the WF becomes unreliable. Ten million photons were launched for every γ-ray energy in the mentioned range. The response functions obtained were convoluted with the experimental resolution calculated in Sec. 4.2 to emulate the response of real detectors.

On the other hand, the C++ application employed for the MC simulations includes the possibility to enable the experimental *self-shielding effect*. The latter accounts for the reduction in the flux of the neutron beam along the sample thickness due to neutrons that are scattered and captured as they enter the sample. This important experimental effect depends on the geometry of the sample and the total cross section, the thicker the sample and larger the cross section, the more noticeable the effect. Fig. 4.10 shows the response functions simulated for the ^{80}Se sample configuration with this effect enabled or disabled. The reduction in counts due to the self-shielding effect is more pronounced for low energy γ-rays since they can suffer a very different attenuation depending on their spatial origin within the sample. Actually, the effect is not negligible in the two first distributions shown in Fig. 4.10 corresponding to γ-rays with energies of 200 keV and 400 keV, respectively. For that reason, in this analysis, the most realistic simulations with the self-shielding effect activated are used.

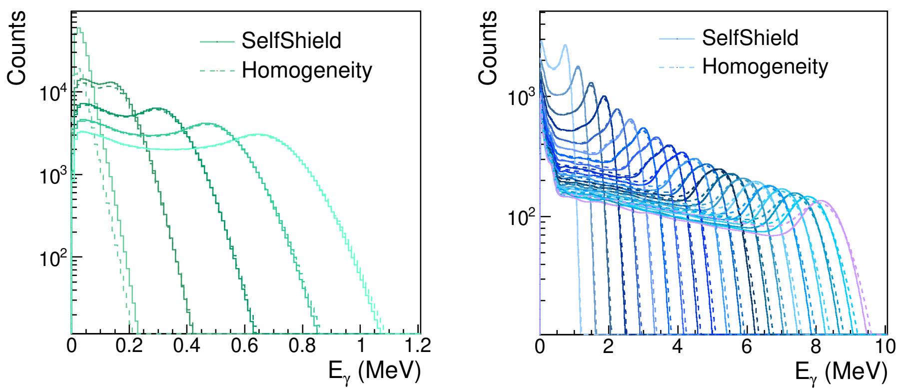

Figure 4.10: Simulated ^{80}Se response functions of the C_6D_6#2 convoluted by the experimental resolution. Emission modes are compared to different line styles (see text).

4.3.2 Weighting function calculation

In this analysis, polynomial functions of different degrees ranging between 3 and 7 were tested to describe the WF. Nevertheless, the best result[1] was obtained by

[1]The quality of the results obtained using different WFs were compared by means of the ratio expressed in Eq. 4.4 and explained below.

using a polynomial of degree $l = 6$, as that shown in Eq. 4.2

$$W_i(E_i) = \sum_{k=0}^{l} a_k E_i^k, \tag{4.2}$$

where E_i is the energy of the bin i, and a_k coefficients are determined by minimization of the Eq. 4.3. The Minuit algorithm, implemented by default in ROOT, is employed for this task.

$$\min \sum_{j}^{m} \left(\sum_{i}^{n} \sum_{k}^{l} a_k E_i^k - E_j \right)^2 \tag{4.3}$$

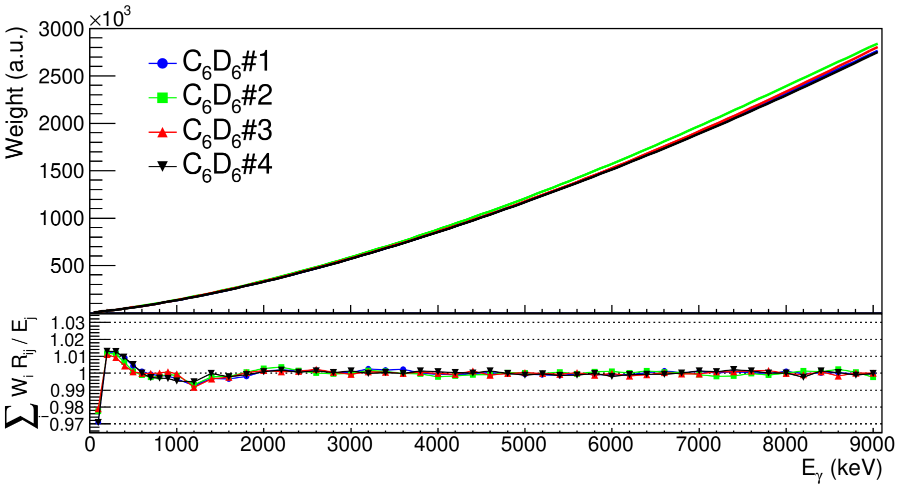

Figure 4.11: Weighting functions for the ^{80}Se sample of all C_6D_6 detectors. Ratio in the bottom panel shows the quality of the WF (see text).

The resulting polynomial functions for the ^{80}Se sample and all C_6D_6 detectors are displayed in Fig. 4.11. In the latter, WFs show a very similar smooth shape between detectors, with weights near to 3×10^6 units at 9 MeV. Special care was taken in the calculation of the WF in the high energy region. Owing to the elevated weights given by the WF in this region, an uncertainty larger than 1% can dramatically affect the final capture yield. In order to quantify the goodness of the WF, we employ the ratio of Eq. 4.4, which takes into account the proportionality condition to be fulfilled by the WF (Eq. 2.2). As it is shown in the bottom panel of Fig. 4.11, this ratio takes values below 1% for energies higher than 500 keV. On the other hand, the deviations between 1% and 3%, obtained below 500 keV, affect the capture yield to a lesser extent since the weights obtained with the WF at this energy region are several orders of magnitude lower.

$$\frac{\sum_i W_i R_{i,j}}{E_j} \tag{4.4}$$

Finally, the experimental efficiency of every C_6D_6 detector is transformed to be proportional to the energy of the detected γ-ray by applying the WF. This transformation can be appreciated in Fig. 4.12.

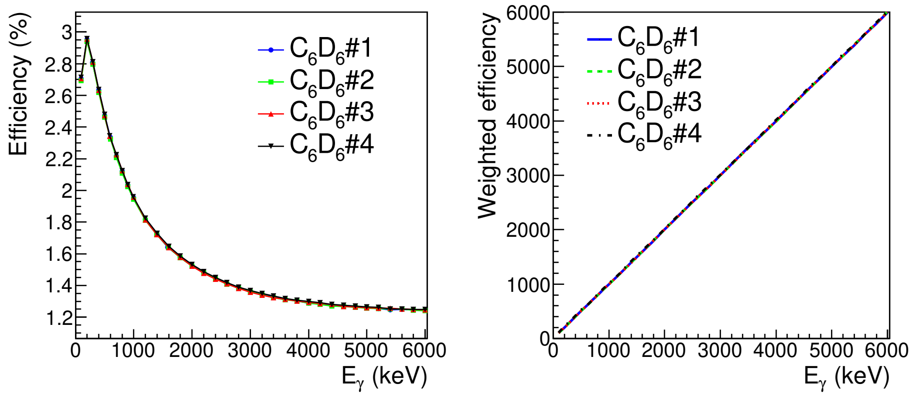

Figure 4.12: (Left panel) Simulated efficiency of the C_6D_6 detectors for the mono-energetic γ-rays generated with the ^{80}Se sample. (Right panel) Weighted efficiency proportional to the γ-ray energy.

4.3.3 Accuracy of the WF

Uncertainties in the WF are calculated by means of simulations of the γ-ray cascades emitted after the capture events. For that, the resulting deposited energy spectra from MC simulations were convoluted with the experimental resolution and weighted with the corresponding WF. Deviations of the weighted efficiency of the cascade from the neutron separation energy are a good estimation of the accuracy of the weighting procedure.

The CAPTUGENS code [97] was employed to model the radiative neutron capture cascades. This code splits the cascade into two regions. Up to a certain cutoff energy (E_{cut}), the energy levels and transition probabilities are introduced from some database because they are assumed to be known experimentally. In this study, the ENSDF database was employed for this purpose [98]. From E_{cut} up to the neutron separation energy, the code makes use of statistical models based on Level Density Parameters to build the remaining levels.

In order to determine E_{cut}, we plot the cumulative distribution of the number of known nuclear levels as a function of their energy, together with the distribution predicted by an statistical nuclear model. The approximate point in which both distributions diverge is selected as E_{cut}. Fig. 4.13 compares both distributions for the case of ^{80}Se. From this comparison, the value of $E_{cut} \approx 1.2$ MeV was chosen as the cut energy.

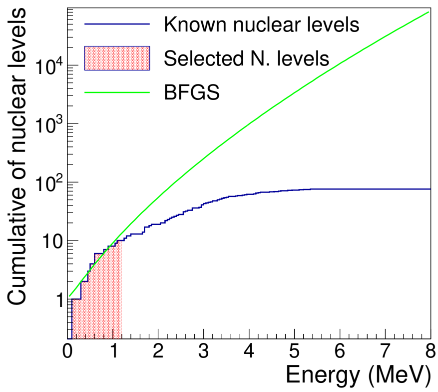

Figure 4.13: Cumulative distribution of known nuclear levels of ^{80}Se (blue line) extracted from [98], depending on their energy. Selected levels are highlighted (dashed red), and the BSFG statistical model is also included (green line).

For the analysis of ^{80}Se, two different level density models, the Constant Temperature (CT) and the Back Shifted Fermi Gas (BSFG), were compared. Their parametrizations were taken from [99]. However, in order to reproduce the experimental deposited energy spectra of ^{80}Se, the CT model had to be complemented with a contribution of the 30% of primary γ-rays with an energy corresponding to the neutron separation energy of the compound nucleus (6.701 MeV). This might indicate some nuclear structure effect that the statistical model could not take into account.

Besides the nuclear level densities, the CAPTUGENS code requires Photon Strength Functions (PSF) to populate the nuclear levels built in the previous step. For the ^{80}Se isotope, the PSF parametrizations for the two studied models, CT and BSFG, were taken from [100]. The electromagnetic transitions between the nuclear levels considered in the code are the Giant Electric Dipole Resonance (E1), the Giant Magnetic Dipole Resonance (M1), and the Giant Quadrupole Resonance (E2). In the case of the well-known ^{197}Au(n,γ) cascade, both the BSFG and the PSF parametrizations were taken from [101].

The Geant4 application introduced in Sec. 4.3.1 was used to simulate the response of the C_6D_6 detectors to the ^{197}Au(n,γ) and ^{80}Se(n,γ) cascades. The latter, generated with the two aforementioned models, are compared with the experimental spectra in Fig. 4.14. Differences in the compared deposited energy spectra are computed in the bottom panels by means of the Pearson's χ^2_P test, whose mathematical expression is given in Eq. 4.5. In order to reduce the background contribution, the experimental spectra were obtained using ToF cuts to select most intense resonance of ^{80}Se(n,γ) at 1.9 keV, where the fraction of capture events is dominant. As can be seen in the figure, each model fits well in a different region of the spectrum. A good agreement is found in the low energy region between the simulated cascade with the BSFG model and the experimental spectrum. In contrast, a better fit in the high energy region is obtained with the combined model of CT and mono-energetic γ-rays. For this reason both models are considered valid for this work.

$$\chi^2_P = \sum_i \frac{(observed_i - theoretical_i)^2}{theoretical_i} \tag{4.5}$$

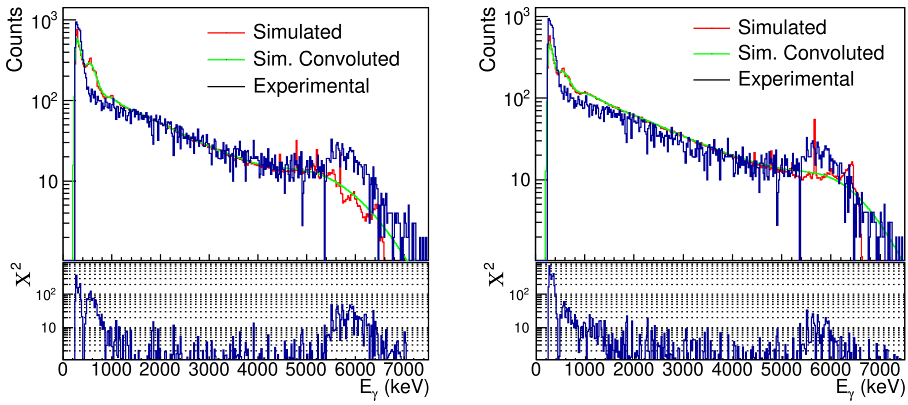

Figure 4.14: Experimental deposited energy spectrum of ^{80}Se(n,γ) with ToF selections restricted to the 1.9 keV resonance (blue line), compared to those simulated using the BSFG method (left panel) and the mixed model based on CT (right panel).

After simulating $N = 25 \times 10^6$ de-excitation cascades with total energy E_C, the ratio of the Eq. 4.6 must be equal 1. Disagreements between reality and simulations translate into a change in the value of this ratio. This change can be interpreted as the uncertainty in the WF calculation procedure. In the particular case of the ^{80}Se, since the two studied models are validated, the uncertainty is obtained as the average between the uncertainties of both models.

$$\frac{\sum_i W_i R_i^C}{N E_C} \tag{4.6}$$

Tab. 4.2 shows the ratio of Eq. 4.6 calculated for all samples and all C_6D_6 detectors. These results indicate that the uncertainties due to the WF do not reach 1% for any of the measured configurations.

Detector	C_6D_6#1	C_6D_6#2	C_6D_6#3	C_6D_6#4
^{80}Se	1.0069(21)	1.0053(21)	1.0060(21)	1.0019(20)
^{197}Au	1.0079(18)	1.0087(18)	1.0071(18)	1.0061(18)

Table 4.2: Ratio of Eq. 4.6 for all the simulated sources and C_6D_6 detectors.

4.4 ToF to neutron energy calibration

As it was introduced in Sec. 2.3, the physical observable measured in the ToF technique is the time lapse between the production of neutrons and the detection of γ-rays coming from capture reactions. From Eq. 2.8, if a neutron with mass m_n travels a distance L in a time t_{ToF}, its kinetic energy E_n is given by Eq. 4.7, where the distance is introduced in m and the time in μs to obtain E_n in eV.

$$E_n = \left(\frac{72.2977L}{t_{ToF}}\right)^2 \tag{4.7}$$

From Sec. 3.1 it is known that at the n_TOF facility neutrons are produced by means of spallation reactions for then being moderated. The $t_{Production}$ of Eq. 2.10 is then divided in two contributions that take into account these two processes,

$$t \approx t_{Spallation} + t_{Moderation} + t_{ToF}. \tag{4.8}$$

In Sec. 3.1, it was also mentioned that the BCT signal acts as a trigger that starts the clock just before the proton beam impinges on the spallation target. After the spallation reactions occur, the γ-flash travels the distance L to the experimental area at the speed of light in a time L/c. The last relation can be used to replace $t_{Spallation}$ in Eq. 4.8 by the measured arrival time of the γ-flash to the experimental area (t_γ), leading to Eq. 4.9.

$$t \approx t_\gamma - \frac{L}{c} + t_{Moderation} + t_{ToF} \tag{4.9}$$

Or solving for t_{ToF},

$$t_{ToF} \approx t - t_\gamma + \frac{L}{c} - t_{Moderation}. \tag{4.10}$$

In a first step of this analysis, the relation $t_{ToF} = t - t_\gamma$ was used for simplicity. After this preliminary result, an extra offset $t_0 = L/c - t_{Moderation}$ was added to t_{ToF} to take into account the γ-flash flight time and the neutron moderation time. Eq. 4.7 is then,

$$E_n = \left(\frac{72.2977L_0}{t_{ToF} + t_0}\right)^2. \tag{4.11}$$

Owing to the large number of available paths for neutrons in the moderation process, this time offset cannot be determined analytically. However, this time will be calculated in Sec. 4.6 by comparing the neutron flux from our experiment, reconstructed using the neutron monitors, to the evaluated version by means of a χ^2 minimization. Finally, the resulting ToF-to-energy calibration is verified using some resonances from the well-known ^{197}Au(n,γ) reaction.

4.4.1 Resolution Function

Ideally, the neutron energy should be univocally related with the ToF. However, as introduced in the previous section, neutrons present multiple moderation paths within the spallation target and the moderator. As a consequence, neutrons of the same energy can reach the experimental area at slightly different times. In addition, the proton pulses that arrive to the spallation target have a temporal width of 7 ns RMS. This widening also contributes to the fact that there is a ToF distribution for each neutron energy, and not a single value.

A distribution, known as Resolution Function (RF), is commonly employed to describe the relation between ToF and neutron energy. The RF can only be determined by means of Monte Carlo simulations, and was validated with experimental measurements of very well-known and narrow resonances located at different neutron energies [66, 71]. The RF can be described in terms of energy, ToF or flight path:

$$R_E(E_n)dE_n = R_t(t)dt = R_L(L)dL \tag{4.12}$$

To account for the effects of the RF in the width of the resonances, a numerical description of the RF distribution is introduced in the resonance analysis SAMMY code [46], as it will be explained in Sec. 5.1.1.

4.5 Background subtraction

A significant part of the γ-rays detected by C_6D_6 detectors does not come from neutrons captured in the sample under study. This contribution introduces an undesired background during the measurement, which needs to be estimated and subtracted for the yield calculation. Depending on the origin of the γ-rays, this background can be divided into different contributions:

1. Background related to the natural or induced radioactivity of the samples or the materials used in the setup. It is a very important contribution in experiments with radioactive samples.

2. Background related to the beam. Neutrons that do not interact with the sample, can be scattered and captured in the materials placed at the experimental hall. This component also includes the contribution of the γ-rays in the beam that do not interact with the sample but are scattered by the experimental setup.

3. Background related to the sample and caused by neutron captures elsewhere. Some neutrons in the flux are scattered by the sample itself before being captured in the surroundings experimental area.

4. Background related to the sample and caused by γ-rays present in the beam. Some in-beam γ-rays are scattered in the sample before being detected.

Hence, there are two contributions independent from the employed sample and two other sample-dependants.

^{80}Se is a stable isotope. As a consequence, the background contribution explained in the first point has a negligible impact in our analysis. On the other hand, the background related to the beam is expected to be one of the most important contributions to the total background. Additionally, the component explained in the third point could be particularly decisive in this experiment due to the thick sample used (see Sec. 3.2.2) and the large ratio between elastic and capture cross sections for ^{80}Se(n,γ), which ranges from 10^2 and 10^3 in the energy range of interest in this work [45].

In order to disentangle these background components, several ancillary measurements were performed by using some of the samples and configurations explained in Sec. 3.2.2:

- **Beam-off**: in this configuration with the neutron beam disabled, the C_6D_6 detectors recorded signals from natural and induced radioactivity of the experimental hall.

- **Dummy**: the measurement of the empty holder was employed to determine the neutron background related to the beam.

- **Lead sample**: the ^{nat}Pb sample was measured to estimate the background related to the presence of the sample itself. Given the small capture cross section of ^{208}Pb, this sample can be considered as a perfect neutron disperser, with only a few resonances. Moreover, the large atomic number Z and density of lead also result in a high γ-ray scattering probability.

- **^{80}Se using filters**: the measurements carried out by using neutron absorbing filters are employed to scale the sample-dependent background related to in-beam γ-rays by using the black filter method [81], as it will be explained below.

A clean neutron energy spectrum for the ^{80}Se(n,γ) yield with the background subtracted can be obtained using a combination of the aforementioned measurements. The two sample-independent contributions can be directly subtracted by using the beam-off and the dummy measurements scaled accordingly. However, the other two components related to the sample cannot be calculated from direct measurements. In these cases, the procedure explained bellow is followed.

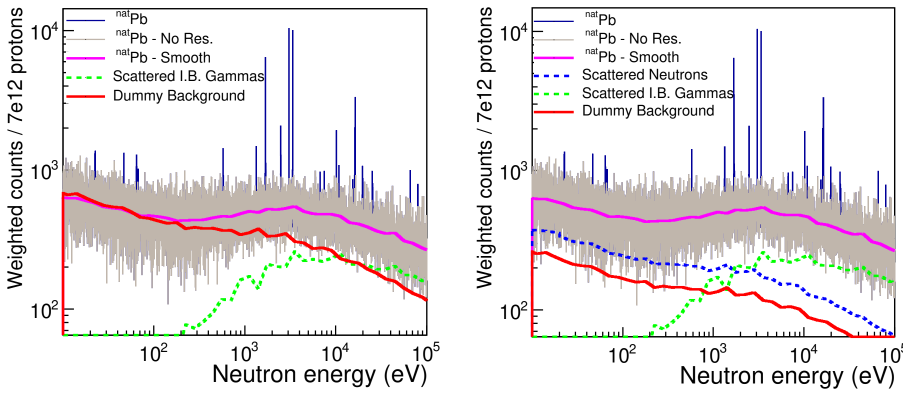

Figure 4.15: ^{nat}Pb(n,γ) neutron energy spectrum measured with C_6D_6#2 in blue. All resonances are removed to obtain the grey spectrum, and then smoothed to provide the pink distribution. (Left panel) The neutron energy spectrum of the dummy sample (red line) is scaled to determine the background related to γ-rays scattered on the sample (dashed green line). (Right panel) The dummy spectrum is re-scaled to calculate the contribution from neutrons scattered by the sample.

1. The ambient background is subtracted. This contribution, determined from the beam-off runs, is normalized to the measurement time and subtracted from the ^{80}Se(n,γ) and ^{nat}Pb(n,γ) neutron energy spectra. Fig. 4.15 shows the ^{nat}Pb(n,γ) spectra, with the ambient background subtracted, scaled to the number of protons per pulse. The capture resonances of lead isotopes are removed as illustrated in the same figure, and the resulting histogram is smoothed to remove statistical fluctuations.

2. The spectrum corresponding to in-beam γ-rays scattered in the sample is determined. From Monte Carlo simulations [66, 71], it is known that in-beam γ-rays arrive to the experimental in a ToF window which corresponds to neutron energies above $\sim$ 20 eV (see Sec. 3.1.1). For that reason, the remaining background contribution below that energy is ascribed to neutron interactions. It is precisely in this energy range in which the dummy neutron energy spectrum is scaled to the ^{nat}Pb one, as shown in the left panel of Fig. 4.15. Differences at higher energies are due to the in beam γ-rays scattered in the sample. Therefore, the latter contribution is found by subtracting these two spectra.

3. The background due to neutrons scattered in the sample and subsequently captured in the surroundings is determined, as it can be seen in Fig. 4.15. To this aim, the component related to the in-beam γ-rays scattered in the

sample, obtained in the previous step, is subtracted from the ^{nat}Pb(n,γ) neutron energy spectra. Last, the contribution of the dummy, scaled to the number of protons per pulse, is subtracted from the ^{nat}Pb(n,γ) spectra as well.

Since the two sample-dependent background components are determined with respect to the ^{nat}Pb sample, a scale factor is needed to account for the difference in scattering cross section and sample thickness between ^{80}Se and ^{nat}Pb samples.

The background component related to neutrons scattered in the sample is scaled using the factor of Eq. 4.13. In the latter, n_X are the areal densities of the samples and σ_{el}^{X} the elastic cross sections of the different isotopes. Since neutrons can suffer several dispersions before being captured in the surroundings of the experimental hall, their reconstructed energies are under-estimated. Thus, it has no sense to calculate this scale factor for each neutron energy. For that reason, the averaged value for the elastic cross section up to 10 eV is selected for each isotope.

$$F_n = \frac{n_{Se}}{n_{Pb}} \frac{\sigma_{el}^{Se}}{\sigma_{el}^{Pb}} \tag{4.13}$$

On the other hand, Monte Carlo simulations of the ^{80}Se and ^{nat}Pb samples were carried out to estimate the scale factor for the background component related to in-beam γ-rays. To this aim, the response of the C_6D_6 detectors to the in-beam γ-rays [71] impinging on both samples was simulated with the same code than in Sec. 4.3.1. Furthermore, a complementary calculation of this factor was performed by applying the black filter method [81] introduced in Sec. 3.2.2. This methodology assumes that the neutron flux at certain energies is almost zero because of the absorption in the filters. At these particular neutron energies, the only contribution is that from in-beam γ-rays. It is in these regions where this component of the background can be scaled.

Tab. 4.3 shows the resulting value for F_n and those calculated for F_γ by using the methods explained above. Both MC simulations and the black filter method give values with less than 5% difference. For the final background subtraction carried out in this analysis, the average value is used.

F_n	F_γ	
	MC simulations	Black filter method
0.649	0.147	0.154

Table 4.3: Scale factors F_n and F_γ calculated in this work.

Finally, Fig. 4.16 shows the weighted neutron energy spectra of the ^{80}Se(n,γ) reaction with all background contributions except the environmental background, which was previously subtracted as mentioned above. The resulting total background matches with the valleys of the resonances in almost all the entire energy range. However, there are some discrepancies specially at high neutron energies due to the complexity of the background subtraction process.

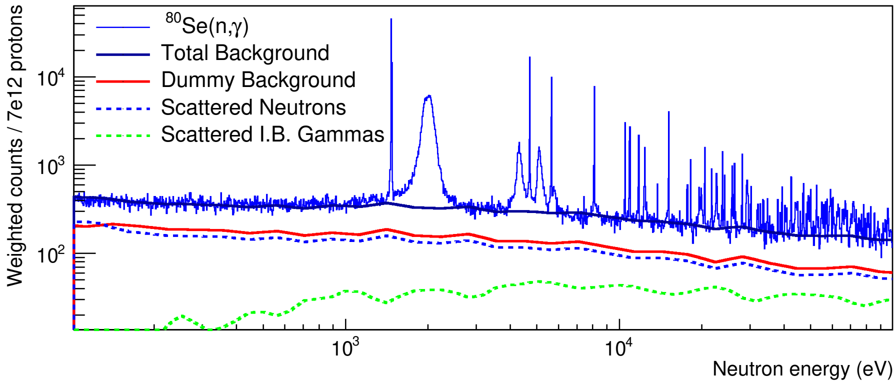

Figure 4.16: Neutron energy spectrum of the ^{80}Se(n,γ) reaction together with all individual background contributions except the already subtracted ambient component.

One possible source of the discrepancies between the total background and the ^{80}Se(n,γ) spectrum, at the high energy region, is the consideration of the lead sample as a perfect neutron scatter. The neutron capture cross sections of some lead isotopes exhibit large resonances, especially in this energy region. The observed discrepancy may be therefore ascribed to the increasing radiative capture contribution of ^{204,206,207}Pb in the $\sim$10-100 keV neutron energy range, where a significant portion of γ-radiation is emitted from the lead sample itself during the background measurement. An alternative method based on MC simulations is presented in [95] to overcome this limitation. Nevertheless, the total background obtained in this study was considered sufficiently accurate and no further effort was made in this respect. In addition, the small remaining residual background was adjusted with the SAMMY code during the resonance analysis, thereby minimizing the possible contribution of the background subtraction to the overall uncertainty budget.

Finally, the impact of the background subtraction on the uncertainty of the final resonance parameter is of $< 2\%$, as it will be shown later in Sec. 5.1.2.

4.6 Neutron flux

The yield is defined as the ratio between the neutrons undergoing radiative capture in the sample and the total number of available neutrons for a certain neutron energy interval. To calculate this ratio, the total amount of neutrons per pulse contained in the beam and their ToF distribution must be known. Nonetheless, in this analysis the yield is normalized by means of the saturated resonance method that will be explained in Sec. 4.7.1. For that reason, only the dependence of the flux with the neutron energy is required to extract the energy differential neutron capture yield, and not the absolute number of neutrons.

Several measurements were developed at n_TOF to evaluate the neutron flux. They were carried out by using different detection systems to keep under control the systematic uncertainties in a large neutron energy range [69]. However, as explained Sec. 3.1.2, the amount of ^{10}B in the moderator circuit varies from one campaign to another because of the chemical interactions of the different elements. Since the neutron absorption cross section of ^{10}B is proportional to $1/\sqrt{E_n}$, a difference is expected between our flux and the evaluated version only in the low neutron energy region. On the contrary, at high neutron energies the flux is expected to remain almost unaltered due to the low absorption cross section of ^{10}B in this energy region.

In order to determine the change in the flux at thermal energies, the count rate registered by the SiMon detectors is compared to the count rate expected from the evaluated version of the flux ($\phi_n(E_n)$). This contribution is determined by using Eq. 4.14, in which $\sigma_\alpha(E_n)$ is the cross section of the reaction ^{6}Li(n,α)^{3}H and n the areal density of the ^{6}Li foils in the SiMon detectors. Owing to the thin foils of ^{6}Li employed by these detectors, this expression is obtained without taking into account the multiple scattering contributions and using the thin target approximation.

$$C(E_n) = \varepsilon_\alpha(E_n) n \sigma_\alpha(E_n) \phi_n(E_n) \tag{4.14}$$

The detection efficiency $\varepsilon_\alpha(E_n)$ is considered constant and used as a scale factor to match both distributions, the measured count rate and the expected one, in the energy region between 100 eV and 1 keV. Above 1 keV, these distributions cannot be compared since the efficiency of the SiMon detector change due to a variation in the angular distribution of the tritium particles [74]. On the other hand, the ratio between these distributions at energies below 100 eV is the correction needed to obtain the version of the flux that is used in this analysis. Fig. 4.17 shows the measured distribution normalized to the expected one, as well as their ratio in the aforementioned energy region.

The ratio shown in Fig. 4.17 is applied to the evaluated version of the neutron flux to obtain the neutron energy spectrum of the neutron flux available in our measurement. Both the evaluated and modified versions of the neutron flux are displayed in Fig. 4.18. As it can be appreciated, these spectra are equivalent for neutron energies beyond 100 eV. Below this point, the expected reduction of the spectra due to the change in ^{10}B is noticeable. In fact, the numerical comparison given in Tab. 4.4 displays a 4% reduction of the integral neutron flux in the 0.01 to 100 eV neutron energy range. Given the amount of counts registered by the SiMon

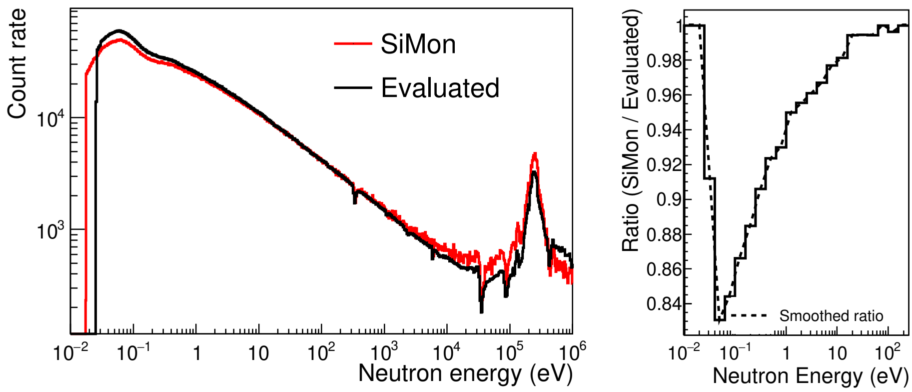

Figure 4.17: (Left panel) Experimental count rate of SiMon detector (red line) compared to the theoretically expected distribution from the evaluated flux (black line). (Right panel) Ratio of the previous two distributions.

during the measurement, the uncertainty related to this correction is negligible compared to the systematic errors listed in Tab. 4.4, which were determined in the measurement of the evaluated version [69].

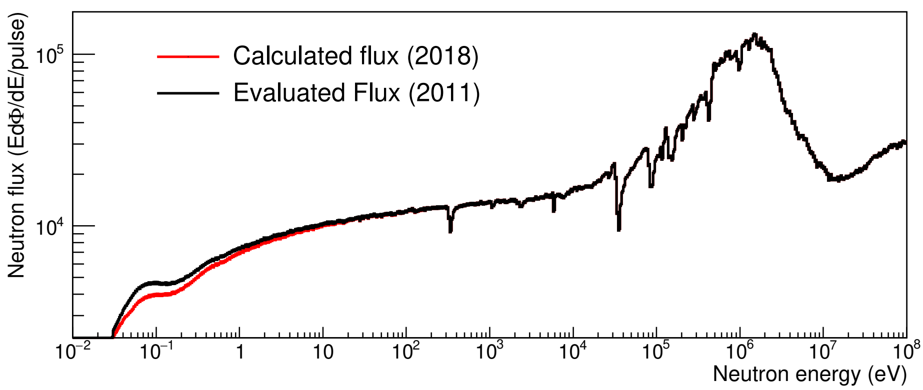

Figure 4.18: Neutron energy spectrum of the evaluated version of the flux at n_TOF EAR1 (black line), compared to that calculated for this analysis (red).

Finally, as it was mentioned in Sec. 4.4, the t_0 offset (see Eq. 4.11) was calculated in order to match, in terms of neutron energy distribution, the measured count rate with the expected one from the evaluated version of the flux. The latter was taken

Energy range	Evaluated (2011) (n/pulse)	This Work (2018) (n/pulse)	Uncertainty (%)
10 meV - 100 eV	$6.4 \cdot 10^4$	$6.1 \cdot 10^4$	1
100 eV - 100 keV	$10.7 \cdot 10^4$	$10.7 \cdot 10^4$	2 - 5
100 keV - 1 GeV	$39.9 \cdot 10^4$	$39.9 \cdot 10^4$	2 - 3

Table 4.4: Number of neutrons per pulse integrated for different energy ranges of the evaluated version of the flux and the corrected one. Systematic uncertainties are given by the neutron flux evaluation [69].

as a reference whereas the neutron energy spectra, from the experimental count rate of the SiMon detectors, were obtained by varying t_0. A χ^2 minimization was performed to ensure the best match between the experimental and theoretical distributions. The dips present in these spectra at several energies facilitated the task. Following this procedure, the best match was found for the value $t_0 = 650$ ns.

4.7 Capture yield calculation

By definition, the capture yield Y represents the fraction of incoming neutrons N_n in the beam that are captured in the sample and is theoretically related to the capture cross section by Eq. 1.2. Experimentally, it is calculated as a function of the neutron energy by means of Eq. 4.15, where N is the number of background-subtracted counts, ε the detection efficiency, and $N_n(E_n)$ corresponds to neutron energy distribution of the corrected flux that was calculated in Sec. 4.6.

$$Y(E_n) = \frac{N(E_n, E_{dep})}{N_n(E_n)\varepsilon(E_{dep})} \tag{4.15}$$

As explained in Sec. 2.1.2, the detection efficiency must be proportional to the energy deposited by the detected γ-ray in order to apply the TED technique. To apply such methodology using C_6D_6 detectors, the PWHT (see Sec. 2.2) was applied to the capture yield by means of the weighting functions calculated in Sec. 4.3. The resulting expression for the neutron capture yield is

$$Y(E_n) = \frac{N^w(E_n)}{N_n(E_n)E_C(E_n)}, \tag{4.16}$$

where $E_C = S_n + \frac{A}{A+1}E_n$ is the energy of the entire cascade. Some correction factors will be calculated in Sec. 4.7.2 to take into account possible experimental effects that affect the detection efficiency and therefore the determined yield.

4.7.1 Saturated resonance method

An absolute normalization to a well known value of the yield in a reference sample is needed to cancel out possible systematic uncertainties in the PHWT due to incertitudes or biases in the Monte Carlo modeling of the experimental setup. Otherwise, differences in detection efficiency between reality and simulation are transferred to the yield by means of the weighting function. For that reason, the saturated resonance method [102] is applied. As mentioned in Sec. 4.6, this method also removes the uncertainty in the absolute value of the flux. Last, it also cancels out any possible miss-alignment of the sample.

The selected sample of reference must have the same diameter to intercept the same fraction of the beam as the sample under study. Also the setup and the energy distribution of the neutron flux have to be the same. These conditions allow us to compare the yield measured with the two samples without applying any correction.

For the reference sample, it is important to select an isotope with a very well known neutron capture resonance featuring a large neutron capture cross section and very dominant over other reaction channels such as scattering. The first condition allows to fit the capture yield of the selected resonance by using the parameters included in databases. Thanks to the second condition, all neutrons in the beam are captured at a certain neutron energy keeping the yield really close to 1 despite using a thin sample. Actually, a thin sample is necessary to avoid thickness effects, such as self-shielding and multiple scattering, and sample-dependent backgrounds.

The ^{197}Au sample with 6.27×10^{-4} at/barn thickness, introduced in Sec. 3.2.2, was measured as a reference. For the normalization, the 4.9 eV resonance of the ^{197}Au(n,γ) reaction, shown in the Fig. 4.19, was selected. In addition to being a very well known resonance, it fulfills the condition of the large capture cross section compared to the rest of contributions. In fact, all 4.9 eV neutrons that go through the sample are captured. The shape of this resonance exhibits a kind of plateau at the top which indicates that it is saturated. It is in this region where we can determine the normalization factor of our yield that accounts for the aforementioned experimental effects.

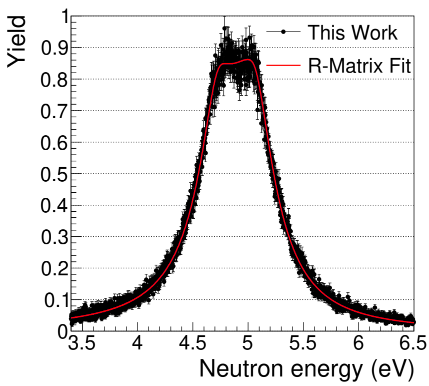

Figure 4.19: 4.9 eV resonance of the ^{197}Au(n,γ) reaction measured with C_6D_6#2 (black points) together with the R-Matrix fit performed with SAMMY (red line).

Fig. 4.19 includes the R-Matrix fit performed with SAMMY by using the resonance parameters from the ENDF/B-VIII data base [45]. A normalization constant A is obtained after this fit. Since this resonance is very well-known in the literature, deviations of this parameter A from unity give an estimation of the corrected systematic bias. The correction factor to apply to the yield is the inverse,

$$f_{sat} = 1/A. \tag{4.17}$$

The final correction factors f_{sat} for all C_6D_6 detectors are listed in Tab. 4.5. The deviation of 21% for detector #3 is the largest one found. This large value can be ascribed to differences in the simulated geometry such as the distance from this detector to the sample, its inclination or most probably the fraction of detection volume filled with C_6D_6. On the contrary, a deviation of only 2% is found for the C_6D_6#1, which corresponds to an accurate simulation of this detector.

Detector	C_6D_6#1	C_6D_6#2	C_6D_6#3	C_6D_6#4
f_{sat}	1.029(4)	1.146(5)	1.210(6)	1.119(5)

Table 4.5: Factors from the saturated resonance method obtained for all C_6D_6 detectors.

4.7.2 Yield correction factors

In addition to the effects included in the normalization of the neutron capture yield, studied in the previous section Sec. 4.7.1, other experimental corrections have to be taken into account. The most relevant ones, hence accounted in this work, are listed below:

- **Deposited energy threshold.** The application of this threshold during the data analysis avoids the registration of the lower amplitude signals, such as the electrical rebounds signals studied in Sec. 4.2.1. The associated reduction of the count rate has an effect on the yield calculation. Experimentally, the emitted γ-rays depositing an energy below the threshold cannot be detected, thus artificially reducing the yield.

- **Summing.** The TED technique allows to count only one γ-ray per de-excitation cascade and detector. However, the size and efficiency of the C_6D_6 detectors used make it possible to detect two or more γ-rays in coincidence from the same cascade by introducing a systematic error in the yield associated to the non-linear WF.

- **Conversion electrons.** In few nuclear transitions that take place after a neutron capture event an electron can be emitted instead of a low energy γ-ray. The electron is stopped inside the sample and this process leads to the generation of X-rays. This radiation most of the time does not reach the detector, with the consequent error in the yield.

- **Other corrections** such as dead time and pile-up effects will be discussed at the end of this section.

All these experimental effects, except for the dead time and pile-up, were studied via Monte Carlo simulations. We simulated N $= 25 \times 10^6$ de-excitation cascades in two different series. One taking into account the aforementioned experimental effects and another one without them. For that, the CAPTUGENS code and the simulated setup introduced in section Sec. 4.3.1 were employed.

The individual effects listed above are combined in the single correction factor of Eq. 4.18. In this equation, $R^{C,seq}$ is the response of the C_6D_6 detector to the N simulated cascades, in which individual γ-rays were generated one by one in a sequentially way to avoid the summing effect. Conversion electrons were not simulated for this contribution. This is compared to the response of these detectors R^C to N simulated cascades where the conversion electrons and the γ-ray cascades were generated simultaneously. Unlike the previous contribution, the low deposited energy thresholds is employed to account for its effect.

$$f_{th,s,ce} = \frac{\sum_{i=0}^{\infty} W_i R_i^{C,seq}}{\sum_{i=th}^{\infty} W_i R_i^{C}} \tag{4.18}$$

Since the same number of cascades were simulated in each case, deviations of $f_{th,s,ce}$ from unity give a measurement of the uncertainty introduced by the experimental effects explained above. Since the saturated resonance method was applied for the normalization of the yield, the correction factor must be calculated for both ^{80}Se and ^{197}Au samples. Thus, the final correction factor F to apply to the capture yield is

$$F = f_{sat} \frac{f_{th,s,ce}^{Se}}{f_{th,s,ce}^{Au}}. \tag{4.19}$$

After including the correction factors in Eq. 4.16, the final corrected yield Y^c is calculated with the equation Eq. 4.20.

$$Y^c(E_n) = F \frac{N^w(E_n)}{N_n(E_n) E_C(E_n)} \tag{4.20}$$

Tab. 4.6 shows the correction factors for ^{80}Se and ^{197}Au, as well as the final factor F for all C_6D_6 detectors.

As it can be appreciated from Tab. 4.6, neglecting these corrections would lead to a bias in the capture yield of up to 16%, which is remarkably larger than the uncertainty of about 2% ascribed to the PHWT itself [63].

The experimental effects studied in this section suppose the most important corrections since they significantly affect to the yield. Another experimental

Detector	f_{sat}	$f_{th,s,ce}^{Au}$	$f_{th,s,ce}^{Se}$	F
C_6D_6#1	1.029(4)	1.071(4)	1.023(9)	0.983(12)
C_6D_6#2	1.146(5)	1.069(4)	1.019(9)	1.093(13)
C_6D_6#3	1.210(6)	1.080(4)	1.033(9)	1.157(14)
C_6D_6#4	1.119(5)	1.093(4)	1.043(9)	1.068(13)

Table 4.6: Factors for all C_6D_6 detectors to correct for some experimental effects of the measured yield

correction, that affects capture yield to a lesser extent, is related to the neutron sensitivity. This will be analyzed for each individual resonance in Sec. 5.1.2. Finally, the *pileup*[2] effect, which could lead to a relevant correction in conditions of high count rates. In this work, a high count rate situation was achieved in the measurement of the 4.9 eV resonance of ^{197}Au(n,γ), due to its large capture cross section. The combination with the same ^{197}Au sample, the same neutron flux and the same C_6D_6 detectors were studied in several previous works [103, 87]. The conclusion is that the pileup is negligible in C_6D_6 detectors measuring that resonance with that sample. Therefore, pileup effects can be considered negligible in the present analysis work.

[2]The pile up takes place when two γ-rays arrive to a detector in a time τ for which the PSA cannot separate the associated signals in two different pulses. This results in a loss of counts and the recording of wrong amplitude signals.

Chapter 5

^{80}Se capture cross section and stellar MACS

After completing the analysis detailed in Chapter 4, the neutron energy distribution of the ^{80}Se(n,γ) yield is obtained, between 1 eV and 100 keV, for each individual C_6D_6 detector used. Once these individual contributions are corrected using the factors calculated in Sec. 4.7.2, they can be added to the final neutron capture yield. Fig. 5.1 shows the fragment of this yield that contains resonances. In this chapter, all these resonances are analyzed to determine the energy differential neutron capture cross section of ^{80}Se, and its MACS at different kT stellar temperatures.

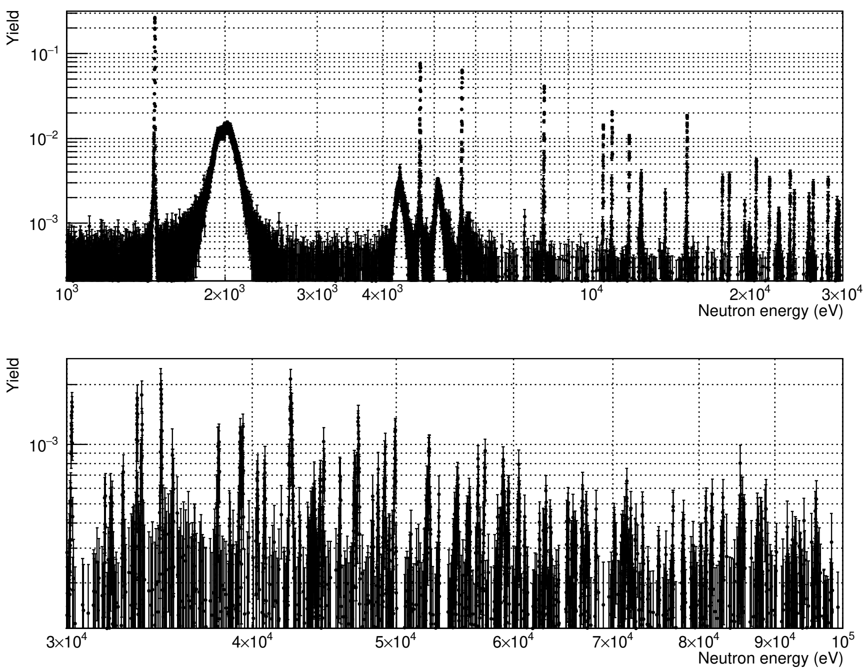

Figure 5.1: ^{80}Se(n,γ) yield reaction measured in this work from 1 keV to 100 keV.

5.1 R-matrix analysis

5.1.1 The SAMMY code

The neutron capture yield shown in Fig. 5.1 is introduced as input to SAMMY [46], which was developed in 1980 for analysis of neutron-induced cross section data at the Oak Ridge Electron Linear Accelerator. This code is based on the R-matrix theory which gives a phenomenological description of the neutron induced reactions (see Sec. 1.2). SAMMY performs a Bayesian fit to the experimental data, using an initial set of R-matrix resonance parameters. By default, the recommended Reich-Moore approximation is selected, and it is applied to this work. Nevertheless, other approximations as single-level and multilevel Breit Wigner (SLBW and MLBW) are also provided for historical reasons. Additionally, SAMMY includes the reaction channels involving charged particles as a byproduct of the nuclear reaction such as (n,p), (n,α) and (n,f).

On the other hand, some experimental effects can be introduced in SAMMY in order to take into account their contributions in the experimental yield:

- Resolution broadening: it accounts for variations in the measured time of flight of neutrons with the same kinetic energy due to experimental effects, the so-called resolution function of the facility. As it was explained in Sec. 4.4.1, a numerical representation of the resolution function (RF) coming from MC simulations [71] is used in this work for this purpose.

- Self-shielding and multiple scattering: SAMMY calculates the experimental yield as the sum of three terms:

$$Y = Y_0 + Y_1 + Y_{ms}. \tag{5.1}$$

  First term Y_0 corresponds to the yield of neutrons captured in the sample without undergoing any previous scattering. This term includes the self-shielding correction, which can affect the yield depending on the total neutron cross section and the sample thickness. As introduced in Sec. 4.3.1, this effect accounts for the decrease in the observed neutron capture cross section due to the reduction of the beam intensity in the sample along the propagation axis. Thus, Y_0 is calculated analytically using the sample thickness and the total and capture neutron cross sections of the studied nucleus (see Eq. 1.2). The sample properties are also employed by SAMMY to calculate the second term Y_1, which is related to neutrons undergoing a single-scattering before being captured. Finally, Y_{ms} represents the contribution of neutrons that are scattered two or more times before being captured in the sample. Unlike Y_0 and Y_1, SAMMY makes some severe approximations to calculate this contribution by reducing the computational cost. The scattering correction terms Y_1 and Y_{ms} lead to an increase in the observed capture yield.

- Residual background: the background components accounted in this work were carefully subtracted, as presented in Sec. 4.5. However, a small residual background is still present due to small differences between the total ^{80}Se counts and the estimated background components. The analytical form presented in Eq. 5.2 is implemented in SAMMY to take into account these differences into a residual background. Parameters from B_0 to B_4 can be fitted on the experimental data to model it.

$$B = B_0 + B_1/\sqrt{E} + B_2 \cdot \sqrt{E} + B_3 \cdot e^{-B_4 \cdot \sqrt{E}} \tag{5.2}$$

  In this work, this equation is fitted in the neutron energy regions near to the individual analyzed resonances. More details will be given in Sec. 5.1.2.

- Doppler broadening: the thermal motion of the nuclei in the sample produces a broadening of the nuclear resonances. Despite this effect has a low impact in the energy range studied in this work, this broadening is included in the analysis with SAMMY. The latter employs by default the widely used Free Gas Model (FGM) [104], which is applied in this analysis.

The input data is introduced in SAMMY by means of different files. One of these files contains information about the analyzed nucleus such as its atomic mass or the spin-group definitions. In these definitions, a group number is assigned to every combination of angular moment l and spin J of the target nucleus. Additionally, this file includes information such as sample thickness or temperature to account for the experimental effects listed above. The RF is introduced using an auxiliary file. On the other hand, the spin group number of each resonance, as well as its energy (E_0), and neutron (Γ_n) and gamma widths (Γ_γ) are included in an additional parameter file. Also the parametrization of the residual background is included there. Finally, the experimental capture yield data and its uncertainty are provided in a separate input file.

After the fitting procedure, SAMMY provides several output files containing different results. In one of these files, the resulting resonance parameters are listed together with the parametrization of the residual background. As explained in Sec. 1.1, SAMMY can compute the neutron capture cross section by using these resonance parameters and the information related to the experimental conditions listed above. With this option enabled, the neutron capture cross section is provided in another output file. Moreover, SAMMY includes calculation of the Maxwellian Averaged Cross Section (MACS). As explained in Sec. 0.1.1, this is a relevant input for astrophysical calculations, which is calculated by averaging the reconstructed cross section in a Maxwellian neutron spectrum at a certain kT temperature. Although an expression for the MACS was already provided (Eq. 2), more details on this magnitude and its calculation will be given in Sec. 5.2.

5.1.2 Resonance Analysis

Preliminary discussion

In this section, the results on the resonance analysis carried out with SAMMY within the energy range of astrophysical interest between 1 eV and 100 keV are provided. To this aim, we divided the yield into neutron energy regions that we call energy sections, which were analyzed individually. From 1 eV up to 30 keV, most of the resonances were studied isolated within their corresponding energy section. The observed level spacing between resonances allows energy sections to be selected to study those resonances individually. From that energy on, the increasing level density coupled with the limited experimental resolution make it more convenient to analyze neutron energy sections containing several resonances. The fitting procedure is carried out in several steps:

1. Firstly, Eq. 5.2 is fitted as the residual background in the neutron energy section under study. Details on this procedure can be found in the following section.

2. The residuals are calculated in sigma units and shown in a secondary panel, as can be seen for example in Fig. 5.5. The energy regions that contain more than two consecutive points with residuals over 2σ are treated as resonances. As it can be appreciated in the figure, the binning is sufficient to apply this statistical criterion.

3. In order to fit the experimental capture yield using SAMMY, initial parameters are extracted from the ENDF/B-VIII.0 [45] database when available. Otherwise a preliminar fit to the experimental data is performed to find that initial set. Resonance energy E_0 is also obtained at this point. The final values for the resonance parameters are found in a χ^2 minimization study where values for Γ_γ and Γ_n parameters are systematically tested in a series of Monte Carlo SAMMY runs. For each pair of Γ_γ and Γ_n values, the reduced chi squared is calculated as in Eq. 5.3.

$$\chi^2 = \left(\frac{1}{N} \sum_i^N \frac{(x_i - T_i)^2}{\sigma_i^2} \right)^{1/2} \tag{5.3}$$

   As a result, a chi-squared surface is obtained as it is shown in the right panel of Fig. 5.5. The minimum of the χ^2 surface corresponds to the best combination of Γ_γ and Γ_n values.

4. Regarding the spin group, the evaluated value is used when available. Otherwise, the spin group 1 is chosen by default, corresponding to s-wave resonances, except in a few cases in which the sensitivity of our fit makes it possible to propose a spin-parity change. These cases are discussed in detail bellow.

The χ^2 study explained in point 3 is systematically performed for all isolated resonances. When more than one resonance is found in an energy section, the χ^2 minimization is not carried out. Instead, the parameters of all resonances within this energy range are varied at the same time in a loop of fits that ends when variations in all parameters studied are below 1%.

The experimental yield from this work, fitted following this procedure, will be shown in the following sections compared to JEFF-3.3 [44] and ENDF/B-VIII.0 [45] evaluated libraries. In these sections, the resonance parameters Γ_γ and Γ_n will be compared to data coming from a transmission measurement performed by Novoselov et al. [49], and measurements reported by Mughabghab [50]. The latter contains most of the resonances present at the aforementioned ENDF/B-VIII.0 library. All the resonance parameters obtained in this work are compiled in Appendix A.

Residual Background

As introduced in the previous section, SAMMY can fit the small residual background remaining in the experimental data by using Eq. 5.2. Fig. 5.2 shows the resulting residual background adjusted for each of the energy sections that enclose the studied isolated resonances or groups of resonances along the whole analyzed range. The global fit included in the figure, over the entire studied energy range, exhibits an approximately constant value of -1×10^{-4} with a relative high dispersion from -2.5×10^{-4} to -5×10^{-5} in yield units. Nevertheless, it does not show a noticeable trend with the neutron energy, indicating the accurate determination of the neutron energy dependence of the background.

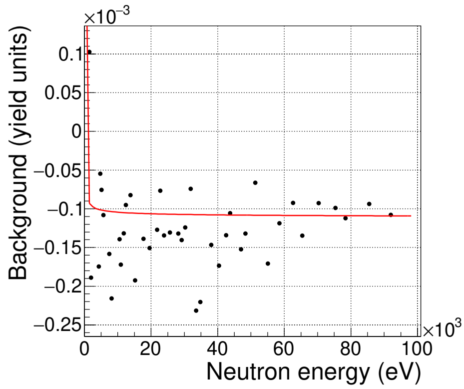

Figure 5.2: Residual background fitted with SAMMY at energy sections close to each analyzed resonances (black points) together with a global fit in the entire energy range (red line).

The observed negatives values might indicate that the background components calculated in Sec. 4.5 are slightly overestimated. A possible source of discrepancies may be the assumptions made in the calculation of background components related to the presence of the sample (i.e. neutron and in-beam γ-ray scattering). Although there is no apparent reason to arbitrarily change the values of the normalization factors for these components F_n and F_γ, we explore the possible systematic impact of their variation. A set of yields was obtained by reducing both parameters approximately by 25%, 50% and 90%, respectively. Results can be seen in Fig. 5.3. A change in the dependence with neutron energy is appreciated when normalization factors decrease. The initial background ($F_n = 0.65$ and $F_\gamma = 0.15$) exhibits an almost constant value, whereas the last obtained background ($F_n = 0.10$ and $F_\gamma = 0.01$) shows a clear dependence with the neutron energy. In fact, the drastic reduction of 50% in the normalization factors, needed to obtain a negligible residual background ($F_n = 0.30$ and $F_\gamma = 0.07$), is accompanied by the corresponding change in trend with neutron energy. For these reasons, F_n and F_γ parameters have remained unaltered in this analysis as calculated in Sec. 4.5. Nevertheless, this study will be useful in the calculation of the systematic uncertainty, in the radiative kernels, related to the calculation of the residual background, which will be explained at the end of this section.

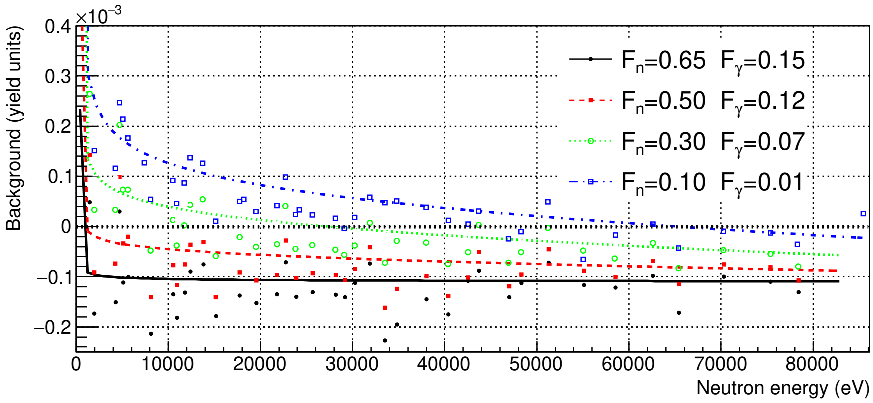

Figure 5.3: Residual backgrounds fitted with SAMMY to four different yields obtained with combinations of the normalization parameters F_n and F_γ.

The resonance fitting procedure described in this section will be illustrated in the following with the most relevant cases for discussion.

1474 eV resonance

This narrow resonance was measured by a transmission experiment, and it is compiled by Mughabghab [50] as a *p*-wave resonance with $l = 1$ and $J = 0.5$. However, as it can be seen in Fig. 5.4, a significantly better fit to the neutron capture yield data is obtained with $l = 1$ and $J = 1.5$. In fact, the fit made using SAMMY does not converge when the spin proposed in the literature is selected.

The neutron energy obtained in this analysis for this resonance is of 1473.74(1) eV, in agreement with the 1470(10) eV reported in [50]. In this compilation, the Γ_γ parameter is not available, but the Γ_n parameter is estimated with a value of 25(7) meV. As explained above, in this work, both resonance parameters, Γ_γ and Γ_n, are obtained by means of a χ^2 minimization whose results can be seen in Fig. 5.5. The latter shows a strong correlation between the parameters and its minimum value is reached for $\Gamma_\gamma = 132(10)$ meV and $\Gamma_n = 36(1)$ meV. This value for Γ_n is not in agreement within 1σ with that reported in [50], however, it is 10 times more precise. Fig. 5.5 shows the resulting fit to the experimental capture yield compared to JEFF-3.3 and ENDF/B-VIII. As it can be seen, resonances from these databases cannot reproduce our experimental data since they clearly underestimate the cross section. On the other hand, some points in the rising flank have residual values to our R-Matrix fit larger than 2σ. This systematic effect appears along this work in the analysis of narrow and strong resonances with very high statistics, and it is ascribed to the limited precision of the numerical RF introduced in SAMMY.

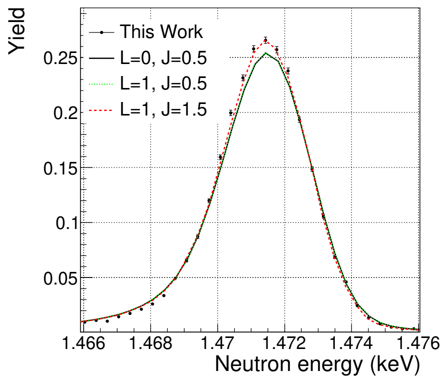

Figure 5.4: 1474 eV resonance SAMMY fitting using different spin groups.

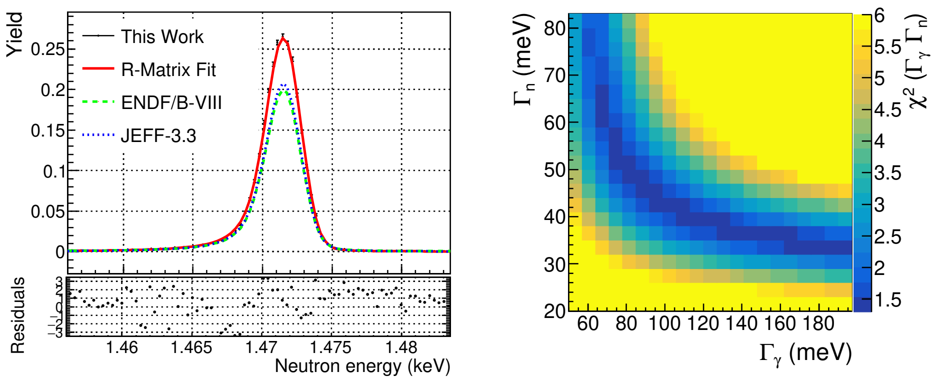

Figure 5.5: (Left panel) 1470 eV resonance analyzed with SAMMY and compared to evaluated data. (Right panel) χ^2 surface resulting from a series of R-matrix runs where both Γ_γ and Γ_n were varied.

1977 eV resonance

This is a very strong s-wave resonance found in transmission measurements with spin J = 0.5, which is in agreement with this work. In this resonance, since Γ_n is 20 times greater than Γ_γ, and due to the characteristics of the sample used in this work, the effects of the multiple scattering are remarkable. Fig. 5.6 shows separately the different components of the capture yield explained in Sec. 5.1.1. The contribution of neutrons captured after suffering two or more scatters in the sample is comparable to that obtained from neutrons directly captured. The shapes of these components are reflected on the top of the resonance. The scattering contribution is dominated by the multiple-scattering. Owing to the approximate numerical calculation of the latter component in SAMMY, the resonance shape cannot be fully reproduced. This causes that several points exhibit residues larger than 2σ. On the other hand, the energy of 1976.9(1) eV found in this analysis does not agree with the value of 1982(3) eV reported in previous transmission measurements [49]. Also the value for Γ_n reported in transmission (50000(900) meV) disagrees with that obtained in this work (62900(250) meV), although the differences are not so large. This is appreciated in Fig. 5.6 by comparing the results from this work to the ENDF/B-VIII.0 database. On the contrary, the JEFF-3.3 evaluation reports a very different shape due to the three times lower value assigned to the Γ_n parameter.

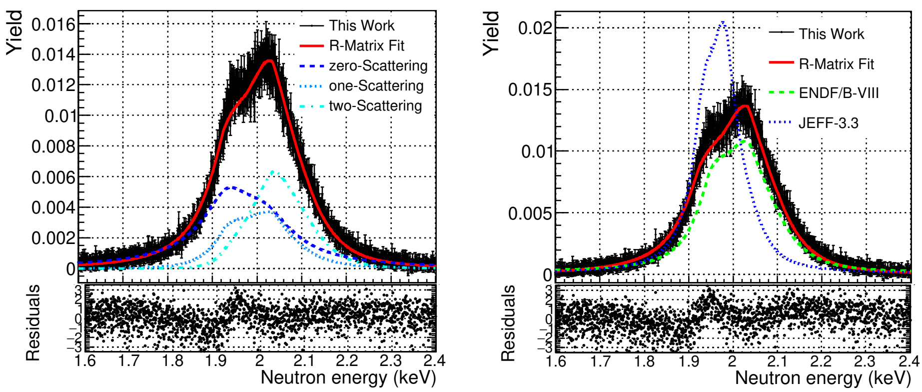

Figure 5.6: 1977 eV resonance fitted using SAMMY. (Left panel) The individual scattering contributions to the yield are displayed using different colored lines. (Right panel) Results from this work compared to ENDF/B-VIII and JEFF-3.3 evaluated libraries.

4 keV to 6 keV

In this neutron energy region, we individually analyzed five different resonances. Fig. 5.7 shows the resulting fits from this analysis compared to JEFF-3.3 and ENDF/B-VIII libraries. In addition, a numerical comparison between the resonance parameters calculated in this work and those reported in previous transmission measurements is given in Tab. 5.1. In the latter, values for Γ_γ are not included since they are only available for two resonances in the literature, which are detailed in the following paragraphs.

This Work		Mughabghab		Novoselov	
E_0 (eV)	Γ_n (meV)	E_0 (eV)	Γ_n (meV)	E_0 (eV)	Γ_n (meV)
4297.3(7) 4314.9(2)	81341(1193) 111(108)	4270(32)	52000(13000)	4348(12)	71200(2000)
4717.4(1)	1139(28)	4720(36)	4800(2400)	4690(100)	6800(1400)
5102.7(8)	70970(1790)	5100(40)	74000(19000)	5210(25)	47000(2200)
5662.9(1)	503(40)	5660(46)	7000(4000)	5566(160)	4500(1500)

Table 5.1: Values of resonance energy (E_0) in eV and neutron width (Γ_n) in meV calculated in this work for the resonances analyzed in the energy range between 4 keV and 6 keV, compared to data from transmission measurements [50, 49].

A wider resonance at 4297.3(7) eV is found in our analysis to be overlapped with another narrower and less intense one at 4314.9(2) that appears on the top. Both are considered as a single large resonance by the evaluated libraries, as it is shown in Fig. 5.7, as probably was deduced from transmission measurements. For that reason, the values for Γ_n calculated in this work disagree with those reported in [50, 49]. The energy E_0 of one of the two resonances adjusted in this work is in agreement with [50] but none of them is compatible with that reported in [49].

The energy E_0 calculated in this work for the resonance at 4717.35(3) eV is compatible with those reported by transmission. In addition, the $\Gamma_\gamma = 224(2)$ meV is in agreement with the previously measured $\Gamma_\gamma = 250(100)$ meV [50] improving the statistical uncertainty from 40% down to less than 1%. However, our determined value for Γ_n is several times less than previously reported. In the comparison with evaluations, the capture yield adjusted in this work is smaller than that provided in the JEFF-3.3 evaluated library, as it is shown in Fig. 5.7. On the contrary, the resonance available in the ENDF/B-VIII evaluation is even less intense.

The E_0 and Γ_n parameters calculated in this work for the resonance at 5102.7(8) eV agree with the values compiled by Mughabghab [50], but disagree with those reported by Novoselov [49]. Furthermore, data from the evaluated libraries exhibit a narrow resonance close to this one that does not appear in our data.

Finally, the resonance at 5662.99(3) eV is only present in the ENDF/B-VIII.0 evaluation with a broaden shape, compared to our high resolution data. For this

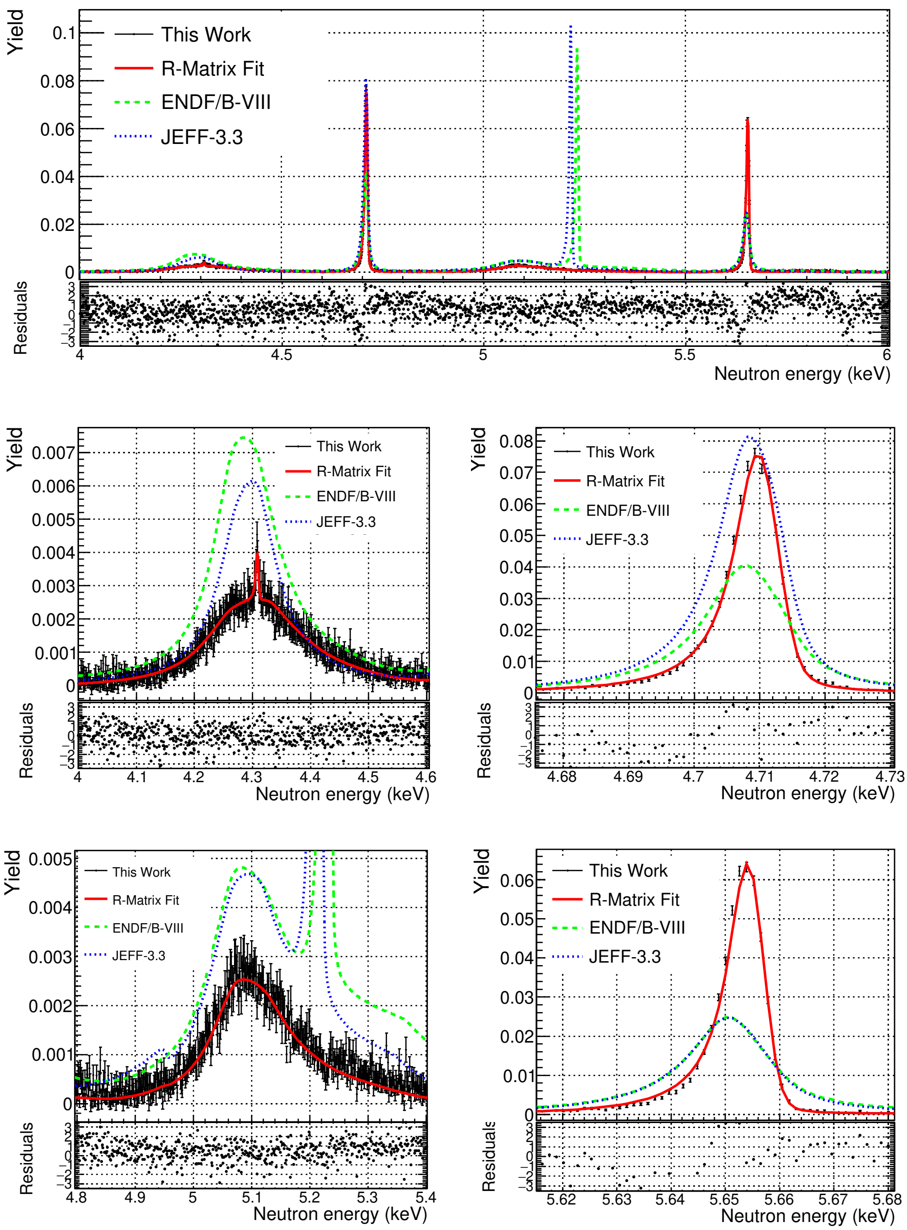

Figure 5.7: (Top panel) Capture yield obtained in this work between 4 keV and 6 keV of neutron energy fitted using SAMMY and compared to evaluations. (Middle and bottom panel) A zoom for each resonance is displayed.

resonance, the $\Gamma_\gamma = 210(55)$ meV reported by Mughabghab [50] is compatible to that calculated in this work $\Gamma_\gamma = 238(6)$ meV. However, values for Γ_n provided by transmission measurements are higher and less accurate than that fitted in this work.

The spin groups of the five resonances in this energy range were left as in the previous transmission measurements, in which they are considered as *s*-wave resonances with spin J = 0.5.

7447 eV resonance

The low background in our experiment has made it possible to find a new resonance at 7447.1(7) eV. The small, but detectable, resonance displayed in Fig. 5.8 is clearly distinguishable from the background. The fit performed using SAMMY provided values of $\Gamma_\gamma = 5(1)$ meV and $\Gamma_n = 3203(1045)$ meV.

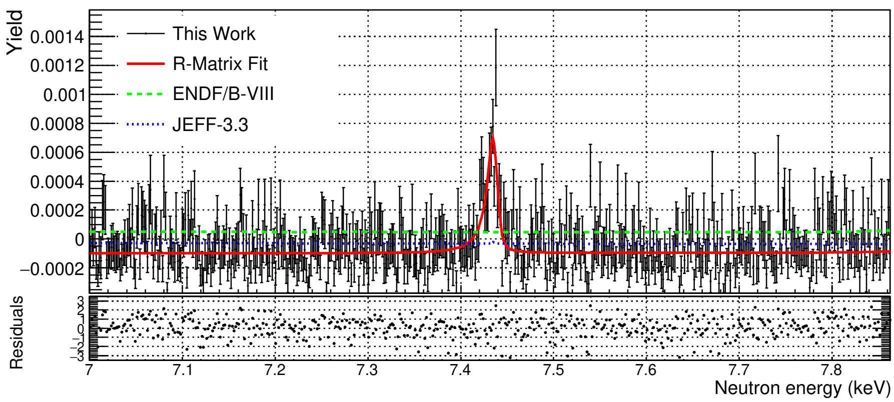

Figure 5.8: Very low resonance of ^{80}Se(n,γ) at 7400 eV fitted using SAMMY.

8122 eV resonance

Fig. 5.9 shows a resonance found at 8122.00(6) eV together with the R-matrix fit. Three different spin groups were tested obtaining similar results of χ^2. In fact, the reduced χ^2 has a value of 1.5 in the three cases. Therefore, and because the low sensitivity to this parameter found in our analysis, there is no any reason to perform a change in the spin group of this resonance corresponding to l = 1 and J = 0.5. The resonance parameters coming from the best fit with SAMMY are Γ_γ = 286(3) meV and $\Gamma_n = 1350(75)$ meV. A small discrepancy on the rising flank can be appreciated in the same figure. As in previous cases, this deviation can be most probably ascribed to limitations of the numerical RF used in this work. The value of the Γ_n parameter can be compared with previous transmission measurements that give an upper limit of $\Gamma_n < 900$ meV, not compatible with the value obtained from this work. Regarding the evaluations, ENDF/B-VIII.0 shows a resonance with a significant larger yield. In the case of JEFF-3.3, there is no resonance at this energy.

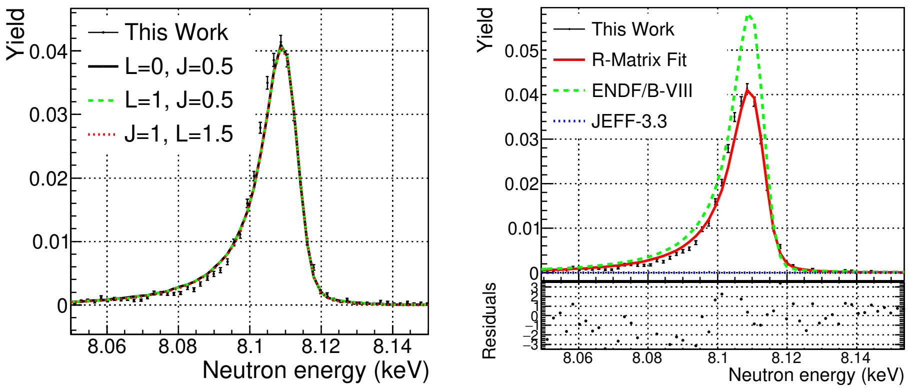

Figure 5.9: (Left panel) 8.1 keV resonance fitted using SAMMY and different spin groups. (Right panel) Results obtained in this work are compared to different evaluations.

10 keV to 16 keV

For neutron energies enclosed within the range from 10 keV to 16 keV the results are shown in Fig. 5.10. In this case, the discrepancies between our experimental data and the evaluated libraries are even larger. Compared to JEFF-3.3, our fit using SAMMY shows a narrower and stronger resonance at 10521.3(1) eV, but a similar one at 11788.5(1) eV. A good agreement is also found between our results and ENDF/B-VIII for the resonance at 12422.8(6) eV. The latter is the only one that was previously measured in a transmission experiment [49] within this neutron energy range. The $\Gamma_n = 26000(8000)$ meV parameter available in the Mughabghab compilation [50] is in agreement with the $\Gamma_n = 25044(1325)$ meV value derived in our analysis. On the other hand, above 12.4 keV, we observe two additional resonances that cannot be compared with the three ones available in JEFF-3.3 due to significant differences in neutron energy.

16 keV to 25 keV

Fig. 5.11 shows the ^{80}Se(n,γ) capture yield in the neutron energy range from 16 keV to 25 keV. Only the resonance at 18285.7(5) eV was previously measured in

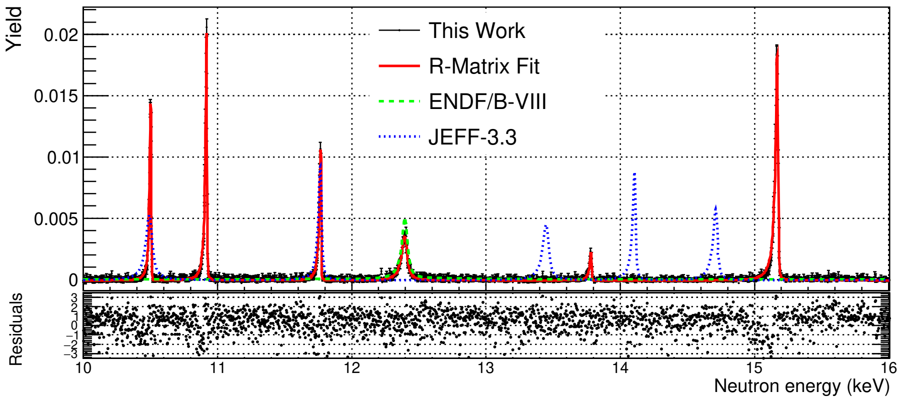

Figure 5.10: Yield of ^{80}Se(n,γ) between 10 keV and 16 keV of neutron energy fitted using SAMMY and compared to evaluated libraries.

transmission reporting an energy $E_0 = 18300$ eV [50]. The value for the neutron width parameter $\Gamma_n = 109800$ meV is remarkably larger from the one calculated in this analysis, $\Gamma_n = 6770(860)$ meV. Other two resonances in ENDF/B-VIII.0 and five resonances in JEFF-3.3 evaluations cannot be compared since their neutron energies do not match with those found in this work. Probably because of the lack of high resolution data and thus, the use of a statistical model to generate them. In particular JEFF-3.3, uses the TENDL-2017 library, based on statistical calculations with the TALYS code [105], to complement the input from previous measurements.

25 keV to 100 keV

The rest of the yield up to 100 keV was analyzed in several neutron energy fragments as it is shown in Fig. 5.12. Only two resonances are present in ENDF/B-VIII.0 library corresponding to this energy range. The first one at 29.6 keV can be compared with a resonance in our data, and they have a very similar shape. But the second one in ENDF/B-VIII.0 at 39.9 keV does not match in energy with any resonance in our data. On the other hand, there are a lot of resonances proposed in the JEFF-3.3 evaluation, but since they come from theoretical estimations performed with TALYS, they do not match in energy with our resonances and they cannot be compared.

Radiative Kernels

In summary, 113 resonances were analyzed in the neutron energy range between 1 eV and 100 keV. The radiative kernels, proportional to resonance area, are

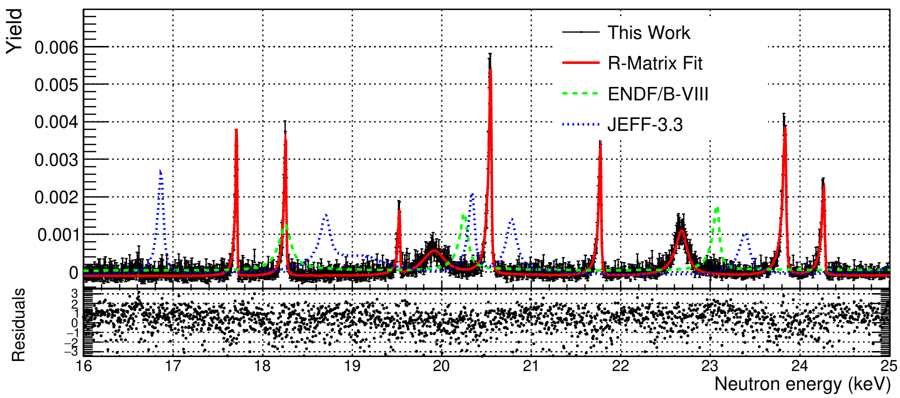

Figure 5.11: Yield of ^{80}Se(n,γ) between 16 keV and 25 keV of neutron energy fitted using SAMMY and compared to evaluated libraries.

calculated from the fitted Γ_γ and Γ_n using Eq. 1.2. Fig. 5.13 shows the radiative kernels of the resonances analyzed in this work up to 30 keV. In this energy range, our data is compared with the evaluated data files and the previous transmission measurements [50] by means of their ratio, which is shown in the bottom panel of that figure. For most of the resonances, the measured radiative kernels are between 10% and 50% lower than the values reported in both, ENDF/B-VIII and JEFF-3.3 evaluations. Additionally, no trend is observed, as a function of the neutron energy, in the results obtained from this work.

Except for a few resonances, the radiative kernels calculated from the resonance parameters in ENDF/B-VIII.0 [45] are in agreement with those measured in previous transmission experiments. On average, our results are 20% lower respect to those with a dispersion about a 30% in both cases. Compared to JEFF-3.3 [44], the radiative kernels calculated in this work are in average a 50% lower, with a dispersion higher than a 40%.

From this comparison, large differences are found not only between our data and evaluations, but also between the different evaluations.

Neutron sensitivity correction

Apart from the experimental effects explained in Sec. 4.7, an additional correction might be necessary for some particular resonances due to neutrons scattered in the sample and captured (prompt) in the surroundings. A lot of efforts have been performed at n_TOF in order to reduce the neutron sensitivity of the detection setup. One example is the development of the C_6D_6 detectors introduced in Sec. 3.2.1, which use carbon fiber to reduce undesired neutron captures [76]. Even

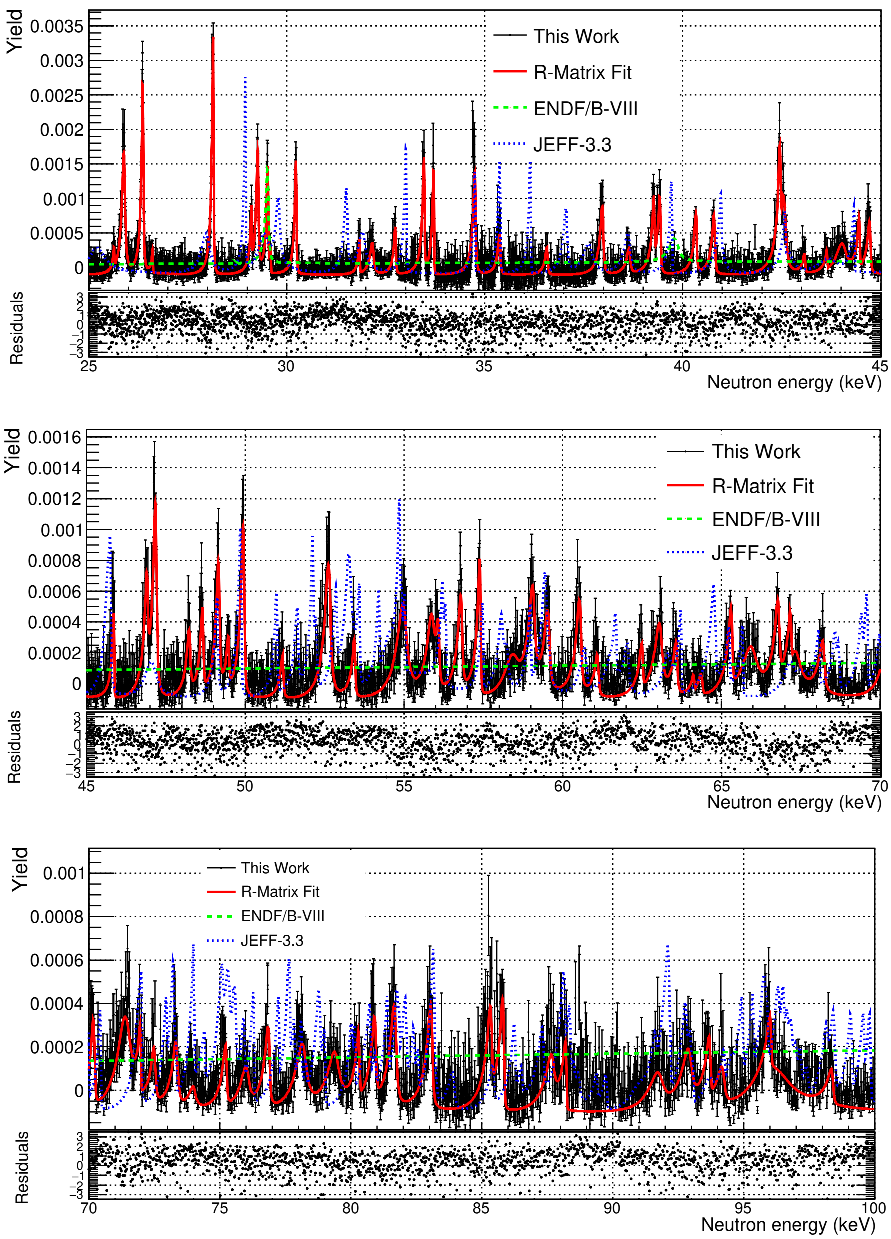

Figure 5.12: Fragments of ^{80}Se(n,γ) yield fitted using SAMMY and compared to evaluated libraries.

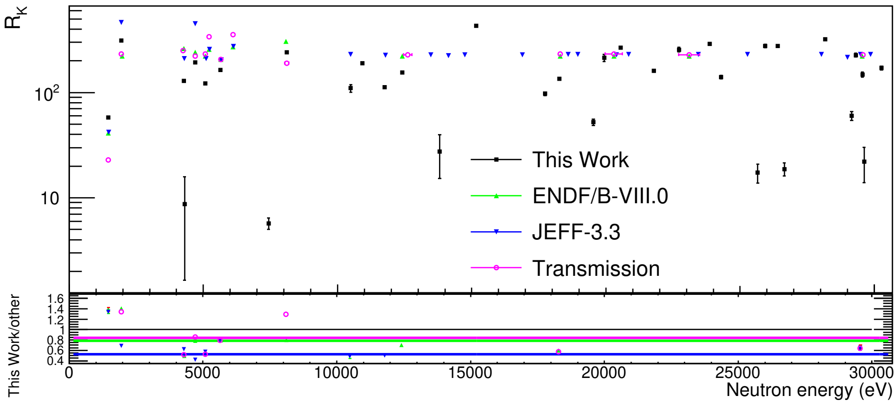

Figure 5.13: Radiative kernels calculated in this work compared to evaluations and previous transmission measurements. The ratio between our data and the rest is included in the bottom panel, where black dashed line represent the unity and colored lines display the average of each comparison.

though, the neutron sensitivity could still play a role in resonances with a large Γ_n/Γ_γ ratio.

The probability that a scattered neutron is captured in the detector itself, is computed by the P_{ns} parameter defined in Eq. 5.4. This parameter is expressed as the ratio between the neutron detection efficiency of the setup (ε_n) over the cascade detection efficiency (ε_c), times the ratio between the neutron and the gamma width (Γ_n/Γ_γ), of the analyzed resonance.

$$P_{ns} = \left(\frac{\varepsilon_n}{\varepsilon_c}\right)\frac{\Gamma_n}{\Gamma_\gamma} = \left(\frac{\varepsilon_n}{\varepsilon_\gamma}\right)\left(\frac{\varepsilon_\gamma}{\varepsilon_c}\right)\frac{\Gamma_n}{\Gamma_\gamma} \tag{5.4}$$

This equation has been rewritten by adding the maximum gamma detection efficiency (ε_γ) corresponding to E_γ = 600 keV. Then, the neutron sensitivity, defined as the ratio $\varepsilon_n/\varepsilon_\gamma$, can be obtained from the MC simulations dedicated to the study of the neutron sensitivity in C_6D_6 detectors that were carried out in [76]. From this study, the value of 2×10^{-5} is extracted as the average of this quantity in the neutron energy range between 1 eV and 100 keV for an early C_6D_6 detector with carbon fiber casing. On the other hand, the ratio $\varepsilon_\gamma/\varepsilon_c \approx$ 0.56 is extracted from the MC simulations performed in this work. Details on the simulations of individual γ-rays and (n,γ) cascades can be found in Sec. 4.3.1.

The final correction, f_{ns}, to be applied to the capture yield in each resonance is proportional to the probability P_{ns}, as it is calculated in Eq. 5.5.

$$f_{ns} = \frac{1}{1 + P_{ns}} \tag{5.5}$$

Values for the ratio Γ_n/Γ_γ are calculated for all analyzed resonances. They are shown in the Fig. 5.14 as a function of neutron energy. The blue dashed line in the figure shows a constant value of 500 which corresponds to a correction of the 0.5% to the yield. As can be seen clearly, most of the resonances ($\sim$ 80%) have a ratio less than that value. On the other hand, only three out of the 113 analyzed resonances have a ratio larger than 1000, which implies a correction of 1% on the capture yield. Hence, for these resonances a 1% systematic uncertainty has been added, whereas for the rest it is considered negligible.

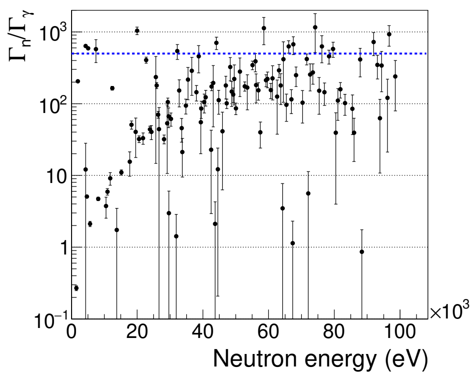

Figure 5.14: Γ_n/Γ_γ ratio as a function of neutron energy for all resonances.

Systematic uncertainties

At the beginning of this section, four different capture yields of ^{80}Se(n,γ) were obtained using different scaling factors F_n and F_γ for the subtraction of the neutron and γ-ray scattering background. These calculated yields were used to assess the impact of the variation of these normalization parameters on the residual background fitted with SAMMY. That study can be also useful to calculate the systematic uncertainty in the radiative kernels associated to the sample-dependent background subtraction and the residual background. With that goal, the resonance parameters were fitted for all the resonances between 1 eV and 100 keV in the four different yields mentioned above. Fig. 5.15 shows all radiative kernels calculated from the extracted Γ_n and Γ_γ values after following this methodology. Their relative differences are calculated and accumulated in the histogram shown in the same figure. The resulting distribution has a narrow peak at 0, with a standard deviation of 1.38%. This result can be used as a good estimation of the systematic uncertainty due to local inaccuracies in the background subtraction.

Besides the background subtraction, other sources of systematic uncertainty in the capture yield have been discussed throughout this thesis. The main sources of systematic uncertainties studied in this work are listed in Tab. 5.2 together with the total budget.

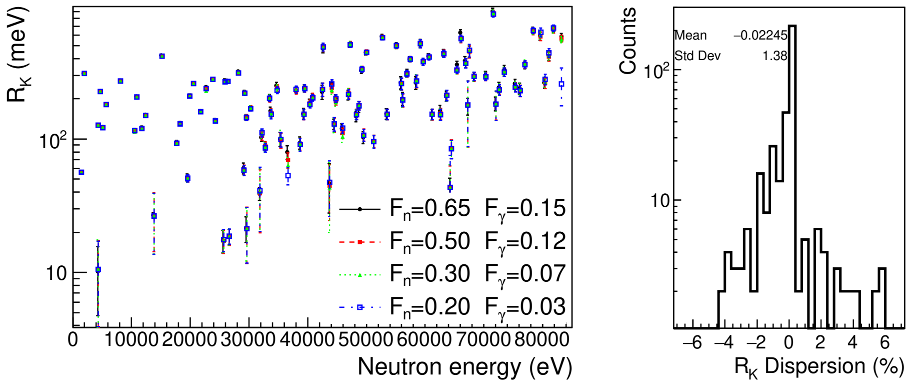

Figure 5.15: (Left panel) Radiative kernels calculated using different background parametrizations. (Right panel) Dispersion between the radiative kernels calculated for each resonance.

Source	Uncertainty (%)
CR stability	1
Gain stability	1
Statistical model of the capture cascade	1
Efficiency (PWHT application)	0.5
Neutron flux (shape)	2 to 5
Normalization	1
Residual background	1.4
Neutron sensitivity[1]	1
Total	**3.2 to 5.7**

Table 5.2: Summary of the main systematic uncertainties of the yield in this analysis.

[1] Applied to resonances at neutron energies of 19956(5) eV, 58549(33) eV and 74158(26) eV.

5.2 MACS calculation

From Sec. 0.1.1, it is known that during the *s*-process, neutrons in the stars are thermalized following the Maxwell distribution of velocities for their corresponding temperatures. For that reason, the Maxwellian Averaged Cross Section (MACS) is the relevant input in astrophysical calculations. At a temperature T, the MACS is given by Eq. 5.6:

$$\text{MACS} = \frac{\langle \sigma_v \rangle}{v_T} = \frac{2}{(kT)^2\sqrt{\pi}} \int_{E_i=0}^{E_f=\infty} \sigma_\gamma(E) E e^{-E/kT} dE, \tag{5.6}$$

which is a more common form of Eq. 2. This expression contains an integral up to the infinity, therefore an error is caused because of the upper limit of the experimental data. The systematic errors due to the initial $E_i > 0$ and a final neutron energy $E_f < \infty$ of our data are calculated using Eq. 5.7 and Eq. 5.8 respectively [106]. The former affects more at low temperatures, whereas the latter becomes more noticeable at high temperatures. Both increase as the difference between real and theoretical energy integration limits increase.

$$\frac{\Delta(\langle \sigma_v \rangle / v_T)}{\langle \sigma_v \rangle / v_T} \leq \frac{2}{\sqrt{\pi}} \sqrt{\frac{E_i}{kT}} \left[1 - e^{-E_i/kT}\right] \tag{5.7}$$

$$\frac{\Delta(\langle \sigma_v \rangle / v_T)}{\langle \sigma_v \rangle / v_T} = \frac{2}{\sqrt{\pi}} \sqrt{\frac{E_f}{kT}} e^{-E_f/kT} \tag{5.8}$$

Despite the absence of ^{80}Se(n,γ) resonances below 1 keV, we can compute the MACS from 1 eV, from the resonance analysis, in order to reduce the uncertainty due to the lower integral limit calculated in Eq. 5.7. This is possible because SAMMY calculates the neutron capture cross section at the thermal region from the tail of the first resonances. A good agreement is found in this region when comparing our result to the evaluations in Fig. 5.16. Furthermore, if this cross section is extrapolated to the thermal point, our result (0.567 mb) is in agreement within 7% with the 0.610 mb reported in [50].

In addition to the systematic uncertainties, the statistical errors associated with the calculation of the resonance parameters must be taken into account. To this aim, a Monte Carlo sampling was carried out in which thousands of MACS were calculated by varying the resonance parameters within their statistical uncertainties. The latter were obtained directly from the Bayesian analysis performed by SAMMY. At the end, a Gaussian distribution of MACS values is obtained at each temperature kT. The σ of the Gaussian is assigned as statistical uncertainty of the MACS.

Fig. 5.17 shows the MACS calculated in this work at different temperatures from $kT = 1$ keV to 60 keV, compared to the values calculated from the resonance parameters in JEFF-3.3. Only the statistical uncertainties of our result are shown in the figure. There is a noticeable discrepancy of up to 20% at low temperatures between JEFF-3.3 and our data, which is highly decreasing as kT increases. The MACS from the KADoNiS v1.0 database [107] is also displayed in the figure for comparison purposes. The latter is an average from recent evaluations which fits the measurement of [108]. The values in KADoNis are compatible with JEFF-3.3 but disagree with our data. The other compared MACS is the measured by Walter

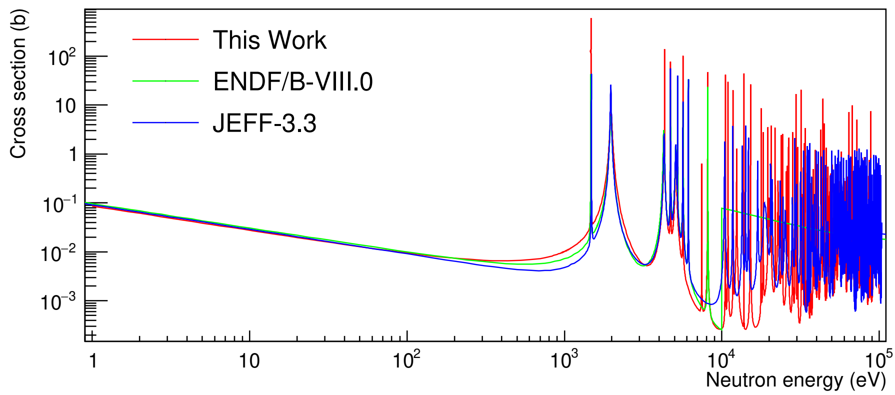

Figure 5.16: Cross section of the ^{80}Se(n,γ) reaction calculated in this analysis and compared to evaluations.

et al. [31], mentioned at the beginning of this chapter as the only one previous neutron capture measurement performed using the ToF technique, which is also in disagreement with our results.

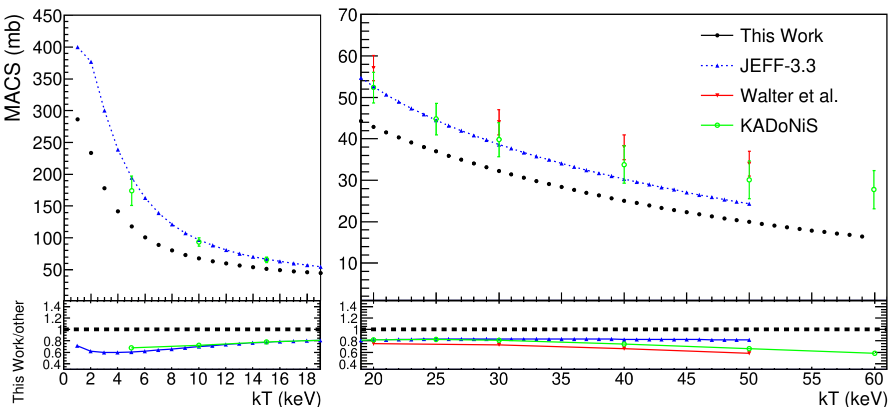

Figure 5.17: MACS of the ^{80}Se(n,γ) reaction found in this analysis compared with evaluations and previous measurements.

Differences between presented MACS are appreciated in the ratio between the MACS of this work and all the others mentioned above, which is shown in the bottom panel of Fig. 5.17. All compared MACS are between a 20% and a 40% overestimated with respect our results. From $kT \approx 5$ keV all results get closer to each other. However, from $kT \approx 30$ keV on, the MACS given by Walter and KADoNiS v1.0 diverge from our result. This reflects the importance of measuring the MACS at several stellar temperatures by using the ToF technique, instead of obtaining the MACS at few points by using the activation technique.

Finally, as it was explained in Sec. 0.1.1, the two main stages of the s-process in AGB stars correspond to energies of $kT \sim 8$ keV for the ^{13}C pocket and of $kT \sim 26$ keV for the He-flash. Differences in the value of the MACS in these regions have more impact in the astrophysical calculations. In order to compare the different models previously shown, they are evaluated at energy points near to these regions where most of them have available data. As can be seen in Tab. 5.3, at $kT = 10$ keV, both the MACS calculated with JEFF parameters and that presents in KADoNiS database are compatible with each other. Our value is approximately 30% lower at this point. However, discrepancies between our data and the evaluations decrease at $kT = 30$ keV. At this temperature, JEFF-3.3 and KADoNiS agree again, but our result disagrees with them. A significant correction of the MACS is recommended thanks to the remarkable improvement in statistical uncertainty at both kT, going from 10% in KADoNiS to about 1% in this work.

	MACS at 10 keV (mb)	MACS at 30 keV (mb)
JEFF 3.3	96.86	38.67
KADoNiS	93.6(6.8)	39.8(4.1)
Walter et al.	–	44(3)
This Work	**67.6(0.4)**	**32.2(0.3)**

Table 5.3: Value of the MACS at two different temperatures. Only statistical uncertainties are included in these results.

Part II

i-TED detection system development

Chapter 1

Introduction

Part I presented in this work was entirely dedicated to obtain high energy resolution and high accuracy experimental data on the neutron capture cross section of ^{80}Se. The next step corresponds to the cross section measurement of the ^{79}Se(n,γ) reaction, which has been approved by the CERN INTC[1] and it is scheduled for the next experimental campaign at the CERN n_TOF facility in 2022 [39]. However, as introduced in Sec. 0.1.2, the experimental difficulties for measuring this unstable selenium isotope require the development of a new detection system with enhanced detection sensitivity, the so-called i-TED detector, which is introduced in this chapter.

Sec. 1.1 of this chapter introduces the need for i-TED, by going into details about the experimental difficulties for the measurement of the ^{79}Se neutron capture cross section. The concept of this detection system and its novel background rejection method by means of the imaging technique are explained in the next two sections Sec. 1.2 and Sec. 1.3, respectively. On the other hand, the following two chapters, Chapter 2 and Chapter 3, describe the components of i-TED and the characterization of the first prototype performed in terms of energy and spatial response. Finally, the first experimental proof of concept of the system is presented in Chapter 4, in which the experimental background rejection has been quantitatively proven using this innovative technique.

1.1 i-TED motivation

In Sec. 0.1.2, it was already pointed out the absence of experimental cross section data data on ^{79}Se due to the difficulty of measuring this unstable isotope. The fabrication of the sample and its final composition play an important role in these difficulties. In order to understand these complications, it is necessary to go into details of its fabrication process.

Since ^{79}Se is radioactive ($t_{1/2} = 3.27(8) \times 10^5$ y [43]), it cannot be extracted directly from nature. For that reason, three options were considered to obtain a

[1] ISOLDE and n_TOF Experiments Committee

sample containing this selenium isotope:

1. Irradiating a ^{78}Se enriched sample in a high neutron flux reactor during a long time period (weeks to months) to produce ^{79}Se by neutron captures. In this process, the higher the purity of the initial sample, the higher the control over the presence of impurities after irradiation. In contrast, additional undesired isotopes in the initial ^{78}Se sample may capture neutrons and cause radioactive contaminants to appear in the final sample, increasing the experimental background. On the other hand, alternative neutron-induced reactions such as (n,p) or (n,α) might occur, producing some undesired contaminants even if the sample was pure ^{78}Se.

2. Chemical extraction of spent fuel from nuclear plants. As mentioned in Sec. 0.1.2, ^{79}Se represents one of the main constituents among the fission products in the high-level radioactive waste. Nevertheless, the main drawbacks of this option are the delicate and expensive chemical extraction procedure, as well as the unavoidable presence of contaminants.

3. Obtaining ^{79}Se from decommissioned targets from the ISOLDE experiment at CERN [109]. In this case, radioactive targets could be extracted in a similar way as explained in 2. This represents also an expensive solution and difficult to control the level of purity.

The first option was preferred due to the balance between cost and limited presence of contaminants. However, for safety reasons, materials with low melting points as Se (217 °C) cannot be irradiated directly in a reactor. Therefore, a Pb-Se eutectic alloy was prepared at the Paul Scherrer Institut (PSI) [110]. Tab. 1.1 shows the composition of the initial ^{208}Pb^{78}Se sample. The latter is a disk-shaped alloy of 3.9028 g mass, 14 mm diameter and 5 mm thickness, encapsulated at CERN in a laser-welded casing of 6N aluminum with a thickness of 0.5 mm.

Isotope	^{78}Se	^{208}Pb	^{27}Al^{1}
Mass (g)	1.067	2.838	1.024
Enrichment (%)	99.34	99.00	>99.9^{2}

Table 1.1: Mass and enrichment of the main components of the primary PbSe sample before irradiation.

^{1} ^{27}Al is part of the encapsulation.
^{2} 6N aluminum 99.9999% pure.

This sample was irradiated in the neutron reactor located at the Institut Laue-Langevin [111] with an equivalent power-weighted fluence of 42 full power days. The expected amount of ^{79}Se is about 3 mg. This value is known with an accuracy of 10% from the reactor fluence data, and it will be accurately measured after the n_TOF experiment by means of ICP-MS or other techniques. Despite the high enrichment of the materials used in the conformation of the initial sample, some radioactive isotopes were produced during the irradiation by means of neutron induced reactions. For that reason, the sample was characterized at PSI in 2019 paying special attention to the precise determination of these radioactive contaminants. This will allow for a realistic estimate of the background conditions in the capture experiment. Tab. 1.2 shows the activity of the main radioactive contaminants in the sample, which results from this characterization study.

Isotope	^{75}Se	^{110m}Ag	^{65}Zn	^{60}Co
Activity (MBq)	387(7)	1.55(4)	1.85(19)	2.82(8)
Half-life (d)	120	250	244	1925

Table 1.2: The activities of the major contaminants in the ^{79}Se sample, measured on November 2019, are shown together with their tabulated half-life.

On the other hand, ^{208}Pb is chosen, among other possible alloys, such as Al, due to its very small neutron capture cross section (0.36 mb at 30 keV) characterized also by the absence of neutron capture resonances up to $\sim$ 47 keV neutron energy. In the following, a qualitative discussion on the experimental difficulties for the ToF measurement of ^{79}Se(n,γ) is made. Fig. 1.1 shows the evaluated [44] neutron capture cross section of ^{79}Se together with the two main isotopes present in the sample, ^{78}Se and ^{208}Pb. All of them have been weighted by their mass fraction with respect to the total mass of the sample. Despite the large contribution of ^{78}Se to the overall capture yield, several of the ^{79}Se(n,γ) resonances can be distinguished. However, no background contribution is added to the figure. Instead, the elastic cross sections of the isotopes that could have more impact in the measurement are also included. These isotopes are ^{78}Se and ^{208}Pb, and their elastic cross sections are between two and three orders of magnitude higher than the expected neutron capture cross section. This can induce a high background due to neutrons scattered in the sample and captured in the surroundings of the experimental setup [75, 112]. This background must be minimized in order to be sensitive to the desired neutron cross section and obtain reliable data, particularly in the keV region of astrophysical interest.

The background present in the experimental hall during the neutron capture measurement will correspond to the sum of the radiation coming from the decay of the ^{79}Se sample, and from the neutrons captured elsewhere in the surroundings of the experimental setup. The impact of the latter in the total background is expected to be high considering the high elastic cross section of the lead and selenium isotopes. Nevertheless, the final level of registered background will severely depend on the detection system employed in the measurement. Here we review shortly the suitability of the detectors introduced in Sec. 2.1 and Sec. 3.2.1

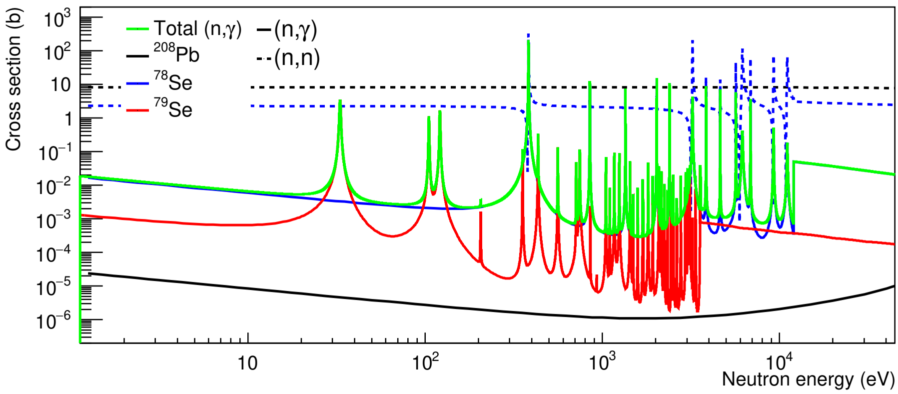

Figure 1.1: (Solid lines) Neutron capture cross section data of ^{78}Se and ^{208}Pb obtained from ENDF/B-VIII [45] and compared with statistical model calculations of ^{79}Se(n,γ) given in JEFF-3.3 [44]. The total expected neutron capture cross section sum of the mentioned individual contributions is shown in green. (Dashed lines) The elastic cross sections of ^{78}Se and ^{208}Pb are also included. All contributions are weighted by the mass portion of the total.

(Part I) to perform this neutron capture measurement by means of the ToF technique:

- TAC: Using the Total Absorption Calorimetry technique, the effect of the sample activity can be properly accounted for by applying selections of multiplicity and deposited energy. However, owing to the big amount of material that surrounds the sample (structural and sensitive), a large number of scattered neutrons can be captured in the detector itself, thus dramatically increasing the total count rate and background registered. This limitation dismisses this detector for such type of measurement.

- C_6D_6: this type of detector has proven successful in a previous similar ToF measurement using an unstable sample with very low mass [113]. Furthermore, reliable data were obtained in another measurement with a sample containing the dominant amount of the parent isotope (A-1), which was used as seed in the preliminary irradiation [87]. However, owing to the low energy resolution of these detectors, the activity of the sample cannot be conveniently suppressed by means of selections in deposited energy. Measuring a sample with an activity, such as that shown in Tab. 1.2, requires a high instantaneous neutron flux to overcome this background level. For this reason, it may be convenient to perform, at least part of the experiment, in the EAR2 station (see Sec. 3.1). Nevertheless, one of the main limitations of using C_6D_6 detectors in ToF capture experiments is related to the background induced by neutrons scattered in the sample and captured around in the experimental area [79]. According to MC studies [75], this type of background represents one of the dominant contributions in many neutron capture experiments especially within the 1 keV to 100 keV neutron energy range of relevance for astrophysics.

- i-TED: the development of this novel detection system is specifically focused on the measurement of samples with a large scattering to capture ratio like the one of ^{79}Se. Unlike C_6D_6 detectors, this system allows one to reject part of the background produced by the scattered neutrons that are captured in the surroundings of the experimental setup using two different pieces of information: the interaction positions of the γ-rays registered in the detectors and their deposited energy. It is expected that, thanks to the enhanced sensitivity achieved by means of this method, the measurement of this sample at n_TOF EAR1 (see Sec. 3.1) becomes feasible [39].

The increment in detection sensitivity makes i-TED a well suited system for the neutron capture cross section measurement of ^{79}Se at EAR1. However, the small mass of ^{79}Se in the sample and its high activity (including contaminants) makes this measurement a clear case for EAR2, in which neutron flux is $\sim$ 25 times greater than that existing at EAR1. Nevertheless, the high counting rates expected at EAR2 ($>$ 10 MHz) represent yet a difficulty for the present acquisition system of i-TED, which can cope with count-rates of up to $\sim$ 600 kHz per module. Finally, the proposed experiment methodology combines the use of i-TED in EAR1 and an array of C_6D_6 detectors at EAR2 [39].

1.2 The i-TED concept

The i-TED imaging capable Total Energy Detector is designed to improve the signal-to-background ratio in neutron capture measurements by means of a further level of background rejection [62].

The further background rejection capability of i-TED is based on the measurement of the spatial origin of the measured radiation. To this aim, i-TED features position- and energy-sensitive γ-ray detectors distributed in two detection planes operated in time coincidence. This allows to apply the Compton principle in order to reconstruct the cone of possible directions of incidence of the incoming radiation [114]. If the resulting directions are compatible with the well-known position of the sample, the event is accepted. Otherwise, it is rejected assuming that it corresponds to the so-called *extrinsic neutron sensitivity*. This is, a γ-ray background event originating from a neutron scattered in the sample and captured elsewhere in the experimental setup outside the sample or the detector volumes. In addition, the higher energy resolution of i-TED compared to the other two aforementioned detectors, allows for more precise selections on the deposited energy of the events. The latter can be used to isolate the strongest decay lines from possible activity of the sample, reducing further their impact in the background. On the contrary, the main drawback of the i-TED system is the attainable efficiency, which is about a factor of 3-4 lower than with existing C_6D_6 detectors [62].

The design of this novel detection system focuses on maximizing detection efficiency while keeping its *intrinsic neutron sensitivity* as low as possible. The latter is related to neutrons scattered in the sample and captured in the detector itself. If not corrected, this increment in the count rate can lead to an overestimation of the measured cross section. In this respect, the use of a massive collimator to determine the direction of the incoming particle was tested in [115] and subsequently discarded. The latter conclusion was mainly based on the prohibitive background level induced by the mechanical collimator, and the large reduction in detection efficiency. To overcome these limitations, i-TED applies electronic collimation by means of the Compton imaging technique, which simultaneously improves detection efficiency and reduces the amount of structural material.

Fig. 1.2 shows the conceptual design of i-TED. In order to maximize detection efficiency, i-TED consists on an array of four Compton modules surrounding the capture sample, each one equipped with the two energy and position detection planes required to apply the Compton method. With the same goal of improving efficiency, the sensitive area of the second detection plane of each module is four times larger than that of the first plane. In contrast, the latter keeps a reduced area to minimize the distance to the sample under the array configuration displayed in the figure. The detection stages can be supplemented by ^{6}LiH layers or any other suitable neutron absorber, following an approach similar to that of the neutron absorber employed in the TAC detector (see Sec. 2.1 of Part I), to reduce the intrinsic neutron sensitivity of the overall apparatus.

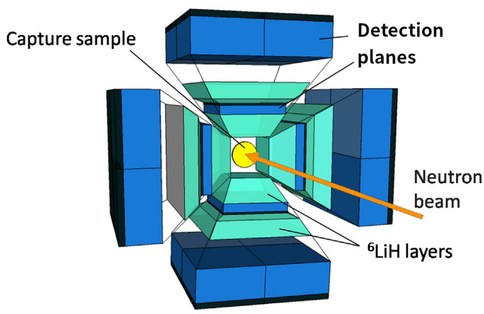

Figure 1.2: Conceptual design of i-TED composed of four Compton modules that are surrounding the capture sample. Extracted from [62].

Finally, in order to apply the TED technique (see Sec. 2.1.2 Part I), the PHWT is employed. As explained in Sec. 2.2 Part I, this makes the detection efficiency independent of the particular decay path or γ-ray detected. To this aim, an analysis similar to that performed in Sec. 4.3 must be carried out. As demonstrated in [62], this task can be successfully accomplished by Monte Carlo simulations and, similarly to C_6D_6 detectors, the proportionality between detection efficiency and deposited energy is achieved by using a weighting function.

1.3 Compton imaging

Compton cameras are widely employed in several fields such as astronomy [116, 117, 118], medicine [119, 120], nuclear structure [121] and treatment of radioactive waste [122]. However, this is the first time that such a device has been proposed and adapted for the measurement of neutron capture cross sections using the ToF technique.

The working principle of i-TED is illustrated in Fig. 1.3. An incoming γ-ray interacts with the first detection plane, undergoing Compton scattering, and then deposits the rest of its energy in the second detection plane, where it undergoes photo-absorption. These planes are hence called *scatter* and *absorber*, and their thicknesses are selected to maximize the scattering probability in the former and the full energy absorption in the latter. The energy, position and time of the γ-ray interactions are registered in each detection stage.

The line defined by the two interaction points, $\boldsymbol{r}_1$ and $\boldsymbol{r}_2$, becomes the axis of a virtual cone whose opening angle θ is given by the Compton formula of Eq. 1.1, where m_e is the mass of the electron in rest, c the speed of light, E_2 the energy deposited in the second interaction, and E_γ the energy of the γ-ray. The latter is assumed to be equal to the sum of energies deposited in both detection planes $E_\gamma = E_1 + E_2$. The wall of the cone contains all possible directions of the incoming radiation. Since the sample position and size are known by construction, this information can be used to check whether the γ-ray comes from the sample or not. As it is shown in the previous figure, the intersection of the cone with the vertical plane located at the sample position just in front of the scatter face (hereafter *image plane*), draws an ellipse. If the latter passes through the point where the sample is located, the event is accepted. Otherwise the event is rejected.

$$\theta = arccos\left[1 - m_e c^2\left(\frac{1}{E_2} - \frac{1}{E_\gamma}\right)\right] \tag{1.1}$$

In a first approach, the intersection of the Compton cone with the image plane can be solved analytically [123]. The result is the quadratic equation:

$$\begin{split}[u_x(x_s - a_x) + u_y(y_s - a_y) + u_z(z_s - a_z)]^2 \\ = cos^2\theta[(x_s - a_x)^2 + (y_s - a_y)^2 + (x_z - a_z)^2],\end{split} \tag{1.2}$$

where u_i with $i = x, y, z$, are the components of a unit vector along the cone axis, a_i the coordinates of the first interaction in the scatter and (x_s, y_s, z_s) the position of the sample.

Considering the sample position as the origin of the coordinate system, i.e. (x_s, y_s, z_s) = (0,0,0), one can use the λ parameter defined in Eq. 1.3 in order to check the compatibility of the measured radiation with the sample position.

$$\lambda = (u_x a_x + u_y a_y + u_z a_z)^2 - \left[1 - m_e c^2\left(\frac{1}{E_2} - \frac{1}{E_\gamma}\right)\right](a_x^2 + a_y^2 + a_z^2) \tag{1.3}$$

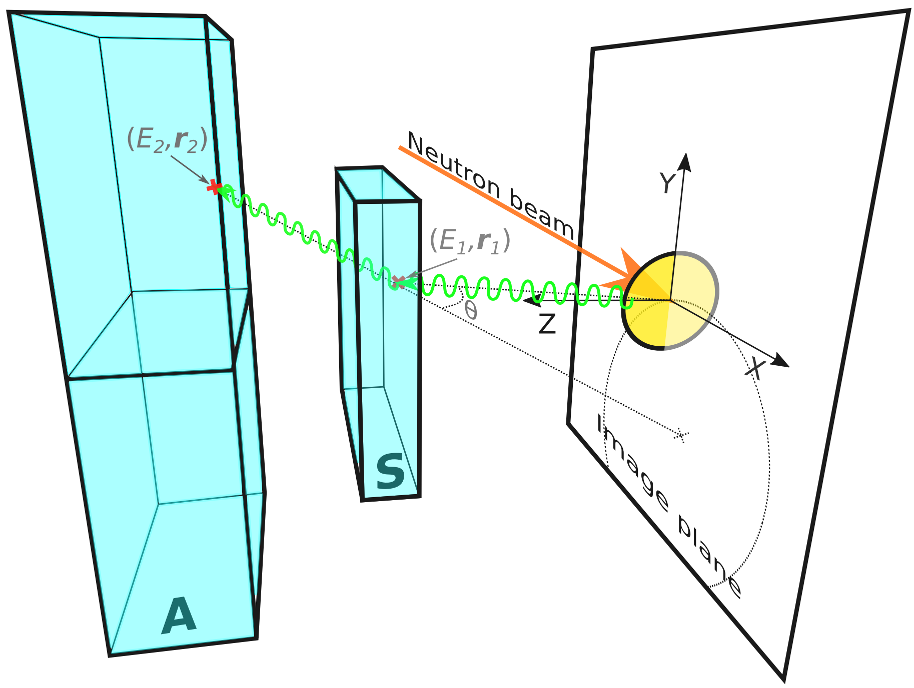

Figure 1.3: Scheme of a valid event registered with the i-TED5.3 prototype (see Sec. 2.4). S and A denote the scatter and absorber planes, respectively, $(E_i,\boldsymbol{r}_i)$ with i=1,2 the energy and position of the interactions in both detection planes, and θ the Compton angle. The neutron beam, capture sample and image plane are also displayed.

Fig. 1.4 shows the λ distribution obtained after 600 s measurement of a point-like ^{137}Cs source with an activity of 325 kBq. This measurement was carried out by placing the i-TED5.3 demonstrator at 63 mm from the center of the sample. This prototype, that will be presented in detail in Sec. 2.4, consists of a single Compton module with an asymmetric absorber which is longer in the Y axis than in the X axis, as it is shown schematically in Fig. 1.3. For that reason, the resolution in the Compton image associated with this distribution, and also displayed in the figure, is limited in the X axis. The effect of making a λ selection is displayed in the figure by means of two different representations of the same image: one contains the events with $\lambda < 1600$, whereas the other shows the rest of events. Owing to that λ selection, mainly those events whose ellipse passes close to the sample position are included in the first figure. In contrast, the ellipses of the events shown in the second image are far from the sample position. Thus, as discussed before, selections in λ values are mostly related to the incoming directions of the γ-rays. Obviously, events rejected with the $\lambda > 1600$ condition may consist of both background events and also "true" events, which do not fulfill the $E_\gamma = E_1 + E_2$ assumption. This aspect will be discussed later in more detail.

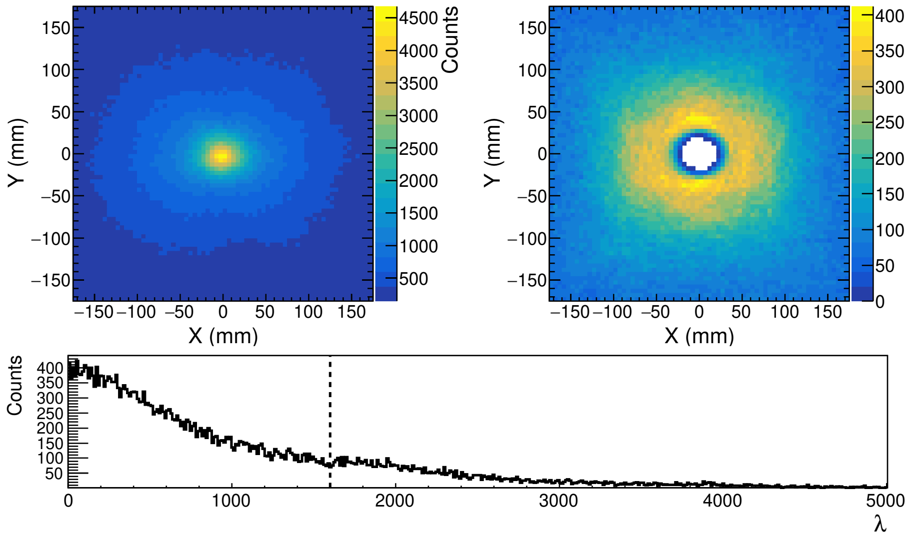

Figure 1.4: (Top panel) Reconstructed Compton images of a ^{137}Cs source placed at the capture sample position corresponding to: (top left) events with $\lambda < 1600$, and (top right) events with $\lambda > 1600$. (Bottom panel) The λ distribution and applied selection are shown.

The main advantages of using this simple back-projection algorithm are the low computational cost, and the possibility to obtain information about the direction of the incoming radiation on an event-by-event basis. On the contrary, the angular/spatial resolution achieved in the final Compton image is limited. There exist other algorithms that can improve the image shown in Fig. 1.4 in terms of spatial resolution [124, 125, 126]. Some of them [127, 128, 129] have been recently investigated for the same background rejection goal, under the framework of the ERC-funded project HYMNS [38, 130, 131]. Nevertheless, due to the early stage of i-TED development, in which the present work has been carried out, all results shown in this manuscript are obtained with the back-projection algorithm explained above.

The first demonstration of the i-TED working principle was carried out by means of Monte Carlo simulations in [62]. In the latter, an isolethargic neutron flux with energies ranging from thermal to 1 MeV impinges on the center of a gold sample, typically measured in ToF experiments as a reference due to its high and very well-known neutron capture cross section. In order to demonstrate the background-rejection capability of i-TED, a background was modeled by generating γ-rays over the surface of a 1 m radius sphere centered in the sample, which emulates the extrinsic neutron sensitivity. For that, γ-rays were generated following a deposited energy distribution measured in a real experiment at the n_TOF facility [66]. Furthermore, the response of i-TED was compared with two common C_6D_6 detectors used as a benchmark. To quantify the change in signal-to-background ratio, the level of the first resonance of gold at 4.9 eV of neutron energy and the valley at 20 eV were compared. The final result is an improvement of a factor of $\sim$ 10 in the signal-to-background ratio of the full i-TED array with respect to C_6D_6 detectors. Nevertheless, the first experimental demonstration of the background-rejection concept of i-TED will be presented in Chapter 4, using the demonstrator i-TED5.3.

1.3.1 Dynamic Electronic Collimation (DEC)

Two of the most relevant aspects of a Compton camera are the detection efficiency and the image resolution. In the case of i-TED, the former allows a measurement to be performed in a reasonable time. The second is directly related to the ability of i-TED to reject background. In this section, we delve into these two characteristics of this detection system via the DEC concept [132].

Assuming that the energy E_γ is known, the angular resolution associated to the uncertainty in the calculation of the Compton angle θ is given by [133]

$$\delta\theta = \frac{1}{sin\theta}\left[\left(\frac{m_e c^2}{E_2^2}\right)^2\left(\frac{\delta E_2}{E_2}\right)^2 + 2sin^2\theta\left(\frac{\delta r}{r}\right)^2\right], \tag{1.4}$$

where r is the distance between the first and the second interaction, and δ denotes the uncertainty in the quantities.

The first conclusion obtained from Eq. 1.4 is the importance of minimizing uncertainties in energy δE and position δr to improve the angular resolution. To this aim, a complete characterization of i-TED is performed in Chapter 3. However, more information can be deduced from that expression. Let us assume energy and position resolutions of 6.5% and 1 mm FWHM at $E_\gamma = 1$ MeV, respectively for the interactions in each stage. These quantities are realistic as it will be seen in Chapter 3. For a sample position r sufficiently far from the detector, one can assume to a good approximation $r \approx d_f/cos\theta$, where d_f is the distance between the detection planes. The suffix f is selected to denote the similar behaviour obtained by varying this quantity compared to the focal distance of a regular photo camera. Therefore, the angular resolution can be expressed as a function of the *focal distance* d_f.

Fig. 1.5 shows the angular resolution in color scale as a function of the focal distance and the Compton angle. The worst results are obtained near to 0° and 180° due to the presence of the factor $1/sin\theta$. Between 20° and 120° the angular resolution improves as d_f increases. However, increasing the focal distance will reduce the detection efficiency. This interplay between resolution and efficiency by varying the focal distance is known as *Dynamic Electronic Collimation* [134]. The latter offers the possibility to select a trade-off configuration in each measurement, or even using several configurations in the same measurement to achieve a better overall performance of i-TED. In order to obtain more details about this feature of i-TED, the reader is referred to reference [132].

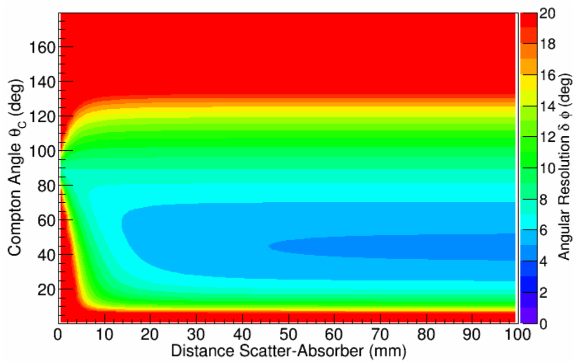

Figure 1.5: Calculated angular resolution for a Compton camera with 6.5% and 1 mm FWHM in energy and position resolutions respectively at $E_\gamma = 1$ MeV, as a function of the focal distance d_f. Extracted from [132]

Chapter 2

i-TED components and i-TED5.3 demonstrator

i-TED will have to deal with the high level of background expected in the measurement of the neutron capture cross section of ^{79}Se (see Sec. 1.1), or other similar isotopes. Excluding the activity of the sample, this background corresponds to the sum of the intrinsic and extrinsic neutron sensitivity (see Sec. 1.2). The design of i-TED and the materials selected for its construction have been carefully chosen to minimize the intrinsic background component, while keeping the detection efficiency as high as possible.

This chapter describes the materials used to build i-TED. In order to detect the γ-radiation and measure the energy and position of these γ-ray interactions i-TED features scintillation crystals optically coupled to silicon photomultipliers, which are introduced in Sec. 2.1 and Sec. 2.2, respectively. The electronic readout system based on Application-Specific Integrated Circuits (ASICs) and Field Programmable Gate Array (FPGA) modules, and the Graphical User Interface (GUI) developed to its control, are explained in Sec. 2.3. All these components are focused on assembling a demonstrator called i-TED5.3, which will be described in Sec. 2.4.

2.1 Scintillator

Nowadays, many of the γ-ray detection systems employed in neutron capture measurements rely on coupling a scintillator to an electronic light sensor [76, 77, 59, 78]. This section focuses on the former, whereas the latter will be addressed in Sec. 2.2.

A scintillator exhibits the property known as *luminescence* [135]. Materials with this property absorb radiation and emit visible light. The number of photons generated will depend on the energy deposited by the detected radiation and the scintillation material itself. A particular scintillator emits a characteristic number of photons per unit of energy deposited. This is known as the light yield of the scintillator, and the higher it is, the better the energy resolution that the final detection system can achieve. On the other hand, the cumulative distribution, that contains the wavelength values of all the photons generated, has a characteristic shape for each scintillation material. In this distribution, the wavelength corresponding to the peak of maximum emission is taken as the representative wavelength of the material. Another important property is the decay time, which is the time after which the intensity of the light pulse has returned to $1/e$ of its maximum value. Most scintillators are characterized by more than one decay time and usually, the effective average decay time is mentioned.

The properties of the scintillators such as the light yield, wavelength or decay time will depend on the nature of the luminescence process and they are unique for each material. According to these properties, a particular scintillation material is selected depending on the final application of the radiation detector. For example, C_6D_6 detectors take advantage of an organic liquid scintillator with a very fast response ($\sim$ 3 ns), which is crucial to apply the ToF technique. On the other hand, the TAC consists of high-density inorganic BaF_2 crystals that increase the detection efficiency. In the case of i-TED, the following properties are required for the candidate scintillator:

- Fast response (short decay time): necessary to apply the ToF technique.
- High light yield: that ensures the high energy resolution required by i-TED to apply the Compton imaging technique.
- High density and high average Z: to maintain a reasonable detection efficiency despite using small detection volumes. As it will be explained in Sec. 3.3, a better resolution in the position reconstruction of the incident radiation is obtained by employing thin scintillators. Therefore, the use of a high density material is also an important point in i-TED to apply the aforementioned Compton imaging technique.
- Low neutron capture cross section: to minimize the intrinsic neutron sensitivity of i-TED.

Organic scintillators are discarded due to their low density ($\lesssim 1$ g/cm^3) and their low photon production yield ($\sim$ 9 photons/keV for C_6D_6). In the following, different options based on inorganic materials will be discussed. Tab. 2.1 shows the main properties of the most commonly employed inorganic scintillation crystals. BaF_2 is not indicated for i-TED due to its low light yield and its relatively high decay time. BGO ($Bi_4Ge_3O_{12}$) is discarded for similar reasons. NaI(Tl) improves both, the decay time and light yield, but the former is still very long. In contrast, LYSO(Ce) (Lu_2SiO_5:Ce) improves the decay time while light yield is reduced by a factor of two. The most promising options are $LaBr_3$(Ce) or $LaCl_3$(Ce), which have the shortest decay time while keeping a high light yield. Although in principle the $LaBr_3$(Ce) scintillator seems a better choice owing to efficiency, $LaCl_3$(Ce) crystals are finally mounted in i-TED due to their lower intrinsic neutron sensitivity.

In inorganic crystals, the scintillation mechanism is characteristic of the electronic band found within each of them [135]. When a γ-ray impinges inside the volume of an inorganic scintillator, it can promote an electron from the valence

Scintillator material	Wavelength[a] (nm)	Decay time (ns)	Light yield (photons/keV)	Density (g/cm^3)	$\langle\sigma_{n,\gamma}\rangle$[b] (mb)
BaF_2	310	630	10	4.893	16
BGO	480	300	8-10	7.13	11
NaI(Tl)	415	230	55	3.67	325
LYSO(Ce)	410	40	25	7.15	380
$LaBr_3$(Ce)	380	25	63	5.2	390
$LaCl_3$(Ce)	350	28	49	3.86	22

Table 2.1: Main properties of some of the most commonly used inorganic crystal scintillators [136].

[a] Wavelength of maximum emission.
[b] Calculated at 30 keV by weighting the neutron capture cross section of the individual components by their mass fraction.

band to the conduction band by Compton, photoelectric or pair creation effect. This electron excites many other electrons by a cascade effect. The posterior de-excitation of these electrons to their previous state causes radiation to be emitted in the visible range. The amount of photons generated will be proportional to the energy of the primary electron, which approximately corresponds to the energy deposited by the γ-ray. This gives the spectroscopic response of a particular inorganic scintillator since the amount of photons generated depends on the deposited energy of the detected γ-ray.

Regarding the decay time, $LaCl_3$(Ce) crystals in particular do not show a unique decay time but a temporal distribution whose shape depends on the Ce concentration [137]. As it is shown in Fig. 2.1, for a $\sim$ 10% Ce doped $LaCl_3$ crystal such as those used in i-TED, 70% of the total number of scintillation photons are generated 20 ns after γ-ray impact. Nevertheless, this time increases up to 233 ns to collect 99% of generated photons.

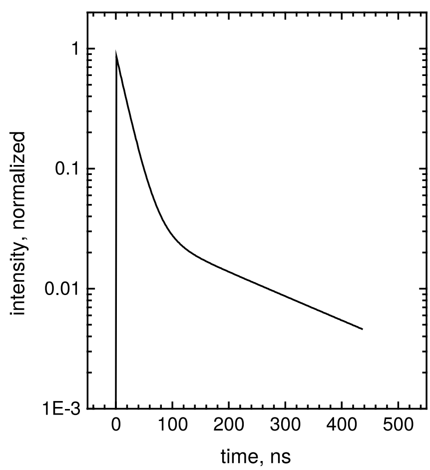

Figure 2.1: Decay time distribution of $LaCl_3$(Ce). Extracted from [137].

However, one drawback of employing $LaCl_3$(Ce) crystals is related to the activity of the natural lanthanum with which they are produced. Particle emission occurs due to the disintegration of the radioactive ^{138}La ($t_{1/2} = 1.06 \times 10^{11}$ y) and its subsequent daughters [138]. Although ^{138}La represents only 0.09% of natural lanthanum, the radiation generated creates an unavoidable background whose intensity only depends on the crystal pureness. This background consists of X-rays, γ-rays , β and α particles with energies between 1.4 MeV and 2.8 MeV. Owing to the random nature of this radiation, the induced background is highly suppressed in i-TED after building the time-coincidence events and applying a ToF window, as it will be shown in Sec. 4.2.

Fig. 2.2 shows a picture of two square-faced $LaCl_3$(Ce) crystals with a surface area of 50 $\times$ 50 mm^2 and different thicknesses. All $LaCl_3$(Ce) crystals employed in this work have been purchased to Beijing Scitlion Technology Corp. [139]. Since these crystals are hygroscopic, they are encapsulated to protect them from humidity. Five of the six faces of the crystals are covered by reflective coating (polytetrafluoroethylene or PTFE), which acts as a reflector preventing photons from escaping from the crystal volume. The remaining face is optically coupled to a 2 mm silica glass window that allows the passage of light for its subsequent collection at the photosensor. Finally, a 0.5 mm aluminum housing covers the PTFE reflector for mechanical protection of the crystal, and its complete isolation.

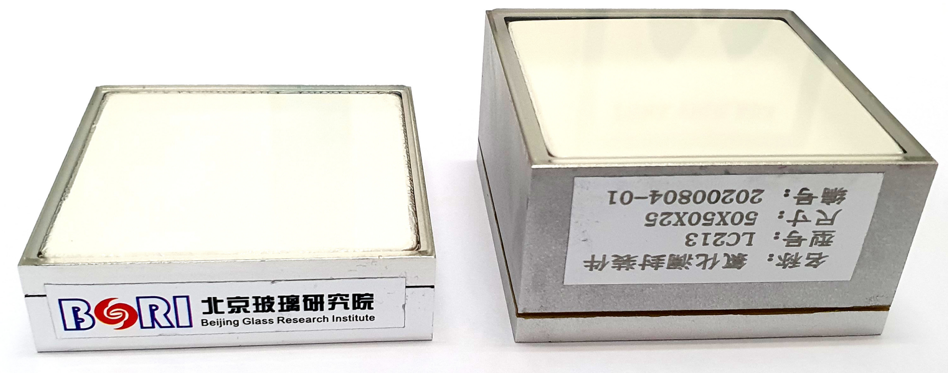

Figure 2.2: From left to right, picture of 10 mm and 25 mm thick $LaCl_3$(Ce) crystals tested during the i-TED development.

2.2 Photosensor

As mentioned above, a photosensor is optically coupled to the scintillator in order to collect the maximum number of photons generated and convert them into an electrical pulse whose amplitude is proportional to the amount of photons detected.

Traditionally, photomultipliers tubes (PMTs) have been extensively used as photosensors in nuclear physics [76, 77, 59]. However, information about the location where the scintillation photons hit cannot be obtained using these devices. In order to obtain this information required for i-TED, a multianode photomultiplier tube (MAPMT) could be employed [115, 140, 141]. In this case, the excessive length of the tube ($\sim$ 4 cm) does not allow the i-TED detection planes (scatter and absorber) to get closer than this distance. Compared to the 1 cm distance established between detection planes during the proof-of-concept experiment (see Sec. 4), the efficiency falls a factor of two with this minimum separation of 4 cm [132]. A further drawback of using PMTs and MAPMTs is their sensitivity to magnetic fields.

A solution to obtain the energy and position information of the detected radiation using pixelated silicon photomultipliers (SiPMs) was found. The SiPM is a solid state photodetector made of an array of thousands of integrated single-photon avalanche photodiodes (SPADs) distributed in pixels. Each SPAD is essentially a p-n junction that, during operation, is biased in reverse mode above the breakdown voltage. This is called the *Geiger mode* of the SPAD [142]. When a photon impinges on this device, a pair electron-hole (e-h) is created. The applied voltage creates an electric field in the junction, where the e-h pair drifts in opposite directions. This electric field is high enough that electrons can create other e-h pairs via impact ionization, as represented in Fig. 2.3. The electron avalanche formed generates an amplified electrical pulse that can be measured. Furthermore, the amplification process is fast enough ($\sim$ 10 ps) to obtain very good temporal information of the arrival of photons. However, the SPAD generates the same output pulse regardless of the initial number of photons detected. Therefore, by itself, the SPAD has no spectrometric response. Placing thousands of these devices closely together gives an overall spectrometric response to SiPMs. That is, the number of SPADs activated in an event, and therefore the intensity of the final pulse, will be proportional to the initial number of photons. As mentioned above, these SPADs are grouped in pixels. Pixelation allows obtaining information about the charge deposited by an event through a two-dimensional distribution. An analytical form can be adjusted to the latter to extract the interaction point of the initially detected γ-ray. Further details on obtaining the spatial information will be given in Sec. 3.3.

Fig. 2.3 shows a picture of the ArrayJ-60035-64P-PCB photosensors from SensL [144] employed for i-TED. These photosensors feature 8$\times$8 pixels over a surface of 50$\times$50 mm^2. Each 6$\times$6 mm^2 pixel contains 22292 square SPADs of 35 μm size.

In order to compare the energy resolution obtained with a traditional PMT (Hamamatsu R6236) and with a SiPM (SensL ArrayJ-60035-64P-PCB), a comprehensive study was performed [145]. Three SiPMs were optically coupled to monolithic $LaCl_3$(Ce) crystals with 10 mm, 20 mm and 30 mm thicknesses, respectively, to measure their response to 662 keV γ-rays. The response of each crystal-photosensor combination was simulated, and the resulting ideal deposited energy spectrum was convoluted by a Gaussian distribution to match the experimental one. Measurements made with the SiPM photosensor showed a

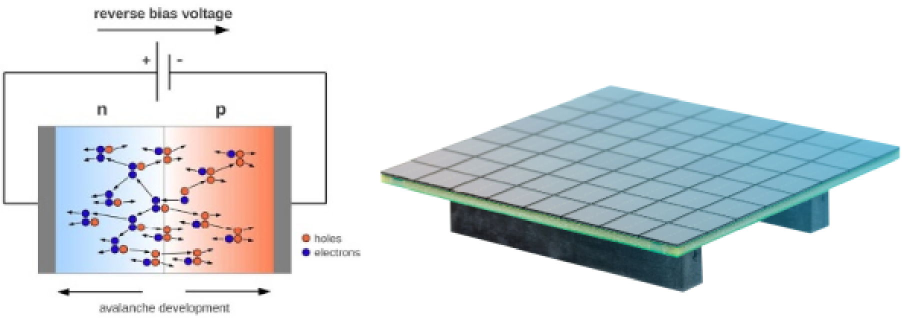

Figure 2.3: (Left panel) Detail of working of a SPAD device in Geiger mode. Extracted from [143]. (Right panel) Picture of the pixelated SiPM used in the development of i-TED.

similar or better energy resolution than those carried out with the conventional PMT. On average, the resolution obtained in that study with SiPM readout was 3.92% FWHM, compared to the 4.49% FWHM found for the measurements with the PMT.

In addition to the energy resolution, one of the main advantages of using SiPMs instead PMTs, is the lower operational voltage of the former ($\sim$ 30 V) with respect to the latter (0.8-1.5 kV). Furthermore, unlike PMTs, SiPMs are insensitive to magnetic fields. Nevertheless, one of the main advantages of employing SiPMs is their slim packaging ($\sim$ 2 mm) that allows i-TED to operate in a very close configuration of its detection planes, which maximizes efficiency and fully exploits its DEC feature [132]. In contrast, spurious pulses can be produced by SiPMs due to the thermal generation of carriers in the semiconductor. This effect has to be minimized with the use of thresholds, while it can only be reduced by better production processes and material pureness. Finally, both photosensors have the disadvantage of being sensitive to temperature fluctuations, an effect which is more severe for SiPMs.

2.3 Readout electronics

The readout electronics are intended to amplify the SiPM output pulses and digitize them for later analysis. A typical electronic chain connected to a PMT is composed by:

- A preamplifier to amplify the signal from the PMT. This device is generally located close to the PMT to avoid losses.

- An amplifier that amplifies the signal from the preamplifier and gives it a convenient shape for further processing.

- An analog-to-digital converter (ADC), which converts an analog signal into digital values proportional to the amplitude of the initial signal.

- A high voltage (HV) supply to power the PMT.

Due to the lower operational voltage of SiPMs compared to PMTs, the use of the HV power supply in i-TED is not necessary. Considering the large number of channels presented in i-TED, 192 channels for i-TED5.3 and 1280 for the future complete i-TED system (see Sec. 2.4), the amount of cables, preamplifiers, amplifiers and ADC modules required by a conventional readout approach would be impractical. For that reason, another strategy was followed.

The i-TED readout electronics rely on the SiPM readout system developed by PETsys Electronics [146]. This system is purely based on integrated circuit modules that allow many channels to be read with very compact devices. All the aforementioned components in the electronic chain are contained in two elements: a front-end and a back-end module. The former consists of ASICs, whereas the latter employs a FPGA board. This electronic system was initially designed for medical applications [147], and it was adapted and applied for Compton imaging in the present work. As it will be seen in the following sections, apart from its good performance, one of the main advantages of using this readout electronics is the compact size and the scalability of the system.

2.3.1 Front-end electronics

The TOFPET2 ASICs were specially designed for the readout of SiPM signals in Position Emission Tomography (PET) applications, by exploiting the ToF technique for enhanced performance [148, 149]. As discussed in [150], the resolution of the PET image can be improved by measuring the ToF of the two photons from the positron-electron annihilation with a time resolution below 200 ps FWHM. The temporal resolution of the TOFPET2 ASIC, ranging from 118 ps to 223 ps FWHM [151], achieves this goal and makes this ASIC particularly interesting for our application in ToF (n,γ) experiments, where a good time resolution is also required.

The TOFPET2 ASIC is developed in CMOS 110 nm technology and it features 64 independent channels in a coin-sized device. Fig. 2.4 shows a picture of this chip and a simplified schematic view of only one of its channels. The latter is formed by independent preamplifiers, amplifiers, discriminators, time-to-digital converters and charge-to-digital converters for digitizing energy and time of the input analogue SiPM signals. During ASIC operation, a signal from one selected preamplifier is replicated into three branches: T, E and Q.

- The T branch has a postamplifier specialized for time resolution with a programmable threshold down to a few photoelectrons. The low level of

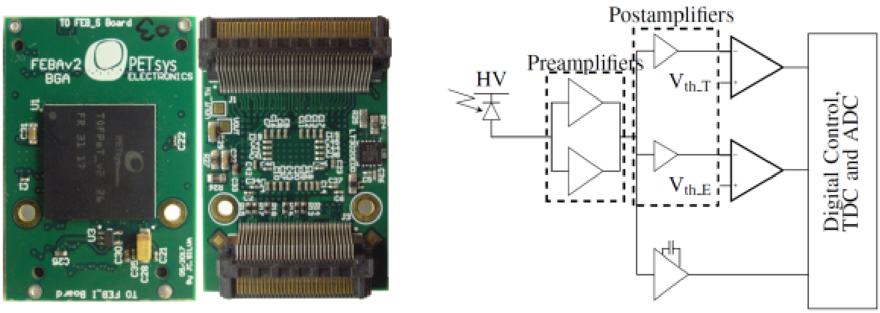

Figure 2.4: (Left panel) Picture of a TOFPET2 ASIC from PETsys [152]. (Right panel) Scheme layout of an only channel. Extracted from [153].

this threshold improves the prompt detection of the event and the temporal resolution of the ASIC.

- The E branch postamplifier focuses on triggering pulses with a threshold higher than that of the T branch. This threshold is used for on-chip rejection of low amplitude signals associated with dark current in SiPMs.

- The Q branch is directly a charge-to-amplitude converter that integrates and digitizes the charge of the event.

The signals from the three branches are fed into a digital logic block that works at 200 MHz of clock frequency and controls the two time-to-digital converters (TDCs) and the charge integrator. Two TDCs measure the rising and falling edge of the low and high threshold discriminators respectively. The time difference of the two measurements can be used to compute the time over threshold (ToT), which is dependent on the pulse amplitude. Thus, the employed architecture allows to digitize the amplitude of a pulse with both, QDC and ToT methods.

2.3.2 Back-end electronic

The FEB/D-1024 module provides the voltage supply for the ASICs, builds-up the event data and runs the interface for the data acquisition. Fig. 2.5 shows a picture of this global controller which has a Kintex-7 FPGA_XC7K160T, a communication mezzanine and a bias voltage mezzanine. Up to eight FEM128 modules can be connected to the FEB/D board, each FEM128 hosting two 64-channel TOFPET2 ASICs. The total number of readout channels can be further increased by using several FEB/D boards measuring in synchronous mode. For that, all modules are connected via an external Clock&Trigger module also shown in Fig. 2.5. The latter allows implementing a hardware event selection, collecting time information from all the FEB/D modules and transmitting only coincidence events.

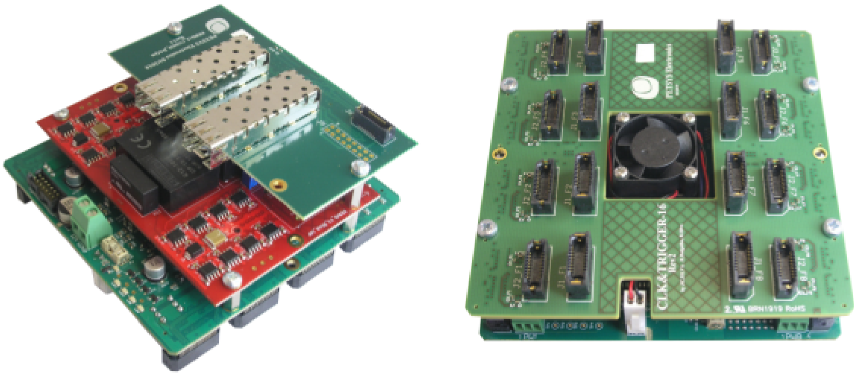

Figure 2.5: (Left panel) FEB/D-1024 board designed by PETsys [152] (Right panel) The Clock&Trigger module required to operate several FEB/D boards in coincidence.

The FEB/D module can be connected to a computer via Ethernet to send digitized event data. The latter consists of an event time, a channel identifier and the measured charge. This data is sent to the computer with a maximum output rate of 15 Mevents/s.

PETsys has also developed a DAQ board that collects data from FEB/D modules and sends it to a PC using a $\times 4$ PCI express port. Both components are connected by means of SFP+ optical/copper connectors. Several FEB/D boards can be chained while transmitting data by only one optical link. The complete system formed by the DAQ board, Clock&Trigger and FEB/D modules can be scaled to handle tens of thousands of SiPM channels.

2.3.3 Graphical User Interface (GUI)

A GUI has been developed in the HYMNS project to communicate with the SiPM readout electronics system PETsys [152] and to control the data acquisition. Fig. 2.6 shows a screenshot of this software which is written in Java and C++.

In addition to starting and stopping the acquisition, this GUI offers other interesting options to control the process such as:

- selecting the threshold configuration for all ASICs employed,
- setting the measurement time,
- programming a series of measurements,
- controlling the micropositioning stage that is mounted below the array of absorber detectors to accomplish the Dynamic Electronic Collimation (see Sec. 2.4),

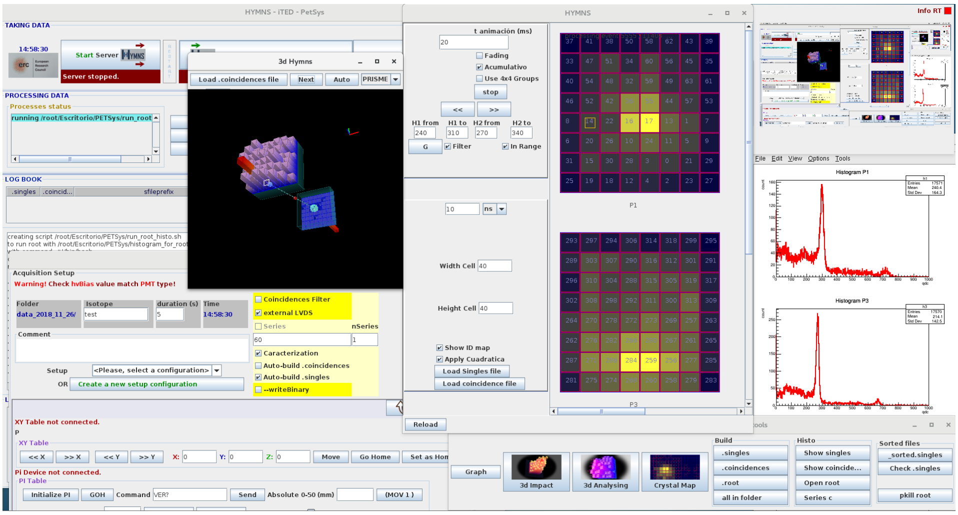

Figure 2.6: Screenshot of the Graphical User Interface developed in the HYMNS project to control the SiPM readout electronics by PETsys [152]. Several pop-up windows are displayed to show the various utilities of this software.

- or enabling the use of an external trigger for ToF measurements (see Sec. 4.3).

Other options are related to the control of different widgets present in the laboratory for the characterization of the detector, such as the XY table that will be introduced in Sec. 3.3 or the vertical gantry employed in the characterization of the Compton image (see Sec. 3.5.1). Finally the software has also tools to check the quality of the data taken, either by showing them in histograms or in three-dimensional maps.

2.4 i-TED5.3 demonstrator

As mentioned in Sec. 1.2, the complete i-TED system will feature four Compton modules, each of them with two detection planes: the scatter and the absorber. The latter is four times oversized with respect to the former in order to increase detection efficiency and angular resolution. Each detection module is formed by Position Sensitive Detectors (PSDs). A PSD consists of a monolithic $LaCl_3(Ce)$ crystals optically coupled to a pixelated SiPM. Thus, each scatter plane will be composed by one PSD hosting a 15 mm thick crystal, whereas every absorber plane will have four PSDs each with a 25 mm thick crystal. A total of 1280 channels will be readout by 20 ASICs connected to three FEB/D-1024 modules that will be working in synchronous mode using the Clock&Trigger module.

With the aim of performing a proof of concept experiment of this novel system, a demonstrator named i-TED5.3 was built in this PhD thesis. For material availability reasons, the demonstrator consisted of three PSDs mounted as shown in Fig. 2.7. The scatter has a 10 mm thickness crystal and the absorber plane contains two 25 mm thick crystals. The selection of these particular scintillator thicknesses will be justified in Sec. 3.3 after introducing details on the position reconstruction procedure. All scintillators are optically coupled to SiPMs by means of a silicon grease (BC-630 from Saint Gobain) to ensure maximum light collection. The TOFPET2 ASICs employed to read the pixelated SiPMs are thermally coupled to 20×20 mm^2 Peltier cells (FPH1-7106NC) by a silicone-free heat transfer compound (HTCP20S from Electrolube) to minimize gain shifts due to changes in operating temperature. Also the hot side of every Peltier cell is thermally coupled to a small aluminum heat sink assembled to a mini DC-axial fan (MC36358 from Multicomp), which helps to dissipate heat efficiently. On the other hand, although the DEC technique was not used during the proof of concept experiment, this feature was implemented in i-TED5.3 by means of a micropositioning stage (M-683 from PI-miCos) embedded under the absorber plane. This stage allows one to remotely control the focal distance d_f between scatter and absorber planes by moving the latter with sub-micrometric precision over a range of 50 mm. Since d_f is required for the Compton image reconstruction, this distance is recorded in the i-TED data acquisition system. Finally, the readout electronics for i-TED5.3 is composed by one FEB/D-1024 board that controls the three aforementioned ASICs.

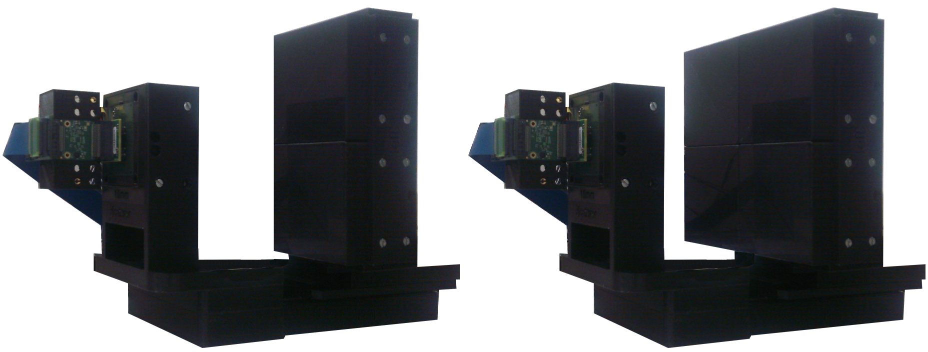

Figure 2.7: Pictures of two i-TED prototypes. (Left panel) The i-TED5.3 demonstrator with three PSDs, one scatter and two absorbers. (Right panel) The i-TED5.5 prototype consisting of five PSDs.

Later, with the availability of new $LaCl_3(Ce)$ crystals, the i-TED5.3 demonstrator was promoted to a complete i-TED module based on four absorber crystals. Only one FEB/D-1024 module was needed to read the 320 channels present in this demonstrator. The latter was employed in laboratory measurements that are referenced throughout this work such as those dedicated to characterize the DEC [132], which are mentioned in Sec. 1.3.1. Furthermore, a set of measurements performed with this device to characterize the final Compton image will be addressed in Sec. 3.5.1.

Chapter 3

Detector Characterization

i-TED aims to reject an important part of the experimental background expected during the cross section measurement of the ^{79}Se(n,γ) reaction (see Sec. 1.1), and other similar ones, by applying the Compton imaging technique introduced in Sec. 1.3. To this aim, the 3D coordinates of the interaction position and the energy deposited by the γ-ray in the two detection planes need to be reconstructed as accurately as possible. This chapter describes the i-TED methodology and characterization required to obtain this information, while keeping the detection efficiency as high as possible.

As introduced in Sec. 1.2, the efficiency is a key aspect for i-TED since its final configuration will have a factor of 3-4 lower efficiency than the C_6D_6 detectors [62]. For that reason, in order to obtain reliable data from the mentioned proof of concept experiment (see Chapter 4), the characterization shown in this chapter focuses on developing methodologies to keep the discrimination efficiency as high as possible despite limiting other aspects of the detector. This means that we will have more room for improvement when the final device is implemented.

In this chapter, Sec. 3.1 describes how events are built from the raw data that is collected by the readout electronics. The posterior energy calibration of every Position Sensitive Detector (PSD) in i-TED will be explained in Sec. 3.2. On the other hand, the spatial response of all PSDs is characterized to obtain a good resolution in the measurement of the interaction position of the detected γ-ray. The details on this characterization will be given in Sec. 3.3. After optimizing the energy and spatial resolutions, a coincidence criterion is imposed between the γ-ray interactions in the scatter and absorber detectors to build the coincidence events, as it will be introduced in Sec. 3.4. The back-projection algorithm, presented in Sec. 1.3, is applied over these coincidence events to obtain an image of the radiative point source. Sec. 3.5 shows some Compton images obtained in real measurements using the i-TED5.3 demonstrator. Furthermore, this section includes more precise results obtained using the improved device i-TED5.5 (see Sec. 2.4).

The tasks necessary to obtain most of the results contained in this chapter were carried out by developing programs written in C++ [154], which employ the CERN ROOT libraries [88].

3.1 Event building

As discussed in Chapter 2, SiPMs collect scintillation photons generated in the volume of $LaCl_3$(Ce) monolithic crystals after γ-ray interactions. If the electronic pulse generated by a single pixel exceeds the thresholds explained in Sec. 2.3.1, it is individually processed by the readout electronics and sent to the computer for further processing. Digitized data consists of a buffer of events containing three values:

- a unique identifier (ID) that distinguishes the channel or pixel fired,
- the timestamp of the processed signal,
- and the charge integrated by the ASIC.

Tab. 3.1 shows some entries from the outgoing data stream file that correspond to a ToF measurement of the ^{197}Au(n,γ) cross section with i-TED5.3. This measurement belongs to the proof of concept experiment whose details will be given in Chapter 4. The first column shows the timestamp of the pixels expressed in picoseconds with a resolution of $\sim$ 26 ps RMS [151]. The charge integrated for each pixel is listed in the second column, whereas the final one corresponds to the pixel ID. In fact, the last column corresponds to the absolute channel ID assigned to a certain pixel by the readout electronics. This identifier is calculated with Eq. 3.1, in which the *chipID* is referred to the number of the port in which the ASIC is connected within the FEB/D module, and the *channelID* is the number of the triggered pixel.

763719708809	21.104099	410
763719710647	28.386639	435
763719708826	16.941536	384
	...	
764043910219	9.992325	62
764043910447	17.190903	34
764043909716	26.687435	41
	...	
764661578567	5.170795	270
764661578530	4.620186	259
764661574209	5.762665	303

Table 3.1: Raw data from a real neutron capture experiment performed with i-TED5.3.

$$Absolute\ channel\ ID = 64 \times chipID + channelID \tag{3.1}$$

In order to build an event, each entry in the data file shown in Tab. 3.1 is assigned to the corresponding PSD using the absolute channel ID. The entries of each PSD are sorted by time, and the temporal differences with the first one of each list are calculated. An event is composed by all entries of a particular PSD within a constant delta time Δt_{ev} selected by the user. In the software provided by PETsys to construct the events [152], the default value is $\Delta t_{ev} = 100$ ns. Despite of obtaining good results using this value, we have studied the impact of a variation in this quantity. This variation is made between reasonable limits taking into account the decay time distribution of $LaCl_3(Ce)$ shown in Sec. 2.1. Since the time resolution of the electronics is of tens of picoseconds, the decay time of the crystals becomes the reference time required to collect the maximum number of scintillation photons generated in each single event.

A reduction of Δt_{ev} can cause the division of long-time events into others of shorter duration and less energy deposition. This may lead to a worsening of the resulting energy resolution and the increase of artifacts from a bad event reconstruction. For that reason, the integration window to build events Δt_{ev} must be wide enough to not degrade the energy resolution. The deposited energy spectra from radioactive sources are a good tool to evaluate the possible loss in energy resolution after a reduction in this parameter. Fig. 3.1 shows these spectra corresponding to the measurement of the ^{22}Na and ^{137}Cs sources with activities of 416 kBq and 210 kBq, respectively. These sources were placed at 15 mm and 100 mm from the scatter of i-TED5.3 during 60 s and 300 s. The energy resolutions at 511 keV and 662 keV are quantified in Tab. 3.2 for different values of Δt_{ev}. The results for $\Delta t_{ev} = 40$ ns at 511 keV and 662 keV are 28% and 16% worse than those obtained using the default value $\Delta t_{ev} = 100$ ns. However, compatible energy resolutions are obtained for integration times ranging between 70 ns and 200 ns. Therefore, valid values for Δt_{ev} are within this time window. It is worth to mention that for the smallest time window (40 ns), the tail at low deposited energies increases in concordance with the production of artifacts from bad event building reconstruction.

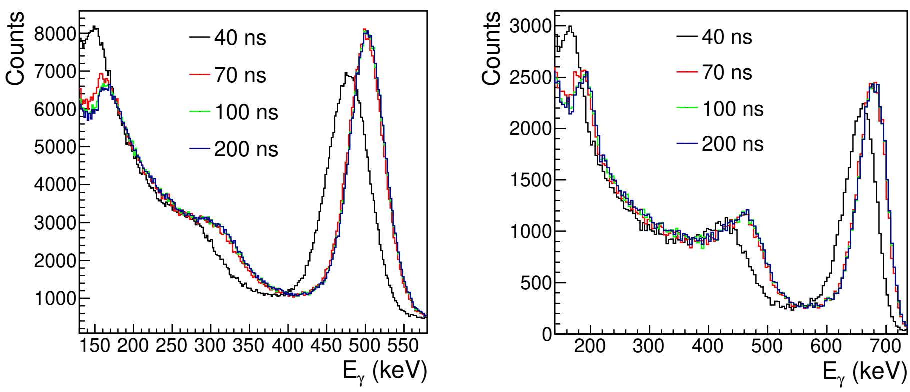

Figure 3.1: E_γ spectra of ^{22}Na (left panel) and ^{137}Cs (right panel) measured with the i-TED scatter and processed with different values of Δt_{ev}.

Δt_{ev} (ns)	40	70	100	200
FWHM/E_γ at 511 keV (%)	14.34(21)	11.31(17)	11.21(17)	11.21(17)
FWHM/E_γ at 662 keV (%)	10.18(16)	8.86(13)	8.76(12)	8.77(12)

Table 3.2: Energy resolution (FWHM) from the spectra of Fig. 3.1 at 511 keV and 662 keV.

On the other hand, in situations involving high count rates, an increment on integration time Δt_{ev} can group two or more consecutive events into only one, reducing the total number of reconstructed events and yielding to a bad energy reconstruction. A perfect example to illustrate this situation is the measurement of the 4.9 eV resonance of the ^{197}Au(n,γ) reaction. As explained in Sec. 4.7.1 of Part I, the yield close to the unit at this resonance indicates that almost all 4.9 eV neutrons in the beam are captured in the sample, ensuring the generation of a large number of γ-rays. This situation was achieved in the gold measurement carried out within the proof of concept experiment, in which the same gold sample as that employed in Sec. 4.7.1 was measured. Since the scatter of the i-TED5.3 demonstrator was located close to the sample (63 mm), a high count rate is expected in this detector. Fig. 3.2 shows a zoom in the 4.9 eV resonance of the neutron energy spectra obtained with this detector using different values of Δt_{ev}. The results for integration times ranging from 70 ns and 200 ns are compatible with each other, and no effect can be ascribed to the increment on this integration time. It is necessary a $\Delta t_{ev} = 5$ μs to see an appreciable change in this resonance. These results agree with those obtained above, where a valid value of Δt_{ev} can be between 70 ns and 200 ns. This confirms the convenience of using a 100 ns time window to build the γ-ray events.

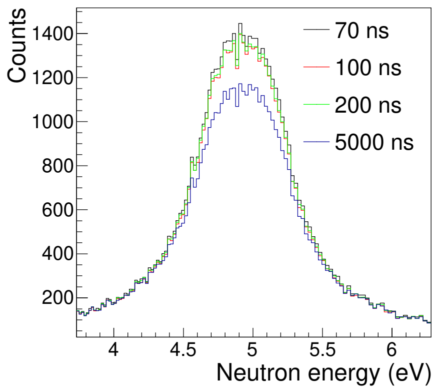

Figure 3.2: First ^{197}Au(n,γ) resonance obtained with different values of Δt_{ev}.

3.2 Low deposited energy calibration

An accurate energy calibration for all i-TED PSDs is needed in order to reconstruct the energy deposited by a γ-ray in its interactions with the detection planes. This calibration has to cover from a few hundreds of keV up to several MeV of deposited energy to become sensitive to the γ-rays generated by neutron captures. This section tackles the energy calibration of i-TED at the low energy region, which is enough to obtain good quality Compton images of radioactive sources in the laboratory, as it will be shown in Sec. 3.5.

Between 120 keV and 1.4 MeV i-TED is calibrated using a ^{152}Eu source ($t_{1/2}$ = 13.5 y). The seven most intense γ-ray transitions of this radioactive isotope, shown in Tab. 3.3, provide a reliable calibration in this energy range. Fig. 3.3 shows the deposited energy spectra directly obtained in the measurement of this source with the three PSDs of i-TED5.3.

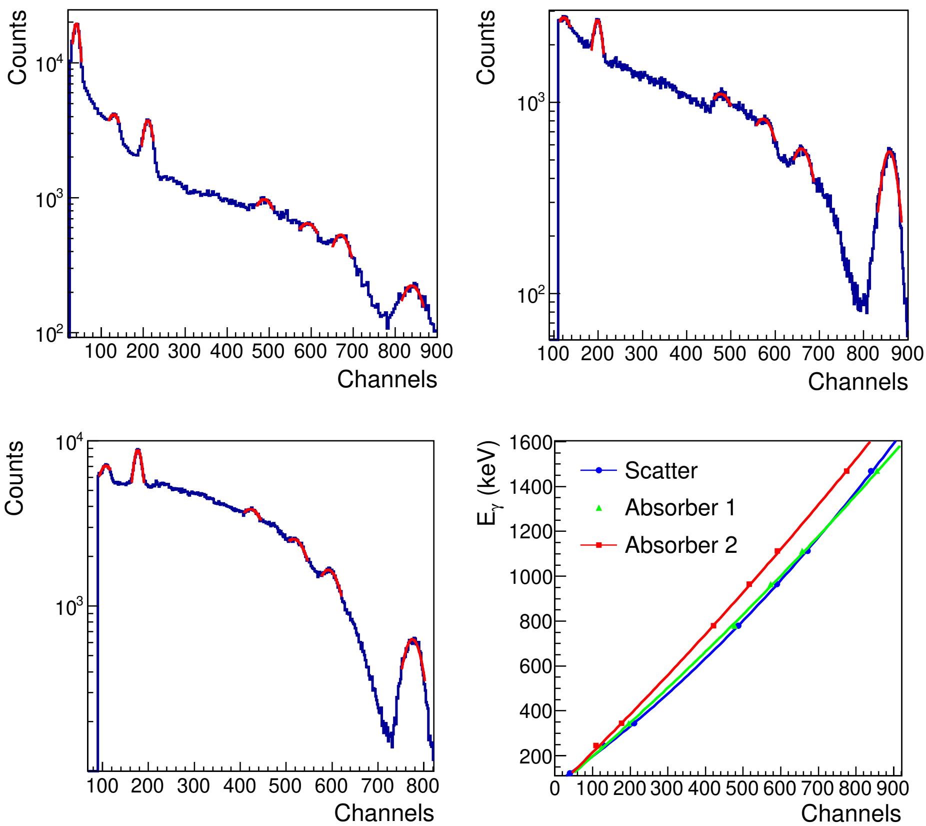

Figure 3.3: Energy spectra of ^{152}Eu measured with the scatter PSD (top left panel) and with those located in position 1 (top right) and 2 (bottom left) of the absorber plane. (Bottom right panel) Calibration functions for the three PSDs.

The three calibration functions, valid up to 1.4 MeV, obtained for the three PSDs present in i-TED5.3 are included in Fig. 3.3. The energy resolutions achieved at 662 keV using these functions are 8.8(4)%, 5.8(4)% and 6.3(4)% FWHM for the PSDs located in scatter and absorber planes, respectively.

Energy (keV)	122	245	344	779	964	1112	1408
Intensity (%)	21	6	8	4	11	10	15

Table 3.3: Energy and intensity of the seven most intense γ-ray transitions of ^{152}Eu.

3.3 Spatial response

As in the case of energy calibration, the position of the γ-ray interactions in the two detection planes of i-TED must be determined as well. The use of pixelated SiPMs allows us to infer these positions by employing algorithms specially developed for this task [155, 156, 157]. As explained in Sec. 1.3, a high spatial resolution is needed to obtain also a good resolution in the final Compton image. This will ensure a good performance of the event selection based on their incoming direction and thus a good background rejection.

In this work, we performed a systematic study to select the most appropriate positioning algorithm from those available in the literature. Furthermore, these algorithms were tested using $LaCl_3$(Ce) monolithic crystals with thicknesses of 10 mm, 20 mm and 30 mm. This provided us a solid base to select the optimum thickness for the crystals to be mounted in i-TED. Part of this study was already published in [158]. Nevertheless, this section goes deeper into some details of this study and includes some enhancements developed after the referred article [158].

Since each SiPM is optically coupled to the 50 $\times$ 50 mm^2 square face of the crystals, XY coordinates of the γ-ray interaction can be inferred from the direct measurement of the charge distribution. However, the rest of the crystal faces are covered with PTFE, thus preventing direct measurement of the Z coordinate or depth of interaction (DoI). Therefore, the DoI needs to be determined by indirect methods, such as the second moment of the light distribution. For the sake of clarity, we have divided the analysis in two different parts. Sec. 3.3.1 will address the reconstruction of the interaction points in the XY plane, whereas Sec. 3.3.2 will tackle the reconstruction of the DoI.

3.3.1 Position reconstruction in the XY plane

In order to characterize the performance of the positioning algorithms in the X and Y axes, we carried out a systematic scan of the 50 $\times$ 50 mm^2 square face of every available crystal. For this purpose, we used the experimental setup shown in Fig. 3.4 that is detailed in the following. The PSD under characterization was mounted on a small movable platform attached to a positioning XY table from Arrick Robotics [159], with 80 μm precision per step. A 10 mm thick platform from Plexiglas was fixed on top of the positioning table. This non movable bench supported a 30 mm thickness collimator made from tungsten with a cylindrical hole of 1 mm diameter. Aligned with the latter was placed a ^{22}Na source with an activity of 416 kBq. A rectangular opening in the Plexiglas (see pictures) allowed collimated γ-rays to reach the crystal surface without interference. On the other hand, an ancillary PSD was placed just above the radioactive source, aligned with it and with the PSD under characterization. This configuration, together with the hardware time coincidence filter provided by the PETsys readout electronics (see Sec. 2.3.2), allowed us to register mainly the 511 keV γ-rays in time coincidence from positron annihilation events from the β-decay of ^{22}Na at each individual scan position (X,Y).

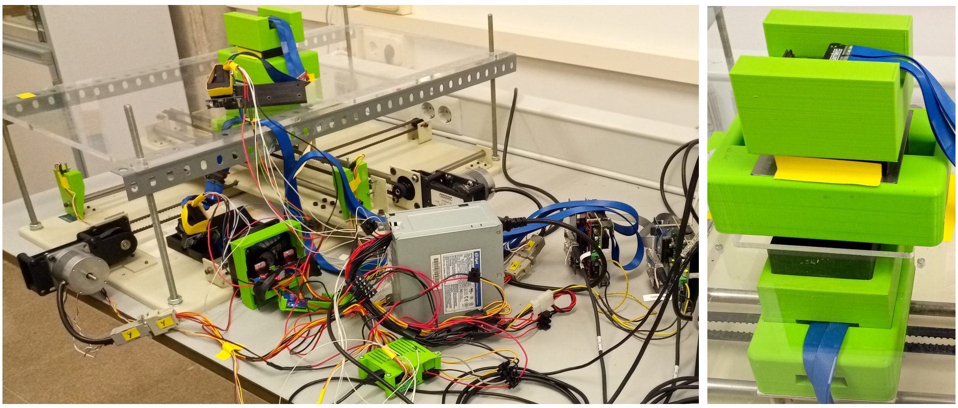

Figure 3.4: Photographs of the experimental setup employed in the position characterization. (Left panel) The XY table is shown together with the PSDs and readout electronics. (Right panel) Zoom in the arrangement composed by (from bottom to top) PSD under characterization on the movable platform, tungsten collimator attached to the ^{22}Na source, and ancillary PSD on the top.

Fig. 3.5 displays an sketched diagram of the experimental setup explained above. Each monolithic crystal of 10 mm, 20 mm and 30 mm thickness was characterized using this configuration. The grid of 35 $\times$ 35 points and 1.5 mm step with which the surface of each crystal was scanned is shown in Fig. 3.6. At each point, data were acquired during a time interval of 600 s. Thus, the scan of each PSD lasted for about 8 days.

At each scan position, the XY coordinates of every detected γ-ray are reconstructed and accumulated in a 2D histogram. The width of the resulting distribution is affected by the intrinsic resolution related to the detector and to the reconstruction algorithm itself. However, the divergence of the γ-ray beam originating from the collimator aperture, the thickness and the distance to the PSD under study also widens this distribution. In order to take into account this contribution, Monte Carlo simulations were performed using the Geant4 code [93, 94]. The experimental setup was included in the simulation with special care for reproducing all sensible distances and materials. For each crystal thickness a total of 1×10^9 events from an isotropic source of 511 keV γ-rays were simulated. The response of the ideal detector was then convoluted using a series of Gaussian functions with widths spanning from 0 mm up to 22 mm FWHM. By measuring the FWHM of the resulting distributions, we obtain the relation between the *true* or intrinsic detector spatial resolution and the total or *measurable* width. Fig. 3.6 shows the deconvolution function for the 20 mm thick crystal as an example. This analysis was performed for the 10 mm and 30 mm thick crystals as well.

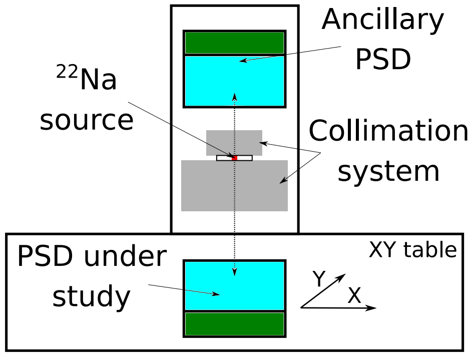

Figure 3.5: Schematic view of the experimental setup shown in Fig. 3.4.

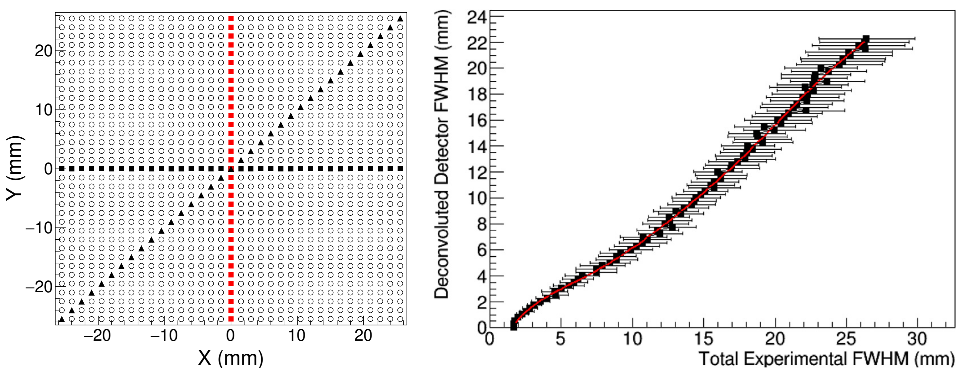

Figure 3.6: (Left panel) Schematic view of the grid with 35 $\times$ 35 scan points (open circles). Solid symbols will be used in the interpretation of the linearity curves described below. (Right panel) Deconvolution function for the 20 mm thick crystal. Extracted from [158].

Regarding the positioning algorithms, two of the most common reconstruction techniques are the Anger-logic method [155, 160] and a variation of it, the so-called squared-charge centroiding approach [161]. Although the performance of these algorithms is in actuality superseded by other techniques, the implementation of these two basic methods gives us a good start point for this study. Furthermore, they will allow us to introduce the main figures of merit used along this section. In the following sections, these two approaches are presented, as well as two other more sophisticated techniques based on analytical descriptions of position reconstruction.

Anger-logic and squared-charge techniques

The Anger technique was included in this work in order to obtain the interaction position of a γ-ray in a similar way as it is commonly done by using a resistor network coupled to an array of phototubes [155, 160]. We adapt this technique to our apparatus via software by determining the γ-ray interaction point using the mean of the charge distribution measured by the pixelated SiPMs. In the case of the squared-charge method, the mean value of the squared-charge distribution is used instead. Fig. 3.7 shows both charge and squared-charge distributions corresponding to the same γ-ray event registered in the 10 mm thick crystal. In this case, the scan position corresponds to a point shifted -9 mm in the X axis from the central position of the crystal surface, but not displaced in the Y axis, i.e. Y = 0 mm. The values for the X coordinate reconstructed with both models are -4.6 mm and -7.2 mm, respectively. Although neither of them provide the exact position, the value reconstructed with the squared-charge approach is closer to the true position (X = -9, Y = 0) mm.

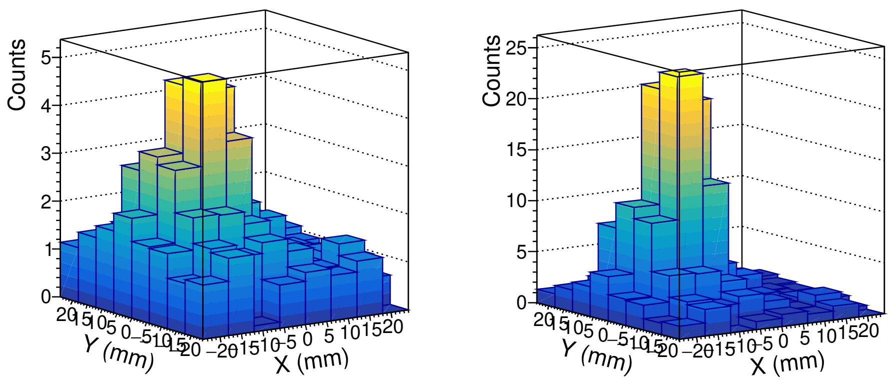

Figure 3.7: (Left panel) Charge distribution deposited by a 511 keV γ-ray in the SiPM. (Right panel) Squared-charge distribution from the same event.

The improvement achieved by the squared-centroid approach compared to the Anger method becomes more evident when comparing the 2D histograms that accumulate the positions reconstructed from all events of a particular scan position.

Fig. 3.8 shows these distributions corresponding with the *true* position (9,9) mm. The positions reconstructed using the Anger method are compressed towards the central region of the crystal surface. This compression also affects the results given by the squared-charge approach, although in a lesser extent.

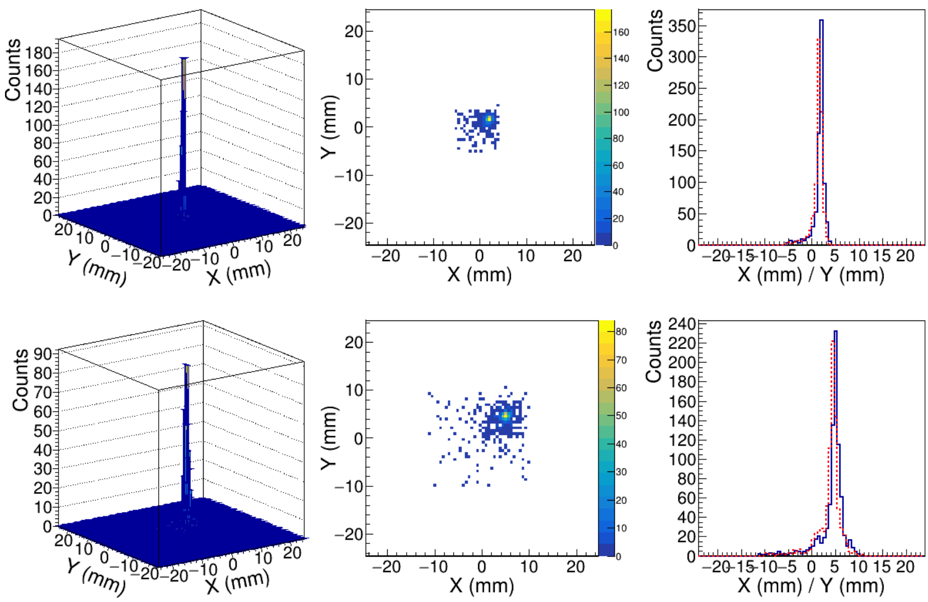

Figure 3.8: Scan positions reconstructed using the Anger (top panel) and squared-charge (bottom panel) approaches. From left to right, distribution of events, the projection in the XY plane and projections over X and Y axes.

In order to quantify the performance of each positioning algorithm, we employ the linearity graphs shown in Fig. 3.9. The latter displays data corresponding to the scan of the 35 points located within the central diagonal of the 50×50 mm^2 surface of the 10 mm thick crystal. This diagonal is represented in the schematic diagram of Fig. 3.6 with solid black triangles. The top panel of Fig. 3.9 displays the linearity curve, defined here as the relation between the mean value of the cumulative distribution containing all the reconstructed positions of a particular scan point, and the true scanned position. Reconstructed X and Y coordinates from the mentioned diagonal positions are shown with solid black circles and red squares, respectively. The behaviour of an ideal detector, in which reconstructed and true positions are equivalent, is shown with a dashed red line. As it can be seen, the linearity curves obtained with Anger and squared-charge approaches deviate quickly from the ideal behaviour already in the central region.

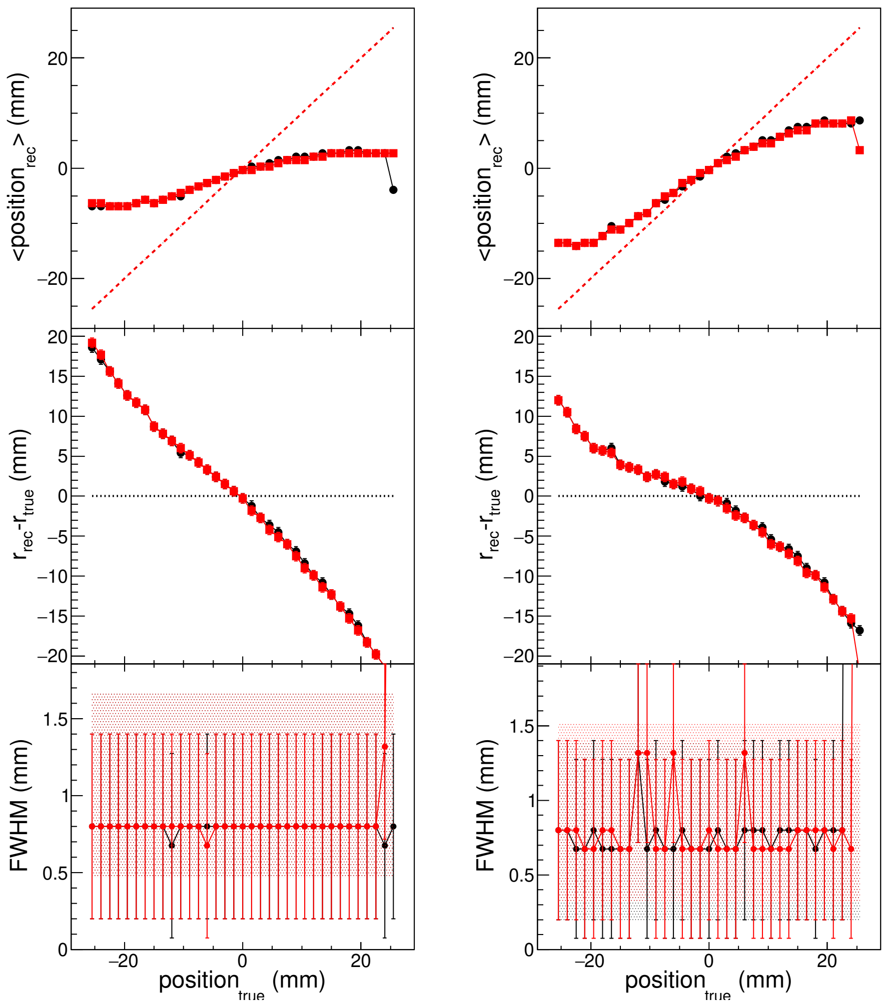

Figure 3.9: Linearity graphs obtained with the Anger (left panel) and the squared-charge (right panel) methods, corresponding to the scanned points in the diagonal of the surface of the 10 mm thickness crystal.

The middle panel of Fig. 3.9 represents the deviations RMS between reconstructed and true positions (r_{rec} - r_{true}). Hereafter these deviations (r_{rec} - r_{true}) will be referred to as dispersion in the reconstructed positions. These differences will be used in the calculation of the field of view (FoV), which is explained below. In this case, the behaviour of the ideal detector draws the horizontal black dashed line at r_{rec} - $r_{true} = 0$. Owing to the great compression of reconstructed positions obtained with the both compared methods, only those really close to the center of the crystal are usable. The lower slope of the curve obtained with the squared-charge method reflects the improvement obtained with this approach compared to the Anger logic technique.

The spatial resolution of the reconstructed positions at each scan point are displayed in the bottom panel of Fig. 3.9. These quantities are determined using the FWHM of the X and Y projection distributions included in Fig. 3.8. As it can be seen, the aforementioned spatial compression of the reconstructed positions apparently leads to resolutions of the reconstructed positions close to 1 mm FWHM. This is an artifact due to the aforementioned compression effect, being the actual resolution values much larger.

Finally, we define the field of view (FoV) of the crystal as the region of sensitive surface in which the linearity curve is close to the ideal curve. The limits of the FoV are determined separately for the X and Y coordinates. For that, we employ the scan series corresponding to the horizontal and vertical lines that are represented in Fig. 3.6 with solid black and red squares, respectively. Appendix B contains all the linearity graphs related to the horizontal and vertical lines corresponding to 10 mm, 20 mm and 30 mm thick crystals. At each axis, the FoV is delimited by the coordinates of the first two positions from the center of the crystal, which are reconstructed at a distance of 2 mm or more from the ideal curve. It is worth to emphasize that the detector is sensitive to position reconstruction along the region where the linearity curves still show a monotonically increasing behaviour. However, large linearity deviations lead to a worsening of the resolution. For that reason, the aforementioned 2 mm criterion was adopted. In the case of the Anger and squared-charge centroiding methods, the FoV becomes 20(1) mm^2 and 81(1) mm^2, respectively. Note that these quantities are below 1 cm^2 of usable FoV. A low FoV reduces the final detection efficiency of i-TED since events with positions reconstructed outside of this FoV have to be discarded or they would lead to a very poor resolution. This highlights the importance of obtaining a large FoV, an objective which is achieved with more advanced algorithms, such as those reported in the following sections.

Analytical model fit

A remarkable improvement on the position reconstruction in terms of FoV and spatial resolution can be achieved by means of more sophisticated algorithms such as the analytical models. By using the latter, it becomes possible to realistically describe the spatial propagation of scintillation photons generated by a point-like photon source in the crystal volume. Here we report on the implementation of two different analytical algorithms.

On the one hand, we have tested the model by Lerche et al. [156], whose analytical form is given by Eq. 3.2. In this equation, L_0 accounts for the intensity of the photon source, whereas α for the photon absorption in the crystal itself. Vectors $\vec{r}$ and $\vec{r_0}$ are referred to the coordinates of the observational point and the interaction position of the γ-ray, respectively. Furthermore, the term τ is included to reproduce a diffuse light registered by the pixels as a constant background.

$$L(\vec{r}) = \frac{L_0}{(\vec{r} - \vec{r_0})^2} \alpha e^{-\alpha|\vec{r} - \vec{r_0}|} + \tau \tag{3.2}$$

Since we scan the surface of all crystals with the same ^{22}Na source in identical conditions, it seems reasonable to fix L_0 and α parameters to their average values, respectively. The fixed values correspond to the mean values of the cumulative distributions for the parameters L_0 and α, obtained after a measurement in which the entire crystal surface was illuminated during 1 h with the same ^{22}Na source but without any collimation system. The reduction in the number of free parameters to be adjusted by the algorithm led to an improvement in the quality of the positions reconstructed provided by this analytical model.

On the other hand, the positioning algorithm provided in [157] has been also included in this study. The analytical form proposed by Li and collaborators is given by Eq. 3.3. As in the previous case, the A_0 parameter takes into account the intensity of the photon source. In this model, the amount of photons that arrive to the SiPM is obtained using the exact solid angle Ω subtended between the photon source position and each pixel. The term $\sigma(\theta_c - \theta)$ removes those photons that do not reach the SiPM due to total reflections at the inter-phase created between the crystal and the optical grease, which optically couples the crystal and the SiPM.

$$\begin{aligned} L(x, y, z) &= A_0 \Omega \sigma(\theta_c - \theta) + \tau = \\ &= A_0 \frac{z}{((x - x_i)^2 + (y - y_i)^2 + z^2)^{3/2}} \frac{1}{1 + e^{-\beta(\theta_c - \theta)}} + \tau \end{aligned} \tag{3.3}$$

The coordinates (x_i, y_i, z_i) are referred to the observation point or SiPM pixel coordinates, whereas (x, y, z) refer to the location of the photon source or γ-ray interaction position. θ_c is the critical angle calculated using the refractive indexes of crystals and optical grease, and θ is given by Eq. 3.4. The β parameter, used in this context as suppression parameter, has not a big impact in the position reconstruction and it was fixed in our analysis as recommended in [157]. However, unlike in the previous case, fixing A_0 parameter do not improve the resulting positions reconstructed.

$$\theta = \frac{\sqrt{(x - x_i)^2 + (y - y_i)^2}}{z} \tag{3.4}$$

In order to illustrate the performance of these analytical models, Fig. 3.10 shows the charge distribution corresponding to an event registered with the 10 mm thick crystal at the central position of the scan (0,0) mm. The analytical forms expressed by Eq. 3.2 and Eq. 3.3 are adjusted on this distribution, which is normalized to unity in order to facilitate the algorithm minimization task. The analytical form proposed by Li [157] fits, in general, better than that developed by Lerche [156], faithfully reproducing the shape of the charge distribution. The XY coordinates reconstructed for both methods are (1.6,1.7) mm and (1.6,1.9) mm, respectively, which are very close to the true position. Furthermore, the constant parameter τ present in both models take similar values, about 0.1 normalized charge units.

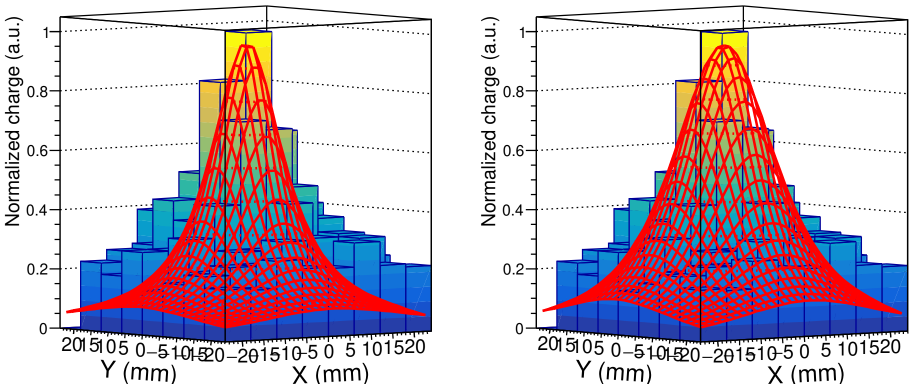

Figure 3.10: Charge distribution corresponding to the same event at the central position of the 10 mm thick crystal scan fitted with the analytical methods proposed in [156] (left panel) and [157] (right panel).

Using the same 10 mm thick crystal, Fig. 3.11 shows the scan position corresponding to (13.5,13.5) mm reconstructed with the Lerche and Li methods. The compression displayed in Fig. 3.8 is drastically reduced here and events are reconstructed along almost the entire surface of the crystal. The XY coordinates reconstructed for both methods are (14.1,13.5) mm and (13.5,13.5) mm, respectively, which are very close to the true positions.

The enhanced performance of these analytical methods is more noticeable in the linearity graphs of Fig. 3.12, which show the series of scans corresponding to the diagonal line of this 10 mm thick crystal. The linearity for both methods is ideal in most of the surface, but the last 5 mm, which correspond to the border of the crystal. In this region, reconstructed positions are compressed towards the center due to reflections in the PTFE that covers the PSDs. In fact, deviations between reconstructed and true positions are always within 1 mm, apart from the aforementioned peripheral region. The average spatial resolution is close to 1 mm, as shown in the bottom panel of the linearity graphs using colored bands, black or red, for the X or Y axes.

Tab. 3.4 quantifies the performance of the positioning algorithms employed in

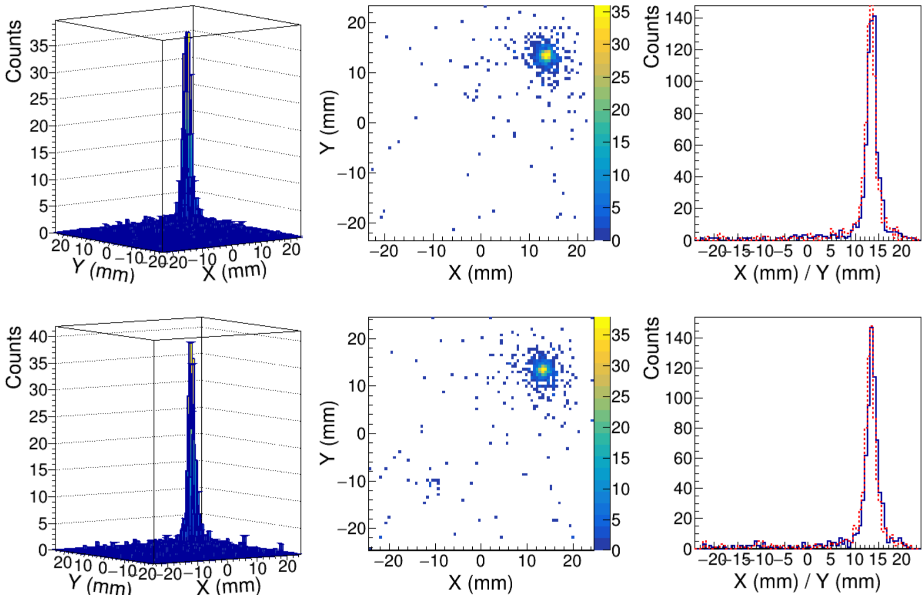

Figure 3.11: Scan positions reconstructed using the Lerche (top panel) and Li (bottom panel) approaches.

this study for the scan of the 10 mm thick crystal. In that table, the FoV, resolution and dispersion are compared. Both the resolution FWHM and the deviation RMS are determined as the average of all results for X and Y axes within the FoV. The uncertainty ascribed to the measured resolution, reported in Tab. 3.4, corresponds to the bin size of 0.6 mm. As it can be appreciated, the FoV achieved by the analytical models is between a factor of 20 to 100 times larger than those obtained with the more basic approaches (i.e. Anger or squared-charge methods). The model proposed by Li provides the largest FoV. The dispersion (see middle panels in Fig. 3.12) is reduced to the half when applying analytical models. The resolution obtained with both analytical models is similar and, on average, close to 1 mm FWHM.

In the following, the results obtained for the 20 mm thick crystal will be discussed. Fig. 3.13 shows the linearity graphs obtained for the diagonal data set. The compression effect in this crystal is more evident at the borders, affecting the last $\sim$ 7 mm. Aside from these regions, the linearity is almost ideal for both models. Regarding the dispersion, it is visibly larger than that obtained for the 10 mm thick crystal and some points within the FoV deviate by more than 1 mm. This behaviour is very similar between the models. The average resolutions (FWHM) are also similar, being slightly better those obtained by means of the Li algorithm.

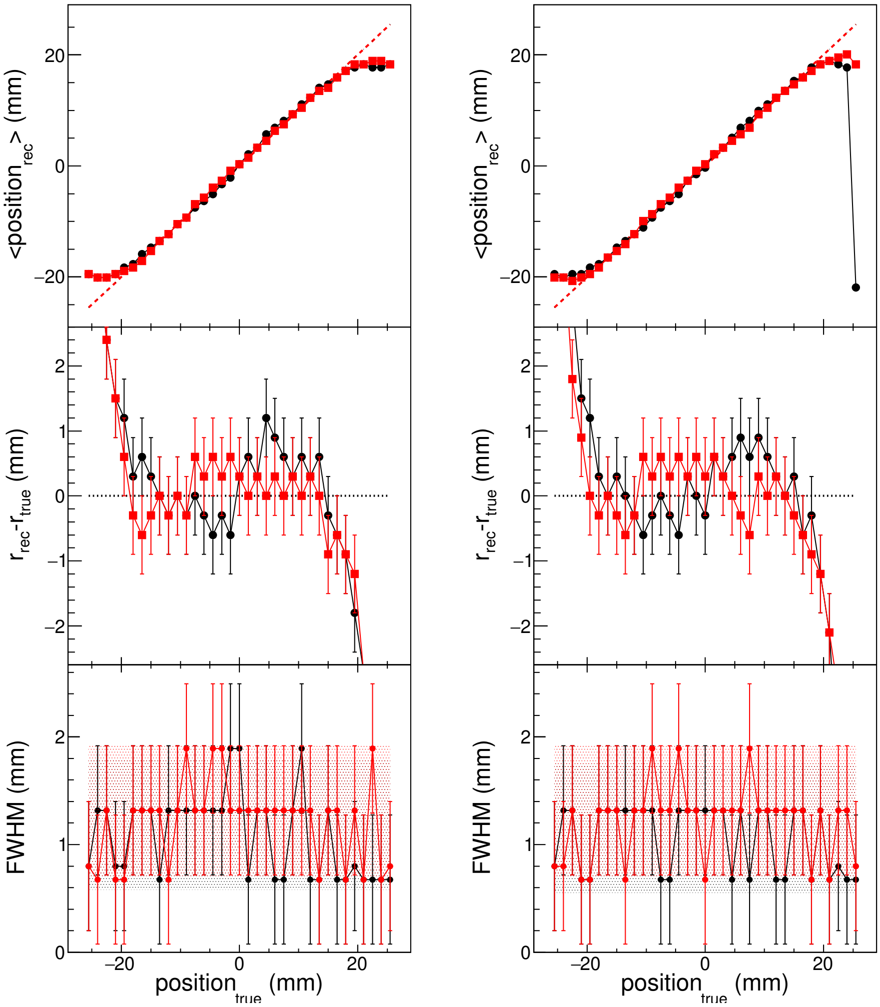

Figure 3.12: Linearity graphs obtained with the Lerche (left panel) and Li (right panel) analytical methods, corresponding to the scanned points in the diagonal of the surface of the 10 mm thickness crystal.

The performance shown so far for Lerche and Li analytical models are very similar. However, differences become more apparent when analyzing the data measured using the 30 mm thick crystal. Fig. 3.14 shows the linearity graphs obtained for the diagonal. These results are more heavily affected by the border effects previously seen in the other crystals. Here, one loses the final ~ 10 mm near

Model	FoV (cm^2)	Dispersion (mm)	Resolution (mm)
Anger	0.20(1)	1.3(6)	1.1(6)[a]
Squared-charge	0.81(1)	1.6(6)	0.9(6)[a]
Lerche	18.27(2)	0.4(6)	1.3(6)
Li	19.58(2)	0.5(6)	1.2(6)

Table 3.4: Summary of results obtained for the 10 mm thickness crystal.

[a] Uncorrected for compression effects.

the corners of the crystal, as it can be seen in the linearity curves. Although the latter look very similar, the dispersion reflects a different behaviour between both models. An increasing trend is observed for the (r_{rec} - r_{true}) differences calculated using the Lerche approach within the central 10 × 10 mm^2 region. This could suggest a misalignment during the scan, however it is not appreciated in the same data when applying the Li model. The dispersion obtained with the latter model does not apparently display any slope within the FoV. Also the spatial resolution for this approach looks more stable along the FoV, remaining always close to the average value.

Tab. 3.5 summarizes the results obtained after applying the two analytical models over the data set measured using the $LaCl_3$(Ce) monolithic crystals of 10 mm, 20 mm and 30 mm thicknesses. In the three cases, results provided by the algorithm developed by Li [157] perform appreciably better than those achieved with the Lerche [156] method in terms of FoV and resolution. This is specially noticeable in the 30 mm data set, in which the FoV is increased by 20% when using the Li model. Most probably, this improvement can be ascribed to the reflections of scintillation photons which are included in the Li method. Since the Lerche model was developed for crystals with absorbent walls [156], it does not take into account any reflections.

Crystal thickness (mm)	Model	FoV (cm^2)	Dispersion (mm)	Resolution (mm)
10 mm	Lerche	18.27(2)	0.4(6)	1.3(6)
	Li	19.58(2)	0.5(6)	1.2(6)
20 mm	Lerche	15.8(4)	0.7(6)	2.0(6)
	Li	17.01(2)	0.8(6)	1.3(6)
30 mm	Lerche	9.90(9)	0.8(6)	3.3(6)
	Li	11.90(7)	0.8(6)	2.7(6)

Table 3.5: Summary of the results obtained for $LaCl_3$(Ce) monolithic crystals with square faces of 50 × 50 mm^2, and 10 mm, 20 mm and 30 mm thicknesses.

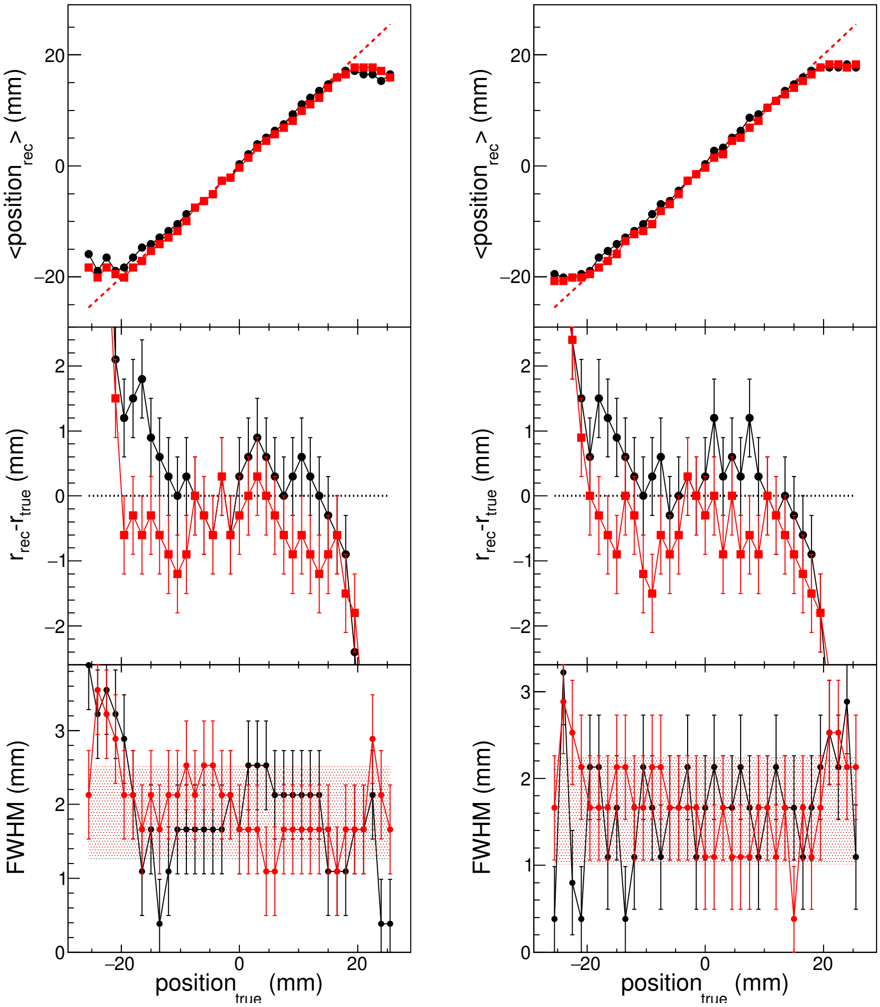

Figure 3.13: Linearity graphs obtained with the Lerche (left panel) and Li (right panel) analytical methods, corresponding to the scanned points in the diagonal of the surface of the 20 mm thickness crystal.

By looking only at the results provided by the Li model in Tab. 3.5, the FoV is reduced by 40% when comparing 10 mm and 30 mm thick crystals. Following this comparison, the dispersion increases a factor of 2, while resolution almost triples. Therefore, the performance deterioration of the positioning algorithms with the crystal thickness is evident. The latter conclusion led us to choose 25 mm thick

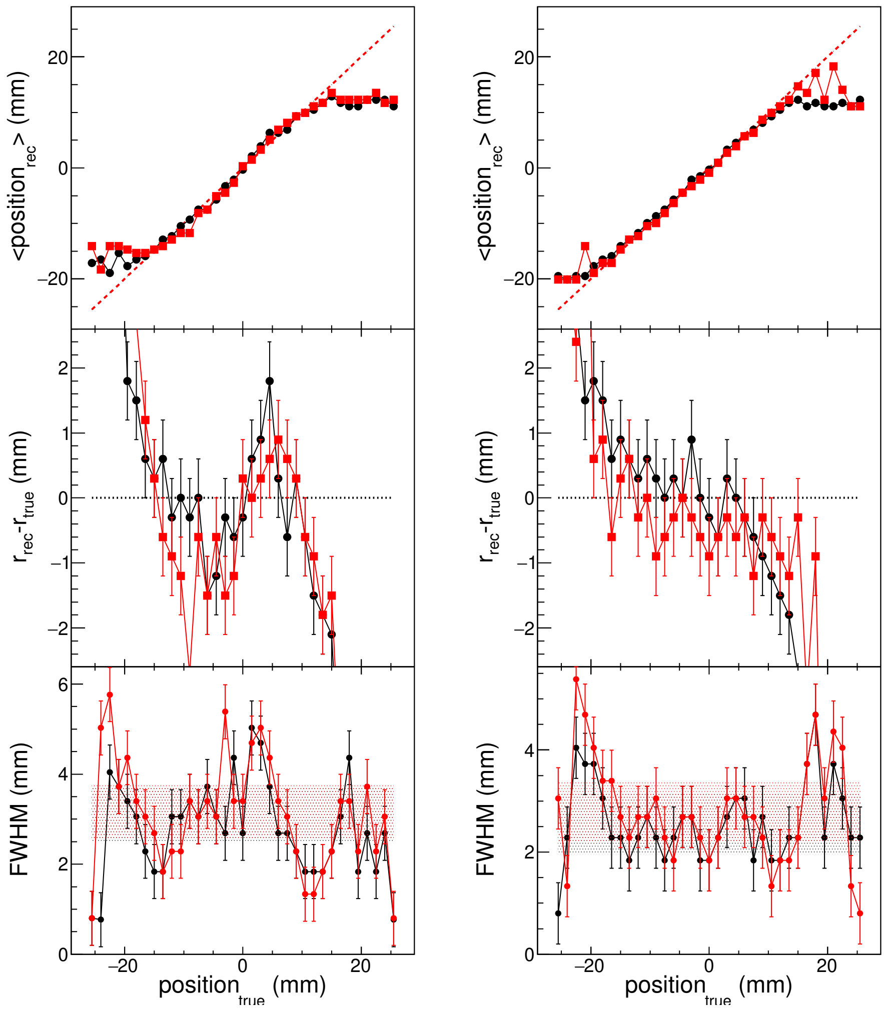

Figure 3.14: Linearity graphs obtained with the Lerche (left panel) and Li (right panel) analytical methods, corresponding to the scanned points in the diagonal of the surface of the 30 mm thickness crystal.

$LaCl_3$(Ce) crystals to be mounted in the absorber plane of i-TED5.3, which is an intermediate value between those of 20 mm and 30 mm thickness studied here.

In terms of computational cost, the complexity of the analytical models is translated into a longer computational time. As it is shown in Tab. 3.6, the event processing rate per second of the Li model is a factor of 4 longer than the fastest

(Anger) approach. However, this increase in processing time does not represent a limitation for the primary i-TED application, where typically an offline analysis is carried out.

Model	Anger	Squared-charge	Lerche	Li
Processing rate (ev/s)	8000	7500	4500	2000

Table 3.6: Comparative of rate of events per second processed by a computer with an Intel core i7 (7700HQ) at 2.80 GHz using the compared models.

Other approaches for the position reconstruction based on artificial neural networks (NNs) were explored in [158]. In the latter, different options were investigated for the nodes-structure of the NN. A single active layer of 64 neurons with a single neuron for the output provided a linearity similar to that obtained with the analytical methods, with a slight worsening in spatial resolution. At the NN-training stage, the single output represents the corresponding X or Y coordinate for the scan position of the 35 $\times$ 35 independent measurements used to train the network. Under this configuration, a couple of NNs are required to obtain information on X and Y coordinates. The main drawback of this technique is related to the costly training required for each NN, which lasted for about 15 hours [158]. Furthermore, the trained NN is unique for each PSD and cannot be shared between them. However, once a NN is trained, it can process events with a rate close to 6000 ev/s, which is almost the processing speed offered by the squared-charge approach.

Finally, further advances in position reconstruction using the present hardware are shown in a more recent publication [130]. In the latter, the implementation of GPU-accelerated programs allowed to test more complex algorithms for the position reconstruction that requires a high computational cost. A very promising solution based on Machine Learning (ML) was explored to correct the image compression produced in the peripheral region of the crystals. In addition, another ML-based solution was investigated to directly reconstruct interaction positions. The reader is referred to [130] for more information about these developments.

3.3.2 DoI

In this work, the DoI is defined as the inverse of the Z coordinate (see Fig. 1.3). As it is displayed in Fig. 3.15, we establish the origin for this magnitude at the square face of each crystal that is located in front of the SiPM, i.e. the entrance face for γ-rays. Two different approaches are followed. On the one hand, analytical models provide information on this coordinate. As it was shown in Eq. 3.2 and Eq. 3.3, the Z coordinate appears in the mathematical forms associated with these models. After adjusting these expressions to the charge distribution measured by the SiPM in each event, the DoI can be obtained. On the other hand, the second momentum of the charge distribution is directly related to the DoI. If a γ-ray impinges far from the SiPM surface (low DoI), the generated scintillation photons will uniformly illuminate a large number of pixels. As it is schematically shown in Fig. 3.15, this results in a wide distribution with a certain area at half height (hereafter AHH) which varies with DoI. Therefore, events with large AHHs correspond to events with low DoIs. In contrast, high DoI events will illuminate only a few pixels, thus resulting in small AHHs. These behaviour was confirmed in this study, as it will be shown below.

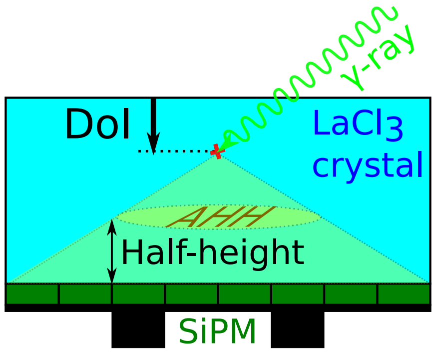

Figure 3.15: Simple diagram to describe the DoI. A γ-ray impinges into the $LaCl_3$(Ce) crystal volume by creating a scintillation photon distribution that illuminates the SiPM at the bottom of the figure. The AHH is included together with the estimated DoI.

In order to check the performance of the studied approaches, another series of scans were carried out by employing the setup previously shown in Fig. 3.4. As for the characterization of the XY coordinates, we used the same collimated ^{22}Na source (416 kBq) that illuminated both the ancillary PSD and the one under characterization. However, in this case the latter was rotated with respect to the movable platform mounted on the XY table, as it is shown in Fig. 3.16. This permitted the collimated γ-rays to hit one of the lateral faces of the crystal.

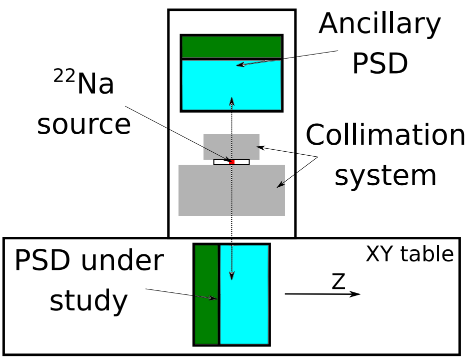

Figure 3.16: Sketched view of the experimental setup mounted for the DoI characterization.

Under the configuration shown in Fig. 3.16, a movement in the X axis direction of the mobile platform allowed to sweep all possible DoIs with the collimated γ-ray beam. As in the previous characterization, most 511 keV γ-rays were measured by using the hardware coincidence filter provided by the readout electronics. In this characterization, we employed $LaCl_3$(Ce) monolithic crystals with thicknesses of 10 mm and 25 mm. Since at the time of this study the crystals mounted in i-TED5.3 were available, it was found more convenient to characterize them rather than the 20 mm or 30 mm thick crystals.

Fig. 3.17 displays the accumulated distributions of both AHH and DoI reconstructed using the Li [157] model or DoI_{Li}. The data correspond to the scan positions DoI_{true} = 5 mm and DoI_{true} = 20 mm from the characterization of the 25 mm thick crystal. In the case of the AHH distributions, the mean value for the scan position DoI_{true} = 5 mm is around 500 mm^2 while for the second position it is close to 100 mm^2. Note that, in order to avoid artifacts in the cumulative distribution arising from the 6 mm wide sampling resolution, we perform a linear interpolation onto a 1 mm grid before computing the AHH by each measured event. Regarding the results provided by the Li analytical method, the mean values of these distributions shift noticeably depending on the scan position.

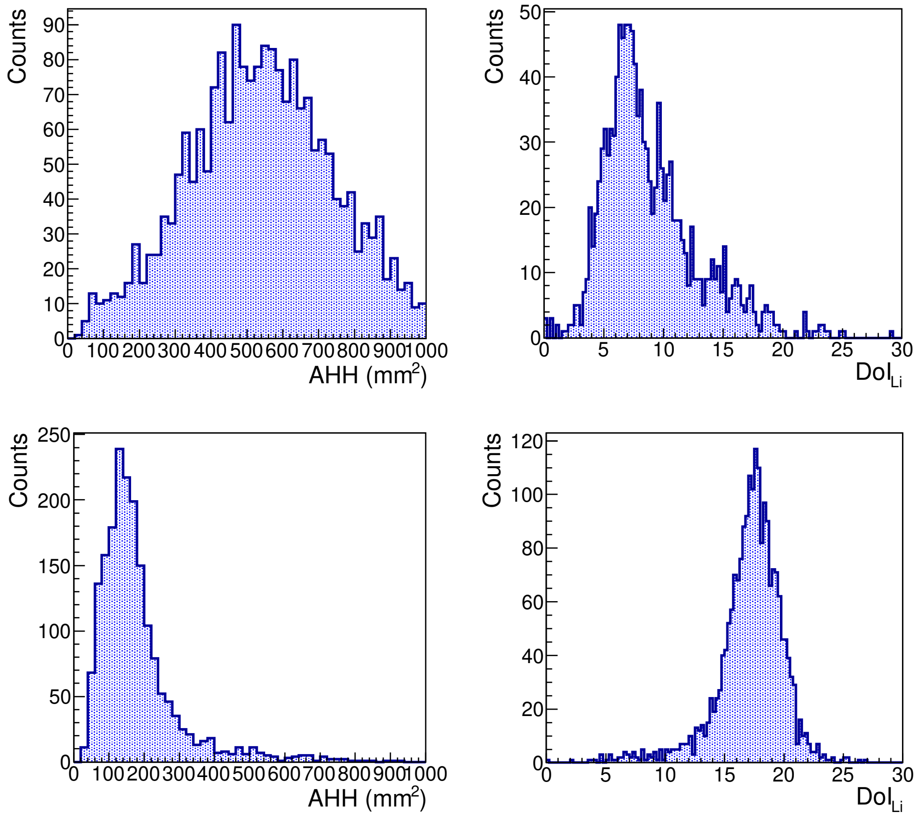

Figure 3.17: Accumulated distributions of AHH (left panels) and DoI_{Li} (right panels) corresponding to the scan position DoI_{true} = 5 mm (top panel) and DoI_{true} = 20 mm (bottom panels).

The displacement of the mean value of the AHH distributions shown in Fig. 3.17 can be translated into changes in true DoI by performing calibrations. Fig. 3.18 displays these displacements compared to the scan position or DoI_{true}. Despite of the *saturation* effect that appears in the 25 mm thick crystal for true DoIs below 5 mm, the overall good linearity demonstrates the initial assumptions. The calibration lines included in the figure can be taken to estimate the DoI of each γ-ray impact as a function of the measured AHH. On the other hand, the response of the Li approach is really similar to that obtained using the AHH-DoI calibration. Thus, apart from the first 5 mm, both AHH and DoI_{Li} are suitable quantities to extract information about the DoI.

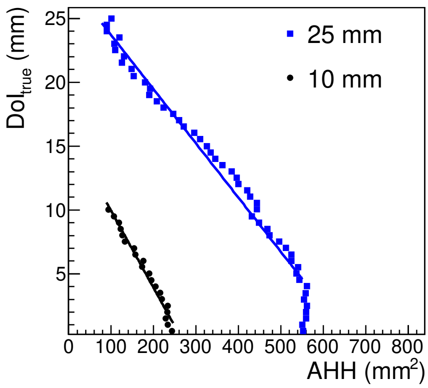

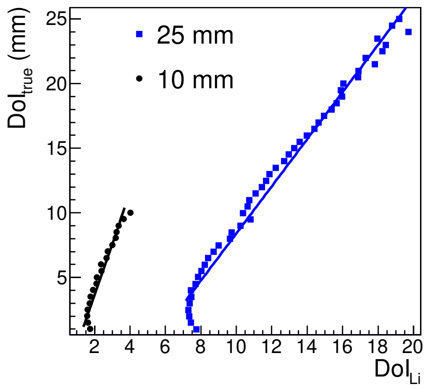

Figure 3.18: Scan position or DoI_{true} as a function of the AHH (left panel), and the DoI reconstructed by the Li model (right panel).

Finally, we opted for an AHH-DoI calibration although, in general, very similar results can be obtained also with the Li method.

3.4 Building coincidence events

Once the PSDs are calibrated in energy and position, the position and energy deposited by the γ-ray interaction in each detection plane can be determined. Events in time coincidence between two detection layers must be identified to apply the Compton imaging technique. As defined here, the coincidence condition is fulfilled by those events that are registered in two or more PSDs within a Δt_c time difference.

As start point, we selected the time window to build coincidences $\Delta t_c = \pm\ 10$ ns, which is also the value by default in PETsys to perform the hardware selection of coincidence events (see Sec. 2.3.2). Despite of obtaining satisfactory results using this time window, we explored the impact of a variation in this parameter by means of a systematic study similar to that explained in Sec. 3.1. In this case, the value for Δt_c was varied between 200 ps and 50 ns. The former corresponds to the coincidence time resolution at FWHM achieved by the readout electronics [151], whereas the latter is a coarse time window, sufficiently large to ensure that the time coincidence has taken place within that interval.

For the systematic study, a ^{137}Cs source of 210.4 kBq activity was measured with i-TED5.3 during 600 s. The front face of the scatter PSD was placed 100 mm from the source position, and the distance between planes was fixed to 20 mm. Fig. 3.19 shows the sum-energy spectra in time coincidence, or add-back mode spectra, from this measurement processed with different values of Δt_c. The same figure includes the relative efficiency, compared to the efficiency obtained for $\Delta t_c = \pm$ 50 ns, as a function of the time window. Below $\Delta t_c = \pm$ 5 ns, the number of coincidence events rises suddenly with each increment in Δt_c. In fact, the relative efficiency increases by 70% after expanding the Δt_c time window from ± 200 ps to ± 5 ns. However, this trend changes for the following coincidence spectra processed with Δt_c of ± 10 ns and ± 20 ns. Only 15% and 8% increments of counting statistic are obtained for these spectra despite adding 10 ns and 20 ns to the time window each step. Finally, there is only 2% difference between spectra with Δt_c of ± 20 ns and ± 50 ns.

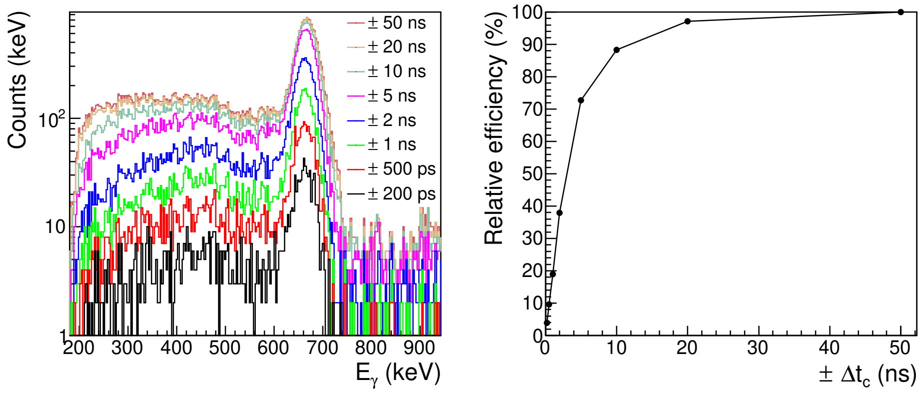

Figure 3.19: (Left panel) Add-back spectra of scatter and absorber in coincidence processed with different values of Δt_c. (Right panel) Relative efficiency compared to the efficiency obtained with $\Delta t_c = \pm$ 50, as a function of $\pm\ \Delta t_c$.

On the other hand, it is important to note that the efficiency of i-TED is mainly constrained by the necessity of building time coincidences. Tab. 3.7 shows the fraction of events detected by the scatter that remains after building coincidences with different values of Δt_c. The processed data corresponds to the spectra shown in Fig. 3.19. More than 90% of the events registered by the scatter are lost in all cases. As expected, the reduction of efficiency is more pronounced for short values of Δt_c. For that reason, it will be important to keep this parameter as high as possible.

Δt_c (ns)	$\pm$ 0.2	$\pm$ 0.5	$\pm$ 1	$\pm$ 2	$\pm$ 5	$\pm$ 10	$\pm$ 20	$\pm$ 50
ε_c (%)	0.27	0.66	1.29	2.52	5.25	6.90	7.99	8.39

Table 3.7: Percentage of coincidence events built with respect to the total number of events registered by the scatter plane as a function of Δt_c.

From the above discussion, a reasonable value for Δt_c ranges between $\pm$ 5 ns and $\pm$ 20 ns. We have chosen to keep the reference value of $\Delta t_c = \pm$ 10 ns as the time window to build the coincidence events. Using this value, we try to maximize the i-TED efficiency in coincidences while rejecting as many random coincidences as possible. However, the optimum value for Δt_c may vary depending on the particular measurement configuration since it can be affected by experimental factors such as the instantaneous count rate, the energies of the detected γ-rays, or the distance between detection planes.

3.5 Compton imaging

i-TED employs the interaction positions and energies registered in each coincidence event in both detection planes to trace a virtual cone, whose wall contains all possible directions of the incoming radiation. As explained in Sec. 1.3, the λ parameter is employed to check the compatibility of these possible directions with the sample position. A selection on λ results in a circular slice of the Compton image, as it was shown in Fig. 1.4. The larger the λ, the wider the slice. Depending on the image resolution, the selected area can be adjusted to the sample size or must be enlarged to fully take the broadened image of the source. In a neutron capture experiment, this last situation means that some γ-rays not generated in the source, but in the vicinity, can be accepted, thus worsening the background rejection performance. The quality of the final background rejection will be mainly constrained by the spatial resolution of the final Compton image.

Before characterizing the resolution of the Compton image, it is necessary to establish a global coordinate system common to all PSDs. As a reference, we select the position of the sample in a neutron capture experiment (see Fig. 1.3) as the origin of this coordinate system. The increasing direction of the reference axes is taken by the right-hand rule (also shown in the previous figure).

The consistency between the 3D coordinates of the positions at each PSD with respect to the reference coordinate system (see Fig. 1.3) was tested by means of a ^{22}Na source arranged in PET configuration between the two detection planes.

The ^{22}Na source, with an activity of 416 kBq, was placed at five different positions within the plane located in the middle of the scatter and absorber planes. The separation distance between the latter was 25 mm, and the measurement at each position lasted 60 s. Furthermore, a selection in deposited energy was made in each PSD to process only data from the 511 keV γ-rays emitted by the source in back-to-back directions. Fig. 3.20 shows the reconstructed PET images normalized to the unit and added in a single histogram. Each image accumulates the intersections between the sample plane and the lines that connect the interaction points of both detection planes. They exhibit an approximate resolution of about 4 mm FWHM on both axes. Since no accurate positioning system was employed for the source, the reconstructed spots are not uniformly distributed within the PET field of view. This does not represent a limitation since only the response of each particular PSD is required to check the consistency between the intrinsic positions and the global reference frame. As an example, if one examines the positions reconstructed within each PSD when the sample is displaced to the increasing X axis direction or *right*, most of them were shifted to that direction. This is shown in the 3D scatter plot[1] of Fig. 3.20, which was also used to validate the reconstructed positions with respect to the global reference system.

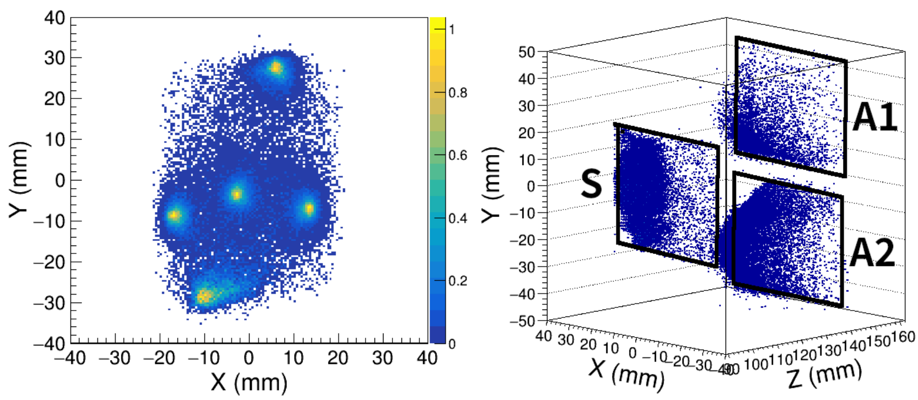

Figure 3.20: (Left panel) PET image of a ^{22}Na source placed in five different points. (Right panel) Reconstructed positions in all PSDs from a PET measurement with the sample shifted to the right.

In order to characterize the spatial resolution of the Compton image provided by i-TED5.3, we carried out several measurements with the ^{137}Cs source in the laboratory. The source with 210.4 kBq of activity was placed at the origin of the coordinate system, whereas i-TED5.3 was located at Z = 100 mm with a distance

[1]Note that the X axis in the scatter plot is reversed and the shift toward the increasing X direction is represented as a displacement to the left side of the figure.

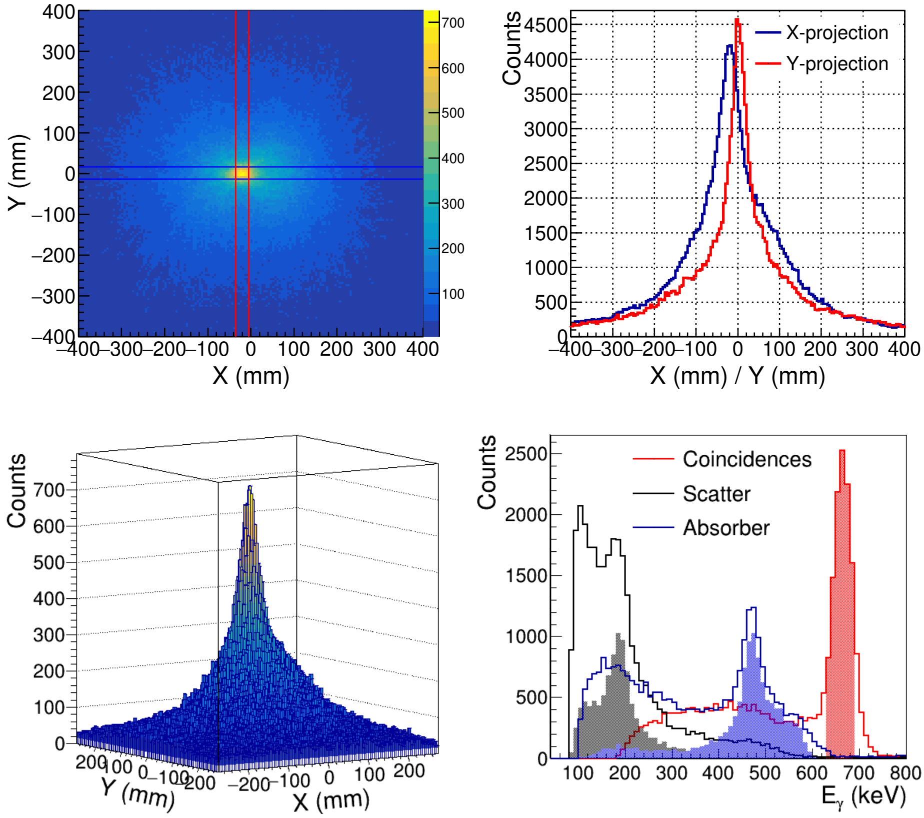

Figure 3.21: (Top left) Back-projected image of a ^{137}Cs source obtained with i-TED5.3. The 3D distribution (bottom left) and X- and Y-projections (top right) are shown, together with the coincidence energy spectra (bottom right). The shaded regions in the latter display the accepted event distributions.

between planes of d_f = 25 mm. Fig. 3.21 shows the resulting back-projected Compton image obtained, after 600 s measurement. The image plane that accumulates the geometric intersections with each Compton cone is pixelated with squared voxels of 5 mm size. Fig. 3.21 also displays the deposited energy spectra obtained from this measurement. A selection is performed to take only those γ-rays generated by the source that deposit 662 keV when adding energies deposited in scatter and absorber. This selection is shown within the add-back energy spectrum in coincidences, which exhibits a resolution of 7.5% FWHM at 662 keV. The distributions of the deposited energy at each separate layer are also displayed, and the selected events highlighted. Taking the mean values of the highlighted distributions, the accepted coincidence events deposit on average around 216 keV in the scatter and 447 keV in the absorber.

The 3D distribution of the accumulated counts in the image plane is included in Fig. 3.21 as well. The position of the maximum of this distribution gives us the most probable location of the sample. In this case, the latter is shifted by -17.5 mm in the X axis and 2.5 mm on Y axis. These results are consistent with the measurement, since an accurate source positioning mechanism was not available at this time. The X and Y projections, corresponding to a selection on the complementary axis of $\pm$ 3 pixels around the maximum of the distribution, are also included in the figure to analyze the image resolution. These projections are composed of a wide base with a narrow peak at the top. This widening especially affects to the X-projection distribution, which displays a small shoulder at half height. This is a reconstruction artifact caused by the accumulation of ellipses when using the back-projection algorithm. This effect is more noticeable when the sample is shifted in some direction, as it occurs in this measurement on the X axis. The image resolution is determined by adjusting two Gaussian forms to each projected distribution: a wide one fits the base of the distribution, and a narrow one reproduces the shape of the peak. The width of this peak gives us an estimate of the resolution of the Compton image. Owing to the vertical array configuration of PSDs in the absorber, the resolution of 80 mm FWHM on the Y axis is slightly better than the 90 mm FWHM achieved on the X axis.

The aforementioned artifact can be more easily appreciated in Fig. 3.22. The latter contains different representations of the images obtained with the ^{137}Cs source shifted 70 mm to the right and left, and 100 mm to the top and bottom. The true 140 mm movement on the X axis is reconstructed within a level of 90% since we obtain $\Delta X = 126$ mm. Y-axis displacement reconstruction gives similar performance, 176 mm against the true 200 mm.

The quality of the Compton images obtained in this section is limited due to the use of i-TED5.3 and the very simple back-projection method. This demonstrator had only half as many PSDs as a single module of the future i-TED. The effect is a reduction in the resolution achieved in the X axis of the image, and in the detection efficiency. Actually, both were improved in [158] with the use of i-TED5.5, an enhanced version that was introduced in Sec. 2.4 consisting of four PSDs in the absorber plane.

3.5.1 i-TED5.5 results

In order to show the improvement in the Compton image achieved by using i-TED5.5 and an accurate positioning mechanism, here we summarize the results from a systematic study carried out to characterize the DEC and the FoV, in the image plane, of this improved demonstrator [132].

In this study, a ^{22}Na source with 416 kBq of activity was placed in nine different positions forming a cross with 150 mm step within the image plane located at

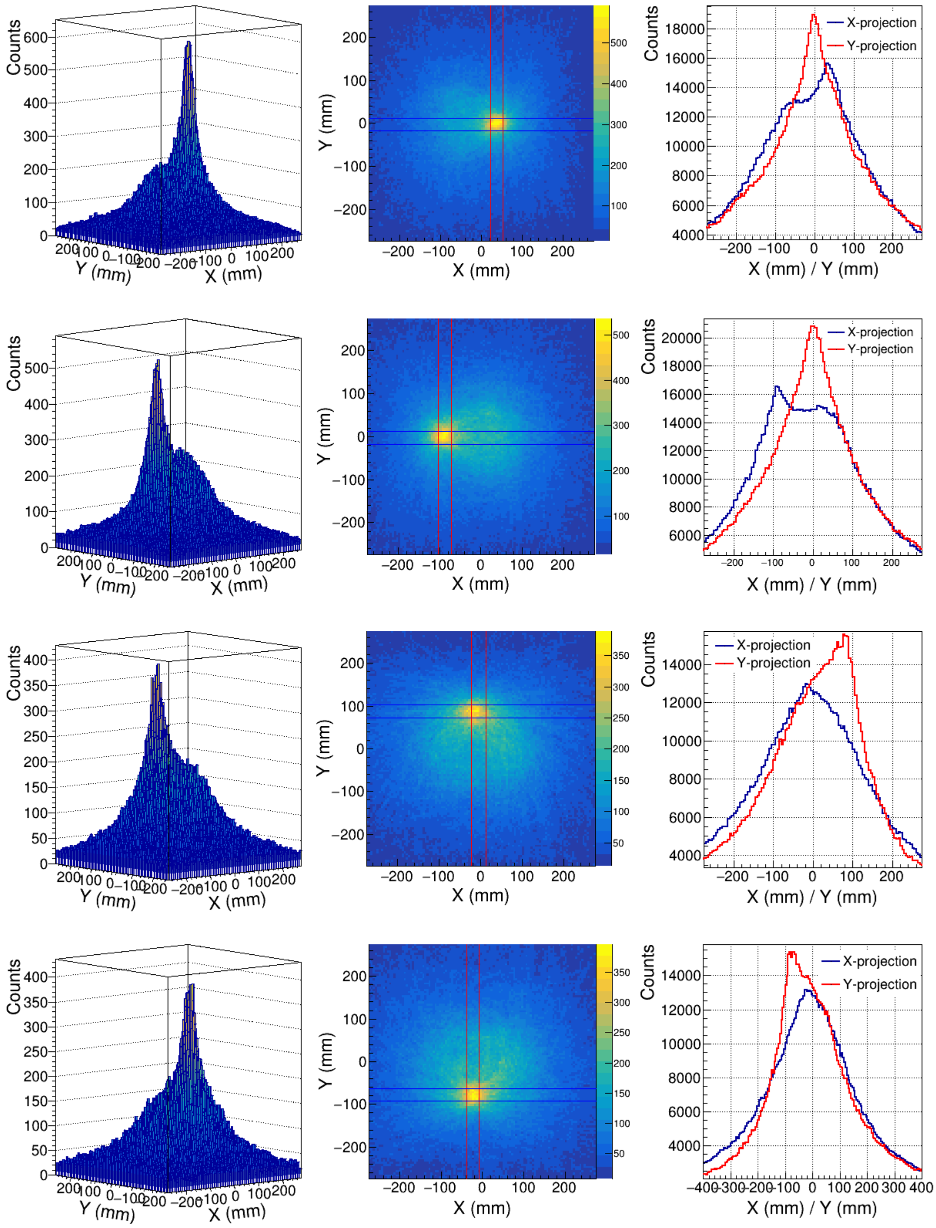

Figure 3.22: From top to bottom, Compton images of a ^{137}Cs source shifted to the right, left, top and bottom. In addition to the back-projected images, their 3D distributions are given along with the X and Y projections.

165 mm from i-TED. The separation between the scatter and absorber layers was fixed to d_f = 30 mm. The vertical gantry shown in Fig. 3.23 was used to reduce any uncertainty related to the positioning of the source with respect to the demonstrator. This device features LRT1500AL linear stages from Zaber Technologies Inc with an accuracy of 375 μm and a repeatability error of < 2 μm. In addition, it was connected to the i-TED GUI (see Sec. 2.3.3) allowing us to remotely control the movement of the radioactive source. The measurement for each position lasted a variable time, between 6 and 30 min, to take into account the differences in detection efficiency related to the changes in the distance between scatter and source.

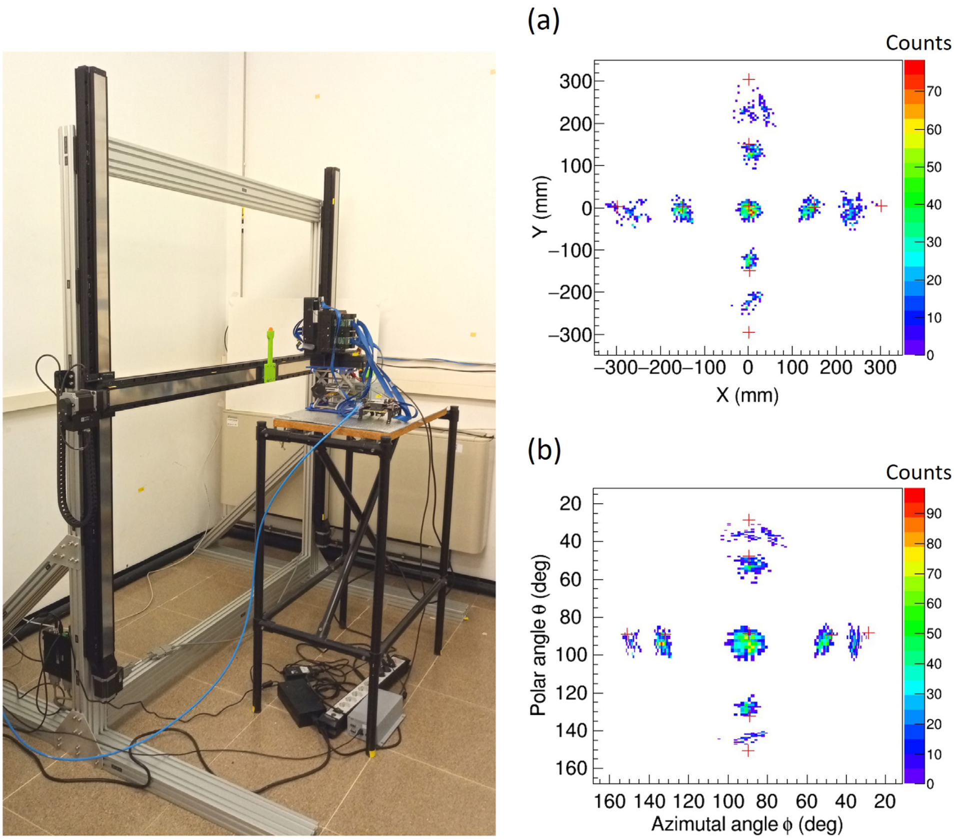

Figure 3.23: (Left panel) Photograph of the experimental setup consisting of the i-TED5.5 demonstrator faced to the vertical gantry positioning device. (Right panel) Compton images, in Cartesian (a) and spherical coordinates (b), of a ^{22}Na source placed at nine positions using the vertical gantry shown on the left panel. Extracted from [132].

The resulting reconstructed positions together with the true positions in which the sample was placed are also displayed in Fig. 3.23. For completeness, the spherical coordinates are included corresponding the polar angle (θ) to the movement on the Y axis and the azimutal angle (ϕ) to that on the X axis. The results are rather satisfactory since reconstructed and true positions coincide in the main part of the field of view. In fact, the four positions around the central one are reconstructed within a 5% of accuracy. In this case, the resolution of the Compton image at the central position is $\sim$ 70 mm FWHM for both axis X and Y. However, a compression effect can be appreciated in the positions placed far away from the center. This can be due to the higher contribution of the peripheral region of the scatter detector, where the linearity is not as good as in the central region, as it was shown in Sec. 3.3.

The quality of the results shown in Fig. 3.23 is limited by the use of the back-projection algorithm. As it was already mentioned in Sec. 1.3, further improvements have been accomplished after the implementation of a new positioning algorithm [130], and the use of Machine Learning solutions to perform the Compton technique [131]. Finally, more sophisticated approaches have been investigated [128, 129] with the goal of enhancing further the Compton image resolution and extend the applicability of i-TED to other fields [162, 163].

Chapter 4

Experimental proof of concept

The materials presented in Chapter 2 and the detector characterization introduced in Chapter 3 are intended to enable i-TED's ability to reject background by applying the Compton imaging technique in neutron-capture ToF experiments. This chapter describes the proof of concept experiment that was carried out at CERN n_TOF [164] with a twofold purpose. The first goal was to demonstrate the i-TED's background rejection capability in a real neutron capture measurement. On the other hand, this experiment aimed to technically validate the suitability of i-TED for ToF measurements, where a sufficiently fast detector response is mandatory to preserve the neutron energy resolution during the measurement. To this aim, the ^{56}Fe(n,γ) and ^{197}Au(n,γ) reactions were measured using the i-TED5.3 demonstrator introduced in Sec. 2.4. Two state-of-the-art C_6D_6 detectors were used as a reference. The final results from these measurements have been already published in [131].

The measuring setup of the proof of concept experiment will be explained in Sec. 4.1. Sec. 4.2 will address some corrections required in the i-TED5.3 prototype characterization to apply the Compton imaging technique under this experimental framework. On the other hand, the i-TED5.3 performance in terms of ToF will be evaluated in Sec. 4.3 using data from the well-known ^{197}Au(n,γ) reaction. Finally, data from the ^{56}Fe(n,γ) reaction will be analyzed in Sec. 4.4 in order to demonstrate the aforementioned background rejection capability.

4.1 Experimental setup

A measuring setup consisting on the i-TED5.3 demonstrator and two carbon fiber C_6D_6 detectors [77] was mounted at CERN n_TOF [66] to experimentally demonstrate the i-TED concept. The experiment was performed at EAR1 [48], which was found more convenient to test the system owing to the high energy resolution and the more moderate neutron flux, 25 times lower than that available at EAR2 [67]. This minimizes the probability that i-TED is affected by problems derived from high count rates, such as pile-up or dead time in the readout electronics, which at this time were not yet characterized.

Fig. 4.1 shows two photographs of the experimental setup. i-TED5.3 was placed at an angle of about 90° with respect to the beam and at 63 mm distance from the center of the capture sample under study. The focal distance d_f between the scatter and absorber plane was kept fixed to 10 mm, thereby favoring efficiency versus angular resolution [132]. This was needed owing to the small size of the detector available. On the other hand, the two C_6D_6 were mounted with an inclination of $\sim 125°$ with the beam line, following the usual configuration for capture measurements in this facility such as that presented in Sec. 3.2 (Part I). Their faces were pointing at the sample at a distance of 100 mm and their PMT outputs were connected to the n_TOF digital acquisition system DACQ (see Chapter 3 Part I). The results obtained with these state-of-the-art detectors will be compared with those obtained using i-TED5.3 to evaluate the performance of the demonstrator.

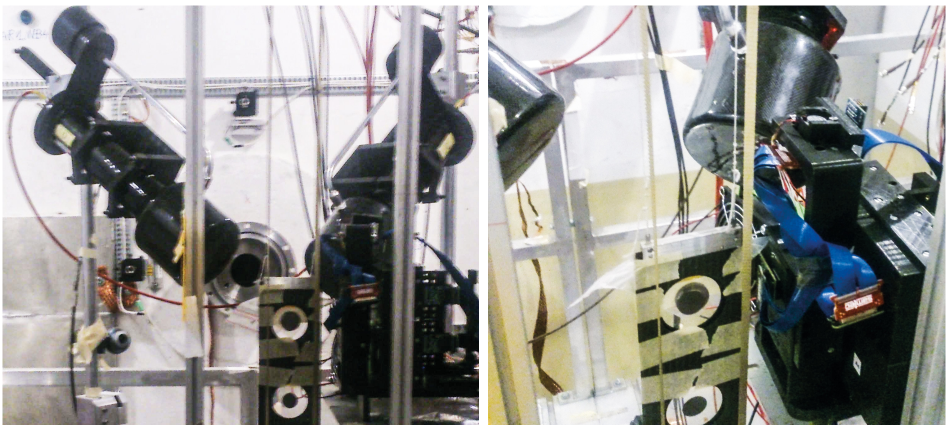

Figure 4.1: Two different photographs of the experimental setup installed at n_TOF EAR1. C_6D_6 detectors are shown in the top region while i-TED5.3 appears in the right side of the images. Gold and iron samples are mounted in the sample exchanger.

Samples of gold and iron were centred in the beam by means of the sample exchanger introduced in Sec. 3.2.2 (Part I). As explained in Sec. 4.7.1 of that part, gold is commonly employed for the normalization of the capture yield [102]. However, in this case it was only measured to validate the ToF resolution of i-TED taking advantage of its well-known neutron capture resonances [165]. The gold sample is a 20 mm diameter disk of 0.125(5) mm thickness and a mass of 0.645(1) g. On the other hand, the iron sample was a 20 mm disk of 0.84(1) mm thickness and 2.104(1) g of mass 99.93% enriched in ^{56}Fe. This isotope was selected because of its high scattering-to-capture ratio and its isolated resonance at 1.15 keV, which will be employed to characterize the signal-to-background ratio of the compared detection systems. Finally, a ^{152}Eu radioactive source with 14 kBq of activity was placed at $\sim$ 100 mm distance from i-TED5.3. In addition to the calibration of the demonstrator, this source allowed us to monitor the detector gain along the experiment and correct for thermal-gain fluctuations.

4.2 Detector response to high energy γ-rays

In order to apply the Compton imaging technique to neutron capture measurements, both the deposited energy and the DoI calibrations must be extended. As it will be explained below, the reason for that is related to the great variety of energies with which γ-rays are generated in capture reactions. This directly affects the reliability of the i-TED calibration, but also the position reconstruction procedure.

As detailed in Sec. 3.2, the calibration obtained using ^{152}Eu is valid in the energy range between 122 keV and 1.4 MeV. However, the γ-ray cascade emitted after a capture event has an approximate energy of $E^C \approx S_n + E_n$ (see Sec. 1.2 of Part I). Taking into account the neutron separation energy of ^{197}Au ($S_n = 6.51$ MeV) and ^{56}Fe ($S_n = 7.65$ MeV), and the neutron energy range of interest (1 eV $< E_n <$ 100 keV), the generated cascades can contain γ-ray energies of up to 7.75 MeV. The varying multiplicity of these cascades produces individual γ-rays with energies ranging from few tens of keV to 7.75 MeV. Therefore, the range for the energy calibration of i-TED5.3 presented in Sec. 3.2 had to be extended.

To this aim, the deposited energy spectra of ^{197}Au(n,γ) and ^{56}Fe(n,γ) were employed. These spectra are obtained by applying ToF selections restricted to the first resonance of gold at 4.9 eV, and to the first resonance of iron at 1.15 keV, respectively. This ensures that mostly γ-rays from ^{197}Au(n,γ) and ^{56}Fe(n,γ) cascades are selected, thus reducing undesired background. Fig. 4.2 shows the aforementioned spectra for C_6D_6 detectors compared to those measured with i-TED5.3 after calibration. For the sake of clarity, an average response of the two PSDs in the absorber is displayed in the figure. As it can be observed, the $LaCl_3$(Ce) intrinsic activity almost disappears from the i-TED spectra after applying the ToF selections. Only the average response of PSDs in the absorber shows this contribution due to the high contamination of one of the crystals, as it will be explained later in Sec. 4.3. Actually, it is the combination of this time window together with the construction of coincidences that completely removes this contribution. The efficiency after building coincidences drops down to 8% with respect to the counts detected only by the scatter, as it was expected from Sec. 3.4.

The location of the Compton edges in the deposited energy spectra of ^{197}Au(n,γ) and ^{56}Fe(n,γ), measured with calibrated C_6D_6 detectors, provides two additional reference points for the i-TED calibration. A second-degree polynomial is adjusted and combined with the previous function obtained from the ^{152}Eu

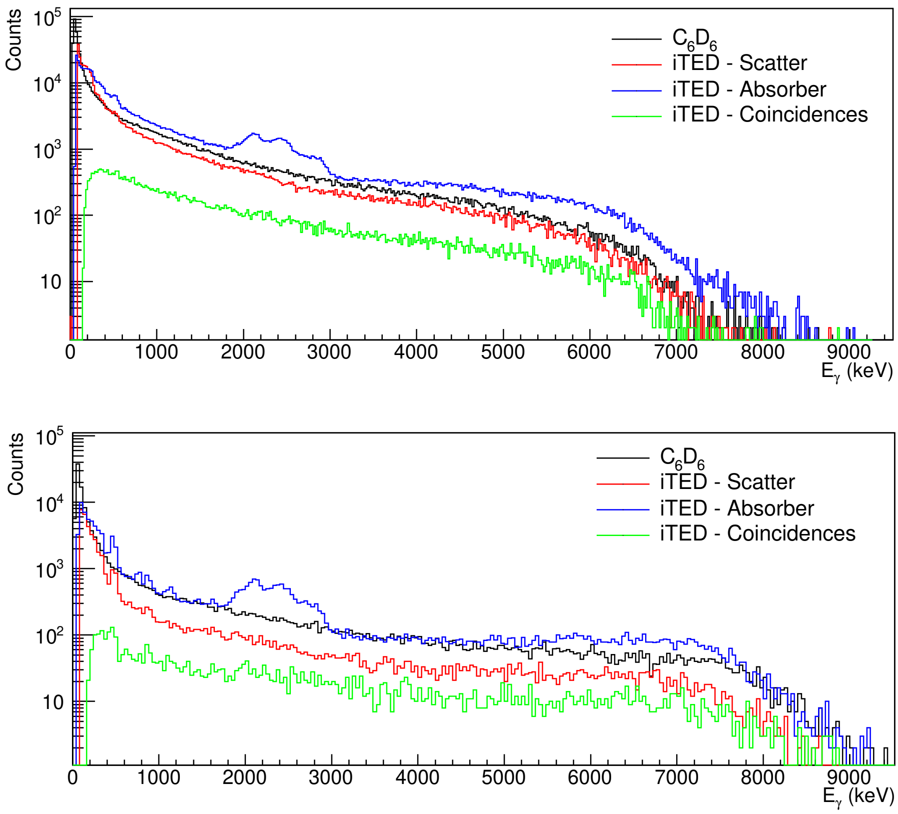

Figure 4.2: Calibrated deposited energy spectra measured with i-TED5.3 and a C_6D_6. Top panel shows spectra from the ^{197}Au(n,γ) measurement while those from the ^{56}Fe(n,γ) measurement are displayed in the bottom panel.

source. Fig. 4.3 shows the resulting calibration functions, which are valid between 122 keV and 7.65 MeV. By using this energy calibration, i-TED5.3 achieves energy resolutions ranging between 7% and 5% FWHM at 662 keV for the crystals placed in the scatter and absorber planes, and 7% FWHM at 662 keV for the add-back spectrum in coincidences.

On the other hand, the great variety of energies with which γ-rays are generated in the capture events not only affects the energy calibration but also the position reconstruction. More precisely the reconstruction of the Z coordinate or DoI. As it was explained in Sec. 3.3, the DoI is determined by measuring the area at half height (AHH) of the charge distribution collected in the SiPM, and performing

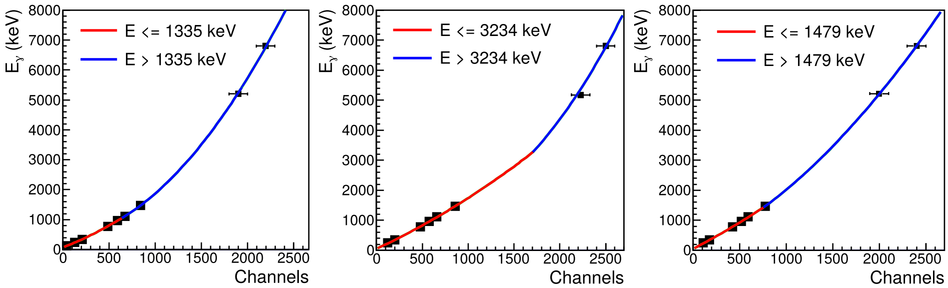

Figure 4.3: From left to right, energy calibration functions for PSDs placed at the scatter and absorber planes.

an AHH-DoI calibration. However, this calibration gives ambiguous results when γ-rays with energies different than 511 keV are measured. This can be understood as a change of the minimum and maximum AHHs that can be measured after the detection of γ-rays with maximum and minimum DoIs, respectively, depending on the energy they deposit. Fig. 4.4 shows this change in AHH for the scatter and absorber as a function of the γ-ray energy. These data correspond to the measurement of the ^{197}Au(n,γ) reaction carried out with i-TED5.3. As it can be appreciated, γ-rays depositing up to 1 MeV of energy in the scatter can achieve AHHs ranging from 20 to 800 mm^2, approximately. Taking these limits for the AHH-DoI calibration, a measured AHH = 800 mm^2 corresponds to a γ-ray event with 0 mm DoI. In that case, the AHH = 1000 mm^2 measured after the impact of a 4 MeV γ-ray would be reconstructed with a negative DoI.

In order to extend the validity of the AHH-DoI calibration to all possible γ-ray energies, we take the AHH limits for this calibration as a function of the deposited energy. For that, we express the boundaries of the 2D histograms from Fig. 4.4 as numerical functions that we can evaluate at any energy. Following the previous example, the new AHH limits for a 4 MeV γ-ray, ranging between 700 mm^2 and 1200 mm^2, allow to reconstruct this event with 4 mm DoI. Fig. 4.5 shows the normalized distributions of calibrated DoIs corresponding to all events registered in scatter and absorber during the mentioned ^{197}Au(n,γ) measurement. Results calculated using fixed AHH limits are compared with those obtained after adding an energy dependency to these limits. On average, about 13% and 7% of reconstructed DoIs in scatter and absorber detectors, respectively, yield a negative value and are discarded. The improvement can be appreciated in the reduction of the tails towards negative DoIs of the distributions shown in this figure.

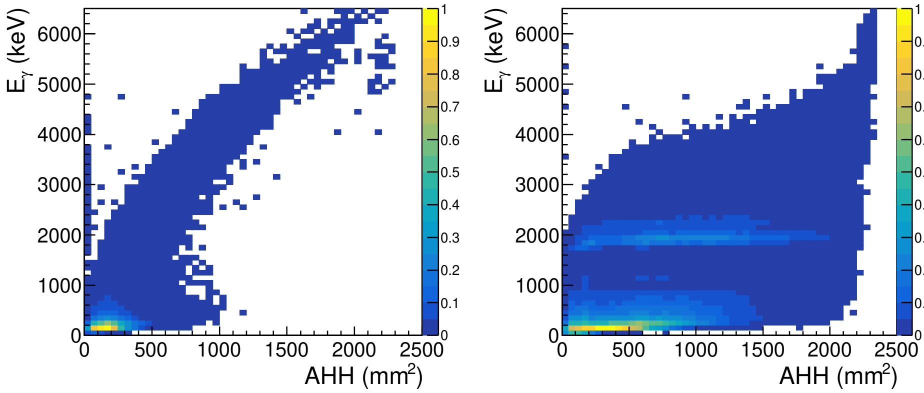

Figure 4.4: AHH of events detected in the scatter (left panel) and absorber (right panel) planes as a function of the deposited energy.

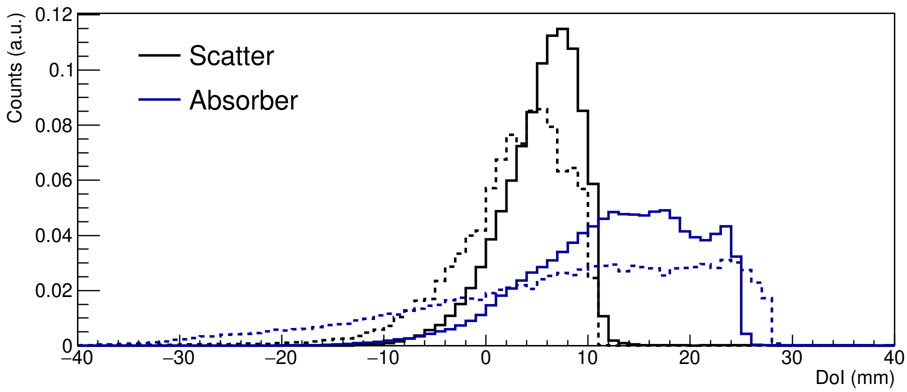

Figure 4.5: Calibrated DoIs of events accumulated in the scatter and absorber detectors. Distributions are obtained using area-DoI calibrations with areal limits fixed (dashed lines) and dependent from γ-ray energy (solid lines).

4.3 ToF performance of i-TED

The feasibility of obtaining the energy distribution of a neutron capture cross section, using the ToF technique, will largely depend on the time-response performance of such a device. A set of ^{197}Au(n,γ) measurements was carried out to characterize this feature with the i-TED5.3 prototype, comparing the response of this demonstrator with that obtained from C_6D_6 detectors. As mentioned above, the ^{197}Au(n,γ) reaction is chosen due to its large cross section and its well-known resolved resonance region (RRR) [165].

As it was explained in Sec. 4.4 (Part I), C_6D_6 detectors use the arrival time of the γ-flash as reference to calculate the ToF of neutrons. Because of the electronic-readout system used, i-TED5.3 is not able to digitize or time-stamp the γ-flash signal. Probably the high intensity of this flash saturates the i-TED readout electronics and prevents its proper identification. As alternative, the transistor-transistor logic (TTL) signal sent by the CERN PS to trigger the n_TOF DACQ (see Sec. 3.1 of Part I), was fed into the PETsys FEB/D module. To this aim, the latter was supplemented with an external trigger-module based on the high-speed differential-line driver SN65LVDS9638 from Texas Instruments [166]. This module converts the TTL signals into a LVDS-pulse, with 500 ps rise- and fall-times, which is digitized by a channel of a TOFPET2 ASIC. Thus, the t_{ToF} of a neutron detected in a time t is calculated by means of Eq. 4.1, in which t_{PS} is the PS trigger time digitized by PETsys and t_{offset} the time difference between t_{PS} and the time arrival of the neutron bunch to the target position.

$$t_{ToF} \approx t - t_{PS} + t_{offset} \tag{4.1}$$

The value of t_{offset} was determined empirically using the thin resonances within the RRR of the ^{197}Au(n,γ) reaction. Once t_{ToF} was obtained,the neutron energy was calculated using equation Eq. 4.7, as explained in the mentioned Sec. 4.4.

Fig. 4.6 compares a fragment of the neutron energy spectra from the ^{197}Au(n,γ) reaction measured with the scatter of i-TED5.3 and one C_6D_6 detector. These spectra are displayed in histograms with 500 bins per decade (bpd) to resolve thin resonances in the RRR. In addition, both are obtained using a 250 keV threshold in deposited energy that prevents the processing of electrical rebounds signals in C_6D_6 detectors (see Sec. 4.2.1 Part I). This initial comparison revealed a problem when determining the ToF in i-TED since resonances in the i-TED spectrum appear broad and split. As it can be seen in the figure, the separation between split resonances increases with the neutron energy. This artifact was due to an inconsistent determination of the origin of the time, whose effect is more noticeable at the low ToF (high neutron energy) region.

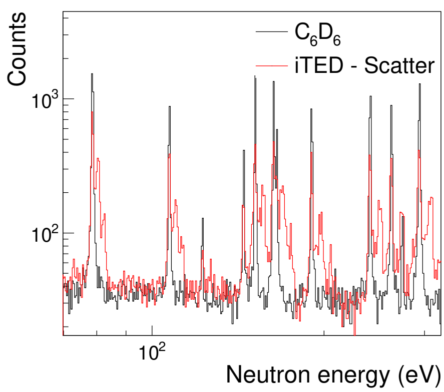

Figure 4.6: Piece of the neutron energy spectra of ^{197}Au(n,γ) reaction.

In order to characterize this problem and find a solution, the time differences between two consecutive PS-triggers Δt_{PS} were investigated. To this aim, data from the ^{197}Au(n,γ) reaction were used. Fig. 4.7 shows the resulting Δt_{PS} distribution up to 20 s. This distribution consists of several structures separated by multiples of 1.2 s, which corresponds to the duty cycle of the PS. By zooming in one of these structures, we distinguish two different contributions separated by $\sim$ 35 ms corresponding to the primary and parasitic pulses introduced in Sec. 3.1 of Part I. However, if one looks at these two contributions with higher temporal resolution, as in the bottom panels of Fig. 4.7, one finds several substructures within a few tens of μs. This sort of jitter in the values of t_{PS} causes the splitting of the high energy resonances. The origin of this time jitter is not fully understood, although it is probably due to an insufficient electromagnetic compatibility of the trigger module used in the harsh conditions of the n_TOF environment. An intense electromagnetic pulse such as the γ-flash may affect also the TOFPET2 ASICs, thus hindering an accurate determination of the trigger time-stamp.

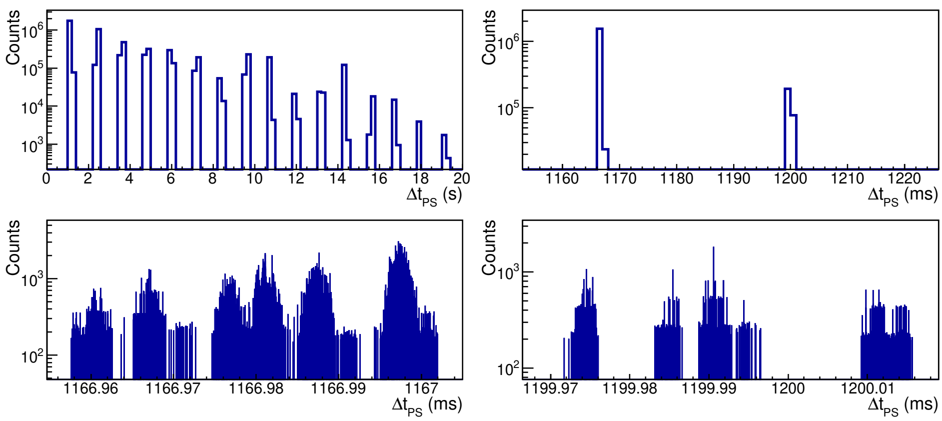

Figure 4.7: (Top left) Time difference between two consecutive triggers registered with i-TED5.3. Some expansions of the previous distribution are shown: between 1155 ms and 1225 ms (top right), between 1166.955 ms and 1167.005 ms (bottom left) and between 1199.965 ms and 1200.015 ms (bottom right).

A method to overcome this difficulty was found after representing separately the ToF spectra of events within each substructure contained in the highest precision representation of the Δt_{PS} distribution (bottom panel of Fig. 4.7). Owing to the high cross section of ^{197}Au(n,γ), only the data collected after a few neutron bunches are needed to correctly represent the first resonances of this reaction. This allowed us to plot the ToF spectrum of only those events grouped within the first substructure of the mentioned representation of the Δt_{PS} distribution. With this approach, the resulting spectrum does not show the jitter effect. We took this first group of events as a reference and grouped the rest according to the substructures found. The ToF spectrum of this reference group was compared to that obtained from the following group. Since a misalignment was observed between these spectra, a χ^2minimization was performed to find the time-shift required to align them. After comparing all the groups with the reference one, we found the time shifts required to correct the ToF of all the events belonging to any of the groups analyzed. Fig. 4.8 shows the same neutron energy distribution fragment as that shown in Fig. 4.6, after correcting the i-TED ToF. For the sake of comparison, we have kept the binning of 500 bpd and included the initial neutron energy histogram reconstructed with the uncorrected ToF. The agreement between the i-TED scatter and a C_6D_6 is excellent, and temporal resolutions of both detection systems are comparable, at least in this energy region. However, the limitations of this procedure begin to emerge from about 1 keV of neutron energy, as it is also displayed in Fig. 4.8.

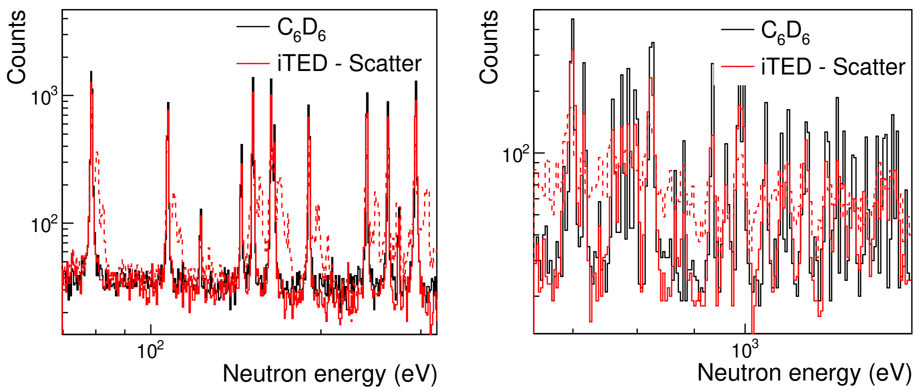

Figure 4.8: Two fragments of the ^{197}Au(n,γ) neutron energy spectra measured with one C_6D_6 detector and compared to that obtained with i-TED scatter after ToF-jitter correction. Uncorrected i-TED spectrum is included with a red dashed line.

The main limitation of this procedure is related to low number of events that some groups contain. Despite of the high cross section of the ^{197}Au(n,γ) reaction, the ToF spectra from these groups cannot be reconstructed with enough statistics to be compared with the reference spectrum. This causes a bad ToF reconstruction and a loss of efficiency since these events have to be discarded. In the case of the gold measurement, a 12% of the total statistic is lost because of this limitation. Nevertheless, the effect is more pronounced in the iron measurement. The low cross section of the ^{56}Fe(n,γ) reaction together with the high neutron energy of the first resonance (1.15 keV) lead to a loss of 18% of the total statistics. During the commissioning of the last version of i-TED, a hardware solution that removes the time jitter was found [167].

Fig. 4.9 shows the comparison between the neutron energy spectra (500 bpd) of the ^{197}Au(n,γ) reaction measured with a C_6D_6 detector and with the i-TED scatter after fixing its ToF. These spectra correspond to the same measuring time and have been obtained using the aforementioned 250 keV low energy threshold. In the neutron energy range between 1 eV and 100 keV, the efficiency of an i-TED scatter placed at 63 mm is 88% of the efficiency of a common C_6D_6 detector separated 100 mm from the capture sample. If the ToF-jitter correction is not applied, the efficiency of the scatter becomes similar than that of the C_6D_6.

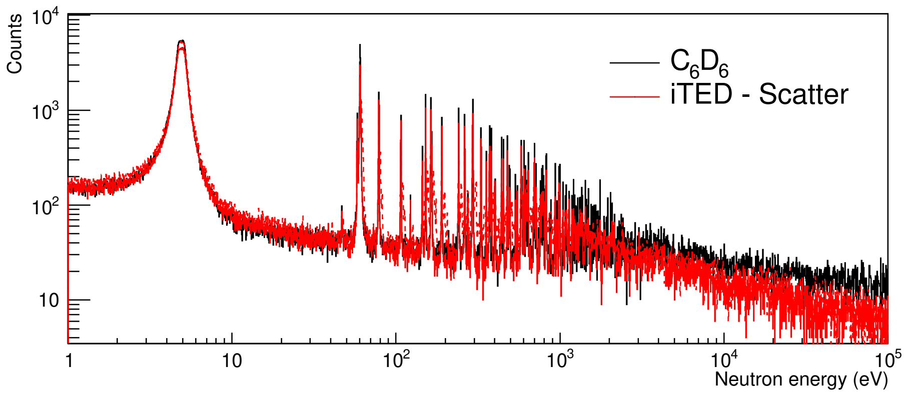

Figure 4.9: Neutron energy spectra of the ^{197}Au(n,γ) reaction as in Fig. 4.8 but in the neutron energy range between 1 eV and 100 keV.

4.4 Background rejection

The Compton imaging capability of i-TED is intended to reject γ-rays that do not originate spatially from the sample during a neutron capture measurement, thus improving the signal-to-background ratio. The ^{56}Fe(n,γ) measurement is a good case to proof this ability of i-TED for two main reasons that are well illustrated in the neutron energy spectra displayed in Fig. 4.10. On the one hand, as it was mentioned at the beginning of this chapter, the isolated resonance at 1.15 keV can be employed to compare the signal-to-background achieved by i-TED with respect to the reference C_6D_6 detectors. On the other hand, the probability of neutron scattering in the keV region is three order of magnitude larger than the probability of neutron capture. Thus, a large number of neutrons is expected to be dispersed by the ^{56}Fe sample. Some of them can be captured in the surrounding walls and by structural materials of the experimental setup thus emitting γ-rays [75]. This radiation creates a "plateau" at $\sim$ 10 keV that we use to compare the background measured by both detection systems. This is therefore a particularly well suited situation to explore the background rejection capability of i-TED.

In Fig. 4.10, the response of the i-TED scatter is compared to that obtained using a C_6D_6 detector. As in Sec. 4.3, these spectra are obtained with 500 bpd and using a low energy threshold of 250 keV. The comparative efficiency is more or less the expected taking into account the ToF-jitter correction explained in Sec. 4.3. The i-TED scatter at 63 mm has approximately a 75% of the efficiency of a C_6D_6 detector placed at 100 mm from the capture sample.

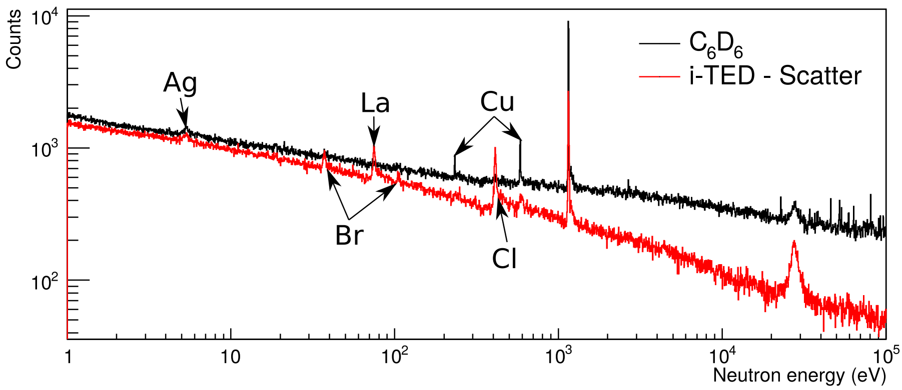

Figure 4.10: Neutron energy spectra of the ^{56}Fe(n,γ) reaction.

Owing to the low cross section of ^{56}Fe(n,γ), some resonances that do not belong to this reaction appear in the neutron energy spectra. These resonances are discussed below:

- The 5.2 eV resonance, measured in both detection systems, corresponds to a small ^{109}Ag impurity ($\leq$ 110 ppm) in the iron sample.
- Resonances at 35.8 eV and 101 eV observed in the i-TED scatter can be related to ^{79}Br and ^{81}Br, respectively. These halogens may be present in the plastics of the readout PCBs of i-TED5.3 [168].
- The 72 eV and 400 eV resonances detected by the i-TED scatter correspond to captures in the ^{139}La and ^{35}Cl present in the $LaCl_3$(Ce) crystals, which dominate the intrinsic neutron sensitivity of this detector.
- Resonances at 230 eV and 580 eV, related to ^{65}Cu and ^{63}Cu, are mainly detected by the C_6D_6 detectors but also dimly registered by i-TED. The

origin of these resonances may be ascribed to other detection systems under test upstream in the beam line.

In principle, this background does not represent a problem since all the mentioned resonances are below the energy range of astrophysical interest for the *s*-process study, for which i-TED is primarily intended. As explained in Chapter 0, the energies of the main *s*-process sites are 8 keV and 23 keV for ^{13}C-pocket and He-flash stages in AGB stars, and 26 keV and 90 keV for He- and C-burning stages in massive stars. There are no other resonances in the energy range between 1 keV and 100 keV excepting those related to the ^{56}Fe(n,γ) reaction, being the largest ones at 1.15 keV and about 30 keV. Despite this, the future i-TED array will use neutron absorbers made from polyethylene enriched in ^{6}Li to reduce the intrinsic neutron sensitivity [62], especially in the region below 1 keV where the ^{139}La and ^{35}Cl capture cross sections are dominant.

In Fig. 4.11, the neutron energy spectra are normalized to the 1.15 keV resonance of iron. This figure also includes results from the absorber PSDs. This normalization makes it easier to graphically determine the signal-to-background ratio (SBR). The latter is defined here as the maximum counts at the 1.15 keV resonance divided by the background level just before it. Tab. 4.1 shows the SBRs calculated for the two main resonances of the ^{56}Fe(n,γ) reaction at 1.15 keV and 30 keV, by comparing the C_6D_6 detector with all PSDs in i-TED5.3. At 1.15 keV, the SBR of a C_6D_6 detector is almost twice the SBR of the i-TED scatter. Nevertheless, the i-TED data in this energy range are affected by the limited precision of the ToF-jitter correction explained in Sec. 4.3. The expansion included in Fig. 4.11 shows the widening corresponding to this ToF limitation. This equally affects the two PSDs in the absorber plane. However, their SBRs are almost half of the value obtained for the scatter due to the high internal activity of the $LaCl_3$(Ce) crystals mounted in these PSDs. The crystal in position 2 exhibits $\sim$ 1 kHz of internal count rate, about one order of magnitude higher than the average value. The trend observed in this neutron energy spectrum reflects the constant background level in time due to the $LaCl_3$(Ce) internal activity. This trend causes the two absorber PSDs to exhibit a similar SBR at the 30 keV resonance, which is only 20% lower than that provided by the i-TED scatter. Furthermore, the SBR = 2.4 shown by the latter at this resonance improves the C_6D_6 SBR by 85% since the limitations of the ToF-jitter correction are not so relevant for this wide resonance.

Neutron energy (keV)	SBR C_6D_6	Scatter	Absorber 1	Absorber 2
1.15	18	11	6	5
30	1.4	2.4	2.0	2.0

Table 4.1: SBR from Fig. 4.11 of C_6D_6 compared to all PSDs in i-TED5.3.

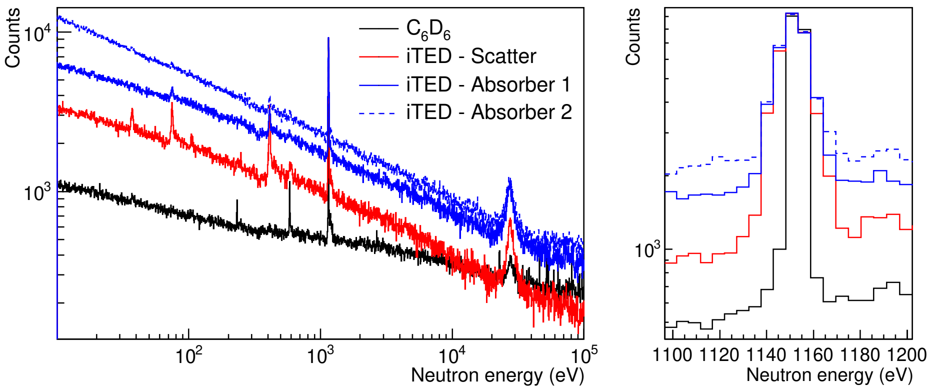

Figure 4.11: Neutron energy spectra of the ^{56}Fe(n,γ) reaction normalized to the top of the 1.15 keV resonance.

In the following, the time-coincidence response of i-TED will be discussed. It is worth recalling first, that both detection layers of i-TED have to be operated in time-coincidence mode in order to apply the Compton imaging technique. Fig. 4.12 shows the neutron energy spectra of ^{56}Fe(n,γ) measured with a C_6D_6 detector and the i-TED scatter. This figure also includes the spectrum measured in time-coincidence between scatter and absorber planes. In this case, the 250 keV threshold in deposited energy is not applied in order to increase the counting statistics of the time coincidence spectrum. Despite this, the marked reduction of the counting statistics after building the coincidence events (see Sec. 3.4) requires one to reduce the binning down to only 40 bpd. In the spectra measured with i-TED, the resized bins allow to group the counts around the 1.15 keV resonance, which was spread by the aforementioned limitations of the ToF-jitter correction. This equates the SBR provided by the C_6D_6 detector and the i-TED scatter to $\sim$ 2.4. At the 30 keV resonance, the re-binning leads to a reduced SBRs of 1.8 and 1.3 for both detection systems, respectively. Nevertheless, these results are improved by the time-coincidence spectrum, for which SBRs of 3 and 2.6 are obtained at 1.15 keV and 30 keV resonances, respectively. This can be ascribed to the decrease in the number of counts of this spectrum above 1 keV of neutron energy, which is explained below.

Regarding the shape of the spectra shown in Fig. 4.12, the time-coincidence spectrum exhibits an excess of counts in the neutron energy region below $\sim$ 300 eV with respect to C_6D_6 and scatter. The aforementioned high internal activity of one of the absorbers crystals causes random coincidences, thus increasing the background level in that region. This does not affect the energy region above 1 keV of this spectrum, in which a decreasing trend is observed. This effect is related to the configuration of the i-TED planes and the origin of the different sources of background [131]. On the one hand, the thick absorber layer prevents the low energetic γ-rays, generated by neutrons captured in the walls of the experimental setup [75], from being registered by the scatter. On the other hand, the soft spectrum of in-beam γ-rays [71], that are scattered by the sample, is almost shielded by the scatter. In contrast to i-TED, C_6D_6 detectors register all γ-rays in the same measure independently of their spatial origin. As a consequence of the different operation of both detection systems, the background level of the i-TED spectrum in time-coincidences is reduced by a factor of ~ 2.5 at 10 keV compared to C_6D_6 detectors.

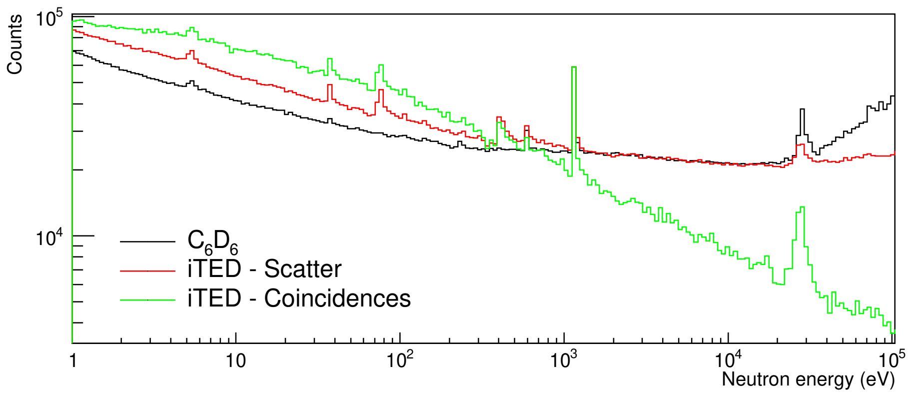

Figure 4.12: Neutron energy spectra of the ^{56}Fe(n,γ) reaction normalized to the top of the 1.15 keV resonance. Add-back spectrum of scatter and absorber in coincidence is included.

Finally, a systematic study was carried out to quantify the additional background rejection achieved by the i-TED5.3 demonstrator using the Compton imaging technique. We define the background reduction factor (BRF) of this prototype with respect to a C_6D_6 detector as the ratio between the background measured by both detection systems at 10 keV of neutron energy within the ^{56}Fe(n,γ) spectra, normalized to the maximum of the 1.15 keV. As mentioned above, the BRF becomes 2.5 just by building the time-coincidence events. In principle, i-TED can further increase this value by selecting events based on the possible incoming direction of the γ-rays. For that purpose, we employ the λ parameter defined by Eq. 1.3, which represents the solution for the quadratic describing the intersection of the Compton cone with the center of the image plane, where the sample is placed. As explained in Sec. 1.3, small values of this parameter correspond to γ-rays generated from the sample location. Thus, a selection of events with low λ values should provide a background reduction since the discarded γ-rays are not generated in the sample but all around the experimental hall. Fig. 4.13 demonstrates this feature. As it can be clearly appreciated, the background level is significantly reduced across the entire spectra for a lambda selection of $\lambda < 1000$. In fact, the BRF increases from the initial value of 2.5 up to 3.3. The following selection, $\lambda < 200$, reduces even more the background level reaching to a BRF of 3.7, almost 50% increase over the initial situation. However, there is also a strong reduction in the counting statistics after applying these cuts. This is very apparent in the large fluctuations observed in the neutron energy spectrum for $\lambda < 200$.

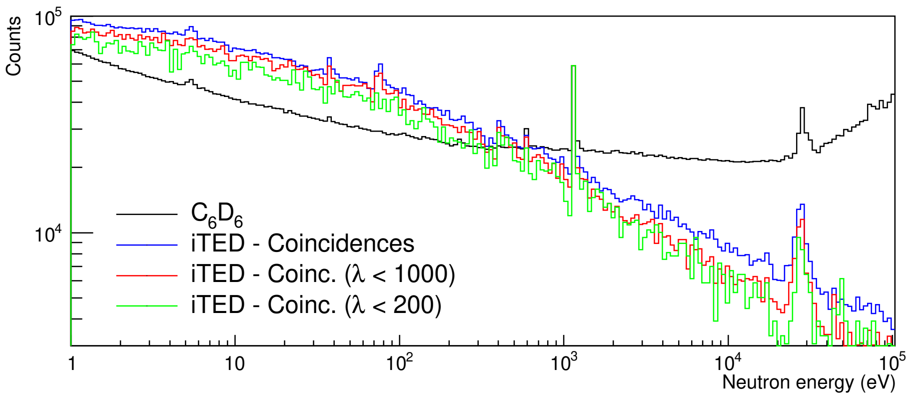

Figure 4.13: Neutron energy spectra of ^{56}Fe(n,γ) normalized to the 1.15 keV resonance. Add-back spectrum in time-coincidence is accompanied by two spectra obtained using different λ selections.

The efficiency reduction is quantified in the graph shown in Fig. 4.14. In the latter, the BRF is displayed along with the relative efficiency as a function of the upper threshold in λ or λ_{max}. As expected, both efficiency and BRF curves follow an opposite trend. Large λ values above 5000 almost recover the initial situation with a BRF close to 2.5 and the 8% efficiency compared to the number of events detected by the i-TED scatter. As the λ_{max} selection becomes more restrictive, the BRF increases up to its maximum mentioned value of 3.7. On the contrary, the efficiency decreases down to 0.6% compared to scatter, which corresponds to 7% of the initial number of coincidence events.

The results presented in Fig. 4.13 and Fig. 4.14 represent the first proof of concept of the background rejection with i-TED carried out with a modest demonstrator whose detection volume corresponds only to 3/20 of the final device. A noticeable improvement is expected in terms of efficiency and background rejection with the implementation of the final i-TED array [62, 131].

Next steps undertaken in the development of a suitable analysis methodology for the i-TED concept have been focused on exploiting Artificial Intelligence and Machine Learning techniques. The latest results in this respect are reported in [131] and have allowed to reduce remarkably the strong efficiency reduction of the analytical method discussed here (Fig. 4.13), while preserving a high SBR of 3-4.

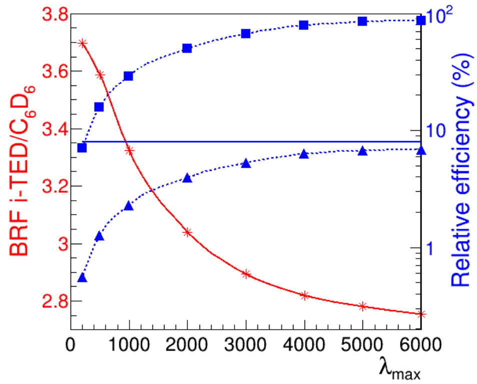

Figure 4.14: BRF of i-TED over C_6D_6 detector as a function of λ_{max} (left axis and solid-red line). Relative efficiencies with respect to the total (squares) and to the scatter efficiency (triangles) are included (right axis and blue lines). The efficiency of the scatter draws the horizontal solid line.

Conclusions

Two relevant contributions have been made with the present work to the forthcoming measurement of the ^{79}Se(n,γ) cross section, which will enable the first consistent interpretation of the the *s*-process branching at ^{79}Se. On one hand, the cross section of the ^{79}Se+n product nucleus, ^{80}Se, has been measured with high accuracy, high resolution and covering the full stellar energy range, from 1 eV up to 100 keV. The results of this experimental work are summarized in the first section below. In addition, this thesis work includes the first developments towards a new detection technique, which exploits Compton imaging as a tool to reduce spatially localized backgrounds in neutron-capture time-of-flight experiments. The development of the the first prototype and proof-of-concept measurements are also summarized below.

Neutron capture cross section measurement of ^{80}Se

The aim of the first part of this thesis was the high resolution time-of-flight (ToF) measurement of the ^{80}Se(n,γ) cross section. The existing previous measurement on this isotope [31] covered only a very limited energy range and suffered of rather low neutron energy resolution. Both aspects have been remarkably improved with the present work.

The new ToF measurement was performed at the CERN n_TOF facility by employing an array of four state-of-the-art C_6D_6 γ-ray detectors and a ^{80}Se sample with a purity of 99.87(10)%. The EAR1 experimental area was utilized due to the $\sim$ 185 m flight path and the attainable ToF resolution. The long flight path in conjunction with the low duty cycle of the Proton Synchrotron (PS) and fast time-response of the C_6D_6 detectors enabled a very high neutron-energy resolution ([1.2% FWHM at 1 keV]) and a large neutron energy span from 1 eV to 100 keV.

Despite of the relatively large scattering-to-capture ratio, the very low neutron sensitivity of the C-fibre based C_6D_6 detectors allowed us to measure a capture yield, that was virtually free of neutron-sensitivity effects.

The capture yield of the ^{80}Se(n,γ) reaction was obtained after applying the pulse-height weighting technique (PHWT) following the methodology originally developed and validated at the Gamma-Ray Spectroscopy Group of IFIC [63]. The latter is based on the combination of the measured data with an statistical Monte-Carlo simulation of the prompt capture cascades, in order to derive accurate yield correction factors that allow one to account for systematic effects such as the electronic threshold in the detectors, γ-ray summing and conversion-electron effects. This methodology, together with a careful analysis and subtraction of experimental backgrounds, allowed us to obtain the capture yield of the ^{80}Se(n,γ) reaction with a low level of systematic uncertainty, between 3.2% and 5.7%, depending mainly on the accuracy of the neutron flux at each neutron-energy region. A resonance analysis of the capture yield was carried out by means of the R-matrix code SAMMY [46]. This analysis delivered ^{80}Se(n,γ) resonance parameters for the first time below 3 keV. In total 113 resonances were characterized between 1 eV to 100 keV, 98 of them for the first time. The remaining 15 resonances were previously known only from transmission measurements [49, 50].

The new resonance parameters allowed one to determine also the Maxwellian Average Cross Section (MACS) in a more consistent and accurate way. The results obtained indicate that the MACS of ^{80}Se(n,γ) is actually between 20% and 30% lower than previously recommended values [107]. In addition, with the present work the relative statistical uncertainty of this MACS could be improved by one order of magnitude, from 10% to only 1% in the energy range of stellar interest.

The astrophysical implication of these results is expected to become most apparent in conjunction with the forthcoming results for the ^{79}Se s-process branching nucleus, whose neutron-capture cross section measurement is scheduled for early 2022 at CERN n_TOF using the i-TED system developed in the second part of this work.

i-TED detection system development

The development of the *i*maging-capable *T*otal *E*nergy *D*etector, *i-TED*, is intended to enable the neutron capture cross section measurement of some isotopes, such as ^{79}Se, that so far could not be experimentally accessed by means of state-of-the-art techniques and instrumentation. In this particular case, the only possibility to obtain a sample of ^{79}Se was by means of a lead-selenide alloy activated in the high neutron-flux reactor of ILL-Grenoble. The low ^{79}Se content of only $\sim$ 3 mg makes any ToF neutron-capture measurement particularly sensitive to γ-ray backgrounds arising from neutrons scattered in the sample, that are subsequently captured in the surroundings. i-TED allows one to significantly suppress this type of background by means of the imaging technique, that can be effectively utilized in order to reject γ-rays that are not arising from the capture-sample under study.

After the initial conceptual design based on Monte Carlo simulations [62] a first prototype was built in order to technically validate the components and experimentally demonstrate the background rejection capability. Due to material availability reasons the demonstrator, i-TED5.3, was mounted with three position sensitive detectors (PSDs) distributed between the scatter (1) and absorber (2) planes. Each PSD was based on a $LaCl_3$(Ce) crystal with a size of 50 $\times$50 mm^2 optically coupled to an 8×8 pixels SiPM of the same size. This prototype was characterized in the laboratory in terms of spatial response and energy resolution. Several algorithms were implemented for the intrinsic position reconstruction, which were systematically tested and optimized by means of a dedicated XY-table setup and utilizing crystals with many different thicknesses. This study allowed one to obtain a resolution in the position reconstruction ranging between 1 mm and 2 mm FWHM, depending on crystal thickness [158, 130]. For the third space coordinate or depth of interaction (DoI), a resolution of about 2 mm was found. The energy resolution of the PSDs was found to be between 6% and 7% FWHM at 661 keV for single-events and time-coincidence spectra, respectively, when using ASIC-based readout electronics from PETsys Electronics. The resolution was better, of about 4.5% on average, when using a traditional readout electronics [145].

Once characterized and calibrated, the i-TED5.3 prototype was tested under real neutron-beam conditions at CERN n_TOF. Two state-of-the-art C_6D_6 detectors [77] were also employed in the measurement as reference for comparison purposes. In summary, two separate measurements of the ^{197}Au(n,γ) and ^{56}Fe(n,γ) reactions allowed us to evaluate the performance of this demonstrator in terms of efficiency, ToF resolution, counting-rate capability and background rejection. The main technical difficulty found in this experiment was related to a time-jitter in the trigger of the i-TED acquisition system, which hindered an accurate determination of the time of flight on a pulse-by-pulse basis. At this stage, this problem could be solved to a large extent by means of a dedicated software algorithm. Despite of this difficulty, the measured resonances in ^{197}Au(n,γ)showed a good agreement up to several keV of neutron energy, between state-of-the-art C_6D_6 detectors and i-TED. In the meantime, a hardware solution has been found for the final i-TED detector, which has allowed one to extend the good TOF resolution up to at least 100 keV. Even so, i-TED5.3 could successfully acquire data for the ^{56}Fe(n,γ) reaction up to 30 keV with acceptable ToF resolution. With this experiment it was possible to experimentally demonstrate the background rejection capability of i-TED at 10 keV of neutron energy. A background suppression factor of 2.5 was achieved with i-TED5.3, when compared to a C_6D_6 detector, just by building time-coincidence events between the two detection layers of i-TED. This factor was further enhanced by up to 50% by applying the Compton imaging technique when using an analytical algorithm. The latter was based on the analytical calculation of the geometrical overlap between the Compton cone and the capture-sample, on an event-by-event basis.

The conclusions obtained in this proof-of-principle experiment with the i-TED5.3 prototype were limited by the low counting statistics rather than by systematic effects. However, based on these satisfactory results, four new i-TED Compton modules have been recently assembled consisting of four PSDs in the absorption plane. Motivated also by the results obtained with the analytical Compton analysis technique, new analysis methodologies based on Machine Learning techniques have been developed [131]. The latter allow one to enhance the true capture-event recognition capability, while preserving a high overall performance and efficiency.

In summary, it can be stated that both the ^{80}Se(n,γ) measurement and the i-TED prototype developments reported in this work represent a valuable contribution towards shedding light on the ^{79}Se *s*-process branching, whose measurement will be carried out in 2022 [39].

Appendices

Appendix A

Resonance Parameters

Table A.1: List of resonance parameters and radiative kernels of the ^{80}Se(n,γ) cross section found in this work. Uncertainties come from the analysis with SAMMY.

E_0 (eV)	J	l	Γ_γ (meV)	Γ_n (meV)	R_K (meV)
1473.74(1)	1.5	1	132(10)	36(1)	56(1)
1976.95(15)	0.5	0	307(2)	62885(230)	306(2)
4297.27(67)	0.5	0	128(2)	81341(1193)	128(2)
4314.87(18)	0.5	0	9(8)	111(108)	9(7)
4717.35(3)	0.5	0	224(2)	1139(28)	187(1)
5102.65(78)	0.5	0	120(3)	70971(1788)	120(3)
5662.99(3)	0.5	0	238(6)	503(40)	162(5)
7447.09(73)	0.5	0	6(1)	3202(1044)	6(1)
8122.00(6)	0.5	1	286(3)	1350(74)	236(3)
10521.3(1)	0.5	0	137(8)	513(165)	108(9)
10937.9(1)	0.5	0	215(3)	1278(135)	184(4)
11788.5(1)	0.5	0	122(2)	1106(218)	110(3)
12422.8(6)	0.5	0	152(4)	25044(1325)	151(4)
13806.7(5)	0.5	0	43(21)	74(65)	27(12)
15195.6(2)	1.5	1	230(4)	2541(208)	422(7)
17736.5(4)	0.5	0	100(3)	1557(580)	94(4)
18285.8(5)	0.5	0	133(4)	6769(857)	131(4)
19559.2(7)	0.5	0	52(4)	2110(1178)	51(3)
19957(5)	0.5	0	208(17)	217199(19452)	208(17)
20579(1)	0.5	0	269(7)	8643(885)	261(6)
21809(1)	0.5	0	165(6)	5449(964)	160(5)
22734(3)	0.5	0	251(13)	101828(8312)	250(13)
23876(1)	0.5	0	288(8)	12601(1272)	282(7)
24308(1)	0.5	0	140(6)	5658(1225)	137(5)
25680(3)	0.5	0	17(4)	3989(3643)	17(4)
25937(2)	0.5	0	272(11)	48617(4333)	270(11)
26412(1)	0.5	0	274(9)	19272(2024)	270(9)

Table A.1: *(continued)*

E_0 (eV)	J	l	Γ_γ (meV)	Γ_n (meV)	R_K (meV)
26654(3)	0.5	0	19(3)	829(824)	18(3)
28190(1)	0.5	0	325(10)	10378(1414)	315(9)
29157(2)	0.5	0	61(6)	3217(2553)	59(6)
29320(1)	0.5	0	224(9)	23598(3143)	222(9)
29570(1)	0.5	0	148(8)	9838(2950)	146(8)
29638(3)	0.5	0	29(11)	86(82)	22(8)
30286(1)	0.5	0	173(8)	10619(2153)	170(8)
31889(2)	0.5	0	66(39)	93(77)	39(19)
32224(5)	0.5	0	103(9)	55779(12151)	103(9)
32797(2)	0.5	0	90(7)	13655(5484)	89(7)
33523(2)	0.5	0	210(12)	9596(3446)	206(11)
33763(2)	0.5	0	173(10)	3658(2009)	165(10)
34812(3)	0.5	0	257(13)	24112(5531)	255(13)
35436(6)	0.5	0	98(12)	21191(9771)	98(12)
36636(6)	0.5	0	73(9)	21039(11140)	73(9)
38039(4)	0.5	0	234(17)	33681(7927)	232(17)
38715(7)	0.5	0	94(13)	42694(16557)	93(13)
39338(3)	0.5	0	159(15)	8711(5469)	156(14)
39492(3)	0.5	0	240(16)	20408(5337)	237(16)
40407(3)	0.5	0	181(11)	19012(5449)	179(10)
40864(3)	0.5	0	204(12)	25108(6083)	202(12)
42525(3)	0.5	0	242(28)	5510(4755)	232(27)
42637(6)	0.5	0	489(34)	84661(9142)	486(33)
43150(6)	0.5	0	58(9)	11317(8382)	58(9)
43712(5)	0.5	0	71(34)	149(136)	48(21)
44123(11)	0.5	0	275(27)	193339(33055)	275(26)
44527(3)	0.5	0	143(15)	1732(1692)	132(16)
44801(3)	0.5	0	208(16)	23266(8332)	206(16)
45935(3)	0.5	0	124(11)	5090(4286)	121(11)
46987(6)	0.5	0	224(22)	40075(13358)	223(22)
47268(3)	0.5	0	520(26)	52325(7462)	514(26)
48325(7)	0.5	0	156(17)	50565(17162)	156(17)
48744(5)	0.5	0	182(17)	26842(9936)	181(17)
49251(4)	0.5	0	342(22)	45891(10147)	340(22)
49558(5)	0.5	0	110(14)	24342(13445)	110(14)
50036(3)	0.5	0	457(23)	39377(6930)	452(22)
51271(7)	0.5	0	101(14)	28223(15010)	101(14)
52735(5)	0.5	0	584(30)	101924(14036)	580(30)
53539(6)	0.5	0	154(16)	25653(12754)	153(16)
55092(9)	0.5	0	663(45)	228316(27514)	661(44)

Table A.1: *(continued)*

E_0 (eV)	J	l	Γ_γ (meV)	Γ_n (meV)	R_K (meV)
55979(13)	0.5	0	344(46)	133192(33660)	343(46)
56199(6)	0.5	0	214(31)	38853(15906)	213(30)
56908(5)	0.5	0	356(26)	54670(14378)	354(26)
57498(3)	0.5	0	386(19)	15373(6030)	376(19)
58549(33)	0.5	0	326(83)	366477(118378)	326(83)
59196(9)	0.5	0	529(38)	112179(19463)	527(38)
59666(7)	0.5	0	392(33)	86727(20422)	390(32)
60660(6)	0.5	0	415(30)	63909(14719)	412(30)
61215(7)	0.5	0	152(17)	34289(16744)	152(17)
62610(7)	0.5	0	159(20)	19897(13690)	158(20)
63193(9)	0.5	0	474(42)	137727(25987)	472(41)
63703(7)	0.5	0	224(26)	39995(17753)	222(26)
64238(9)	0.5	0	60(42)	208(204)	46(27)
64486(12)	0.5	0	86(17)	35775(25873)	86(17)
65430(6)	0.5	0	328(26)	31576(12800)	325(25)
66097(19)	0.5	0	599(72)	375818(58734)	598(72)
66918(7)	0.5	0	378(32)	43339(15452)	374(32)
67295(7)	0.5	0	340(258)	388(265)	181(93)
67527(25)	0.5	0	498(86)	334004(73695)	498(85)
68347(8)	0.5	0	304(28)	75480(21969)	302(28)
70316(7)	0.5	0	299(27)	30749(14421)	296(27)
71595(16)	0.5	0	921(90)	386713(56256)	919(90)
72089(5)	0.5	0	218(47)	1224(1210)	185(44)
72643(10)	0.5	0	245(29)	62266(24378)	244(29)
73486(10)	0.5	0	322(34)	87646(26177)	320(34)
74158(26)	0.5	0	125(28)	144208(73087)	124(28)
75373(9)	0.5	0	255(30)	38483(19924)	253(29)
76190(18)	0.5	0	296(59)	185325(66167)	295(59)
77010(7)	0.5	0	387(35)	56076(18717)	385(34)
78363(17)	0.5	0	615(64)	280628(54419)	614(64)
79629(21)	0.5	0	586(72)	339652(68121)	585(71)
80451(7)	0.5	0	262(26)	10293(9192)	256(25)
81081(9)	0.5	0	410(40)	45199(20734)	406(39)
81855(8)	0.5	0	659(52)	104305(23834)	655(52)
83237(7)	0.5	0	586(42)	59824(18932)	581(41)
85505(12)	0.5	0	467(45)	39598(21982)	462(44)
85978(7)	0.5	0	570(44)	22348(13312)	556(42)
87863(30)	0.5	0	431(58)	178562(72847)	430(57)
88364(10)	0.5	0	651(507)	563(369)	302(152)
91955(34)	0.5	0	511(81)	368067(116743)	510(81)

Table A.1: *(continued)*

E_0 (eV)	J	l	Γ_γ (meV)	Γ_n (meV)	R_K (meV)
93122(23)	0.5	0	593(76)	205948(70039)	591(75)
93869(13)	0.5	0	360(43)	22535(18449)	354(42)
94382(21)	0.5	0	327(56)	111215(60300)	326(56)
96178(18)	0.5	0	314(80)	37679(29520)	311(79)
96660(93)	0.5	0	1629(355)	1507724(346810)	1627(354)
98572(19)	0.5	0	266(38)	63733(41611)	265(37)

Appendix B

Linearity graphs

This appendix compiles the linearity graphs corresponding to the horizontal and vertical lines of the 10 mm, 20 mm and 30 mm thick crystals. Scan positions related to these lines are shown with solid black and red circles in Fig. B.1. These data sets are employed in Sec. 3.3 for the calculation of the FoV, the averaged resolution FWHM, and the averaged dispersion RMS.

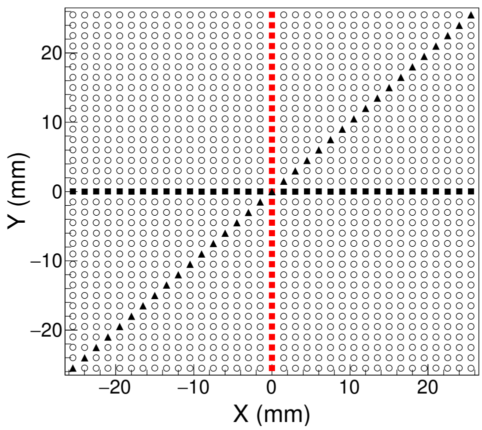

Figure B.1: Scheme layout of the 35 × 35 grid of 1.5 mm step with which the 50 × 50 mm^2 face of the crystals are scanned. Extracted from [158].

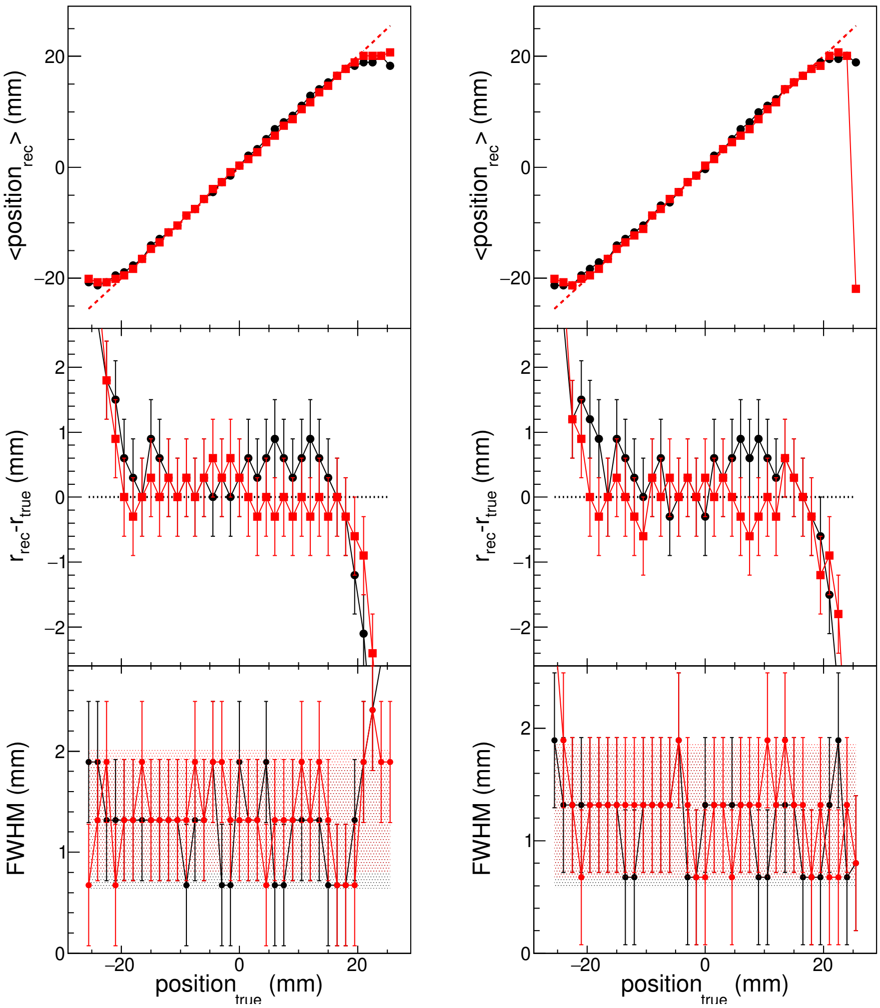

Figure B.2: Linearity graphs obtained with the Lerche (left panel) and Li (right panel) analytical methods, corresponding to the scanned points in the horizontal and vertical lines of the surface of the 10 mm thickness crystal.

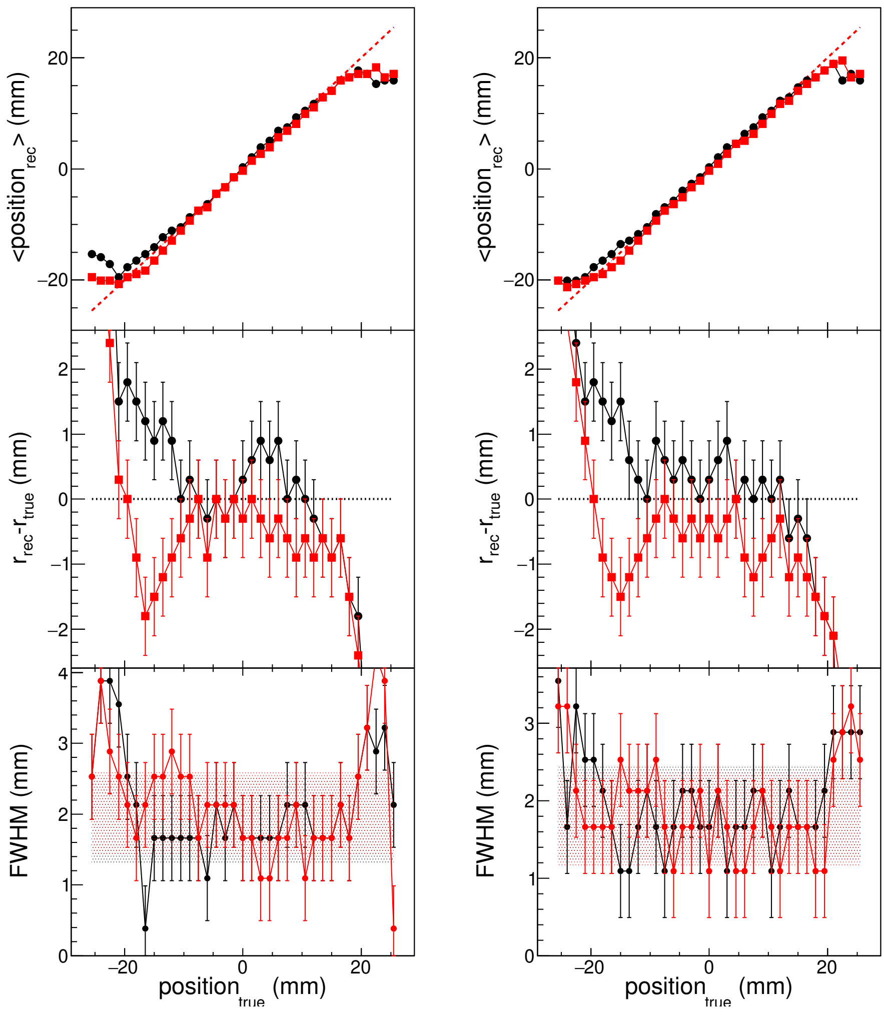

Figure B.3: Linearity graphs obtained with the Lerche (left panel) and Li (right panel) analytical methods, corresponding to the scanned points in the horizontal and vertical lines of the surface of the 20 mm thickness crystal.

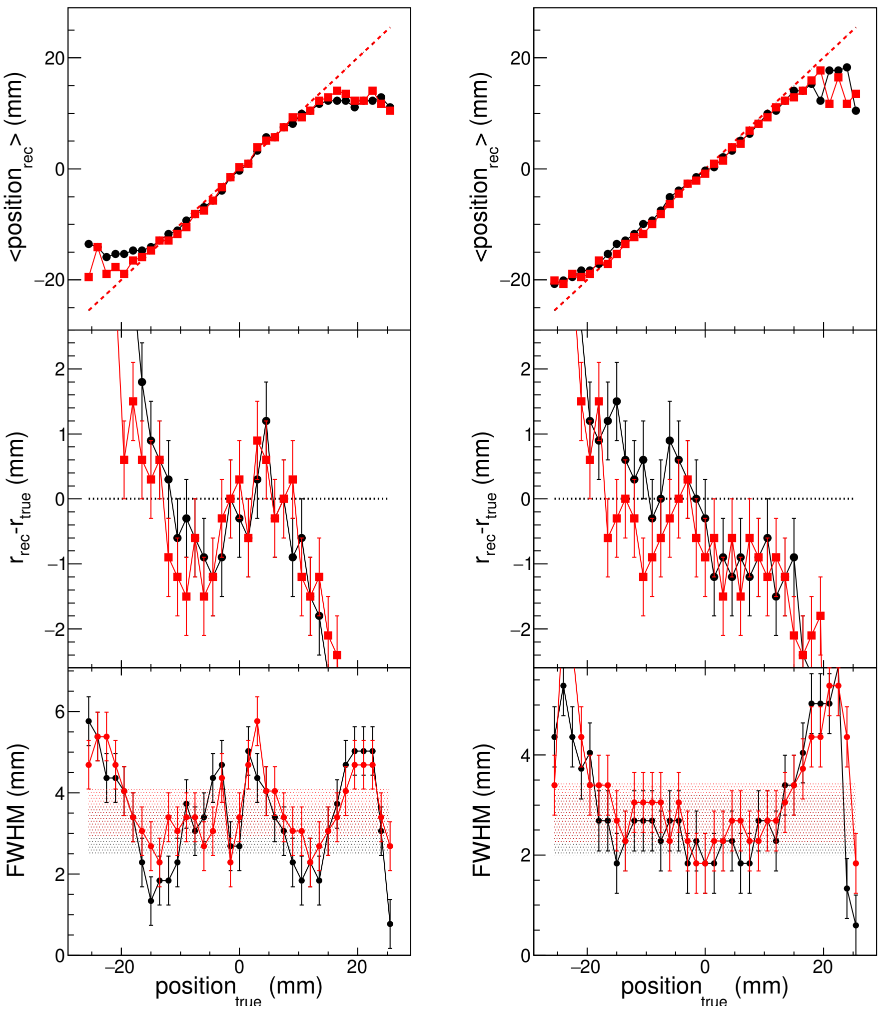

Figure B.4: Linearity graphs obtained with the Lerche (left panel) and Li (right panel) analytical methods, corresponding to the scanned points in the horizontal and vertical lines of the surface of the 30 mm thickness crystal.

Resumen

El proceso de captura lenta de neutrones (s-) es responsable de la formación de la mitad de los elementos más pesados que el hierro en el universo. A pesar de la larga escala de tiempo de este proceso, la larga vida media de algunos isótopos inestables a lo largo del flujo de reacción crea puntos de ramificación que conducen a una división del camino de la nucleosíntesis. ^{79}Se ($t_{1/2} = 3.27 \times 10^5$ y) representa uno de los núcleos ramificados del proceso-s más relevantes y debatidos por dos razones principales. Por un lado, la existencia de estados excitados de baja energía en ^{79}Se, cuya población puede variar con la temperatura del medio estelar, hace que el patrón de abundancia local alrededor de esta ramificación sea especialmente sensible a las condiciones térmicas. Por otro lado, las abundancias observadas de los isótopos de criptón (^{80,82}Kr) son muy conocidas a partir de datos meteóricos. Por lo tanto, al comparar estas abundancias con las predichas por los modelos estelares, se puede obtener información sobre las condiciones térmicas del medio estelar en el que ocurre el proceso-s. Para este objetivo, los modelos estelares hidrodinámicos de última generación necesitan datos experimentales de sección eficaz de captura neutrónica de los isótopos implicados en la ramificación, y en un amplio rango de energía térmica. La última afirmación es cierta para el isótopo inestable ^{79}Se y sus núcleos vecinos más cercanos, ^{78,80}Se. Sin embargo, las mediciones de captura de neutrones en núcleos radiactivos son muy desafiantes y, de hecho, hasta el momento, no hay datos experimentales sobre la reacción ^{79}Se(n, γ). Además, los datos experimentales anteriores sobre ^{80}Se eran bastante limitados en términos de resolución y completitud.

En este contexto, el presente trabajo ha contribuido en dos frentes diferentes con el objetivo de arrojar luz sobre la ramificación ^{79}Se del proceso-s.

Medida de la sección eficaz de captura neutrónica del ^{80}Se

La primera parte de este trabajo describe la medición de la sección eficaz de captura de neutrones del ^{80}Se en el CERN n_TOF, con una resolución de muy alta energía y que cubre por primera vez todo el rango de energía estelar de interés. La medición anterior en ^{80}Se(n,γ) sufre de una resolución de energía muy limitada y un rango corto de energía de neutrones. Estos inconvenientes se han mejorado notablemente en este trabajo por medio de una medición de tiempo de vuelo (ToF) de alta resolución empleando una muestra de alta pureza de 3,8 g de masa. La elección de la instalación de n_TOF para realizar el experimento está fundamentada en la línea de haz de unos 185 m disponible en el área experimental 1 o EAR1. Gracias a esta gran longitud, se pueden obtener una alta resolución en las medida de energía del neutrón usando la técnica del tiempo de vuelo. Esta alta resolución es clave para la mejora de la anterior medida disponible en la sección eficaz de captura neutrónica del isótopo ^{80}Se.

Una configuración experimental basada en cuatro detectores de energía total C_6D_6 fue instalada en EAR1 (n_TOF) para el desarrollo de esta medida. El uso de detectores de energía total C_6D_6 en combinación con la técnica de ponderación de altura de pulso (PHWT), nos ha permitido obtener "yield" de captura con alta precisión y cubriendo todo el rango de energía de interés astrofísico entre 1 eV y 100 keV. Con "yield" de captura nos referimos a la fracción de neutrones en el haz que son capturados por la muestra. El cálculo de esta cantidad es el paso previo para obtener la sección eficaz de captura neutrónica.

La realización de simulaciones Monte Carlo con el código de simulación Geant4 fueron clave para la implementación de la técnica de ponderación de altura de pulso. La geometría completa de la configuración de captura fue simulada con un alto nivel de detalle, incluyendo detectores y materiales de soporte, para la obtención de la función peso encargada de ponderar la altura de cada pulso en función de su energía depositada. Las incertidumbres relativas a la aplicación de esta técnica (PHWT) fueron computadas simulando la emisión de las cascadas de rayos gamma sucedidas tras los eventos de captura. Estas cascadas radiativas se obtuvieron empleando el código estadístico CAPTUGENS. Este código divide la cascada en dos regiones. Hasta una cierta energía de corte, los niveles de energía y las probabilidades de transición se ingresan desde alguna base de datos porque se supone que se conocen experimentalmente. En este trabajo se empleó la base de datos ENSDF para este propósito. Desde la energía de corte hasta la energía de separación neutrónica, el código utiliza modelos estadísticos basados en parámetros de densidad de nivel para construir los niveles restantes. Dos modelos estadísticos fueron utilizados en este estudio, CT y BSFG, ambos exhibiendo buenos resultados en distintas regiones del espectro, baja y alta energía, respectivamente.

Las mismas simulaciones Monte Carlo fueron empleadas en el estudio del fondo de radiación existente durante la medida. Los espectros de las distintas contribuciones de fondo debidas a la actividad ambiental, rayos gammas en el haz y neutrones capturados en el material estructural presente en el área experimental, fueron obtenidas a partir de medias de muestras auxiliares como por ejemplo el plomo. Una vez obtenidos, los espectros fueron pesados de acuerdo a diferencias entre las muestras auxiliares y la muestra problema de ^{80}Se. El fondo total resultante coincide con los valles de las resonancias en casi todo el rango de energía. Sin embargo, existen algunas discrepancias, especialmente a altas energías de neutrones, debido a la complejidad del proceso de sustracción de fondo. No obstante, el fondo total obtenido en este estudio se consideró suficientemente preciso y no se hizo ningún esfuerzo adicional al respecto. Además, el pequeño fondo residual restante se ajustó con el código SAMMY durante el análisis de resonancia, minimizando así la posible contribución de la sustracción de fondo a la incertidumbre total. Así, el impacto de la sustracción de fondo sobre las incertidumbres de los parámetros de resonancias finales es menor del 2 %.

Tal y como se ha mencionado, el "yield" de captura se define como la relación entre los neutrones que sufren captura radiativa en la muestra y el número total de neutrones disponibles para un cierto intervalo de energía neutrónica. Para calcular esta relación se debe conocer la cantidad total de neutrones por pulso contenidos en el haz y su distribución en tiempo de vuelo. No obstante, en este análisis se normaliza el rendimiento mediante el método de resonancia saturada. Gracias a esta normalización, las posibles incertidumbres sistemáticas provenientes de la aplicación de la técnica de pesado de pulsos (PHWT), debido a incertidumbres o sesgos en el modelo de Monte Carlo de la configuración experimental, son canceladas. Por esa razón, solo se requiere la dependencia del flujo con la energía del neutrón para extraer el rendimiento de captura de neutrones diferencial de energía, y no el número absoluto de neutrones. Se desarrollaron varias medidas en n_TOF para evaluar el flujo de neutrones utilizando diferentes sistemas de detección para mantener bajo control las incertidumbres sistemáticas en un amplio rango de energía de neutrones. Sin embargo, la cantidad de ^{10}B en el circuito moderador varía de una campaña experimental a la siguiente debido a las interacciones químicas de los diferentes elementos. Dado que la sección eficaz de absorción de neutrones de ^{10}B es proporcional a $1/E_n$, se espera una diferencia entre nuestro flujo y la versión evaluada solo en la región de baja energía de neutrones. Por el contrario, a altas energías de neutrones, se espera que el flujo permanezca casi inalterado debido a la baja sección eficaz de absorción de ^{10}B en esta región de energía. Para determinar el cambio en el flujo a energías térmicas, se comparó la tasa de conteo registrada por los monitores de flujo de neutrones (SiMon) con la tasa de conteo esperada de la versión evaluada del flujo. De esta manera se obtuvo la versión del flujo correspondiente al experimento realizado, manteniendo las incertidumbres sistemáticas bajo control.

Una vez obtenido el "yield" de captura en todo el rango energético de interés astrofísico, se procedió al análisis de resonancias usando la teoría de la Matriz-R. Esta teoría fue introducida por primera vez por Wigner y Eisenbud en 1947 y es la forma más precisa de describir la física existente, no solo para la captura de neutrones radiativos sino, de una manera más general, para cualquier sistema binario. En la teoría de la Matriz-R, una colisión se describe mediante dos funciones de onda: una función de onda entrante que describe dos partículas incidentes y una función de onda saliente para los productos de reacción emergentes. De la misma forma, el espacio de reacción se divide en dos regiones: una región externa en la que las fuerzas nucleares son despreciables y una región interna donde predominan las fuerzas nucleares. Hacer coincidir las funciones de onda externas e internas en el límite entre estas dos regiones proporciona una forma de describir la sección eficaz de la reacción en términos de las propiedades de los niveles nucleares del núcleo compuesto. Estas propiedades son la energía E_0, el espín y la paridad J^P, y los anchos parciales Γ_c relacionados con cada canal de desintegración c del núcleo compuesto. Por lo tanto, este método no se ocupa de las fuerzas nucleares involucradas en la reacción, sino que describe el comportamiento de resonancia de su sección eficaz utilizando solo las propiedades mencionadas anteriormente. En este trabajo, obtuvimos los parámetros E_0, J^P y Γ_c tras ajustar todas las resonancias de captura disponibles en el "yield" de captura usando el código SAMMY, que fue desarrollado en 1980 para el análisis de datos de sección eficaz inducida por neutrones en el Acelerador Lineal de Electrones de Oak Ridge. Este código se basa en la teoría de la Matriz-R, que proporciona una descripción fenomenológica de las reacciones inducidas por neutrones. SAMMY realiza un ajuste bayesiano a los datos experimentales, utilizando un conjunto inicial de parámetros de resonancia de Matriz-R. En este análisis, ciento trece resonancias fueron caracterizadas, noventa y ocho de ellas por primera vez.

El impacto de este nuevo análisis es considerable en el resultado final de la sección eficaz de captura neutrónica, y más concretamente en la sección eficaz promediada o MACS (Maxwellian Averaged Cross Section). Esta última es la magnitud más relevante para los cálculos astrofísicos, ya que durante el proceso-s, los neutrones en las estrellas se termalizan siguiendo la distribución de velocidades de Maxwell para su correspondiente temperatura. Por esta razón, en este trabajo se obtuvieron los valores para la MACS del ^{80}Se entre 1 keV y 100 keV de temperatura. El valor MACS obtenido a kT = 8 keV resultó un 36 % menor que el valor recomendado en KADoNiS. La incertidumbre estadística que afecta a esta nuevo MACS se reduce del 10 % al 1 %, mientras que la precisión sistemática alcanzada, entre el 3.2 % y el 5.7 %, es comparable a las incertidumbres de las abundancias isotópicas de los isótopos de Kr solo-s, que es el requisito de los modelos estelares hidrodinámicos para ofrecer resultados precisos.

Desarrollo del detector i-TED

La segunda contribución principal de este trabajo al estudio del punto de ramificación ^{79}Se, consistió en los primeros desarrollos hacia un novedoso sistema de detección llamado i-TED. Este último ha sido diseñado para medir (n,γ) secciones transversales con mayor relación señal-fondo. Este nuevo sistema de detección se aplicará por primera vez en la medición de la sección eficaz ^{79}Se(n,γ) en el CERN n_TOF en 2022.

El detector de energía total i-TED con capacidad de generación de imágenes aprovecha la técnica de imagen de Compton para seleccionar principalmente los rayos gamma generados en la muestra por los neutrones capturados en ella, al tiempo que rechaza los rayos gamma contaminantes provenientes de los neutrones dispersados y capturados en el entorno. El diseño de este novedoso sistema de detección se centra en maximizar la eficiencia de detección manteniendo su sensibilidad intrínseca a los neutrones lo más baja posible. Este último está relacionado con los neutrones dispersados en la muestra y capturados en el propio detector. Si no se corrige, este incremento en la tasa de conteo puede conducir a una sobrestimación de la sección eficaz medida. En este sentido, el uso de un colimador masivo para determinar la dirección de la partícula entrante fue probado durante el desarrollo de los primeros prototipos y posteriormente descartado. La última conclusión se basó principalmente en el nivel de fondo prohibitivo inducido por el colimador mecánico y la gran reducción en la eficiencia de detección. Para superar estas limitaciones, i-TED aplica la colimación electrónica por medio de la técnica de imágenes de Compton, que simultáneamente mejora la eficiencia de detección y reduce la cantidad de material estructural. El principio de funcionamiento de i-TED se detalla a continuación. Un rayo gamma entrante interactúa con el primer plano de detección, sufre una dispersión Compton y luego deposita el resto de su energía en el segundo plano de detección, donde sufre una foto-absorción. Por ello, estos planos se denominan Scatter (dispersor) y Absorber (absorbente), y sus espesores se seleccionan para maximizar la probabilidad de dispersión en el primero y la absorción total de energía el segundo. La energía, posición y tiempo de las interacciones de los rayos gamma se registran en cada una de las dos etapas de detección. La línea definida por los dos puntos de interacción, r_1 y r_2, se convierte en el eje de un cono virtual cuyo ángulo de apertura θ viene dado por la fórmula de Compton, que depende de la energía depositada por el rayo gamma en los dos planos de detección. La pared del cono Compton contiene todas las direcciones posibles de la radiación entrante. Dado que la posición y el tamaño de la muestra se conocen por construcción, esta información se puede usar para verificar si el rayo gamma proviene de la muestra o no. Como se muestra en la figura anterior, la intersección del cono con el plano vertical situado en la posición de la muestra justo delante de la cara de dispersión (en adelante plano imagen), dibuja una elipse. Si este último pasa por el punto donde se encuentra la muestra, se acepta el evento. De lo contrario, el evento es rechazado.

En este trabajo de tesis se ha desarrollado y caracterizado un primer demostrador denominado i-TED5.3, con tres detectores sensibles a la posición (PSDs), y se ha realizado la primera prueba de concepto experimental. En i-TED5.3, un PSD se coloca en el Scatter mientras que los dos restantes se organizan en una configuración vertical dentro de la capa Absorber. Cada PSD consta de un cristal de centelleo $LaCl_3(Ce)$ monolítico acoplado ópticamente a un fotomultiplicador de silicio (SiPM), que está conectado a un sistema de lectura basado en ASIC fabricado por PETsys Electronics. El cristal centelleador instalado en el Scatter, de 10 mm de grosor, trata de maximizar la probabilidad de dispersión del rayo gamma, mientras que dos cristales monolíticos de 25 mm de grosor fueron montados en el Absorber para favorecer la absorción total del rayo gamma.

La calibración energética de cada detector sensible a la posición entre 120 keV y 1.4 MeV i-TED se realizó utilizando una fuente de ^{152}Eu ($t_{1/2}$ = 13.5 y). Las siete transiciones de rayos gamma más intensas de este isótopo radiactivo, proporcionaron una calibración fiable en este rango de energía. Sin embargo, la cascada de rayos gamma emitida después de un evento de captura tiene una energía aproximada de $E_C \approx S_n + E_n$. Teniendo en cuenta la energía de separación de neutrones de ^{197}Au ($S_n = 6.51$ MeV) y ^{56}Fe ($S_n = 7.65$ MeV), y el rango de energía de los neutrones de interés (1 eV $< E_n <$100 keV), las cascadas generadas pueden contienen energías de rayos gamma de hasta 7.75 MeV. La multiplicidad variable de estas cascadas produce rayos gamma individuales con energías que van desde unas pocas decenas de keV hasta 7.75 MeV. Por lo tanto, el rango para la calibración de energía de i-TED5.3 obtenida con la fuente de ^{152}Eu tuvo que ser ampliado. Para ello, se emplearon los espectros de energía depositada de ^{197}Au(n,γ) y ^{56}Fe(n,γ). La ubicación de los bordes Compton en los espectros de energía depositados de estas reacciones, medidos con detectores C_6D_6 calibrados, proporciona dos puntos de referencia adicionales para la calibración i-TED. Unn polinomio de segundo grado fue ajustado y combinado con la función anterior obtenida usando la fuente ^{152}Eu. Mediante el uso de esta calibración de energía, i-TED5.3 logra resoluciones de energía que oscilan entre el 7 % y el 5 % FWHM a 662 keV para los cristales colocados en los planos Scatter y Absorber, y 7 % FWHM a 662 keV para el espectro add-back en coincidencias.

Por otro lado, la cara cuadrada de cada detector sensible a la posición fue escaneada con una fuente colimada de sodio y usando una mesa de posicionamiento XY con el objetivo de implementar y probar distintos algoritmos de reconstrucción de la posición sobre cristales centelleadores $LaCl_3$(Ce) de distintos espesores. Finalmente, los mejores resultados fueron obtenidos tras la implementación de los modelos analíticos, especialmente del modelo propuesto por Li y colaboradores. Así, tras una caracterización completa del prototipo i-TED5.3, resoluciones de posición que oscilan entre 1 mm y 2 mm FWHM fueron obtenidas.

Tras la caracterización en energía y posición del detector, imágenes Compton pudieron ser obtenidas con el prototipo i-TED5.3. La resolución de la imagen obtenida se determinó ajustando dos formas gaussianas a cada distribución proyectada: una ancha se ajustó a la base de la distribución y una estrecha a la forma del pico. El ancho de este pico nos dió una estimación de la resolución de la imagen Compton. Debido a la configuración de matriz vertical de los PSD en el Absorber, la resolución de 80 mm FWHM en el eje Y es ligeramente mejor que los 90 mm FWHM logrados en el eje X.

Finalmente, un primer experimento de prueba de concepto llevado a cabo en el CERN n_TOF con i-TED5.3 permitió validar técnicamente el sistema en su uso para experimentos de tiempo de vuelo y demostrar las capacidades de rechazo de fondo. El experimento se realizó en EAR1, que se consideró más conveniente para probar el sistema debido a la alta resolución de energía y al flujo de neutrones más moderado, 25 veces menor que el disponible en EAR2. Se utilizaron como referencia dos detectores C_6D_6 de última generación. Después de corregir una dificultad en la lectura del tiempo de vuelo en i-TED, la resolución temporal de ambos sistemas de detección se volvieron comparables, al menos en la región de energía estudiada hasta 1 keV. Por otro lado, se logró una reducción de fondo de hasta un factor de 3.8 en los espectros de energía de neutrones ^{56}Fe(n,γ) con i-TED5.3 con respecto los detectores C_6D_6 de última generación.

Los resultados presentados en esta tesis representan la primera prueba de concepto del rechazo de fondo con i-TED realizada con un modesto demostrador cuyo volumen de detección corresponde solo a 3/20 del dispositivo final. Se espera una mejora notable en términos de eficiencia y rechazo de fondo con la implementación de la matriz i-TED final.

Los siguientes pasos emprendidos en el desarrollo de una metodología de análisis adecuada para el concepto i-TED se han centrado en explotar técnicas de Inteligencia Artificial y Aprendizaje Automático. Los últimos resultados a este respecto han permitido reducir notablemente la fuerte reducción de la eficiencia del método analítico discutido aquí, al tiempo que se mantiene una SBR alta de 3-4. Otras mejoras realizadas fuera del alcance de este trabajo de tesis comprenden el ensamblaje y la caracterización de una matriz de 4 detectores i-TED, cada uno con 5 PSD, y el uso de técnicas de inteligencia artificial y aprendizaje automático para mejorar aún más la capacidad de rechazo de fondo. y el rendimiento general del sistema.

Conclusiones

El presente trabajo, se han realizado dos contribuciones relevantes para la próxima medición de la sección eficaz ^{79}Se(n,γ) que permitirá la primera interpretación consistente del punto de ramificación del proceso-*s* situado en ^{79}Se. Por un lado, la sección eficaz del núcleo producto ^{79}Se+n, ^{80}Se, ha sido medida con alta precisión, alta resolución y cubriendo todo el rango de energía estelar, desde 1 eV hasta 100 keV. Los resultados de este trabajo experimental se resumen en la primera sección a continuación. Además, este trabajo de tesis incluye los primeros desarrollos hacia una nueva técnica de detección, que aprovecha las imágenes de Compton como una herramienta para reducir los fondos localizados espacialmente en los experimentos de tiempo de vuelo de captura de neutrones. El desarrollo del primer prototipo y las mediciones de prueba de concepto también se resumen a continuación.

Medida de la sección eficaz de captura neutrónica del ^{79}Se

El objetivo de la primera parte de esta tesis fue la medición de tiempo de vuelo (ToF) de alta resolución de la sección eficaz ^{80}Se(n,γ). La medición previa existente sobre este isótopo cubría solo un rango de energía muy limitado y sufría de una resolución de energía de neutrones bastante baja. Ambos aspectos se han mejorado notablemente con el presente trabajo.

La nueva medición de ToF se realizó en las instalaciones n_TOF del CERN empleando una matriz de cuatro detectores de rayos gamma C_6D_6 de última generación y una muestra de ^{80}Se con una pureza del 99.87(10) %. Se utilizó el área experimental EAR1 debido a la trayectoria de vuelo de $\sim$ 185 m y la resolución en tiempo de vuelo alcanzable. La larga trayectoria de vuelo junto con el bajo ciclo de trabajo del Proton Synchrotron (PS), sumado al tiempo de respuesta rápido de los detectores C_6D_6, nos permitieron obtener una resolución de energía de neutrones muy alta (1.2 % FWHM a 1 keV) además de un intervalo amplio de energía de neutrones de 1 eV a 100 keV.

A pesar de la relación relativamente grande entre dispersión y captura, la sensibilidad neutrónica muy baja de los detectores C_6D_6 basados en fibra de carbono nos permitió medir un rendimiento de captura prácticamente libre de efectos de sensibilidad neutrónica.

El rendimiento de captura de la reacción ^{80}Se(n,γ) se obtuvo después de aplicar la técnica de ponderación de altura de pulso (PHWT) siguiendo la metodología originalmente desarrollada y validada en el Grupo de Espectroscopía de Rayos Gamma de IFIC. Este último se basa en la combinación de los datos medidos con una simulación estadística de Monte Carlo de las cascadas de captura rápida, con el fin de derivar factores de corrección de rendimiento precisos que permitan tener en cuenta efectos sistemáticos como el umbral electrónico en los detectores, efectos de suma de rayos gamma y electrones de conversión. Esta metodología, junto con un cuidadoso análisis y sustracción de fondos experimentales nos permitió obtener el rendimiento de captura de la reacción ^{80}Se(n,γ) con un bajo nivel de incertidumbre sistemática, entre 3.2 % y 5.7 %, dependiendo principalmente de la precisión de la flujo de neutrones en cada región de energía de neutrones. Se realizó un análisis de resonancia del rendimiento de captura mediante el código de Matriz-R SAMMY. Este análisis entregó parámetros de resonancia ^{80}Se(n,γ) por primera vez por debajo de 3 keV. En total se caracterizaron 113 resonancias entre 1 eV y 100 keV, 98 de ellas por primera vez. Las 15 resonancias restantes se conocían anteriormente solo a partir de mediciones de transmisión.

Los nuevos parámetros de resonancia permitieron determinar también la sección eficaz maxwelliana promedio (MACS) de una manera más consistente y precisa. Los resultados obtenidos indican que la MACS de la reacción ^{80}Se(n,γ) es en realidad entre un 20 % y un 30 % más bajo que los valores recomendados previamente. Además, con el presente trabajo se podría mejorar en un orden de magnitud la incertidumbre estadística relativa de esta MACS, desde un 10 % a sólo un 1 % en el rango de energía de interés estelar.

Se espera que la implicación astrofísica de estos resultados se vuelva más evidente junto con los próximos resultados para el núcleo de ramificación del proceso-s ^{79}Se, cuya medición de la sección eficaz de captura de neutrones está programada para principios de 2022 en el CERN n_TOF utilizando el sistema i-TED desarrollado en la segunda parte de este trabajo.

Desarrollo del detector i-TED

El desarrollo del detector de energía total (TED) con capacidad de generación de imágenes (i-), i-TED, está destinado a permitir la medición de la sección eficaz de captura de neutrones de algunos isótopos, como ^{79}Se, a los que hasta ahora no se podía acceder experimentalmente mediante técnicas e instrumentación de última generación. En este caso particular, la única posibilidad de obtener una muestra de ^{79}Se era mediante una aleación de plomo-selenio activada en el reactor de alto flujo de neutrones de ILL-Grenoble. El bajo contenido de ^{79}Se de solo $\sim$ 3 mg hace que cualquier medición de captura de neutrones, usando la técnica de tiempo de vuelo, sea particularmente sensible a los fondos de rayos gamma que surgen de los neutrones dispersados en la muestra y posteriormente capturados en los alrededores. i-TED permite suprimir significativamente este tipo de fondo por medio de la técnica de imagen, que se puede utilizar de manera efectiva para rechazar rayos gamma que no surgen de la muestra de captura en estudio.

Después del diseño conceptual inicial basado en simulaciones de Monte Carlo se construyó un primer prototipo para validar técnicamente los componentes y demostrar experimentalmente la capacidad de rechazo de fondo. Por razones de disponibilidad de material, el demostrador i-TED5.3 se montó con tres detectores sensibles a la posición (PSD) distribuidos entre los planos Scatter (1) y Absorber (2). Cada PSD se basó en un cristal $LaCl_3$(Ce) con un tamaño de 50 $\times$50 mm^2 acoplado ópticamente a un SiPM de 8$\times$8 pixels del mismo tamaño. Este prototipo se caracterizó en el laboratorio en términos de respuesta espacial y resolución energética. Se implementaron varios algoritmos para la reconstrucción de la posición intrínseca, que se probaron y optimizaron sistemáticamente por medio de una configuración de mesa de posicionamiento XY dedicada y utilizando cristales con espesores diferentes. Este estudio permitió obtener una resolución en la reconstrucción de la posición que oscila entre 1 mm y 2 mm FWHM, dependiendo del espesor del cristal. Para la tercera coordenada espacial o profundidad de interacción (DoI), se encontró una resolución de alrededor de 2 mm. Se encontró que la resolución de energía de los PSD está entre 6 % y 7 % FWHM a 661 keV para eventos únicos y espectros de coincidencia de tiempo, respectivamente, cuando se usa electrónica de lectura basada en ASIC de PETsys Electronics. La resolución obtenida fue mejor, de un 4.5 % de media, con el uso de la electrónica tradicional.

Una vez caracterizado y calibrado, el prototipo i-TED5.3 se probó en condiciones reales de haz de neutrones en el CERN n_TOF. También se emplearon dos C_6D_6 detectors de última generación en la medición como referencia para propósitos de comparación. En resumen, dos mediciones separadas de las reacciones ^{197}Au(n,γ) y ^{56}Fe(n,γ) nos permitieron evaluar el desempeño de este demostrador en términos de eficiencia, resolución ToF, capacidad de tasa de conteo y rechazo de fondo. La principal dificultad técnica encontrada en este experimento estaba relacionada con un time-jitter en el disparador del sistema de adquisición i-TED, que impedía determinar con precisión el tiempo de vuelo pulso a pulso. En esta etapa, este problema podría resolverse en gran medida mediante un algoritmo de software dedicado. A pesar de esta dificultad, las resonancias medidas en ^{197}Au(n,γ) mostraron una buena concordancia hasta varios keV de energía neutrónica, entre detectores C_6D_6 de última generación e i-TED. Mientras tanto, se ha encontrado una solución de hardware para el detector i-TED final, que ha permitido ampliar la buena resolución TOF hasta al menos 100 keV. Aun así, i-TED5.3 pudo adquirir con éxito datos para la reacción ^{56}Fe(n,γ) hasta 30 keV con una resolución ToF aceptable. Con este experimento fue posible demostrar experimentalmente la capacidad de rechazo de fondo de i-TED a 10 keV de energía de neutrones. Se logró un factor de supresión de fondo de 2.5 con i-TED5.3, en comparación con un detector C_6D_6 , simplemente construyendo eventos de coincidencia de tiempo entre las dos capas de detección de i-TED. Este factor se mejoró aún más hasta en un 50 % al aplicar la técnica de imagen de Compton al usar un algoritmo analítico. Este último se basó en el cálculo analítico de la superposición geométrica entre el cono Compton y la muestra de captura, evento por evento.

Las conclusiones obtenidas en este experimento de prueba de principio con el prototipo i-TED5.3 estuvieron limitadas por las bajas estadísticas de conteo más que por los efectos sistemáticos. Sin embargo, en base a estos resultados satisfactorios, recientemente se han ensamblado cuatro nuevos módulos i-TED Compton que consisten en cuatro PSD en el plano de absorción. Motivados también por los resultados obtenidos con la técnica de análisis analítico Compton, se han desarrollado nuevas metodologías de análisis basadas en técnicas de Machine Learning. Estos últimos permiten mejorar la verdadera capacidad de reconocimiento de eventos de captura, al tiempo que conservan un alto rendimiento y eficiencia generales.

En resumen, se puede afirmar que tanto la medición de la reacción ^{80}Se(n,γ) como los desarrollos del prototipo i-TED reportados en este trabajo representan una valiosa contribución para arrojar luz sobre la ramificación del proceso-s ^{79}Se, cuya medición se llevará a cabo en 2022.

Agradecimientos

Según un dicho popular muy arraigado en mi familia, *es de bien nacido ser agradecido*. Por lo tanto, aquí van mis agradecimientos.

En primer lugar, comienzo agradeciendo a una persona sin la cual muy probablemente no me habría embarcado en esta aventura que ha sido el doctorado. Gracias Pablo, gracias por hacerme ver que podía y debía. Toda la ayuda que me has prestado desinteresadamente durante todos estos años no cabe en un simple gracias pero, "¡acho es lo que hay!". Gracias por tus explicaciones clarificadoras y por las discusiones constructivas, pero sobre todo, por estar ahí siempre para compartir mis crisis predoctorales.

De mi etapa como doctorando, hay una persona a la que tengo mucho que agradecer, mi director de tesis y mentor César. Muchas gracias por la confianza depositada en mí para sacar adelante este trabajo y por darle una oportunidad a la ilusión y la pasión. Gracias por esos momentos de *coaching* que nunca olvidaré y que tanta fuerza me aportaron para continuar adelante durante los momentos más difíciles de la tesis. Y gracias, muchísimas gracias, por tu (infinita) paciencia estos años en los que has logrado que (al menos en algunos momentos) un extremeño consiga hablar con propiedad y manteniendo las exageraciones a raya.

Mención especial merecen mis compañeros de equipo, *hymnies*. Luis, Ion, Jorge, Javi, Adrià y Ariel muchísimas gracias por el apoyo moral y profesional, por enseñarme tanto sobre tantos aspectos de la vida, y por esas cervezas sanadoras. Sin vosotros nunca habría podido sacarle tanto partido a esta experiencia, gracias de corazón.

I could not forget to thank the *ntofers*. Both senior: Alberto, Nicola, Enrico, Carlos, Laurent, Daniela... and young: Massimo, Mario, Federica, Lucia, Michi, Alice, Sebastian, Veatriki, Sam, Simone, Adhitya, Zina, Víctor, Llanlle, Tere... You all made me feel at home despite being more than a thousand km away. Thanks you for welcoming me in this great family called n_TOF.

Durante estos años en el IFIC he disfrutado de momentos excepcionales con compañeras y compañeros a los que también tengo mucho que agradecer. Álvaro, Davide, Alberto, Varsha, Javi Nano, Mariluz, Rosa, Gustavo, Selene, David... Muchas gracias a todas y todos por esos momentos tan divertidos durante las comidas y esas charlas que me aportaron tanta calma y distintas perspectivas. Ir a trabajar con vosotros allí siempre será un placer.

Aprovecho la ocasión para retroceder un poco más en el tiempo y agradecer también a todas y todos mis compañeras y compañeros de andanzas durante la vida universitaria, tanto en Badajoz: Churro, Pablo, Pedro, Juan, Tejeda, Juan Ángel, Mario, Luis, Zanga... como en Salamanca: Patri, Pablo, Ferre, Zinani, Mele, Oliva, Deiv... De esta etapa me llevo amistades infinitas de esas que no se apagan nunca, algo que ha sido fundamental para afrontar este reto.

En el plano personal, tengo que agradecer todo el apoyo recibido por mi familia, tíos y primos que siempre estáis ahí, gracias. Esta etapa ha servido además para acercarme de nuevo a la familia de la que, por distancia, estaba más alejado. Suerte que el CERN y vuestra casa están en el mismo país, muchas gracias Dani y Viti por vuestra hospitalidad. Y no puedo olvidarme de mi nueva gran familia. Gracias Javi por aguantar al zombi pegado al ordenador que no sale del salón de casa de tu novia. Y por supuesto, gracias a las muchachas y muchachos integrantes de la familia Sastre Miguel: Emilia, Josep, Pau, Astrid y abuela Emilia, por acogerme como uno más y regalarme esos almuerzos al sol y esas sobremesas de las que tanto me queda por aprender. Sin esos momentos y vuestro incesante apoyo este camino habría sido infinitamente más complicado.

Finalmente:

Por las vacaciones de fin de semana de cuyas experiencias nacen grandes viñetas y en las que las horas se vuelven segundos. Por tu apoyo incondicional y diario, tu paciencia y pasión sin los que este día difícilmente habría llegado. Por ser tú misma sin filtros. Pero sobre todo, por quererme bien, Pepa, tuyos son mis agradecimientos, mi amor.

Por traerme al mundo, criarme, educarme y sacarme adelante. Por vuestra paciencia y amor incondicional que han sido clave para llegar hasta aquí, gracias mamá y papá, Julia y Antonio, siento orgullo y admiración por vosotros. Os quiero mucho.

Por ayudarme a mantener una alimentación medianamente saludable y conectarme al mundo durante todos estos meses de escribano. Por ser como eres, por aguantarme, por apoyarme y por aceptar este regalo tan bonito de la vida que está siendo vivir juntos, gracias hermana. Ica te quiero.

Por último, no se me puede escapar la oportunidad de agradecer a Walter. Sin sus maullidos, juegos y, especialmente, sus paseos frente a la pantalla del ordenador nunca habría sabido cuando parar de escribir al final del dia. Gracias compañero.

Gracias a todas y a todos de corazón.

Bibliography

[1] F. W. Clarke. The Relative Abundance of the Chemical Elements. *Bull. Phil. Soc. Washington*, 11:131–142, 1889.

[2] W. D. Harkins. The evolution of the elements and the stability of complex atoms I. A new periodic system which shows a relation between the abundance of the elements and the structure of the nuclei of atoms. *Journal of the American Chemical Society*, 39(5):856–879, 1917.

[3] V. M. Goldschmidt. Geochemische Verteilungsgesetze der Elemente, IX. *Skrifter Norske Videnskaps-Akad. Oslo. I. Mat. Naturv. Kl.*, 4(1), 1937.

[4] H. E. Suess and H. C. Urey. Abundances of the Elements. *Reviews of Modern Physics*, 28(1):53–74, January 1956.

[5] M. G. Mayer and E. Teller. On the Origin of Elements. *Physical Review*, 76(8):1226–1231, October 1949.

[6] R. A. Alpher and R. C. Herman. The Origin and Abundance Distribution of the Elements. *Annual Review of Nuclear and Particle Science*, 2:1–40, January 1953.

[7] P. W. Merrill. Spectroscopic Observations of Stars of Class S. *Astrophysical Journal*, 116:21, July 1952.

[8] Planck Collaboration et al. Planck 2018 results. VI. Cosmological parameters. *Astronomy & Astrophysics*, 641:A6, September 2020.

[9] E. M. Burbidge et al. Synthesis of the Elements in Stars. *Reviews of Modern Physics*, 29(4):547–650, January 1957.

[10] A. G. W. Cameron. *Stellar evolution, nuclear astrophysics, and nucleogenesis. Second edition.* Dover Publications, 2013. originally published as a technical report by Atomic Energy of Canada, Ltd., 1957.

[11] Takigawa, Noboru and Washiyama, Kouhei. *Synthesis of Elements: Fundamentals of Nuclear Physics.* Springer Japan, Tokyo, 2017.

[12] F. Käppeler et al. The *s*-process: Nuclear physics, stellar models, and observations. *Reviews of Modern Physics*, 83(1):157–194, January 2011.

[13] S. Degl'Innocenti et al. The FRANEC stellar evolutionary code. *Astrophysics and Space Science*, 316(1-4):25–30, August 2008.

[14] B. Paxton et al. Modules for Experiments in Stellar Astrophysics (MESA). *Astrophysical Journal Supplement*, 192:3, jan 2011.

[15] D. Watson et al. Identification of strontium in the merger of two neutron stars. *Nature*, 574(7779):497–500, October 2019.

[16] M. Arnould et al. The *r*-process of stellar nucleosynthesis: Astrophysics and nuclear physics achievements and mysteries. *Physics Reports*, 450(4-6):97–213, September 2007.

[17] M. Arnould and S. Goriely. The *p*-process of stellar nucleosynthesis: astrophysics and nuclear physics status. *Physics Reports*, 384(1-2):1–84, September 2003.

[18] P. A. Seeger et al. Nucleosynthesis of Heavy Elements by Neutron Capture. *Astrophysical Journal Supplement*, 11:121, February 1965.

[19] D. D. Clayton and R. A. Ward. *s*-process Studies: Exact Evaluation of an Exponential Distribution of Exposures. *Astrophysical Journal*, 193:397–400, October 1974.

[20] M. Pignatari et al. The Weak *s*-process in Massive Stars and its Dependence on the Neutron Capture Cross Sections. *The Astrophysical Journal*, 710(2):1557–1577, February 2010.

[21] C. Arlandini et al. Neutron Capture in Low-Mass Asymptotic Giant Branch Stars: Cross Sections and Abundance Signatures. *Astrophysical Journal*, 525(2):886–900, November 1999.

[22] M. Pignatari et al. NuGrid Stellar Data Set. I.Stellar Yields from H to Bi for Stars with Metallicities Z = 0.02 and Z = 0.01. *Astrophysical Journal Supplement*, 225(2):24, August 2016.

[23] R. Gallino et al. Evolution and Nucleosynthesis in Low-Mass Asymptotic Giant Branch Stars. II. Neutron Capture and the *s*-process. *The Astrophysical Journal*, 497(1):388–403, April 1998.

[24] S. Cristallo et al. Evolution, Nucleosynthesis, and Yields of Low-Mass Asymptotic Giant Branch Stars at Different Metallicities. *The Astrophysical Journal*, 696(1):797–820, May 2009.

[25] O. Straniero et al. *s*-process in low-mass asymptotic giant branch stars. *Nuclear Physics A*, 777:311–339, October 2006.

[26] F. Herwig. Evolution of Asymptotic Giant Branch Stars. *Annual Review of Astronomy & Astrophysics*, 43(1):435–479, September 2005.

[27] U. Ott et al. *s*-process krypton of variable isotopic composition in the Murchison meteorite. *Nature*, 332(6166):700–702, April 1988.

[28] R. S. Lewis et al. Meteoritic silicon carbide: pristine material from carbon stars. *Nature*, 348(6299):293–298, November 1990.

[29] R. S. Lewis et al. Interstellar grains in meteorites: II. SiC and its noble gases. *Geochimica et Cosmochimica Acta*, 58(1):471–494, January 1994.

[30] F. Kappeler et al. *s*-process nucleosynthesis-nuclear physics and the classical model. *Reports on Progress in Physics*, 52(8):945–1013, August 1989.

[31] G. Walter et al. The *s*-process branching at ^{79}Se. *Astronomy and Astrophysics*, 167(1):186–199, October 1986.

[32] G. Cescutti et al. Uncertainties in *s*-process nucleosynthesis in low-mass stars determined from Monte Carlo variations. *Monthly Notices of the Royal Astronomical Society*, 478(3):4101–4127, August 2018.

[33] N. Prantzos et al. Chemical evolution with rotating massive star yields II. A new assessment of the solar s- and *r*-process components. *Monthly Notices of the Royal Astronomical Society*, 491(2):1832–1850, January 2020.

[34] C. Lederer-Woods et al. Neutron capture measurements on ^{77,78}Se and ^{68}Zn, and the origin of selenium in massive stars. Technical Report CERN-INTC-2017-038 / INTC-P-509, CERN, 2017.

[35] M. Heil et al. Stellar (n,γ) cross sections for Br and Rb: Matching the weak and main *s*-process components. *Physical Review C*, 78(2):025802, August 2008.

[36] P. Mutti et al. New Kr Cross Sections and Astrophysical Constraints on Presolar Grains. In R. C. Haight et al., editors, *International Conference on Nuclear Data for Science and Technology*, volume 769 of *American Institute of Physics Conference Series*, pp. 1327–1330, May 2005.

[37] V. Babiano-Suárez et al. Completing the puzzle around the ^{79}Se *s*-process branching with the ^{80}Se(n, γ) cross-section measurement . Technical Report CERN-INTC-2018-005, INTC-P-536, CERN, Geneva, Jan 2018.

[38] High-sensitivitY Measurements of key stellar Nucleo-Synthesis reactions (HYMNS). ERC-consolidator grant agreement no. 681740, PI: C. Domingo Pardo.

[39] V. Babiano-Suárez et al. First measurement of the *s*-process branching ^{79}Se(n,γ). Technical Report CERN-INTC-2020-065, INTC-P-580, CERN, Geneva, Sep 2020.

[40] M. Salvatores et al. The Transmutation of Long-Lived Fission Products by Neutron Irradiation. *Nuclear Science and Engineering*, 130(3):309–319, 1998.

[41] W. S. Yang et al. Long-Lived Fission Product Transmutation Studies. *Nuclear Science and Engineering*, 146(3):291–318, 2004.

[42] S. Chiba et al. Method to Reduce Long-lived Fission Products by Nuclear Transmutations with Fast Spectrum Reactors. *Scientific Reports*, 7:13961, October 2017.

[43] G. Jörg et al. Preparation of radiochemically pure ^{79}Se and highly precise determination of its half-life. *Applied Radiation and Isotopes*, 68(12):2339–2351, 2010.

[44] A. J. M. Plompen et al. The joint evaluated fission and fusion nuclear data library, JEFF-3.3. *European Physical Journal A*, 56(7):181, July 2020.

[45] D. A. Brown et al. ENDF/B-VIII.0: The 8^{th} Major Release of the Nuclear Reaction Data Library with CIELO-project Cross Sections, New Standards and Thermal Scattering Data. *Nuclear Data Sheets*, 148:1–142, February 2018.

[46] N. M. Larson. Updated Users' Guide for SAMMY: Multilevel R-Matrix Fits to Neutron Data Using Bayes' Equations. *ORNL/TM-9179/R8, Oak Ridge National Laboratory, Oak Ridge, TN*, 2008.

[47] M. Weigand et al. ^{63}Ni (n ,γ) cross sections measured with DANCE. *Physical Review C*, 92(4):045810, October 2015.

[48] T. n_TOF Collaboration. CERN n_TOF Facility: Performance Report. Technical Report CERN/INTC-O-011, INTC-2002-037, CERN-SL-2002-053 ECT, CERN, 2006.

[49] G. M. Novoselov et al. Total neutron cross-sections and resonance parameters for ^{80}Se in the energy range up to 10 keV. *Jadernye Konstanty (Nuclear Constants)*, 1-2:3, 1995.

[50] S. F. Mughabghab and D. I. Garber. *Neutron cross sections. Volume I. Resonance parameters.* Academic Press Inc, United States, 1973.

[51] E. P. Wigner and L. Eisenbud. Higher Angular Momenta and Long Range Interaction in Resonance Reactions. *Physical Review*, 72(1):29–41, July 1947.

[52] A. M. Lane and R. G. Thomas. R-Matrix Theory of Nuclear Reactions. *Reviews of Modern Physics*, 30(2):257–353, April 1958.

[53] F. Fröhner. Evaluation and analysis of nuclear resonance data, jeff report 18. *Nuclear Energy Agency,(OECD)*, 2000.

[54] N. Bohr. Neutron Capture and Nuclear Constitution. *Nature*, 137(3461):344–348, February 1936.

[55] J. M. Blatt and L. C. Biedenharn. The Angular Distribution of Scattering and Reaction Cross Sections. *Reviews of Modern Physics*, 24(4):258–272, October 1952.

[56] C. W. Reich and M. S. Moore. Multilevel Formula for the Fission Process. *Physical Review*, 111(3):929–933, August 1958.

[57] G. Breit and E. Wigner. Capture of Slow Neutrons. *Physical Review*, 49(7):519–531, April 1936.

[58] M. Heil et al. Quasistellar spectrum for neutron activation measurements at kT=5keV. *Physical Review C*, 71(2):025803, February 2005.

[59] C. Guerrero et al. The n_TOF Total Absorption Calorimeter for neutron capture measurements at CERN. *Nuclear Instruments and Methods in Physics Research A*, 608(3):424–433, September 2009.

[60] M. C. Moxon and E. R. Rae. A gamma-ray detector for neutron capture cross-section measurements. *Nuclear Instruments and Methods*, 24:445–455, July 1963.

[61] R. L. Macklin and J. H. Gibbons. Capture-Cross-Section Studies for 30-220-keV Neutrons Using a New Technique. *Physical Review*, 159(4):1007–1012, July 1967.

[62] C. Domingo-Pardo. i-TED: A novel concept for high-sensitivity (n,γ) cross-section measurements. *Nuclear Instruments and Methods in Physics Research A*, 825:78–86, July 2016.

[63] U. Abbondanno et al. New experimental validation of the pulse height weighting technique for capture cross-section measurements. *Nuclear Instruments and Methods in Physics Research A*, 521(2-3):454–467, April 2004.

[64] Centre Européenne pour la Recherche Nucléaire, CERN. `https://home.cern/science/accelerators`.

[65] D. Mancusi et al. On the role of secondary pions in spallation targets. *European Physical Journal A*, 53(5):80, May 2017.

[66] C. Guerrero et al. Performance of the neutron time-of-flight facility n_TOF at CERN. *European Physical Journal A*, 49:27, February 2013.

[67] C. Weiß et al. The new vertical neutron beam line at the CERN n_TOF facility design and outlook on the performance. *Nuclear Instruments and Methods in Physics Research A*, 799:90–98, November 2015.

[68] T. n_TOF Collaboration. The new n_TOF NEAR Station. Technical Report CERN-INTC-2020-073, INTC-I-222, CERN, 2020.

[69] M. Barbagallo et al. High-accuracy determination of the neutron flux at n_TOF. *European Physical Journal A*, 49:156, December 2013.

[70] S. Andriamonje et al. A New 2D-micromegas Detector for Neutron Beam Diagnostic at n_TOF. *Journal of Korean Physical Society*, 59:1601–1604, August 2011.

[71] S. Lo Meo et al. GEANT4 simulations of the n_TOF spallation source and their benchmarking. *European Physical Journal A*, 51:160, December 2015.

[72] J. Lerendegui-Marco. *Neutron radiative capture on ^{242}Pu: addressing the target accuracies for innovative nuclear systems*. PhD thesis, Universidad de Sevilla, 2018.

[73] J. M. Belleman et al. A new wall current monitor for the CERN Proton Synchrotron. In *Proceedings of the 5^{th} International Beam Instrumentation Conference*, 2016.

[74] S. Marrone et al. A low background neutron flux monitor for the n_TOF facility at CERN. *Nuclear Instruments and Methods in Physics Research A*, 517(1-3):389–398, January 2004.

[75] P. Žugec et al. GEANT4 simulation of the neutron background of the C_6D_6 set-up for capture studies at n_TOF. *Nuclear Instruments and Methods in Physics Research A*, 760:57–67, October 2014.

[76] R. Plag et al. An optimized C_6D_6 detector for studies of resonance-dominated (n,γ) cross-sections. *Nuclear Instruments and Methods in Physics Research A*, 496(2):425–436, January 2003.

[77] P. F. Mastinu et al. New C_6D_6 detectors: reduced neutron sensitivity and improved safety. Technical Report CERN-INTC-2013-002, CERN, 2013.

[78] J. Balibrea-Correa et al. A first prototype of C_6D_6 total-energy detector with SiPM readout for neutron capture time-of-flight experiments. *Nuclear Instruments and Methods in Physics Research A*, 985:164709, January 2021.

[79] C. Domingo-Pardo et al. Resonance capture cross section of Pb207. *Physical Review C*, 74(5):055802, November 2006.

[80] O. Klein and T. Nishina. Über die Streuung von Strahlung durch freie Elektronen nach der neuen relativistischen Quantendynamik von Dirac. *Zeitschrift fur Physik*, 52(11-12):853–868, November 1929.

[81] D. B. Syme. The black and white filter method for background determination in neutron time-of-flight spectrometry. *Nuclear Instruments and Methods in Physics Research*, 198(2):357–364, July 1982.

[82] U. Abbondanno et al. The data acquisition system of the neutron time-of-flight facility n_TOF at CERN. *Nuclear Instruments and Methods in Physics Research A*, 538:692–702, February 2005.

[83] A. Masi et al. The CERN n_TOF Facility Data Acquisition System. In *Proc. of International Conference on Accelerator and Large Experimental Control Systems (ICALEPCS'17)*, number 16 in International Conference on Accelerator and Large Experimental Control Systems, pp. 1900–1905, Geneva, Switzerland, Jan. 2018. JACoW. https://doi.org/10.18429/JACoW-ICALEPCS2017-THPHA195.

[84] F. Gunsing et al. Nuclear data activities at the n_TOF facility at CERN. *European Physical Journal Plus*, 131(10):371, October 2016.

[85] L. Mascetti et al. Disk storage at CERN. In *Journal of Physics Conference Series*, volume 664 of *Journal of Physics Conference Series*, pp. 042035, December 2015.

[86] P. Žugec et al. Pulse processing routines for neutron time-of-flight data. *Nuclear Instruments and Methods in Physics Research A*, 812:134–144, March 2016.

[87] A. Casanovas. *Neutron capture cross section measurement of the heaviest s-process branching ^{204}Tl and of ^{203}Tl at CERN n TOF.* PhD thesis, CSIC - Universitat Politècnica de Catalunya, 2020.

[88] R. Brun and F. Rademakers. ROOT — An object oriented data analysis framework. *Nuclear Instruments and Methods in Physics Research A*, 389(1):81–86, February 1997.

[89] K. Fraval et al. Measurement and analysis of the ^{241}Am(n,γ) cross section with liquid scintillator detectors using time-of-flight spectroscopy at the n_TOF facility at CERN. *Physical Review C*, 89(4):044609, April 2014.

[90] M. Wang et al. The Ame2012 atomic mass evaluation. *Chinese Physics C*, 36(12):003, December 2012.

[91] H. P. K. K. E. Committee. *Photomultiplier tubes - Basics and applications.* Hamamatsu Photonics K. K., Japan, 2007.

[92] N. Akchurin and H. Kim. A study on ion initiated photomultiplier afterpulses. *Nuclear Instruments and Methods in Physics Research A*, 574(1):121–126, April 2007.

[93] J. Allison et al. Geant4 developments and applications. *IEEE Transactions on Nuclear Science*, 53(1):270–278, February 2006.

[94] J. Allison et al. Recent developments in GEANT4. *Nuclear Instruments and Methods in Physics Research A*, 835:186–225, November 2016.

[95] P. Žugec et al. An improved method for estimating the neutron background in measurements of neutron capture reactions. *Nuclear Instruments and Methods in Physics Research A*, 826:80–89, August 2016.

[96] J. Lerendegui-Marco et al. Geant4 Simulations for the Analysis of (n, γ) Measurements at n_TOF. In *Basic Concepts in Nuclear Physics: Theory*, volume 182, pp. 209, January 2016.

[97] J. L. Tain and D. Cano-Ott. The influence of the unknown de-excitation pattern in the analysis of β-decay total absorption spectra. *Nuclear Instruments and Methods in Physics Research A*, 571(3):719–727, February 2007.

[98] ENSDF. ENSDF database as of November 11, 2021, 2021. `http://www.nndc.bnl.gov/ensarchivals/`.

[99] T. V. Egidy and D. Bucurescu. Systematics of nuclear level density parameters. *Physical Review C*, 72(4):044311, October 2005.

[100] S. Valenta et al. First results on photon strength functions of ^{78}Se from the two-step γ Cascades measurement. In *European Physical Journal Web of Conferences*, volume 146 of *European Physical Journal Web of Conferences*, pp. 05010, September 2017.

[101] J. Kopecky and M. Uhl. Test of gamma-ray strength functions in nuclear reaction model calculations. *Physical Review C*, 41(5):1941–1955, May 1990.

[102] R. L. Macklin et al. Absolute neutron capture yield calibration. *Nuclear Instruments and Methods*, 164(1):213–214, August 1979.

[103] C. Domingo-Pardo. *New radiative neutron capture measurement of* ^{207}*Pb and* ^{209}*Bi*. PhD thesis, CSIC - Universitat de València, 2004.

[104] N. M. Larson et al. Doppler Broadening Revisited. *Oak Ridge National Laboratory, Oak Ridge, TN*, ORNL/TM-13525, 1998.

[105] A. J. Koning et al. TALYS: Comprehensive Nuclear Reaction Modeling. In R. C. Haight et al., editors, *International Conference on Nuclear Data for Science and Technology*, volume 769 of *American Institute of Physics Conference Series*, pp. 1154–1159, May 2005.

[106] H. Beer et al. On the Calculation of Maxwellian-averaged Capture Cross Sections. *Astrophysical Journal Supplement*, 80:403, May 1992.

[107] I. Dillmann et al. The Karlsruhe Astrophysical Database of Nucleosynthesis in Stars Project – Status and Prospects. *Nuclear Data Sheets*, 120:171–174, 2014.

[108] M. Igashira et al. Systematic Study on KeV-Neutron Capture Reaction of Se Isotopes. *Journal of Korean Physical Society*, 59:1665–1669, August 2011.

[109] Isotope mass Separator On-Line, CERN. `https://home.cern/science/experiments/isolde`.

[110] N. M. Chiera et al. Preparation of PbSe targets for ^{79}Se neutron capture cross section studies. *Submitted to Nuclear Instruments and Methods in Physics Research A (under review)*, November 2021.

[111] Institut Laue-Langevin, ILL. `https://www.ill.eu/`.

[112] G. Tagliente et al. The ^{93}Zr(n,γ) reaction up to 8 keV neutron energy. *Physical Review C*, 87(1):014622, January 2013.

[113] C. Guerrero et al. Neutron Capture on the s -Process Branching Point Tm 171 via Time-of-Flight and Activation. *Physical Review Letters*, 125(14):142701, October 2020.

[114] D. B. Everett et al. Gamma-radiation imaging system based on the Compton effect. *Proceedings of the Institution of Electrical Engineers*, 124:995–1000(5), November 1977.

[115] D. L. Pérez Magán et al. First tests of the applicability of γ-ray imaging for background discrimination in time-of-flight neutron capture measurements. *Nuclear Instruments and Methods in Physics Research A*, 823:107–119, July 2016.

[116] V. Schönfelder et al. The imaging Compton telescope COMPTEL on the Gamma Ray Observatory. *IEEE Transactions on Nuclear Science*, 1:766–770, January 1984.

[117] Y. Ichinohe et al. The first demonstration of the concept of "narrow-FOV Si/CdTe semiconductor Compton camera". *Nuclear Instruments and Methods in Physics Research A*, 806:5–13, January 2016.

[118] H. Tajima et al. Design and performance of Soft Gamma-ray Detector onboard the Hitomi (ASTRO-H) satellite. *Journal of Astronomical Telescopes, Instruments, and Systems*, 4:021411, April 2018.

[119] M. Singh. An electronically collimated gamma camera for single photon emission computed tomography. Part I: Theoretical considerations and design criteria. *Medical Physics*, 10(4):421–427, July 1983.

[120] S. Aldawood et al. Development of a Compton camera for prompt-gamma medical imaging. *Radiation Physics and Chemistry*, 140:190–197, November 2017.

[121] S. Tashenov and J. Gerl. Imaging algorithm for background suppression in the planned gamma tracking array of DESPEC. *Nuclear Instruments and Methods in Physics Research A*, 586(2):224–228, February 2008.

[122] G. Phillips. Applications of compton imaging in nuclear waste characterization and treaty verification. In *1997 IEEE Nuclear Science Symposium Conference Record*, volume 1, pp. 362–364. IEEE, 1997.

[123] S. J. Wilderman et al. Fast algorithm for list mode back-projection of Compton scatter camera data. *IEEE Transactions on Nuclear Science*, 45(3):957–962, June 1998.

[124] H. H. Barrett et al. Maximum-likelihood methods for processing signals from gamma-ray detectors. *IEEE Transactions on Nuclear Science*, 56(3):725–735, 2009.

[125] D. Xu and Z. He. Gamma-ray energy-imaging integrated spectral deconvolution. *Nuclear Instruments and Methods in Physics Research A*, 574(1):98–109, April 2007.

[126] W. Wang et al. Maximum-Likelihood Deconvolution in the Spatial and Spatial-Energy Domain for Events With Any Number of Interactions. *IEEE Transactions on Nuclear Science*, 59(2):469–478, April 2012.

[127] S. Wilderman et al. List-mode maximum likelihood reconstruction of compton scatter camera images in nuclear medicine. In *1998 IEEE Nuclear Science Symposium Conference Record. 1998 IEEE Nuclear*

Science Symposium and Medical Imaging Conference (Cat. No.98CH36255), volume 3, pp. 1716–1720 vol.3, 1998.

[128] T. Tomitani and M. Hirasawa. Image reconstruction from limited angle Compton camera data. *Physics in Medicine and Biology*, 47(12):2129–2145, June 2002.

[129] A. Andreyev et al. Fast image reconstruction for Compton camera using stochastic origin ensemble approach. *Medical Physics*, 38(1):429, January 2011.

[130] J. Balibrea-Correa et al. Machine Learning aided 3D-position reconstruction in large $LaCl_3$ crystals. *Nuclear Instruments and Methods in Physics Research Section A: Accelerators, Spectrometers, Detectors and Associated Equipment*, 1001:165249, 2021.

[131] V. Babiano-Suárez et al. Imaging neutron capture cross sections: i-TED proof-of-concept and future prospects based on Machine-Learning techniques. *European Physical Journal A*, 57(6):197, June 2021.

[132] V. Babiano et al. First i-TED demonstrator: A Compton imager with Dynamic Electronic Collimation. *Nuclear Instruments and Methods in Physics Research A*, 953:163228, February 2020.

[133] L. Mihailescu et al. SPEIR: A Ge Compton camera. *Nuclear Instruments and Methods in Physics Research A*, 570(1):89–100, January 2007.

[134] C. Domingo-Pardo et al. Focusable Compton Camera equipped with variable separation detectors, 2015. Patentscope, PCT/ES2016/070916.

[135] Leo, William R. *Techniques for Nuclear and Particle Physics Experiments: A How-to Approach.* Springer Berlin, Heidelberg, 1994.

[136] Advatech. `https://www.advatech-uk.co.uk/`.

[137] K. S. Shah et al. $LaCl_3(Ce)$ scintillator for γ-ray detection. *Nuclear Instruments and Methods in Physics Research A*, 505(1-2):76–81, June 2003.

[138] J. K. Hartwell and R. J. Gehrke. Observations on the background spectra of four $LaCl_3(Ce)$ scintillation detectors. *Applied Radiation and Isotopes*, 63(2):223–228, 2005.

[139] Scitlion. `http://www.scitlion.com`.

[140] C. Domingo-Pardo et al. A position sensitive γ-ray scintillator detector with enhanced spatial resolution, linearity, and field of view. *IEEE Transactions on Medical Imaging*, 28(12):2007–2014, 2009.

[141] L. Caballero et al. Gamma-ray imaging system for real-time measurements in nuclear waste characterisation. *Journal of Instrumentation*, 13(3):P03016, March 2018.

[142] F. Acerbi and S. Gundacker. Understanding and simulating SiPMs. *Nuclear Instruments and Methods in Physics Research A*, 926:16–35, May 2019.

[143] S. Gundacker and A. Heering. The silicon photomultiplier: fundamentals and applications of a modern solid-state photon detector. *Physics in Medicine and Biology*, 65(17):17TR01, September 2020.

[144] SensL. `https://sensl.com/`.

[145] P. Olleros et al. On the performance of large monolithic $LaCl_3$(Ce) crystals coupled to pixelated silicon photosensors. *Journal of Instrumentation*, 13(3):P03014, March 2018.

[146] R. Bugalho et al. Experimental characterization of the TOFPET2 ASIC. *Journal of Instrumentation*, 14(3):P03029, March 2019.

[147] E. Albuquerque et al. Experimental characterization of the 192 channel Clear-PEM frontend ASIC coupled to a multi-pixel APD readout of LYSO:Ce crystals. *Nuclear Instruments and Methods in Physics Research A*, 598(3):802–814, January 2009.

[148] M. D. Rolo et al. TOFPET ASIC for PET applications. *Journal of Instrumentation*, 8(2):C02050, February 2013.

[149] A. Di Francesco et al. TOFPET 2: A high-performance circuit for PET time-of-flight. *Nuclear Instruments and Methods in Physics Research A*, 824:194–195, July 2016.

[150] E. Garutti. Endotofpet-us a novel multimodal tool for endoscopy and positron emission tomography. In *2012 IEEE Nuclear Science Symposium and Medical Imaging Conference Record (NSS/MIC)*, pp. 2096–2101, 2012.

[151] R. Bugalho et al. Experimental results with TOFPET2 ASIC for time-of-flight applications. *Nuclear Instruments and Methods in Physics Research A*, 912:195–198, December 2018.

[152] PETsys. `https://www.petsyselectronics.com/web/`.

[153] A. Di Francesco et al. TOFPET2: a high-performance ASIC for time and amplitude measurements of SiPM signals in time-of-flight applications. *Journal of Instrumentation*, 11(3):C03042, March 2016.

[154] ISO/IEC. ISO International Standard ISO/IEC 9899:2018(E) – Programming Language C++.

[155] H. O. Anger. Scintillation Camera. *Review of Scientific Instruments*, 29(1):27–33, January 1958.

[156] C. W. Lerche et al. Depth of interaction detection with enhanced position-sensitive proportional resistor network. *Nuclear Instruments and Methods in Physics Research A*, 537:326–330, January 2005.

[157] Z. Li et al. Nonlinear least-squares modeling of 3D interaction position in a monolithic scintillator block. *Physics in Medicine and Biology*, 55(21):6515–6532, November 2010.

[158] V. Babiano et al. γ-Ray position reconstruction in large monolithic $LaCl_3$(Ce) crystals with SiPM readout. *Nuclear Instruments and Methods in Physics Research A*, 931:1–22, July 2019.

[159] Arrick Robotics, 2021. `https://www.arrickrobotics.com/z2.html`.

[160] H. O. Anger. Sensitivity, Resolution, and Linearity of the Scintillation Camera. *IEEE Transactions on Nuclear Science*, 13(3):380–392, December 1966.

[161] R. Pani et al. Revisited position arithmetics for $LaBr_3$:Ce continuous crystals. *Nuclear Physics B Proceedings Supplements*, 197(1):383–386, December 2009.

[162] J. Lerendegui-Marco et al. Towards machine learning aided real-time range imaging in proton therapy. *Accepted on Nature Scientific Reports*, January 2022.

[163] J. Balibrea-Correa et al. Hadron therapy range verification via machine-learning aided prompt-gamma imaging. In *Submitted to IEEE Nuclear Science Symposium Conference Record (under review)*, 2021.

[164] F. Gunsing et al. The measurement programme at the neutron time-of-flight facility n_TOF at CERN. In *European Physical Journal Web of Conferences*, volume 146 of *European Physical Journal Web of Conferences*, pp. 11002, September 2017.

[165] C. Massimi et al. ^{197}Au(n,γ) cross section in the resonance region. *Physical Review C*, 81(4):044616, April 2010.

[166] Texas Instruments. SN65LVDS9638 1500 Mbps LVDS Dial High Speed Differential Driver, 2020. `https://www.ti.com/product/SN65LVDS9638`.

[167] J. Lerendegui-Marco et al. i-TED Commissioning 2021. Technical report, CERN, 2021. `https://indico.cern.ch/event/1084557/contributions/4628294/attachments/2353894/4016289/i-TED_Commissioning_CollabMeetingNov21%281%29.pdf`.

[168] N. Nimpuno et al. *Greening Consumer Electronics*. ChemSec, 2009.